

AD-AL91 297

INVESTIGATION OF NON-LINEAR OPTICAL BEHAVIOR OF  
SEMICONDUCTORS FOR OPTICA. (U) FLORIDA UNIV GAINESVILLE  
DEPT OF MATERIALS SCIENCE AND ENGINE. J H SIMMONS

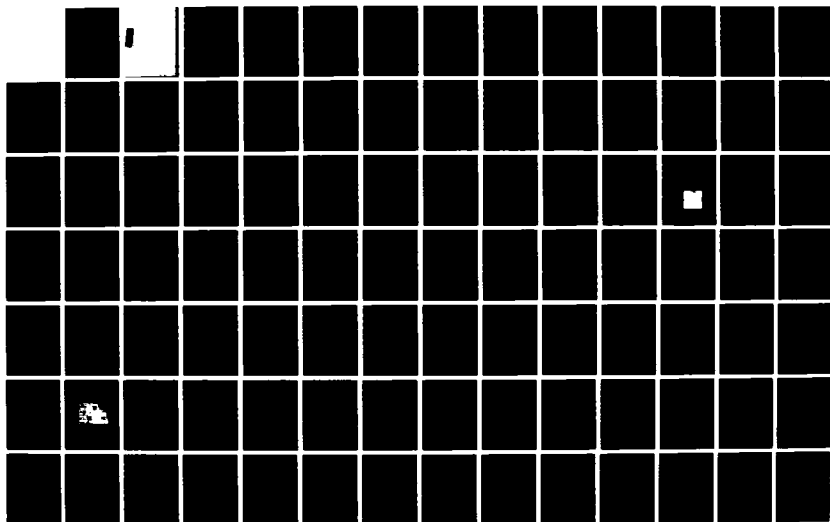
1/3

UNCLASSIFIED

30 SEP 87 AFOSR-TR-88-0133 AFOSR-84-0395

F/O 20/6

NL



1·0

2·5

1

3·5

2·

1·1

2·0

1·8

1·25

1·4

1·6

SECURITY CLASSIFICATION OF THIS PAGE

AD-A191 297

# REPORT DOCUMENTATION PAGE

|  |  |  |                            |
|--|--|--|----------------------------|
| 1. REPORT SECURITY CLASSIFICATION<br>Unclassified  |  | 1b. RESTRICTIVE MARKINGS   |                            |
| 2. SECURITY CLASSIFICATION AUTHORITY   |  | 3. DISTRIBUTION / AVAILABILITY OF REPORT<br>Approved for Public Release<br>Distribution Unlimited                  |                            |
| 4. DECLASSIFICATION / DOWNGRADING SCHEDULE   |  | 5. MONITORING ORGANIZATION REPORT NUMBER(S)<br><br>AFOSR-TR- 88 - 0133   |                            |
| 6. PERFORMING ORGANIZATION REPORT NUMBER(S)  |  | 7a. NAME OF MONITORING ORGANIZATION<br>Air Force Office of Scientific Research                                     |                            |
| 7. NAME OF PERFORMING ORGANIZATION<br>University of Florida  | 8b. OFFICE SYMBOL<br>(If applicable)         | 7b. ADDRESS (City, State, and ZIP Code)<br>Directorate of Chemical & Atmospheric Sciences<br>Bolling AFB, DC 20332 |                            |
| 8. ADDRESS (City, State, and ZIP Code)<br>Department of Materials Science & Engineering<br>Gainesville, Florida 32611                      |  | 9. PROCUREMENT INSTRUMENT IDENTIFICATION NUMBER<br>AFOSR-84-0395   |                            |
| 9. NAME OF FUNDING / SPONSORING ORGANIZATION<br>Air Force Office of Scientific Research  | 8b. OFFICE SYMBOL<br>(If applicable)<br>NC   | 10. SOURCE OF FUNDING NUMBERS  |                            |
| 10. ADDRESS (City, State, and ZIP Code)<br>Dr. Donald R. Ulrich<br>Directorate of Chemical & Atmospheric Sciences<br>Bolling AFB, DC 20332 |  | PROGRAM ELEMENT NO.<br>61102F  | PROJECT NO.<br>2303        |
|  |  | TASK NO.<br>A3   | WORK UNIT<br>ACCESSION NO. |
| 11. TITLE (Include Security Classification)<br>Investigation of Non-Linear Optical Behavior of Semiconductors for Optical Switching        |  |  |                            |
| 12. PERSONAL AUTHOR(S)<br>L. H. Simmons  |  |  |                            |
| 13. TYPE OF REPORT<br>Final Technical  | 13b. TIME COVERED<br>FROM 10/1/84 TO 9/30/87 | 14. DATE OF REPORT (Year, Month, Day)<br>9/30/87   | 15. PAGE COUNT             |
| 16. SUPPLEMENTARY NOTATION   |  |  |                            |

| COSATI CODES |       |           | 18. SUBJECT TERMS (Continue on reverse if necessary and identify by block number)<br>Non-Linear Optics<br>Halide Glasses |
|--------------|-------|-----------|--|
| FIELD        | GROUP | SUB-GROUP |  |
|              |       |           |  |
|              |       |           |  |

19. ABSTRACT (Continue on reverse if necessary and identify by block number)

(on reverse)

|  |  |  |                          |
|--|--|--|--------------------------|
| 20. DISTRIBUTION / AVAILABILITY OF ABSTRACT<br><input checked="" type="checkbox"/> UNCLASSIFIED/UNLIMITED <input type="checkbox"/> SAME AS RPT <input type="checkbox"/> DTIC USERS |  | 21. ABSTRACT SECURITY CLASSIFICATION<br>Unclassified |                          |
| 22a. NAME OF RESPONSIBLE INDIVIDUAL<br>Dr. Donald R. Ulrich  |  | 22b. TELEPHONE (Include Area Code)<br>(202) 767-4963 | 22c. OFFICE SYMBOL<br>NC |

FORM 1473, 84 MAR

83 APR edition may be used until exhausted  
All other editions are obsolete

SECURITY CLASSIFICATION OF THIS PAGE

### Abstract

Studies were conducted on semiconductor doped filter glasses which have been observed to exhibit third order optical non-linearity. This NLO behavior switches on and off in sub-picosecond times. However, the switching time, the NLO coefficient and the operating temperature are affected by the microstructure of the precipitated CdS and CdSe semiconductors. Studies were conducted to examine the crystal microstructures developed in these filter glasses and to correlate them with the optical properties of the semiconductors. There appears to be a potential for an increase in NLO coefficient by a factor of 10 to 1000 with the development of a suitable microstructure. Results and implications of the studies are presented. Studies on thin films of semiconducting CdS showed that microstructure can be controlled by suitable sputtering conditions. Strong exciton transitions were observed and have a high potential for NLO behavior. Composite thin films of CdS semiconducting crystals confined in a glass matrix were formed by co-evaporation. This is a novel method which produces quantum-confined exciton behavior and promises very high NLO coefficients. However, the lack of suitable instrumentation due to a severe funding cut in the third year has made impossible to measure the NLO coefficients of these films.

Studies of the phase separation behavior of fluoride glasses were continued in the system:  $\text{CdF}_2$ ,  $\text{LiF}$ ,  $\text{AlF}_3$ ,  $\text{PbF}_2$ . Two levels of phase separation were observed, consisting of a large microstructure of isolated spheres 3-10  $\mu\text{m}$  in diameter, and a very small interconnected microstructure resulting from secondary phase separation. The analysis of phase compositions is expected to yield new glass compositions with very high phase stability. A paper reporting these results has been accepted for publication by the Journal of the American Ceramic Society.



5 144

INVESTIGATION OF NON-LINEAR OPTICAL BEHAVIOR  
OF SEMICONDUCTORS FOR OPTICAL SWITCHING

FINAL TECHNICAL REPORT

TO

DR. DONALD R. ULRICH, PROGRAM MANAGER  
DIRECTORATE OF CHEMICAL AND ATMOSPHERIC SCIENCES  
AIR FORCE OFFICE OF SCIENTIFIC RESEARCH  
BOLLING AIR FORCE BASE, DC 20332

GRANT AFOSR-84-0395

PERIOD COVERED:

OCTOBER 1, 1984 - SEPTEMBER 30, 1986

SUBMITTED BY:

JOSEPH H. SIMMONS  
DEPARTMENT OF MATERIALS SCIENCE AND ENGINEERING  
UNIVERSITY OF FLORIDA  
GAINESVILLE, FLORIDA 32611

### Abstract

Studies were conducted on semiconductor doped filter glasses which have been observed to exhibit third order optical non-linearity. This NLO behavior switches on and off in sub-picosecond times. However, the switching time, the NLO coefficient and the operating temperature are affected by the microstructure of the precipitated CdS and CdSe semiconductors. Studies were conducted to examine the crystal microstructures developed in these filter glasses and to correlate them with the optical properties of the semiconductors. There appears to be a potential for an increase in NLO coefficient by a factor of 10 to 1000 with the development of a suitable microstructure. Results and implications of the studies are presented. Studies on thin films of semiconducting CdS showed that microstructure can be controlled by suitable sputtering conditions. Strong exciton transitions were observed and have a high potential for NLO behavior. Composite thin films of CdS semiconducting crystals confined in a glass matrix were formed by co-evaporation. This is a novel method which produces quantum-confined exciton behavior and promises very high NLO coefficients. However, the lack of suitable instrumentation due to a severe funding cut in the third year has made impossible to measure the NLO coefficients of these films.

Studies of the phase separation behavior of fluoride glasses were continued in the system:  $\text{CdF}_2$ ,  $\text{LiF}$ ,  $\text{AlF}_3$ ,  $\text{PbF}_2$ . Two levels of phase separation were observed, consisting of a large microstructure of isolated spheres 3-10  $\mu\text{m}$  in diameter, and a very small interconnected microstructure resulting from secondary phase separation. The analysis of phase compositions is expected to yield new glass compositions with very high phase stability. A paper reporting these results has been accepted for publication by the Journal of the American Ceramic Society.



|                      |         |
|----------------------|---------|
| Available to the     |         |
| Aviation, Space, and |         |
| Dist                 | Special |
| A-1                  |         |

## Introduction

The research program has consisted of six tasks, arranged in such a way that research is not conducted on all six tasks simultaneously but rather, it flows from task to task as the research progresses.

- Task I - Investigations of Non-Linear Processes in Semiconductors
- Task II - Fundamental Studies of Sol-Gel Microengineering Processes for Digital Optical Circuits
- Task III - Device Physics Studies of Multiple Faced Fabry-Perot Cavities
- Task IV - Computer Simulation Studies of Systems Designs
- Task V - Phase Instability Processes in Fluoride Glasses
- Task VI - Investigation of Parameters for the Formation of Optical Fibers from Sol-Gel Solutions

### Tasks I and II

Tasks I and II have received the majority of our research effort in the past three years. Under these tasks, we have conducted a study of the mechanisms which lead to non-linear optical behavior in 2-6 semiconductors, which are currently the most promising NLO materials both in bulk form and in thin film form. Results are reported below. Five papers are in preparation.

### Tasks III and IV

Tasks III and IV on device design were conducted initially and were completed as reported in the FY 85 report. We have designed Multiple-Face Fabry-Perot cavities for all optical logic operation. Further work in this area requires the development of non-linear optical (NLO) materials. We have prepared a patent application which is awaiting a release for prior work from the Office of Naval Research.

#### Task V

Task V has been continued for three years, although the incremental funding is usually available for only three months of each year. Our studies of the immiscibility phase instability in fluoride glasses have concentrated on the system  $\text{PbF}_2\text{-CdF}_2\text{-LiF-AlF}_3$ . We have measured the extent of phase-separation in several compositions. Our research has led us to show that this system also exhibits secondary phase separation, and that crystallization results as a direct product of the phase separation process. Four publications will result (two are in print, two are in preparation).

#### Task VI

Studies of conditions for drawing optical glass fibers from sol-gel solutions were ended in 1985 with the identification of aging and solution preparation conditions for optimum spinnability of fibers. This completed the scope of the program and no further work was conducted on this Task in the remainder of the contract.

## Report of Results

### A. Foreword

The research covered by this grant extended over three years from October 1, 1984 to September 30, 1987. Six tasks as described in the Introduction were covered. The major goals were:

- (1) to investigate optical processes in 2-6 semiconductors which enhance optical non-linearity
- (2) to study the fabrication and microstructure properties of these NLO materials
- (3) to study phase-instabilities in fluoride glasses.

The contract was begun as the principal investigator, J. H. Simmons, joined the faculty at the University of Florida, and the research went through a period of nucleation which consisted of setting up the optical testing laboratory and training new students. This was reflected in the first year progress report.

The third year of the contract was conducted at a severely reduced support level which had the effect of preventing measurements of non-linear optical coefficients in the sample prepared due to a lack of an adequate laser source. The measurements could not be conducted at other laboratories due to the highly specialized nature of the tests. A system is being assembled at Bellcore Research Laboratories, which will enable us to conduct the necessary tests.

On the whole, however, this was a very successful research project. We developed two material systems which show great promise in non-linear optical device applications and developed a novel parallel processing architecture for non-linear optical logic operations. The parallel processing architecture is

simple and takes advantage of the desirable characteristics of NLO devices to produce massively parallel processing of data signals.

The two new materials developed have shown strong exciton resonances and quantum confinement effects. Both of these combine to yield non-linear optical behavior with a high coupling coefficient at room temperature. The first is a totally novel material made as a glass-CdS composite thin film. Recent measurements at Bellcore Laboratories have found this material to be the best current candidate for NLO applications. The second material is made up of specially treated commercial filter glasses. We have developed process modifications which promise to yield similar materials with high NLO behavior. We expect to implement these processes in the fabrication of a new composite if this research is continued. During this project, we graduated one Ph.D. and two M.S. students in the Department of Materials Science and Engineering. The Ph.D. graduate is currently employed at Bellcore Research Labs, in Red Bank, N.J. with the Optical Devices Group. His group was so interested in the research conducted under this contract, as reported below, that he will continue working on this project, thus conducting the effective transfer of technology from University to Industry which AFOSR encourages.

The research conducted under this grant has been reported in 12 journal articles and over 25 oral presentations. The 12 journal articles are listed below:

1. "Non-Linear Optical Composite Materials, Using CdS," J. H. Simmons, E. M. Clausen, Jr. and B. G. Potter, Jr., "Science of Ceramic Chemical Processing, (3rd Ultrastructure Conference).
2. "Quantum Size Effects in CdS-Glass Composites," B. G. Potter, Jr. and J. H. Simmons, submitted to Phys. Rev. B.
3. "Resonance Raman in CdS and CdS<sub>x</sub>Se<sub>1-x</sub> Composites with Glass," B. G. Potter, Jr. and J. H. Simmons, in preparation for Optics Communications.

4. "Band-Gap Structure Modifications from the Size Confinement of CdS and  $\text{CdS}_x\text{Se}_{1-x}$  Crystals in Glass," in preparation for the Journal of the American Ceramic Society.
  5. "Optical Properties of CdS Thin Films Prepared by RF Magnetron Sputtering," E. M. Clausen, Jr. and J. H. Simmons, in preparation for the Journal of the American Ceramic Society.
  6. "Non-Linear Optical Properties of Co-Sputtered Semiconductor-Glass Composites," E. M. Clausen, Jr. and J. H. Simmons, in preparation for Applied Optics.
  7. "Phase Separation in a  $\text{ZrF}_4$ - $\text{ThF}_4$ -Based Glass," J. H. Simmons and C. J. Simmons, Materials Science Forum 5, 265 (1985).
  8. "Immiscibility and Crystallization in Heavy Metal Fluoride Glasses," O. H. El Bayoumi, C. J. Simmons, M. J. Suscavage, E. M. Clausen, J. H. Simmons, Materials Science Forum 5, 263 (1985).
  9. "Liquid-Liquid Immiscibility in Mixed  $\text{ZrF}_4$ - $\text{ThF}_4$  Glass," C. J. Simmons and J. H. Simmons, Journal of the American Ceramic Society 68, C-258 (1985).
  10. "Phase Stability of  $\text{CdF}_2$ - $\text{LiF}$ - $\text{AlF}_3$ - $\text{PbF}_2$  Glasses," O. H. El Bayoumi, C. J. Simmons, E. M. Clausen, Jr., M. J. Suscavage, J. H. Simmons, accepted for publication, Journal of the American Ceramic Society.
  11. "Primary and Secondary Phase Separation in  $\text{CdF}_2$ - $\text{UF}$ - $\text{AlF}_3$ - $\text{PbF}_2$  Glasses," M. S. Randall and J. H. Simmons, submitted to the Journal of the American Ceramic Society.
  12. "Phase-Separation Induced Crystallization in  $\text{CdF}_2$ - $\text{LiF}$ - $\text{AlF}_3$ - $\text{PbF}_2$  Glasses," M. S. Randall and J. H. Simmons, in preparation for the Journal of the American Ceramic Society.
- B. Tasks I and II -Optical Properties of 2-6 Semiconductor Materials for Non-Linear Optical Behavior.

The research conducted in these two tasks culminated in a successful achievement of the three-year goals.

At present CdS single crystals at 1.2°K have shown the best NLO characteristics, but single crystal are not suitable for applications and the temperature is too low. We have studied processes which will allow us to make easily fabricated semiconductor-glass composites which can maintain the single crystal properties and operate at room temperature. This work has great

promise, we now understand the underlying processes and have initiated studies on new materials fabrication techniques. We have demonstrated that these semiconductor-glass composites have a good chance to achieve desirable NLO properties. We now know how to modify the compositions to achieve this.

#### 1. Studies of Quantum Confinement in Semiconductor-glass Composites.

This work was divided into two parts:

- (a) Studies of the confinement effect and its origin in LDC semiconductors.
- (b) Fabrication of new materials.

This research in part (a) was completed at the end of this contract. The results are discussed below.

The second part of this research, part (b) was conducted using commercially available glasses. Controlled heat-treatments showed that exciton behavior could be developed over a wide range of energies, using quantum-confinement effects and crystal stoichiometry variations. These materials have exhibited a very large NLO coefficient with rapid on and off switching rates. However, high power tests conducted at the University of Arizona revealed a low damage threshold which is associated with fabrication conditions. It is the current consensus, between our laboratories and those of Drs. George Stegeman and Dr. Colin Seaton at the University of Arizona, that no glasses commercially available today satisfy the requirements for NLO applications and that there is a great need for new fabrication efforts.

Our studies have shown the direction to follow in producing the new glass-crystal composites, and this approach will be implemented if this research is continued.



1998, 1999, 2000, 2001, 2002, 2003, 2004, 2005, 2006, 2007, 2008, 2009, 2010, 2011, 2012, 2013, 2014, 2015, 2016, 2017, 2018, 2019, 2020, 2021, 2022, 2023, 2024, 2025, 2026, 2027, 2028, 2029, 2030, 2031, 2032, 2033, 2034, 2035, 2036, 2037, 2038, 2039, 2040, 2041, 2042, 2043, 2044, 2045, 2046, 2047, 2048, 2049, 2050, 2051, 2052, 2053, 2054, 2055, 2056, 2057, 2058, 2059, 2060, 2061, 2062, 2063, 2064, 2065, 2066, 2067, 2068, 2069, 2070, 2071, 2072, 2073, 2074, 2075, 2076, 2077, 2078, 2079, 2080, 2081, 2082, 2083, 2084, 2085, 2086, 2087, 2088, 2089, 2090, 2091, 2092, 2093, 2094, 2095, 2096, 2097, 2098, 2099, 2100, 2101, 2102, 2103, 2104, 2105, 2106, 2107, 2108, 2109, 2110, 2111, 2112, 2113, 2114, 2115, 2116, 2117, 2118, 2119, 2120, 2121, 2122, 2123, 2124, 2125, 2126, 2127, 2128, 2129, 2130, 2131, 2132, 2133, 2134, 2135, 2136, 2137, 2138, 2139, 2140, 2141, 2142, 2143, 2144, 2145, 2146, 2147, 2148, 2149, 2150, 2151, 2152, 2153, 2154, 2155, 2156, 2157, 2158, 2159, 2160, 2161, 2162, 2163, 2164, 2165, 2166, 2167, 2168, 2169, 2170, 2171, 2172, 2173, 2174, 2175, 2176, 2177, 2178, 2179, 2180, 2181, 2182, 2183, 2184, 2185, 2186, 2187, 2188, 2189, 2190, 2191, 2192, 2193, 2194, 2195, 2196, 2197, 2198, 2199, 2200, 2201, 2202, 2203, 2204, 2205, 2206, 2207, 2208, 2209, 2210, 2211, 2212, 2213, 2214, 2215, 2216, 2217, 2218, 2219, 2220, 2221, 2222, 2223, 2224, 2225, 2226, 2227, 2228, 2229, 2230, 2231, 2232, 2233, 2234, 2235, 2236, 2237, 2238, 2239, 2240, 2241, 2242, 2243, 2244, 2245, 2246, 2247, 2248, 2249, 2250, 2251, 2252, 2253, 2254, 2255, 2256, 2257, 2258, 2259, 2260, 2261, 2262, 2263, 2264, 2265, 2266, 2267, 2268, 2269, 2270, 2271, 2272, 2273, 2274, 2275, 2276, 2277, 2278, 2279, 2280, 2281, 2282, 2283, 2284, 2285, 2286, 2287, 2288, 2289, 2290, 2291, 2292, 2293, 2294, 2295, 2296, 2297, 2298, 2299, 2300, 2301, 2302, 2303, 2304, 2305, 2306, 2307, 2308, 2309, 2310, 2311, 2312, 2313, 2314, 2315, 2316, 2317, 2318, 2319, 2320, 2321, 2322, 2323, 2324, 2325, 2326, 2327, 2328, 2329, 2330, 2331, 2332, 2333, 2334, 2335, 2336, 2337, 2338, 2339, 2340, 2341, 2342, 2343, 2344, 2345, 2346, 2347, 2348, 2349, 2350, 2351, 2352, 2353, 2354, 2355, 2356, 2357, 2358, 2359, 2360, 2361, 2362, 2363, 2364, 2365, 2366, 2367, 2368, 2369, 2370, 2371, 2372, 2373, 2374, 2375, 2376, 2377, 2378, 2379, 2380, 2381, 2382, 2383, 2384, 2385, 2386, 2387, 2388, 2389, 2390, 2391, 2392, 2393, 2394, 2395, 2396, 2397, 2398, 2399, 2400, 2401, 2402, 2403, 2404, 2405, 2406, 2407, 2408, 2409, 2410, 2411, 2412, 2413, 2414, 2415, 2416, 2417, 2418, 2419, 2420, 2421, 2422, 2423, 2424, 2425, 2426, 2427, 2428, 2429, 2430, 2431, 2432, 2433, 2434, 2435, 2436, 2437, 2438, 2439, 2440, 2441, 2442, 2443, 2444, 2445, 2446, 2447, 2448, 2449, 2450, 2451, 2452, 2453, 2454, 2455, 2456, 2457, 2458, 2459, 2460, 2461, 2462, 2463, 2464, 2465, 2466, 2467, 2468, 2469, 2470, 2471, 2472, 2473, 2474, 2475, 2476, 2477, 2478, 2479, 2480, 2481, 2482, 2483, 2484, 2485, 2486, 2487, 2488, 2489, 2490, 2491, 2492, 2493, 2494, 2495, 2496, 2497, 2498, 2499, 2500, 2501, 2502, 2503, 2504, 2505, 2506, 2507, 2508, 2509, 2510, 2511, 2512, 2513, 2514, 2515, 2516, 2517, 2518, 2519, 2520, 2521, 2522, 2523, 2524, 2525, 2526, 2527, 2528, 2529, 2530, 2531, 2532, 2533, 2534, 2535, 2536, 2537, 2538, 2539, 2540, 2541, 2542, 2543, 2544, 2545, 2546, 2547, 2548, 2549, 2550, 2551, 2552, 2553, 2554, 2555, 2556, 2557, 2558, 2559, 2560, 2561, 2562, 2563, 2564, 2565, 2566, 2567, 2568, 2569, 2570, 2571, 2572, 2573, 2574, 2575, 2576, 2577, 2578, 2579, 2580, 2581, 2582, 2583, 2584, 2585, 2586, 2587, 2588, 2589, 2590, 2591, 2592, 2593, 2594, 2595, 2596, 2597, 2598, 2599, 2600, 2601, 2602, 2603, 2604, 2605, 2606, 2607, 2608, 2609, 2610, 2611, 2612, 2613, 2614, 2615, 2616, 2617, 2618, 2619, 2620, 2621, 2622, 2623, 2624, 2625, 2626, 2627, 2628, 2629, 2630, 2631, 2632, 2633, 2634, 2635, 2636, 2637, 2638, 2639, 2640, 2641, 2642, 2643, 2644, 2645, 2646, 2647, 2648, 2649, 2650, 2651, 2652, 2653, 2654, 2655, 2656, 2657, 2658, 2659, 2660, 2661, 2662, 2663, 2664, 2665, 2666, 2667, 2668, 2669, 2670, 2671, 2672, 2673, 2674, 2675, 2676, 2677, 2678, 2679, 26

© 2004 Blackwell Publishing Ltd *Journal of Internal Medicine* 255: 105–112

During the first year of the research, the principal investigators, we obtained a new material with great increase in existing quantum confinement and nonlinear optical effects. While some research still needs to be completed on the characteristics of the new material, regarding fabricating a number of better samples and more fully characterizing the fabrication process, the majority of the research is reported below. The research in part of the measurements of optical behavior of the films, had to be postponed, because of the reduction in funding the third year. We were not able to purchase the laser needed for tests, and could find no other laboratory with adequate facilities, or willingness to set up the proper tests. This lack of optical data has frustrated our attempts at working toward a patent on this subject. Dr. Clausen, who performed his research on this work is presently at the Bellcore Research Laboratories in Red Bank, N.J. and they have consented to let him set up some testing apparatus for preliminary non-linear optical measurements.

The development of parallel processing optical architecture and the multiple-face, cross-point switches which form its elements was finished in the first year of this project. Much of the background research was conducted while the Principal Investigator was at the Naval Research Laboratory. The work was reported in detail in the first annual report and a patent application has been prepared for submission through the University of Florida. We

are presently awaiting clearance from the Naval Research Laboratory before submission.

D. Task V - Phase Equilibria in Fluoride Glasses.

This research was funded on a supplementary funding basis from the RADC research laboratories at Hanscom AFB, MA. We had great difficulties with handling these funds, as they always arrived very close to the end of the fiscal year. There was always much uncertainty about our being able to use them. Therefore, proper planning of the research was difficult.

Nevertheless, Catherine J. Simmons and Michael S. Randall donated their time to the project, and we were able to meet all the goals, to the great satisfaction of Dr. El Bayoumi from RADC. The research results are presented below.

E. Task VI - Sol-Gel Processes for Continuous Fiber Drawing.

The research conducted in this task was also a supplementary project, conducted in the first year, and completed in that year. The results were included in an M.S. Thesis by Mr. R. S. Sheu and are described in the first annual report.

F. Detailed Description of Results.

Below are the texts for three theses which describe in detail the results of the research conducted on Tasks I and II and Task V.

OPTICAL PROCESSES IN CADMIUM SULFIDE  
THIN FILMS

## TABLE OF CONTENTS

|  | PAGE |
|--|------|
| ACKNOWLEDGMENTS . . . . .                            | iii  |
| ABSTRACT . . . . .                                   | vii  |
| CHAPTERS   |      |
| I      INTRODUCTION . . . . .                        | 1    |
| Optical Signal Processing . . . . .                  | 1    |
| Nonlinear Optical Materials . . . . .                | 2    |
| Thin Films . . . . .                                 | 5    |
| II     THEORY OF NONLINEAR OPTICS . . . . .          | 8    |
| Nonlinear Optical Susceptibility . . . . .           | 8    |
| Optical Bistability . . . . .                        | 19   |
| III    BACKGROUND - BIBLIOGRAPHICAL REVIEW . . . . . | 28   |
| Bulk Properties of Cadmium Sulfide . . . . .         | 28   |
| Photoluminescence of CdS . . . . .                   | 32   |
| Resonant Raman Scattering in CdS . . . . .           | 37   |
| Nonlinear Susceptibility . . . . .                   | 38   |
| CdS Thin Films . . . . .                             | 39   |
| Vacuum Deposition . . . . .                          | 39   |
| RF Sputtering . . . . .                              | 45   |
| Semiconductor Doped Filter Glasses . . . . .         | 50   |
| IV     EXPERIMENTAL METHOD . . . . .                 | 52   |
| Vacuum Deposition System . . . . .                   | 52   |
| RF Magnetron Sputtering . . . . .                    | 60   |
| Thin Film Deposition . . . . .                       | 63   |
| Substrate materials . . . . .                        | 64   |
| Substrate temperatures . . . . .                     | 66   |
| Deposition rates . . . . .                           | 68   |
| Co-Sputter Alternating Deposition (COSAD) . . . . .  | 68   |
| Post Deposition Treatments . . . . .                 | 70   |
| Thin Film Characterization . . . . .                 | 71   |
| Microstructure . . . . .                             | 71   |
| Chemical Analysis . . . . .                          | 73   |

|                               |  |     |
|-------------------------------|--|-----|
|                               | Optical Measurements . . . . .                         | 76  |
|                               | Index of Refraction . . . . .                          | 77  |
|                               | UV-VIS Absorption . . . . .                            | 86  |
|                               | Photoluminescence and Raman . . . . .                  | 88  |
| V                             | RESULTS AND DISCUSSION . . . . .                       | 96  |
|                               | Thin Film Physical Properties . . . . .                | 96  |
|                               | Microstructure Characterization . . . . .              | 96  |
|                               | Transmission electron microscopy . . . . .             | 96  |
|                               | Scanning electron microscopy . . . . .                 | 109 |
|                               | X-ray diffraction experiments . . . . .                | 123 |
|                               | Compositional Analysis . . . . .                       | 132 |
|                               | Stoichiometry determination of target material         | 132 |
|                               | Analytical techniques . . . . .                        | 134 |
|                               | Co-Sputter Alternating Deposition . . . . .            | 149 |
|                               | Microstructure . . . . .                               | 149 |
|                               | Composition . . . . .                                  | 163 |
|                               | Thin Film Optical Properties . . . . .                 | 165 |
|                               | Absorption Spectra . . . . .                           | 167 |
|                               | Room temperature UV-VIS absorption . . . . .           | 168 |
|                               | Low temperature UV-VIS absorption . . . . .            | 174 |
|                               | Index of refraction . . . . .                          | 185 |
|                               | Photoluminescence and Raman Spectroscopy . . . . .     | 190 |
|                               | Photoluminescence spectra . . . . .                    | 193 |
|                               | Raman spectroscopy . . . . .                           | 207 |
|                               | COSAD Optical Properties . . . . .                     | 211 |
| VI                            | CONCLUSIONS . . . . .                                  | 218 |
| VII                           | FUTURE WORK . . . . .                                  | 224 |
| APPENDICES                    |  |     |
| A                             | BASIC PROGRAM FOR LAMBDA 9 SPECTROPHOTOMETER . . . . . | 227 |
| B                             | ELLIPSONOMETRY . . . . .                               | 230 |
| BIBLIOGRAPHY . . . . .        |  | 235 |
| BIOGRAPHICAL SKETCH . . . . . |  | 240 |

## CHAPTER I INTRODUCTION

### Optical Signal Processing

With the very intense development of optical communications in recent years, the need for integrated optical systems for the processing of optical signals has greatly increased. To take full advantage of the speed and information bandwidth available at optical frequencies, an all optical system is desired. All of today's systems operate by the high bandwidth transmission of optical signals in optical fibers, followed by conversion to lower bandwidth electrical signals before any processing, such as amplification and multiplexing, can take place. The limiting drift velocity of charge carriers in a semiconductor and the capacitive coupling between adjacent elements present the fundamental limit for processing speed in these systems. Also, the serial nature by which the electronic data must be manipulated presents another speed barrier. An alternate approach would utilize optical bistability and optical switching demonstrated in certain materials for all-optical modulation, detection and multiplexing. Optical switching is achievable with materials which display a third order nonlinear susceptibility. A third order susceptibility leads to an intensity dependent index of refraction or absorption. This nonlinear refractive index can exhibit onset and decay on a very fast time scale, which makes it an attractive

phenomenon for optical signal processing. With the proper material, all optical operations could conceivably be carried out in a monolithic thin film, which would act as a guiding medium with both active and passive regions. An optical communications fiber could be coupled directly to this thin film, thereby fully utilizing the speed and bandwidth of the optical signal.

A complementary application of an integrated optics technology which utilizes optical switching would be in the area of high speed logic operations for the next generation of computers. Logic gate operation has been demonstrated with several materials which exhibit a nonlinear optical susceptibility and optical bistability. A few of these gates have been shown to switch on a subnanosecond time frame, which is competitive with present day high speed electronic systems. The primary advantage of the optical gate is the possibility of parallel processing on the fundamental logic cell level, which adds tremendous speed advantages over electronic systems. Most optical computer designs today are based on integrated optics, in which the active regions consist of arrays of bistable devices arranged with a high spatial density. A high density of gates is possible because optical gates are not subject to capacitive coupling, thus making possible massive parallel processing without the connection problems encountered in today's electronic systems.

#### Nonlinear Optical Materials

A large number of architectures have been proposed for both computer systems and multiplexing circuits based on optical switching.

While this field has greatly advanced, there is, however, a very great need for suitable materials and systems. Many materials exhibit a third order nonlinear susceptibility,<sup>1</sup> but very few have the characteristics necessary for an integrated optics system. A few of the semiconductors which have been investigated include InSb, GaAs, GaP, CdS, and CdTe. Most of these semiconductor materials which show optical switching have been investigated in bulk form. Only the multiple quantum well (MQW) structures made from gallium arsenide are the notable exception and are made in thin film form.<sup>2</sup> This material is perhaps the most promising today for use in optical signal processing systems, primarily because its nonlinearity occurs at the same wavelength as the semiconductor lasers which are currently available. For an integrated optical system this is an essential consideration because most of the processes which produce the nonlinear susceptibility require laser light of energy near the band gap of the material.

Equally important considerations, however, include the value of the nonlinear coefficient, the switching speed, and the absorption coefficient, since these values determine how much power is required to switch the device, and how fast recovery will be. Low power operation is essential for any large scale integration, although the figure of merit (FOM) most often quoted is given by

$$\text{FOM} = \frac{n_2}{\tau \alpha} \quad (1.1)$$

where  $n_2$  is the nonlinear index,  $\tau$  is the switch-off time, and  $\alpha$  is the absorption coefficient. Obviously the larger the FOM the more



attractive a system is. MQW gallium arsenide has an additional advantage of room temperature operation, but suffers from a slow switch-off time and very large absorption. There are other materials which have been shown to exhibit a much larger nonlinear effect than MQW gallium arsenide. A material which has been demonstrated to exhibit one of the largest nonlinear coefficients is cadmium sulfide (CdS).<sup>3</sup> The large coefficient was obtained by saturating a bound exciton level in the band gap.<sup>4</sup> The mechanism which leads to the large exciton saturation effect in CdS is central to this dissertation and will be described in a subsequent section. However, only a very few groups have looked at CdS, and no one has either investigated the bound exciton saturation mechanism in thin films or explored the possible applications in integrated optics.

The most important consideration for any practical nonlinear application is the temperature at which the nonlinear process predominates. To the present day the largest nonlinear coefficients are only measured at very low temperatures. For example, the large coefficient obtained by saturating the bound exciton level in CdS occurs at 2° K. Since the binding energy of the bound exciton only corresponds to a few millielectron volts, the state is thermally annihilated at higher temperatures, and the large nonlinear effect disappears.

The electronic structure of the band gap, however, may be altered to permit access of exciton levels at higher temperatures by controlling the physical size of the material. The phenomenon by which this occurs is known as quantum confinement. When the crystal size of

a material is on the order of the radius of the exciton state, new boundary conditions can distort the translational motion of the exciton, its binding energy and the individual orbits of the electron and hole. At this size the electron and hole interactions with the crystal surface begin to govern the electronic properties of the semiconductor. Quantum confinement also occurs in the MQW structures of GaAs; however the exciton is only confined in one direction. A much stronger effect occurs when the confinement is in two or three dimensions.

#### Thin Films

A study of CdS thin films was chosen for a number of reasons: 1) very few semiconductors which display a nonlinear susceptibility have been tested in a thin film form, despite the potentially dominating role in applications. 2) Cadmium sulfide displays one of the largest excitonic saturation effects, and thus the influence of film structure due to deposition conditions or subsequent treatments could be investigated. 3) Quantum confinement effects and their interaction with the perturbation of the exciton absorption process are of great interest to the future of nonlinear optical developments and applications. Cadmium sulfide promises to offer a means of studying both the effects and their interplay with the development of the thin film structure. 4) Since the energies of the exciton states correspond to wavelengths in the visible part of the spectrum, the experimental optics for the measurement of these states is simplified, and many

investigative tools become available for following the underlying processes.

The study of any thin film for this application should start with examining the properties of the bulk material which contribute to the specific origin for the nonlinear effect. In the case of CdS this means looking at the electronic states of the material which lead to the presence of excitons. These states have been thoroughly examined for more than 30 years and they are probably the best understood in this material. Exciton states have been shown to occur in thin epitaxial films, but no one has investigated the presence of these states in polycrystalline thin films, nor have the effects of preparation conditions on the excitonic transitions of a thin films been investigated. The objective of this study therefore is to determine how exciton states would occur in polycrystalline thin films of the material, how they are affected by structure and formation conditions, and how size variations and grain boundary structures might affect their energy level structure.

A supplementary part of this study will investigate the possibility of producing thin film structures consisting of a glass matrix with small isolated crystals whose sizes matched those needed to develop quantum confinement effects. The investigation will use spectroscopic techniques to determine if quantum confinement effects can be induced on the exciton states in the material. The objective is to produce a thin film of semiconductor doped filter glass.

The process of quantum confinement has been and still is under investigation in bulk semiconductor doped filter glasses, which have

received considerable attention lately for nonlinear optics application. These are crown base glasses which contain one or two percent of CdS or mixtures of CdS and CdSe. It has been postulated that the semiconductor crystals exist in the glass matrix as finely dispersed microcrystallites, which are small enough to permit quantum confinement effects to occur. This effect is still not well understood and has not been clearly demonstrated. Many authors have observed energy shifts that may be due to compositional effects rather than microstructure size. However, it appears theoretically that with sufficient confinement, the exciton state will be accessible at room temperature.

## CHAPTER II THEORY OF NONLINEAR OPTICS

### Nonlinear Optical Susceptibility

The nonlinear refractive index which is observed in certain semiconductor materials is a result of an electronic polarization which is induced by the interaction with a monochromatic radiation field. The susceptibilities of the polarization determine the values of the experimentally measured optical properties. To understand the relationships between the susceptibilities and the optical properties we must first consider the electro-magnetic field,  $E$ , which is given by

$$E(t) = E(\omega)e^{-i\omega t} + E^*(\omega)e^{i\omega t} . \quad (2.1)$$

The resulting polarization has frequency components at all multiples of  $\pm\omega$ , but considering only those that occur at  $\omega$

$$P(\omega) = \chi^{(1)}E(\omega) + \chi^{(2)}[E]E(\omega) + \chi^{(3)}[E]^2E(\omega) + \dots \quad (2.2)$$

The first term in the series,  $\chi^{(1)}$  is the linear susceptibility and by using first order perturbation theory,<sup>5</sup> the linear dispersion of the refractive index below the band gap can be calculated. The higher

order terms in the series are the nonlinear susceptibilities, and although their magnitudes are much smaller than the first term, under very high field intensities a number of different effects can be observed. For non-centrosymmetric crystals (i.e. crystals without an inversion center), under appropriate conditions, the second order term is manifested as two different effects. The first is a quadratic variation of the refractive index with applied voltage, which is known as the Kerr effect. The second is the generation of a second harmonic radiation field. Second harmonic generation is a very useful effect for doubling the frequency of a laser beam. Both of these effects have many important applications; however, the primary interest of this study is the effects which lead to the third order term  $\chi^{(3)}$ . One consequence of the third order term is the generation of a third harmonic radiation field. For the current topic of this study, however, the manifestation of this term as a nonlinear refractive index is of primary interest. The relationship between the third order susceptibility and the nonlinear refractive index can be understood by first considering basic dielectric theory for the displacement of a charge in response to an applied electric field:

$$D(\omega) = E(\omega) + 4\pi P(\omega) = \epsilon E(\omega) \quad (2.3)$$

where  $D(\omega)$  is the frequency dependence of the displacement and  $\epsilon$  is the complex dielectric constant. The variable,  $\epsilon$  can be defined as

$$\epsilon = \left( n + \frac{ica}{2\omega} \right)^2 \quad (2.4)$$

where  $ca/2\omega$  is the extinction coefficient. By combining these two equations a relation between the polarization and the index of refraction can be written.

$$\left( n + \frac{ica}{2\omega} \right)^2 = 1 + 4\pi P(\omega)/E(\omega) \quad (2.5)$$

The nonlinear susceptibility can be defined by expansion of the refractive index in terms of the intensity  $I$ , of the radiation inside the sample:<sup>5</sup>

$$n = n_1 + n_2 I + n_3 I^2 + \dots \quad (2.6)$$

Next we assume that the extinction coefficient is very small compared to  $n$ . Then by using equations 2.5 and 2.6 and expanding the terms,

$$n^2 = n_1^2 + 2n_1 n_2 I + (n_2 I)^2 = 1 + 4\pi \chi^{(1)} + 4\pi \chi^{(3)} [E]^2. \quad (2.7)$$

Finally we assume  $n_2$  is much smaller than  $n_1$  and by comparing coefficients of  $[E]^2$  and  $I$

$$n_1^2 \approx 1 + 4\pi \chi^{(1)} \quad (2.8)$$

and

$$n_2 \approx \frac{2\pi \chi^{(3)}}{n_1} \quad (2.9)$$

There are essentially four electronic processes which can produce a reactive nonlinear susceptibility in semiconductors. These are known as 1) the induced free-carrier plasma, 2) the dynamic Burstein-Moss effect, 3) the direct saturation of interband excitations, and 4) the saturation of exciton absorption.<sup>5</sup> Of these 1 and 2 are the most commonly studied, 3 occurs in most direct band gap semiconductors, and 4 is the most promising for high speed operations. All four processes can occur in some materials. The most dominating process which is observed depends somewhat on the material, but mostly on the particular experimental setup and measurement temperature. As shown in Table 1, different processes result in widely different values of the reported nonlinear index and saturation intensity.

The four processes listed above basically describe how the transitions between different levels in a semiconductor and the saturation of those levels result in the observed nonlinear susceptibility. Depending on the band structure of a material and the particular wavelength of light used for the analysis, one of the four processes will dominate. The one process that can occur in nearly every semiconductor, however, is the induced free-carrier plasma. Assuming that photo induced transitions produce electron-hole pairs, the number of these free carriers will be intensity dependent.



TABLE 1

Listing of Nonlinear Optical Values for Certain  
Semiconductor Materials

| Material       | Electronic<br>Process | $I_s$ ( $\text{W}/\text{cm}^2$ ) | $n_2$ ( $\text{cm}^2/\text{W}$ ) | $t_{\text{off}}$ (sec) | FCM  |
|----------------|-----------------------|----------------------------------|----------------------------------|------------------------|------|
| GaAs<br>(MQWS) | FES                   | 150                              | $10^{-14}$                       | $10^{-8}$              | 1    |
|                | DBM                   | 500                              |                                  |                        |      |
| InSb           | DIS                   | 2000                             | $6 \times 10^{-5}$               | $10^{-6}$              | 0.06 |
| CdS            | BES                   | 58,26                            | $10^{-14}, 10^{-12}$             | $10^{-9}$              | 1    |
|                | FCP                   | $1.2 \times 10^5$                |                                  | $10^{-10}$             |      |

Key for Electronic Processes: FES - Free Exciton Saturation  
 DBM - Dynamic Burstein-Moss  
 DIS - Direct Interband Saturation  
 BES - Bound Exciton Saturation  
 FCP - Free Carrier Plasma

Depending on the recombination time  $\tau_R$ , and the absorption coefficient  $\alpha$ , the steady state density of free carriers will be given by

$$N = \frac{\alpha I \tau_R}{h \omega} \quad (2.10)$$

Once these carriers are formed, they are allowed to diffuse and form an electron-hole plasma. The plasma will respond to an applied electric field and the resulting undamped oscillations will produce a polarization which can be related to the index of refraction through the dielectric constant<sup>6</sup>

$$n^2 = \left( \epsilon - \frac{4 \pi N e^2}{m^* \omega^2} \right). \quad (2.11)$$

By use of equation 1.10, the nonlinear refractive index for a plasma can be written as

$$n_2(P) = \frac{-2 \pi e^2 \alpha \tau_R}{n m^* \omega^3} \quad (2.12)$$

where  $n$  is the refractive index of the material without the plasma and  $m^*$  is the effective mass. The transient susceptibility is determined by the time it takes for the free carriers to build up;<sup>7</sup> however, this can be a very short time. This process will also occur at room temperature. The disadvantage of this process for nonlinear optical applications is that the effect is very small because there is no coupling between the states, and therefore no resonance effects take place. The process also can suffer from a very slow recovery time because the recombination time in certain semiconductors is on the order of  $\mu\text{sec}$ .<sup>7</sup>

Another process that is based on an intensity dependent free carrier concentration is the dynamic Burstien-Moss or blocking effect. Again a steady state density of charge carriers is given by equation 2.10; however, the origin of the absorption is not considered explicitly. At low temperatures the carriers are assumed to thermalize by a phonon scattering process so that they fill the bottom of the conduction band. The top of the valance band becomes empty and the shift of the effective band gap to higher energy becomes intensity dependent. In association with this shift there must be an intensity dependent contribution to the refractive index.<sup>5</sup> This is because the filled conduction band effectively blocks absorptive transitions, and the blocked transitions no longer contribute to polarization and refraction. Also, some type of unspecified coupling takes place between excited states, so that the effect is enhanced somewhat. The nonlinear refractive index for this process is given by

$$n_2(\text{BM}) = \frac{2 \pi}{3 n} \left( \frac{e P}{h \omega} \right)^2 \frac{N}{h (\omega_G - \omega) I} \quad (2.13)$$

where  $N$  is the free carrier density given by equation 2.10,  $P$  is a momentum matrix element, and  $\omega_G$  is the effective band gap. For nonlinear optical applications the advantage of this process is that the occupied states are closer to resonance so that a larger  $n_2$  results. There also is the possibility that this process can occur at energies below the band gap, as saturation of excited carriers can be produced not by direct optical absorption, but by scattering from other excited states.<sup>6</sup> The one disadvantage of the process that is similar to the induced plasma process is that the interband relaxations required for decay of the state can be very slow. In some materials a faster decay process can occur by scattering to intraband transitions, which effectively relaxes the system by transferring the population to other states.<sup>6</sup>

Another mechanism for the nonlinearity observed in some materials is by a direct interband saturation process. This process assumes that the band structure in a direct gap semiconductor can be modeled as a set of uncoupled two level systems which are homogeneously broadened by a dephasing time  $T_2$ . Homogeneous broadening means that the individual transitions are indistinguishable. The  $T_2$ -Lorentzian broadening results in absorption below the band gap and excitation into the  $T_2$ -broadened "band-tail" is assumed to be responsible for the nonlinear refraction.<sup>6</sup> At some high level of intensity the two level system should become saturated, and associated with this saturation is a

nonlinear contribution to the refractive index.<sup>5</sup> The nonlinear index of refraction for this process is expressed by

$$n_2(S) = - \frac{1}{h^3} \left( \frac{e P}{h \omega} \right)^4 \frac{\tau}{T_2} \frac{2 \pi}{15 n^2 c} \times \left( \frac{2 m^*}{h} \right) (\omega_G - \omega)^{-3/2} \quad (2.14)$$

where  $\tau$  is the relaxation time, and  $c$  is the speed of light. The advantage of this process for nonlinear applications is that the effective nonlinear refractive index is inversely proportional to the band gap energy, so for small band gap materials this process leads to a very large effect. As indicated above, the broadening results in an effect which occurs below the band gap energy, so absorption losses are reduced. The disadvantage of utilizing this process is the same as for the other two processes; in some materials there is no fast mechanism for decay of the excited state.

The final process that will lead to an electronic nonlinear refractive index in certain semiconductors is the saturation of bound exciton levels. These particular defect states are characterized by a very narrow transition linewidth, which is comparable to atomic resonances. A bound exciton is an associated electron-hole pair that is bound to an impurity site. The oscillator strength of the bound exciton, which is related to the polarizability, is extremely large in comparison to oscillator strengths of molecules.<sup>1</sup> In addition, there is a very high density of oscillators, which contributes to a very large nonlinear effect. The absorption transition of the bound exciton

is modeled as a saturable two level system, inhomogeneously broadened by a  $T_2$  dephasing time. The transition linewidth is inhomogeneously broadened because excitons bound at different locations see different environments.<sup>4</sup> An inhomogeneously broadened system is described as a distribution of groups or classes of transitions, and within each class the transitions are assumed to be identical (homogeneously broadened). The saturation of the inhomogeneously broadened system does not depend on the homogeneous lineshape function, but rather on the linewidth of these "homogeneous packets".<sup>8</sup> This means that the saturation intensity is inversely dependent upon the dephasing time  $T_2$  as shown by

$$I_s = \frac{2 \pi^2 n^2 h \nu \Delta \nu}{\phi \lambda^2} \quad (2.15)$$

where  $\Delta \nu = (\pi T_2)^{-1}$  (2.16)

and  $\phi$  is the ratio of the radiative lifetime to the spontaneous decay time, which is usually taken as equal to one. In semiconductor systems the dephasing time is on the order of 0.1 psec,<sup>4</sup> which means that very low saturation intensities are required to saturate bound exciton transitions. The importance of the saturation intensity will be described in a following section; however, a small value indicates that the nonlinear refractive index is very large, as the two are inversely proportional (see equation 2.25). As shown in Table 1, in CdS a saturation intensity as small as 26 W/cm<sup>2</sup> has been measured, which corresponds to  $n_2$  value of  $1.3 \times 10^{-2}$  cm<sup>2</sup>/W.<sup>10</sup> This is the largest  $n_2$

value ever reported. Additional advantages of bound exciton saturation are that the state decays by a radiative transition and the lifetime is on the order of 500 psec. This would make for a very fast, low power switch. Also, since the excitons are bound to defect sites, there are no carrier diffusion problems, which in the other three processes tend to wash out the effect. The one primary disadvantage of utilizing this process is that the strongest exciton resonance occurs at 2° K. As the temperature is increased, the transition broadens, thereby requiring a larger saturation intensity and hence a smaller  $n_2$  is observed. In addition, since the exciton binding energy is only a few millielectron volts, the state is thermally annihilated at higher temperatures.

As previously described the process of quantum confinement could be used to access exciton levels at higher temperatures if the physical size of the material could be made small enough. Multiple quantum well structures produce quantum confinement in one direction because the structure is made up of alternating layers in which the layers act as infinite potential wells and the layer thickness is smaller than the exciton radius. Although the exciton is not confined in the other two directions, the effect is strong enough that nonlinearity can be observed at room temperature. The effect would be larger if confinement was made in the other two directions.

Optical Bistability

The primary means for measuring nonlinearity in materials is through an internal feedback device known as a Fabry-Perot interferometer. The saturation intensity of such a system is the intensity at which the gain of the feedback saturates. This is the point at which optical bistability occurs, and from the saturation intensity and the interferometer parameters the nonlinear index of refraction can be determined.

The Fabry-Perot consists of a cavity formed by two plane parallel, highly reflecting mirrors. The transmission of monochromatic light through the device is determined by the optical path length of the cavity. If the cavity is not tuned to the wavelength of the light, then a transmission of  $\approx 1\%$  results. When the optical path length is exactly equal to an integer number of wavelengths, then a resonance effect occurs and the output intensity from the device reaches nearly 100 % of the input intensity. A diagram of this process is shown in Figure 1. The optical path length is determined by the physical length  $d$ , times the refractive index  $n$  of the material within the cavity. The condition for resonance therefore is given by

$$2 n d = m \lambda \quad (2.17)$$

where  $m$  is the integer order number.



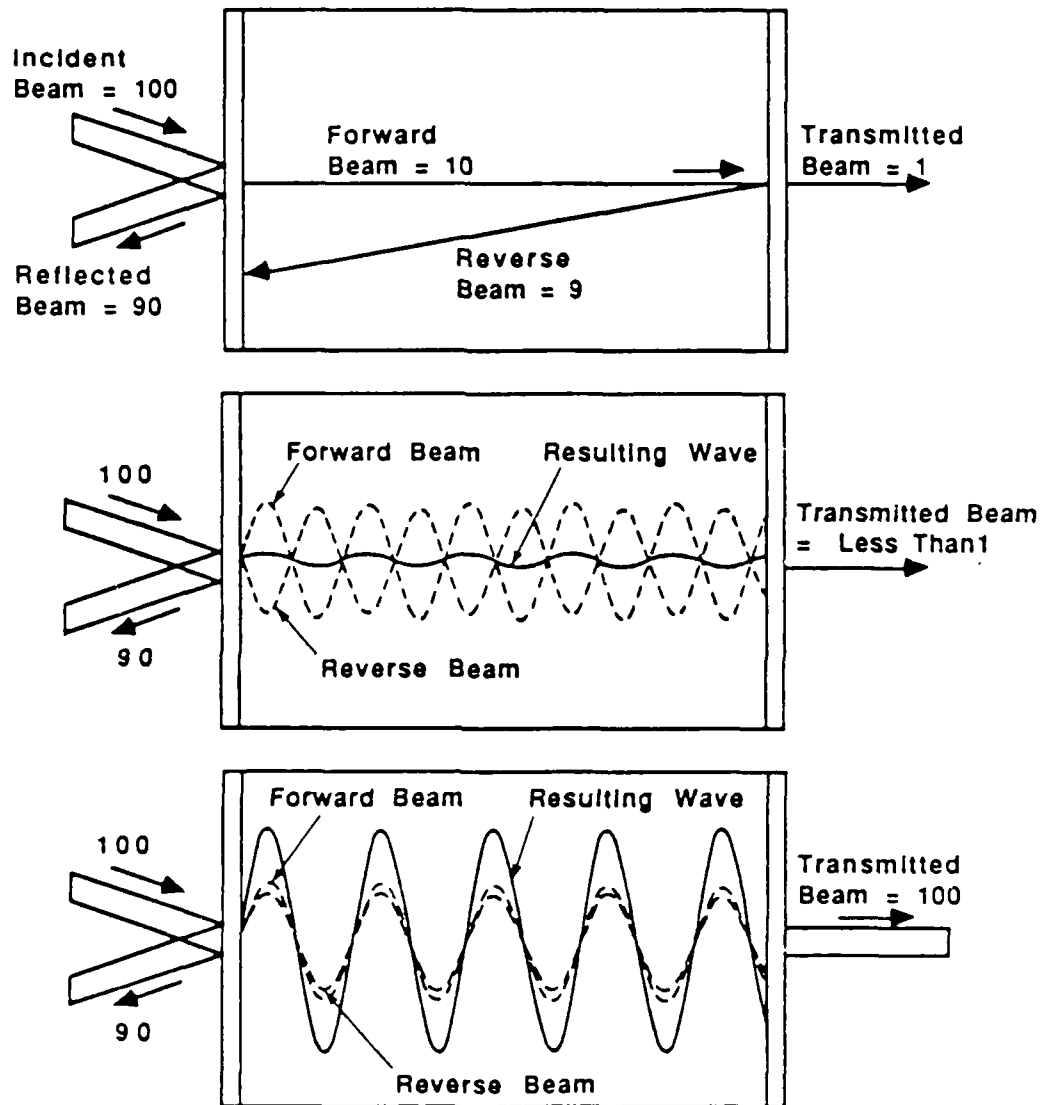


Figure 1 Schematic diagram of a Fabry-Perot interferometer showing how interference of the forward and reverse beams changes the output intensity.<sup>9</sup>

When the cavity does not satisfy the above requirement, then a linear relationship will exist between the incident and transmitted intensity. If a material with a nonlinear refractive index is placed in the cavity, then a positive feedback loop will occur where the refractive index and the light intensity become mutually reinforcing. As the incident intensity is increased, a change in refractive index occurs which brings the device closer to resonance, which further increases the intensity inside the cavity, which further changes the index, etc. This continues until a saturation intensity is reached, at which point a phase shift to resonance occurs within the cavity and the transmitted intensity suddenly increases.

The ratio of the incident intensity to the transmitted intensity as a function of the phase shift  $\delta$  is given by the Airy function  $A(\theta)$

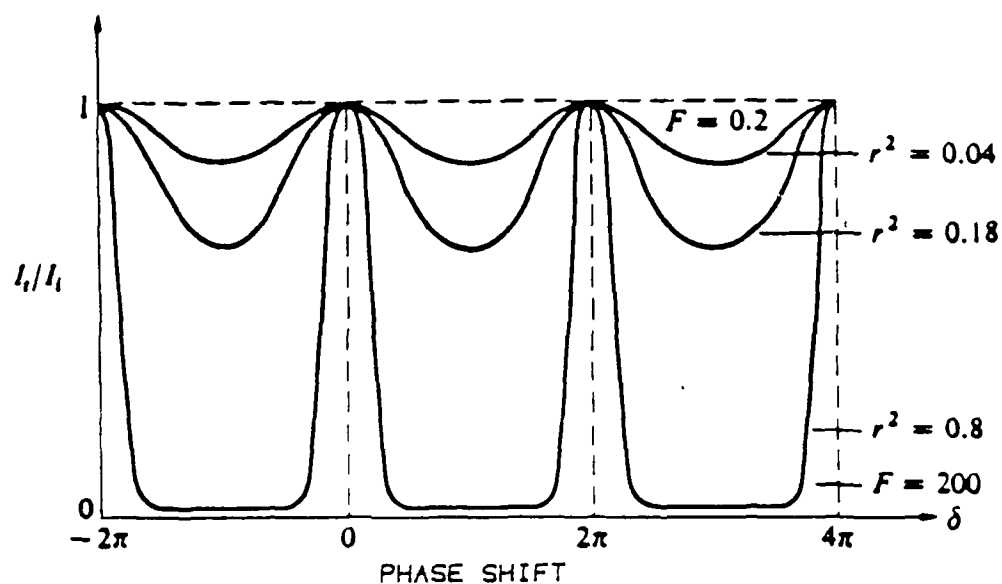
$$\frac{I_t}{I_i} = A(\theta) \quad (2.18)$$

where

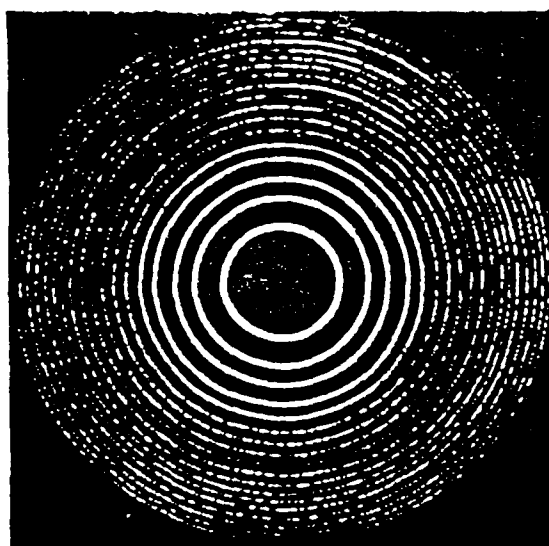
$$A(\theta) = \frac{1}{1 + F \sin^2(\delta/2)} \quad (2.19)$$

and  $F$  is related to the reflectivities of the mirrors  $R$  by

$$F = \frac{4 R}{(1 - R)^2} \quad (2.20)$$



a)



b)

Figure 2 Descriptions of the operation of a Fabry-Perot. a) plot of the Airy function as a function of the phase shift  $\delta$ , reflectivities  $r$ , and the finesse  $F$ ; b) transmitted image from a high finesse Fabry-Perot.<sup>53</sup>

Figure 2a displays how the relative transmitted intensity and the sharpness of the transition is related to the reflectivities and finesse of the cavity. As the reflectivity of the mirrors is decreased, the finesse is decreased and the transition at the critical phase shift broadens. When the reflectivities and the finesse of the cavity are large, then the transitions are sharp. For these conditions, the transmitted image from a diffuse source through the Fabry-Perot will appear as a series of sharp concentric rings, as shown in Figure 2b.

For a nonlinear Fabry-Perot, however, the Airy function must be slightly modified to account for the nonlinear index by

$$A(\theta)_{NL} = \frac{1}{1 + F \sin^2(\tau I_{eff} - \delta)} \quad (2.21)$$

where  $\tau$  is a constant describing the nonlinear refraction,<sup>10</sup> and  $I_{eff}$  is the effective mean intensity within the cavity. The total Fabry-Perot fractional transmission can be written as<sup>10</sup>

$$T = \frac{(1 - R)^2 (1 - A)}{(1 - R(1 - A))^2} \cdot A(\theta)_{NL} \quad (2.22)$$

where the intensity absorption per pass  $A$  is given by

$$A = 1 - e^{-\alpha d} \quad (2.23)$$

and  $\alpha$  is the absorption coefficient. A second equation can be written which is parametric in  $I_{\text{eff}}$  for the Fabry-Perot transmission:<sup>10</sup>

$$T = \frac{\alpha d}{A} \frac{(1 - R)(1 - A)}{(1 - R(1 - A))} \frac{I_{\text{eff}}}{I_0} \quad (2.24)$$

The condition for optical bistability can be determined by simultaneously solving equations 2.22 and 2.24. A graphical solution of these equations which shows the criterion for optical bistability is shown in Figure 3.

The critical intensity  $I_c$  for the onset of bistability is given by the intensity  $I_0$  which gives more than one intersection with the line and curve. This is the intensity at which the saturation of the feedback occurs. Once this saturation is achieved, it is found that if the input intensity is reduced, the output intensity does not drop until a finite decrease in the input has occurred. In other words, a hysteresis effect is observed. The switching between the two intensity levels can be considered as a change in logic state. The nonlinear Fabry-Perot interferometer therefore can be used as an optical logic

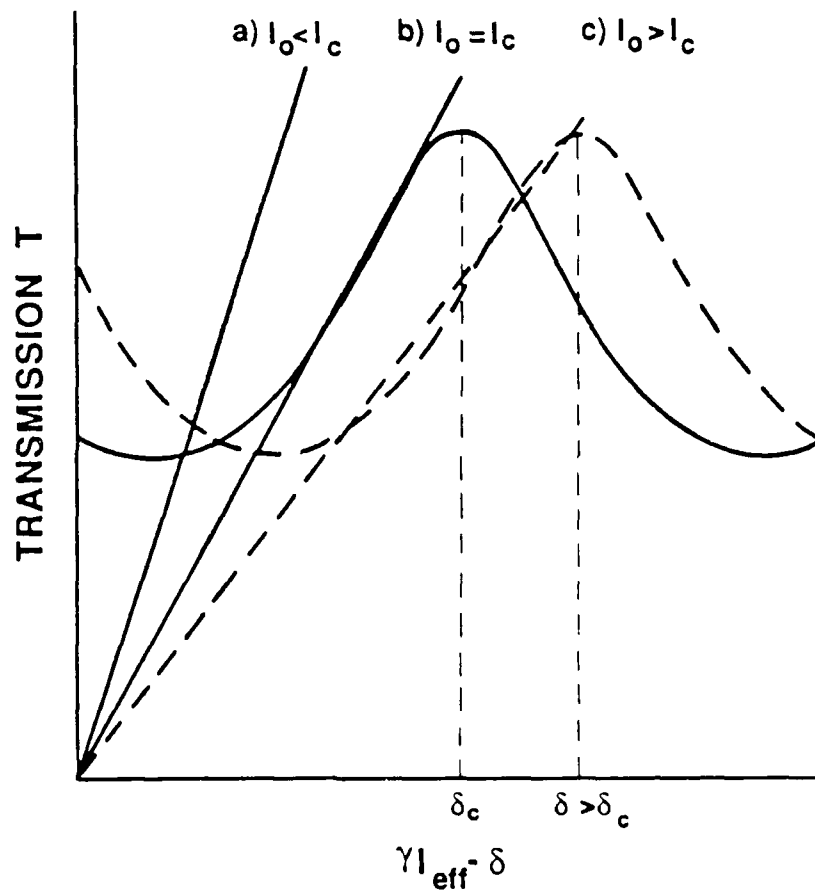


Figure 3 Graphical solution to the Airy function showing the critical phase shift required for the onset of bistability.<sup>10</sup>

gate. The great interest for logic gate applications is that the switching between the two levels can occur on a subnanosecond time period in some materials.

The saturation or critical intensity  $I_c$  is found to be inversely proportional to the nonlinear refractive index and is given by

$$I_c = \frac{1}{\beta} \cdot \frac{1}{\mu} \quad (2.25)$$

where

$$\beta = \frac{3 n_2}{\lambda \alpha} \quad (2.26)$$

and  $\mu$  is a figure of merit value for the cavity, relating the reflectivities of the two mirrors and the attenuation of light as passes through the cavity. Equation 2.25 indicates that for fixed cavity conditions, a small saturation intensity corresponds to a large nonlinear refractive index. The total index of refraction is given by

$$n_t = n_1 + \Delta n \quad (2.27)$$

$$\text{where } \Delta n = n_t - n_1 \quad (2.28)$$

The value of  $n_t$  is what actually determines the phase shift but as indicated by equation 1.1, the figure of merit for nonlinear optical applications also includes the switching times and the absorption coefficient.



### CHAPTER III BACKGROUND - BIBLIOGRAPHICAL REVIEW

#### Bulk Properties of Cadmium sulfide

Nearly all of the early work on cadmium sulfide was carried out on single crystal platelets which were made by a chemical vapor phase growth process. The natural crystal structure of cadmium sulfide is hexagonal wurtzite, although single crystals of the cubic zincblende structure have been fabricated. Within either of the two crystal structures it is possible to have regions which are made up of the alternate crystal structure. The transition from a hexagonal to a cubic lattice or visa versa can occur through a well known twinning mechanism,<sup>12</sup> in which the twinned region is bound by stacking faults. The twinned regions can be manifested during deformation of the crystal or under particular growth conditions, although it is difficult to differentiate these two sources when crystals are grown from the vapor phase. In either case, the two crystal structures do not have a center of symmetry or inversion, which leads to the unique properties of noncentrosymmetric crystals such as piezoelectricity, pyroelectricity, and third order optical susceptibility.

Another important physical property of CdS is the stoichiometry of the crystal. Very little work has been done on the defect chemistry of CdS; however, the work done on other II-VI semiconductors such as Zn<sub>1-x</sub> and CdTe indicates that the range of nonstoichiometry at room temperature is very small, e.g. 0.01 to 0.1 %.<sup>13</sup> Early work by Collins

which involved sulfur atmosphere heat treatments and electron bombardments, showed that sulfur vacancies were the predominant native defect and that they acted as the recombination center responsible for the green edge emission associated with CdS luminescence.<sup>14</sup> Other studies which investigated impurity doping effects are described in a following section on photoluminescence.

A detailed knowledge of the band gap structure of CdS has come from the extensive study of exciton states. Cadmium sulfide is found to be a direct gap semiconductor with a band gap equal to 2.59 eV at 0° K. The wurtzite lattice of the material is described by a p-like valance band consisting of two gamma-7 states and one gamma-9 state, and a s-like conduction band made up of one gamma-9 state. A diagram of the band extrema is shown in Figure 4. The three states in the valance band are also known as the A, B, and C free exciton states. These intrinsic exciton states are modeled as Wannier excitons; i.e. the electron and hole behave like a hydrogen atom. The orbital movements of the electron and hole are determined by their effective masses within the band extreme. As shown in Figure 5, the solution for the wave function of this model results in a series of discrete parabolic bands below  $E_g$  which merge into a continuum at higher energies.<sup>15</sup> Because of the unique band structure of this material there are a large number of possible exciton states. Any of the exciton energy levels (i.e.  $n=1,2,3$ , etc.) can be associated with the three primary states (A,B and C) in the valance band. In addition, any one of these free excitons can be associated with an impurity center,

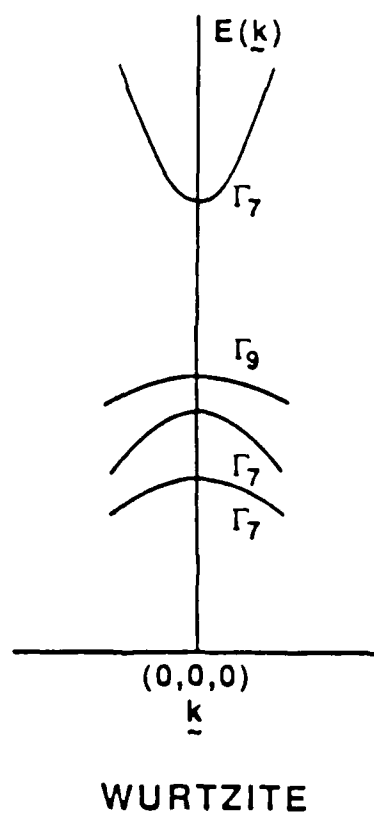


Figure 4 Band gap structure for wurtzite crystals near  $\underline{k}=0$ .<sup>14</sup>

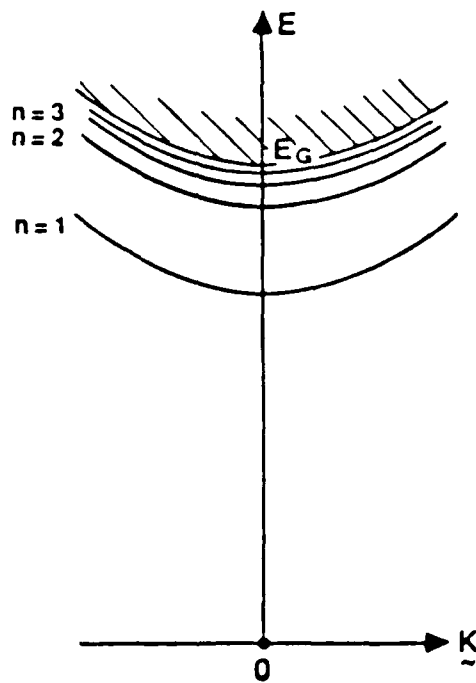


Figure 5 Energy diagram for Wannier excitons as a function of exciton momentum  $K$ , showing "hydrogenic" states which merge into a continuum at energies greater than  $E_G$ .<sup>15</sup>

forming a bound exciton complex, which will have a lower energy than the corresponding free exciton.

Of all the II-VI semiconductor materials, the exciton states in bulk CdS have been studied the most and are perhaps the best understood. Reflection, absorption, and luminescence studies dating back to the mid-fifties have investigated the exciton states in this material. Excitation of the states can be accomplished by either electron bombardment or by photon absorption. When the emission is due to the latter process it is known as photoluminescence and the results reported for CdS are detailed below.

#### Photoluminescence of CdS

When CdS is excited by photons of energy greater than the band gap the characteristic luminescence which results from the decay of excited states is shown to consist of two primary emission bands. The first, known as the "green-edge emission" is due to the edge emission of various states in the band gap, i.e. shallow donor-acceptor recombinations. Studies of the edge emission of CdS were made by Kroger as early as 1940.<sup>16</sup> At a slightly higher energy, a band known as the "blue-edge emission" occurs and is due to emission from free and bound exciton complexes.<sup>17</sup> A typical low resolution spectrum displaying these two bands is shown Figure 6, and a high resolution spectrum of a portion of the blue band is shown in Figure 7. The intensity of the bands is dependent upon the polarization of the incident light with respect to the c-axis of the crystal.

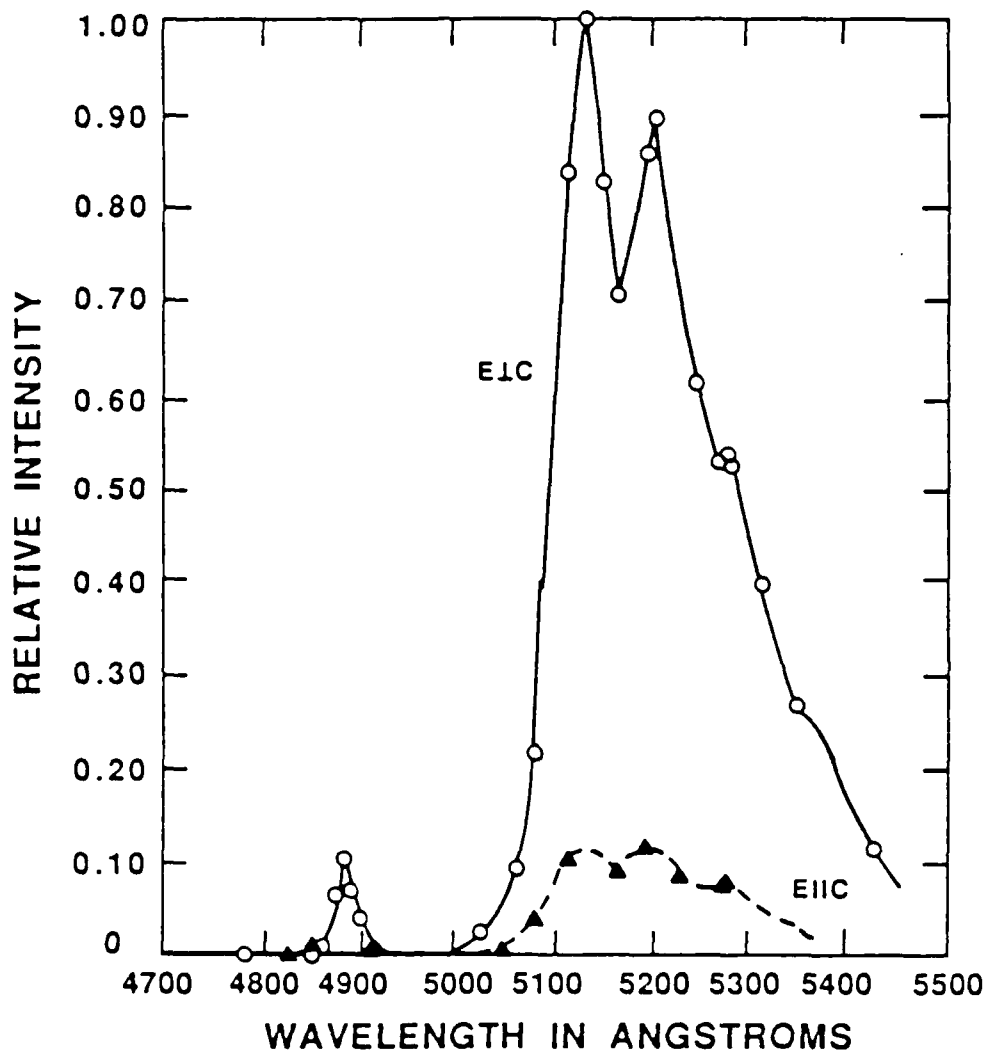


Figure 6 Low resolution photoluminescence spectrum of CdS single crystal showing "green-edge" emission due to band edge recombinations and "blue-edge" emission due to excitons. Figure shows emissions are dependent upon the polarization of the excitation source.<sup>18</sup>

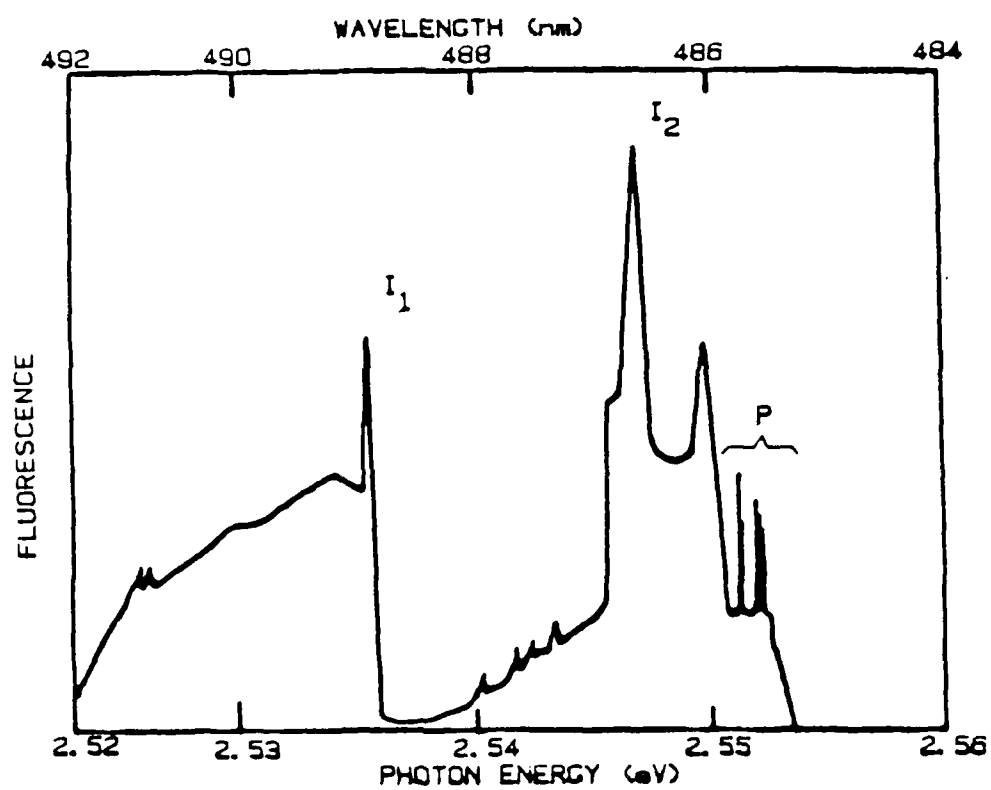


Figure 7 High resolution photoluminescence spectrum of CdS single crystal at 4.2° K, showing bound exciton peaks for excitation perpendicular to the c-axis. Peaks labeled P are observed with parallel excitation.<sup>19</sup>

The exciton states were first extensively studied and characterized by Thomas and Hopfield.<sup>19</sup> They have shown that within the higher energy band a number of sharp luminescence lines occur which correspond to transitions of both free excitons (A, B, and C) and excitons bound to neutral donors or acceptors. A designation of  $I_1$  was given to excitons which are bound to neutral acceptors and  $I_2$  was given to the excitons bound to neutral donors. These two peaks are labeled in Figure 7. The distinctions between the various transitions were made by using the Zeeman effect. When a strong magnetic field is imposed on the sample, many of the luminescent lines split due to the spin moments of the ground and excited states. From the group theory of bound complexes,<sup>19</sup> they were able to assign the transitions to the different defect states.

A later study by Henry, Faulkner, and Nassau showed for the first time donor-acceptor pair lines in the photoluminescence spectra of CdS.<sup>20</sup> These pair lines are narrowly spaced transitions which were observed in the green-edge emission band and correspond to closely spaced donor-acceptor pair-recombination bands. Again the confirmation of these lines was made by Zeeman experiments. The significance of the study is that for the first time direct spectroscopic evidence for the existence of these states was made. This is important point because in the study by Thomas and Hopfield it was assumed that these states must exist based on the Zeeman experiments, but they had no direct evidence.

Henry, Nassua, and Shiever studied the impurity doping of CdS and showed that Na and Li are the only shallow acceptors that can act as substitutional impurities.<sup>21</sup> These shallow acceptors give rise to the



$I_1$  bound exciton that was described by Hopfield and Thomas. Usually two  $I_1$  lines are observed, and by varying the doping level these authors proved the lines to only be due to Na and Li. High purity crystals grown in clean reactor tubes were found to only exhibit the  $I_1(\text{Li})$  line. When Na was added a considerable broadening of the  $I_1$  line occurred, but as successive runs were made in the same tube, these authors showed the Na line could be resolved. Doping with K, Rb, or Cs, only resulted in a sharp  $I_1(\text{Li})$  line, and P was found to give a complex shallow acceptor. The identity of the shallow donor level responsible for the  $I_2$  bound exciton could not be determined; however, the authors showed by donor-acceptor pair line splitting that the donor was not a native double donor such as a cadmium vacancy, or a sulfur interstitial. The authors reasoned that the donor may be Na or Li interstitials because of the small size of these atoms, and when crystals are heavily doped, they become highly compensated. Unfortunately they were unable to prove the identity of the donor.

Later work by Henry and Nassau involved measuring the spectroscopic lifetimes of the two bound exciton complexes.<sup>22</sup> They were basing their work on another study by Thomas and Hopfield which showed the measured oscillator strength of the bound excitons to be very large, which meant that the radiative decay of the weakly bound exciton would be very fast. Thomas and Hopfield determined an oscillator strength of  $9 \pm 2$  corresponding to a radiative lifetime of  $0.4 \pm 0.1$  nsec.<sup>23</sup> This oscillator strength is about  $10^4$  greater than the strength of a free exciton.<sup>11</sup> Henry and Nassau with their experimental setup were able to measure a radiative lifetime for the  $I_2$

exciton to be  $0.5 \pm 0.1$  nsec. The very fast decay time of this state is what makes CdS so attractive for nonlinear optical application.

#### Resonant Raman Scattering in CdS

Further studies of exciton levels in CdS have involved the measurement of multiple phonon scattering from exciton states. Leite, Scott, and Damen found that the scattering of longitudinal optical (LO) phonons was enhanced when the scattering-phonon frequency coincided with that of excitons.<sup>24</sup> They were able to show up to nine orders of resonant Raman scattering occurring at frequencies shifted less than 1% from multiples of the  $305 \text{ cm}^{-1}$  line (the first LO line). These authors were not able to determine the identity of the exciton state (i.e. free or bound) which was acting as the intermediate state for the resonant scattering in this study, but in a latter paper by Leite, Scott, and Damen free excitons were proven to be the primary intermediate state.<sup>25</sup> They also showed that bound excitons participated as intermediates by observing phonon sideband features on the photoluminescence of the bound excitons. The  $I_1$  exciton was found to be a stronger resonant state compared to the  $I_2$  bound exciton.

In a more recent paper by Mashshenko,<sup>61</sup> the temperature dependence of the LO and 2LO lines associated with the A exciton were investigated. At  $77^\circ \text{ K}$  the A-LO phonon predominates the emission, but as the temperature is increased to  $110^\circ \text{ K}$ , this line decreases and the A-2LO line increases. This increase in the 2LO line indicates that an increase in the probability of a two-phonon process occurs at high temperatures.

### Nonlinear Susceptibility of CdS

Even with the obvious advantages of using CdS for nonlinear optical applications, very few groups have investigated this material. The primary amount of work in this area on CdS has been carried out by Dagenais.<sup>3,4,11</sup> As would be expected from the large oscillator strength of the bound exciton, a very large nonlinear refractive index results when this level is saturated, and the decay time is very short. By use of a Fabry-Perot arrangement and a narrow bandpass tunable dye laser, Dagenais reported a cw saturation intensity for this level of only  $58 \text{ W/cm}^2$ , which corresponds to a nonlinear index of refraction of  $1 \times 10^{-4} \text{ cm}^2/\text{W}$ .<sup>3</sup> In a later publication, Dagenais and Sharfin<sup>11</sup> report that by using a high finesse Fabry-Perot, a saturation intensity of only  $26 \text{ W/cm}^2$  is required, which for the experimental setup corresponds to a nonlinear refractive index of  $2 \times 10^{-2} \text{ cm}^2/\text{W}$ . They also reported a switch up and switch down time of one and two nanoseconds respectively. These are the largest values of a nonlinear refractive index ever to be reported.

Other work on CdS has been done by Bohnert, Kalt, and Klingshirn.<sup>26</sup> They did not, however, study nonlinearity by exciton saturation, but rather by the formation of an electron-hole plasma. High intensity laser pulses of energies just above the band gap energy were used to study this effect. By measuring the temporal line shape of the transmitted laser pulse they were able to determine the renormalization of the band gap due to the formation of an electron-hole plasma. Because this is a much smaller effect, intensities of  $120 \text{ kW/cm}^2$  were required to produce a change in the transmitted pulse.

CdS Thin FilmsVacuum Deposition

A great number of studies have investigated the thermal evaporation of CdS for the deposition of thin films. Although all thin films for this study were deposited by RF-magnetron sputtering, some of the results of these investigations are relevant to the present work. Many of the studies of thermal evaporation were undertaken to research the electrical properties of CdS thin films, although some optical properties have been studied. The problem is that most of these studies present results which both show differences from single crystal results and also differ from each other.<sup>27</sup> The reasons for the discrepancies are related to the difficulties in evaporating CdS, which lead to problems with maintaining stoichiometry and crystal structure in the deposited films. The difficulty in evaporating CdS, as well as other chalcogenide compounds, is that complete dissociation of the compound occurs during evaporation.<sup>28</sup> If too high a temperature is used, then the compound will dissociate incongruently and because Cd has a higher volatility than S, non-stoichiometric thin films result. Source temperatures between 650° and 700° must be accurately controlled to avoid excess cadmium.<sup>28,29</sup> Due to differences in the sticking coefficients of Cd and S, a non-stoichiometric thin film will also result if the an improper substrate temperature is used. Cook and Christy<sup>27</sup> have found that if fused quartz substrates are used at temperatures greater than 200° C, then non-uniform films result. In comparison, Wohlgemuth et al.<sup>29</sup> have found that if the substrate is

cooled to  $\text{LN}_2$  temperatures, then an amorphous film results which is Cd rich.

The optical properties of CdS thin films are central to this study; however, the reported results for vacuum vapor deposited thin films are found to vary greatly. Most notably is the variation in the reported optical band gap and absorption coefficient, and the calculated index of refraction. Some of these differences can be realized by examining Figure 8 and Figure 9 which show the refractive index and absorption coefficient obtained by several authors.<sup>29</sup> Referring to Figure 8 the results for single crystal CdS obtained by Cardona and Harbeke<sup>30</sup> are given by curve a. Curve b is for polycrystalline film deposited onto fused silica at  $180^\circ \text{C}$  by Khawaja and Tomlin.<sup>31</sup> Curve c corresponds to a polycrystalline film also deposited on silica at  $180^\circ \text{C}$  by Wohlgemuth et al.<sup>29</sup> and curve d is for an amorphous film deposited at  $\text{LN}_2$  temperatures by Wohlgemuth et al. The same authors correspond to the same curve letters of the reported absorption coefficients shown in Figure 9. As shown in Figure 8 the results by Khawaja and Tomlin show the closest resemblance to single crystal results, while the Wohlgemuth et al. results show a marked difference. In contrast, as shown in Figure 9, the absorption coefficient of polycrystalline films deposited by Wohlgemuth et al. model single crystal results best. The highest quality films in these studies were deposited at high temperatures, although a more recent study by Cook and Christy<sup>27</sup> reports similar results for room temperature depositions. It is obvious that subtle differences in the deposition technique result in a wide variation in the optical

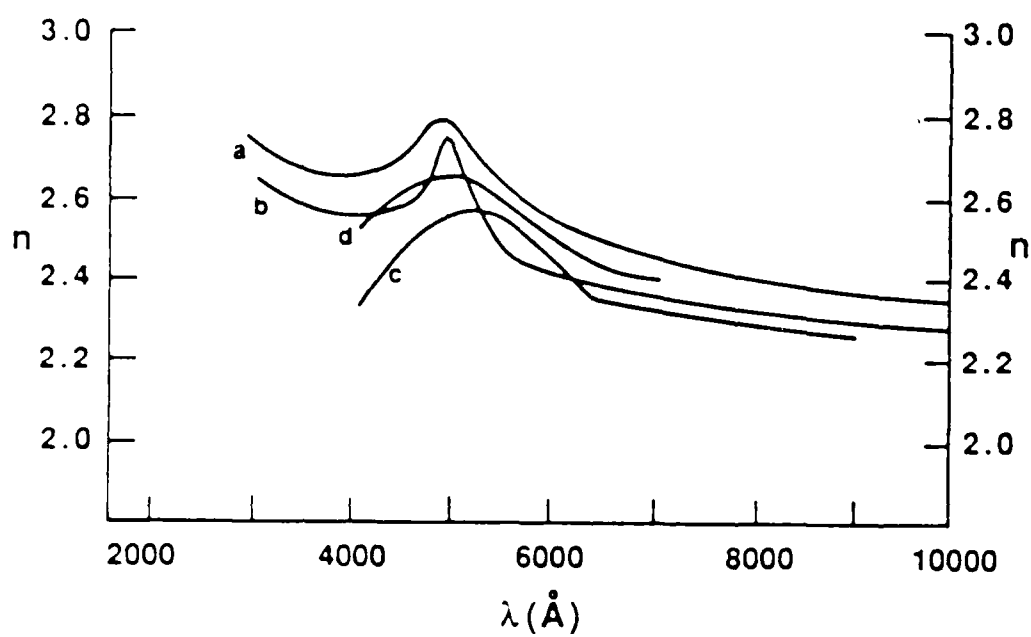


Figure 1 Variation of index of refraction reported by several authors.<sup>1-4</sup>

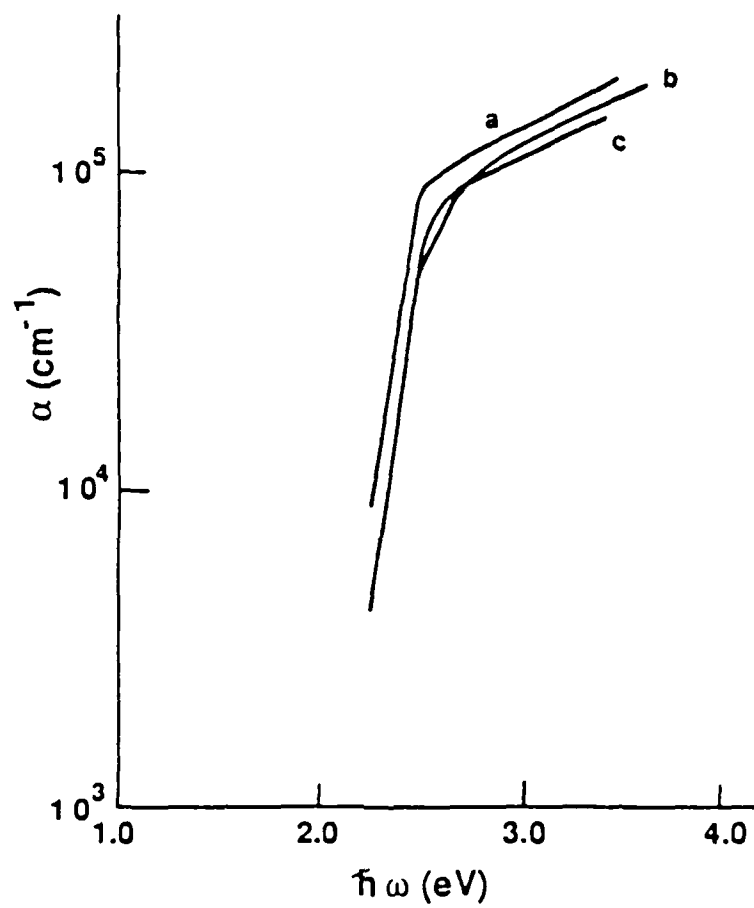


Figure 9 Variation of the absorption coefficient reported by several authors.<sup>29</sup>

properties. This is probably due to differences in thin film microstructures, which in the above studies were only determined by X-ray diffraction. No direct measurements (i.e. electron microscopy) were used to examine thin films.

Although some of the optical properties of evaporated thin films have been investigated, albeit there are differences in the results, apparently very few studies have been made of the photoluminescence of thin films produced by this technique. Christmann et al.<sup>32</sup> describe evaporation deposited epitaxial CdS films which displayed both green and blue edge luminescence. This is one of the first studies to relate both the morphology and composition of thin films to the observed photoluminescence. Thin films were deposited on cleaved surfaces of  $\text{SrF}_2$  at temperatures from  $210^\circ$  to  $310^\circ$  C. Variation of the supersaturation by controlling either the source temperature or the substrate temperature resulted in three basic morphologies. At low supersaturations, smooth CdS thin films were produced which only displayed broad band green photoluminescence. By decreasing the substrate temperature or increasing the source temperature, films were produced which displayed a structure with many hexagonal flat tops. These films showed green edge emissions and very low intensity blue edge emissions. Finally, at very high supersaturations, films which displayed a morphology with many hexagonal pyramids were found to show very intense blue edge, or bound exciton photoluminescence.

Through cathodoluminescence and microprobe studies it was determined that the hexagonal pyramids were cadmium rich, and they did not contribute to the luminescence. Only the areas adjacent to the



hexagonal pyramids were found to show bound exciton luminescence. The pyramids were thought to have nucleated from Cd droplets, and as they grew, the adjacent areas were depleted of cadmium. The required donor states for  $I_2$  bound excitons were therefore provided by cadmium vacancies. Other films were found to be uniformly slightly cadmium rich, and it was thought that cadmium interstitials were responsible for the broad band photoluminescence.

Humenberger et al.<sup>33</sup> also reported thin films which displayed bound exciton luminescence. These films, however, were made by a hot-wall epitaxial technique, which is similar to the vapor phase technique used to make bulk single crystal platelets. Films were deposited on  $BaF_2$  substrates. The surface morphology was found to be smooth with a low density of hexagonal flat tops. No compositional data were given for thin films; however, acceptor states were provided by indium doping thin films during the deposition process. Free carrier concentrations as a result of the indium doping were measured to be on the order of  $10^{17}$  to  $10^{18} \text{ cm}^{-3}$ .<sup>33</sup>

The above two studies are the first to show by photoluminescence the presence of exciton levels in thin films. Studies of several other thin film deposition techniques such as chemical bath,<sup>34</sup> or spray pyrolysis<sup>35</sup> have reported photoluminescence, but none have shown exciton emissions. To see these transitions, it is apparent that very high quality thin films are required, and it is obvious that standard vacuum techniques or other techniques such as those described here are not capable of producing thin films of the necessary degree of quality. A deposition technique which permits greater control over the

deposition process is RF sputtering, and several investigations of the deposition of CdS by this technique are presented below.

### RF Sputtering

Only recently has the deposition of CdS thin films by RF sputtering been investigated to any great extent. One of the first investigations was reported by Lagnado and Lichtensteiger.<sup>36</sup> They described some of the properties of CdS thin films produced by RF-diode sputtering. A very strong preferred orientation of the CdS crystallites was found to occur with the c-axis parallel to the substrate plane. Electrical resistivity measurements at different temperatures revealed two activation energies for conduction, interpreted to show the activation of an unspecified trap below the conduction band, although no data on the chemical analysis for impurities was presented.

Recently the technique of RF-diode sputtering has received considerable attention for producing CdS thin films for solar cell heterojunctions.<sup>37</sup> The large photoconductivity of CdS makes it an attractive material for both solar cell and sensitive photodetector applications. A number of investigations on the RF diode-sputtering of CdS for these applications have been reported by Marti et al.<sup>38-41</sup> These workers have investigated the dependence of the physical, electrical, and optical properties on both deposition parameters and post-deposition heat treatments.

The first investigation of CdS by Marti et al.<sup>38</sup> reported the dependence of the photoconductivity on both grain size and grain boundary

a function of sputtering power, pressure, substrate temperature and substrate bias. Thin films were deposited onto fused silica substrates. The first effect they describe is the dependence of the deposition rate and resistivity on the pressure of gas used. A maximum in the deposition rate and a minimum in resistivity occurred for a sputtering pressure of 5  $\mu\text{m}$  ( $5 \times 10^{-3}$  torr). For higher pressures they found the rate actually decreased, and the resistivity increased. The decrease in deposition rate at higher pressures was explained by a backscattering mechanism which increases the probability that more sputtered atoms will return to the target at higher pressures. The minimum in resistivity at 5  $\mu\text{m}$  pressure was claimed to be a result of the maximum deposition rate that occurred at this pressure. Although no direct proof was given, the authors claim the high deposition rate decreased the number or concentration of impurities that were trapped in the film.

The second effect described in this early paper by Martil et al.<sup>38</sup> was the dependence of thin film grain size on the substrate temperature and substrate bias. The grain size was determined by SEM observations. As would be expected, the grain size of films increased from 300 Å to 3500 Å as the substrate temperature was increased from 90° C to 300° C. The deposition rate accordingly decreased as the temperature was increased. When the substrate bias was increased to above -100 volts, the resulting thin films were found to be amorphous. The temperature effects can be explained by considering that with increasing temperature 1) the critical size for a nucleus increases, 2) the surface diffusion coefficient increases and 3) the sticking coefficient

for a material decreases.<sup>28</sup> The appearance of an amorphous structure with high substrate bias was explained by the authors as a result of structural damage that occurred due to ion bombardment (which was increased by the high negative bias).

The second report published by Martil et al.<sup>39</sup> further explored the effects of substrate temperature and bias on the electrical properties of CdS thin films. They found that the resistivity increased from 10 to  $10^8 \Omega \text{ cm}$  as the temperature was increased from 60° C to 250° C, which they claimed was due to a change in stoichiometry (i.e. a loss of cadmium with increasing temperatures), although no chemical analysis was presented to back up this claim. A minimum in resistivity was also found with a substrate bias of -50 volts, or with a floating substrate (which developed a self bias of -28 volts). This effect was explained by the ion bombardment that results from these bias voltages preferentially resputting oxygen and other impurities from the growing film. Oxygen has been shown to be a acceptor-like trapping center, located 0.9 eV below the conduction band.<sup>42</sup> Again no chemical analysis was reported to prove that a decrease in oxygen occurs. Also the variation in activation energy for conduction that occurs with temperature as seen by Lagnado and Lichtensteiger<sup>36</sup> was not explored by these authors.

The third publication by Martil et al.<sup>40</sup> reports the influence of the above sputtering parameters on the optical properties of thin films. The structural changes which occur under different conditions were also further explored. Increasing the substrate temperature resulted in similar structural changes to those reported in the earlier

study; the grain size varied between 500 Å and 3000-4000 Å as the substrate temperature was increased from 60° to 300° C. This report, however described the sputtering pressure dependence of the crystallinity. The sputtering pressure determines how much structural damage occurs due to ion bombardment. At low pressures, bombardment is enhanced by a large self-bias that develops on the substrate, and an amorphous structure results as previously described. At higher pressures, the crystallinity was also found to decrease, which was explained by the authors as due to a porous structure that develops from trapped gases.

Optical properties were found to be a function of both substrate bias and sputtering pressure. A maximum in the optical band gap (2.36 eV) was found to occur for a floating substrate bias, whereas the minimum in the band gap (2.30 eV) occurred for a -110 volt bias. The band gap was found to increase with an increase in sputtering pressure and became nearly constant for pressures above 10  $\mu$ m. The pressure dependence of the refractive index however contradicts the pressure dependence of the band gap. The index of refraction was found to be a maximum with 5  $\mu$ m pressure, and it decreased with increasing pressure. This was explained in terms of the porous structure which occurred at higher pressures; however, if the refractive index is reduced at higher sputtering pressures due to a more porous, less crystalline structure, then the band gap energy should also decrease. An increase in the number of crystalline defects should cause tailing of the band gap, which is seen as a decrease in the gap energy.<sup>29</sup>

The latest investigation to be reported by Martil et al.<sup>41</sup> describes the effects of heat treatments on the electrical and optical properties of sputtered films. Heat treatments were carried out under H<sub>2</sub> and N<sub>2</sub> atmospheres at temperatures ranging from 100° C to 550° C and for times ranging from 20 minutes to 5 hours. The primary effect on the electrical properties was a two order of magnitude reduction in the resistivity to  $4 \times 10^{-2} \Omega \text{ cm}$  for heat treatments at 200° C. Carrier mobilities accordingly increased to 50 - 70 cm<sup>2</sup>/Vs for this treatment. Higher temperatures were found to increase the resistivity and decrease the mobility. The decrease in resistivity was explained by claiming that oxygen desorption from the grain boundaries occurs at 200° C. As previously described, oxygen is a trapping center which in this case decreased the carrier concentration and simultaneously increased the scattering which reduces the mobility.<sup>41</sup> No explanation was given for the increase in resistivity with increasing temperature, although it could be due to a loss of cadmium.

The optical absorption edge was shown to become sharper and occur at a higher energy for heat treatments at 200° C. Temperatures higher than this were not reported to significantly alter the absorption edge; however, treatments above 550° C produced an overall decrease in the transmission. This was explained by a dissociation or reevaporation process that occurred as a consequence of the higher temperatures. The optical band gap was found to increase from 2.36 eV to 2.39 eV for treatments at 200° C, which was again explained in terms of oxygen desorption from the grain boundaries, although no chemical analysis was reported to prove this hypothesis.

Semiconductor Doped Filter Glasses

Sharp cutoff filter glasses are silica based glasses which contain a fine dispersion of semiconductor microcrystallites. The variation of the sharp absorption edge position is achieved by either varying the composition and or heat treatment schedule. Great interest has been generated recently because it is thought by many authors that the crystal size developed in these materials by thermal treatments is on the size order for quantum confinement effects to occur. For glasses containing a mixture of CdS and CdSe many authors have reported a blue shift in the absorption band edge. In addition, a blue shift of the high energy exciton photoluminescence peak has been interpreted in terms of quantum confinement.

Warnock and Awashalom<sup>43,44</sup> in two publications on mixed crystal glass (those containing CdS<sub>.27</sub>/Se<sub>.73</sub>) report that the glasses which displayed smallest size distribution (average size = 94 Å) exhibited the largest shift in the exciton photoluminescence, and this photoluminescence was shown to decay on a time scale of only 18 psec, which is nearly two orders of magnitude faster than the lifetime displayed by excitons in bulk material.<sup>44</sup> The shifts in peak position and fast lifetime were interpreted in terms of a quantum confinement effects.

A very recent paper by Borrelli et al.<sup>45</sup> has shown that the blue shift in the photoluminescence displayed by this particular mixed crystal glass is not due to confinement effects, but rather to compositional effects. A careful study of the crystal structure by X-ray diffraction revealed that a change in the stoichiometry occurs

during the heat treatments which develop the microcrystallites. It was postulated by these authors that more of the selenium remains in glass, while sulfur is more easily incorporated in the crystallites.<sup>45</sup>

Therefore, at the lower temperatures which produce the smaller crystallites, the crystallites end up containing more sulfur, so the optical properties of glasses containing these crystallites are blue shifted toward the optical properties of pure CdS. True quantum confinement effects were, however, shown to occur in a series of experimental glasses which contained either CdS or CdSe, but not both.



## CHAPTER IV EXPERIMENTAL METHOD

### Vacuum Deposition System

Thin films for this study were made with a specially designed vacuum system. A schematic of the deposition chamber is shown in Figure 10, and a picture of the complete system is shown in Figure 11. The deposition chamber consists of a rectangularly shaped stainless steel box which measures 12" X 18" X 18". This chamber was custom built by MDC Vacuum Corp. (Haywood, CA.). Numerous ports and feedthroughs on the chamber permit a wide variation of deposition configurations. The vacuum pumping system utilizes a 330 l/sec turbomolecular pump (Balzers, Hudson, NH), a molecular sieve trap (MDC Vacuum Corp.), and a 300 l/min two-stage mechanical pump (Sargent Welch, Skokie, IL). With the molecular sieve trap activated, pressures in the high  $10^{-5}$  torr range were possible using the mechanical pump only. Pumpdown from atmosphere pressure to  $1 \times 10^{-6}$  torr could be accomplished in 2 hours with use of the turbopump. Vacuum gauging was performed with a Leybold Heraeus (East Syracuse, NY) model CM 330 combined Penning discharge and thermocouple gauge controller.

Pressures for sputter deposition were controlled by using a micrometer adjustable throttle valve (Sputtered Films Inc. Santa Barbara, CA.) and a mass flow meter/controller (Matheson Gas Products Norcross, GA). High purity argon gas (99.9995%) was used as the

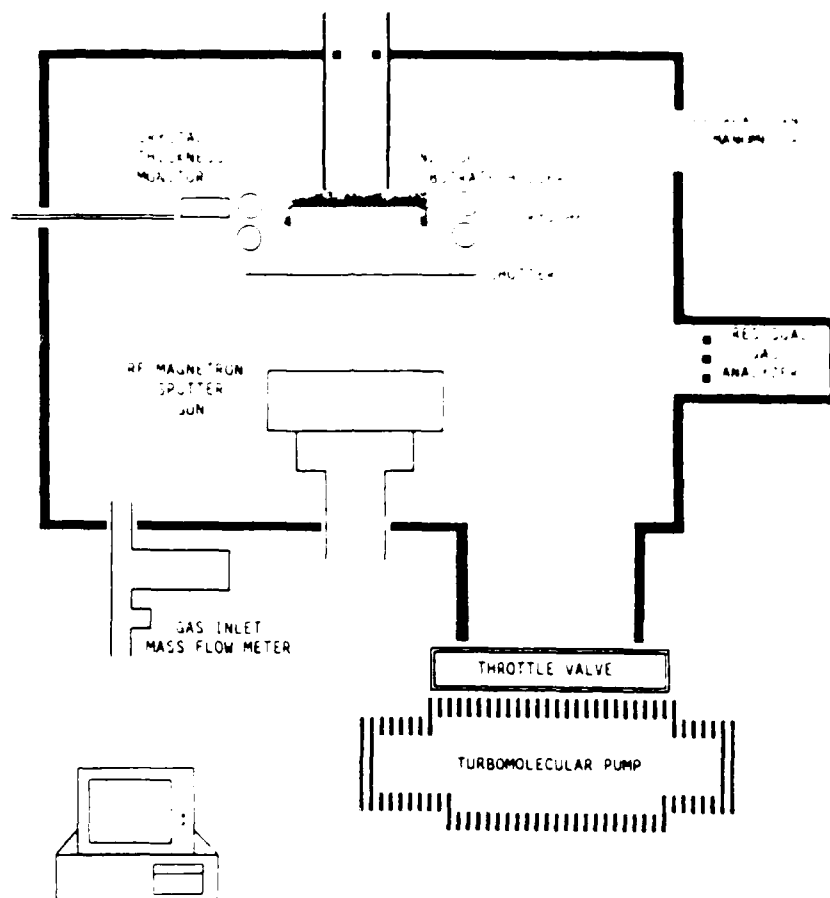


Figure 10 Schematic diagram of sputter deposition chamber. Computer figure shown to indicate computer control of system.



Figure 11    Photograph of complete deposition system showing  
                 sputtering chamber and instrumentation.

computer. The IC thickness monitor is capable of six different films, and by using a sample and hold program, two different films can be monitored and controlled simultaneously. A separate control of deposition rates was achieved by connecting the IC-buBu thickness monitor to the RF power supplies.

For semi-automatic control and constant monitoring of the deposition process a Zenith 2-158 personal computer with 512K RAM and a 20 megabyte hard disk was interfaced to the system. A Dascon 1 I/O board (Metrabyte Corp.) which provides four channels of analog and 12 bits of digital input/output was installed in the computer. With this interface board and with RS-232 communications to the IC 6000 deposition controller, it was possible to monitor nearly every aspect of the deposition process. The RS-232 communications permitted direct

programming control over deposition parameters and constant monitoring of deposition rate, thickness, power output and crystal oscillator status. The analog portion of the I/O board was connected to the pressure gauge controller and to the RF power supplies. Connection to the power supplies permitted recording of the DC bias which develops on the target as a result of the sputtering process. All of these process parameters were stored on disk during a deposition run. This made it possible to go back and review the deposition process, if a film was later found to have anomalous properties.

A unique feature of the deposition system has to do with the various substrate holders which could be used. For low temperature depositions, a liquid nitrogen ( $\text{LN}_2$ ) cooled substrate holder was employed. This holder is made up of two double concentric tubes in which the center tube acts as a reservoir for  $\text{LN}_2$  and the outer tube, which is open at the bottom to the vacuum system, acts as an insulating vacuum jacket. An aluminum plate with a slightly recessed area to hold the substrate is attached to the end of the inner reservoir tube with a copper screw. To reduce the amount of contamination that would occur on the cold substrate, an additional  $\text{LN}_2$  cooled coil was positioned around the substrate holder assembly. This coil is referred to as the cryoshield in Figure 10. For room temperature depositions, the same holder was used, however, without filling the  $\text{LN}_2$  reservoir.

High temperature depositions were accomplished by replacing the  $\text{LN}_2$  feedthrough assembly with a resistively heated substrate holder. This holder was made by drilling holes lengthwise in a thin aluminum block and inserting nichrome wound ceramic heaters. A Chromel-Alumel

thermocouple was embedded in the core of the holder, and control of the temperature was made by controlling the input power to the holder with a variable autotransformer. Substrates could be heated to  $1100^{\circ}\text{C}$  with this arrangement with a temperature control of  $\pm 5^{\circ}\text{C}$ .

A single planar magnetron sputter gun supplied by US Ions (Campbell, CA) was used for sputter depositing the CdS thin films. The gun accepts two inch diameter targets, which can range from 1 inch to a quarter of an inch in thickness. An Eratron RF power supply (Campbell, CA) operating at 13.57 MHz with a power capability of 500 watts was used to supply RF power to the gun, through an auto load match tuning network. The matching network is required to balance the impedance of the gun and plasma to the 50 ohm output from the power supply. If the impedance is not matched, then the RF power is reflected, and the only thing that is accomplished is heating of the heat sinks in the power supply. The utility of an auto load network is that when conditions of the plasma change, the network will automatically match the impedance, thereby eliminating any reflected RF power.

High purity cadmium sulfide sputtering targets were obtained from CVD Industries (Woburn, MA). These targets are made by a chemical vapor deposition process so they are supplied with a bulk density of nearly 98% of theoretical density. High bulk density reduces the amount of outgassing during sputtering. All impurities were less than 1 ppm and the stoichiometry of the target material was slightly cadmium rich (50.46%). Nearly all thin films for this study were made from CVD targets; however, a different type of sputtering target was obtained

[illegible]

For producing DSAM films, the deposition chamber was reconfigured to accept a second RF planar magnetron sputter gun, for sputtering the glass target. This gun was used with a second 500 watt Eratron supply and the two power supplies were driven by a common oscillator to phase match the two plasmas. In addition, a set of baffling plates were mounted inside the chamber as shown in Figure 12. The center baffle plate was used to isolate the two plasmas. A pair of three inch

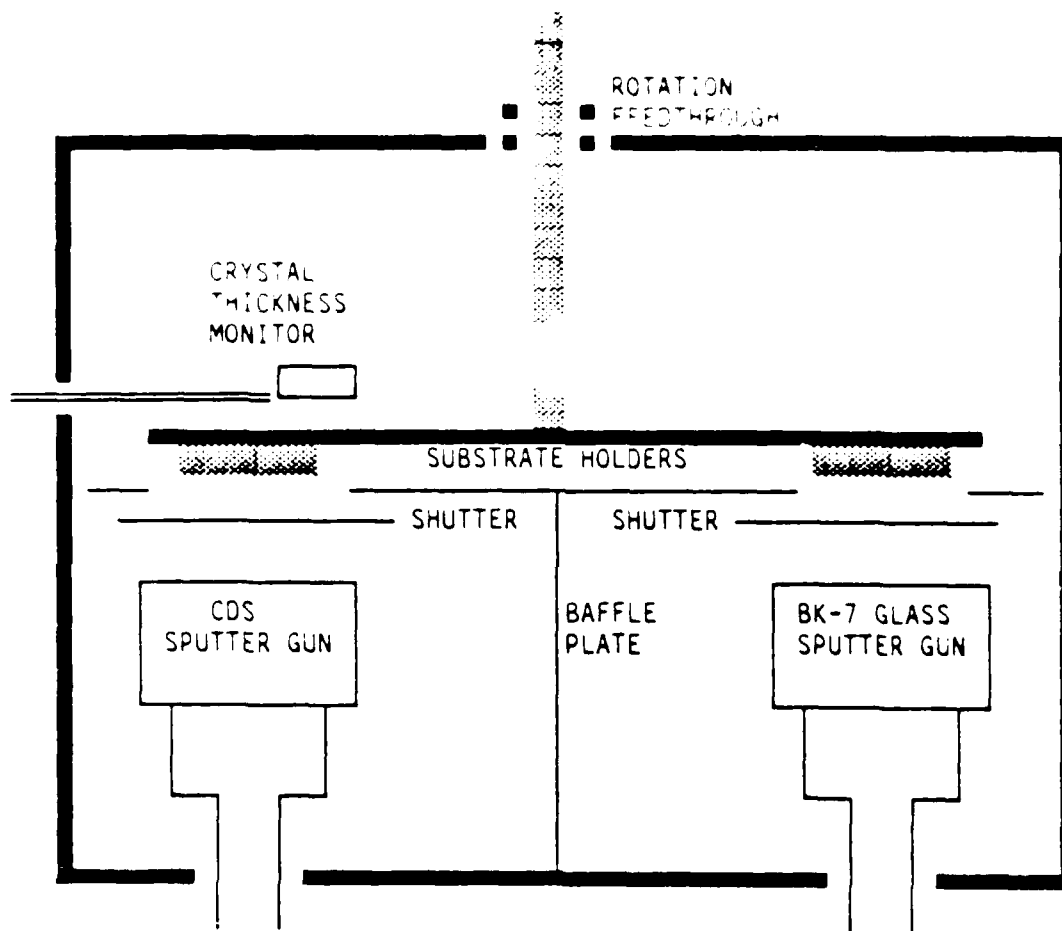


Figure 12 Schematic diagram of deposition chamber configured for COSAD.





Electrons in the plasma can be accelerated by the positive half of the RF field, which results in both the ionization of argon atoms, and the bombardment of the target. This bombardment results in the development of a negative potential on the target surface, which is called the DC bias. The argon ions in the plasma are too massive to be accelerated by the RF field; however, they are accelerated towards the target by the DC bias, which results in sputtering of the target material.

The configuration of diode sputtering results in exposing the substrate and growing films to the full energy of the plasma. The growing film is continuously bombarded by a number of energetic particles, both charged and neutral. This bombardment can either be enhanced or reduced by applying a potential to the substrate during deposition. Substrate biasing can only reduce the amount of bombardment to a certain extent, essentially because the substrate is totally immersed in the plasma during deposition. Considerable heating of the substrate and film occurs as a result of the bombardment, even at moderate plasma powers.

RF planar magnetron sputtering reduces the amount of bombardment by incorporating a strong permanent magnet behind the cathode assembly. The configuration of a US sputter gun is shown schematically in Figure 13. Curved magnetic field lines force the electrons in the plasma into circular orbits, which both enhances the plasma immediately above the target, and reduces the amount of electron bombardment on the growing film. The target is a circular disk that is secured to the magnet housing, which comprises the cathode. The anode is comprised of a circular cap (called the ground shield in the Figure) which fits over

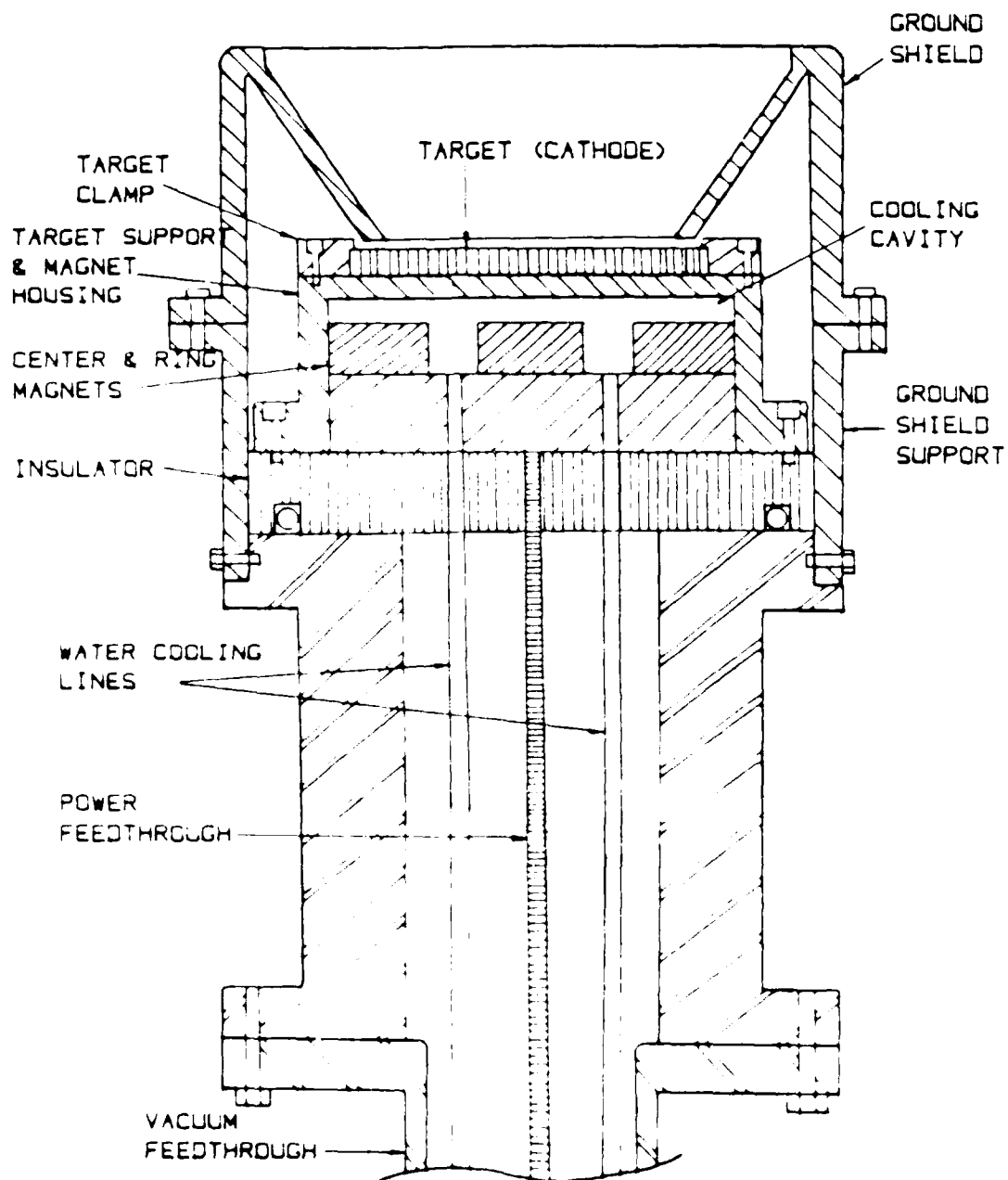


Figure 13 Cross-sectional view of RF magnetron sputter gun made by S. Guns Inc.<sup>4b</sup>

the gun assembly. Most of the plasma is constrained to the area immediately above the target, so a large reduction in substrate bombardment and substrate heating is realized. The substrate and growing film, however, can still be bombarded by energetic neutral particles, which has been shown to be a major cause of substrate heating.<sup>47</sup> Still the heating is reduced and as will be pointed out in the Results section (Chapter 5), a considerable difference in the as deposited film properties occurs with RF planar magnetron sputtering, compared to RF diode sputtering.

#### Thin Film Deposition

Prior to deposition of thin films, all substrates were subjected to a three phase cleaning procedure. The first phase of the process was an ultrasonic bath in DI water for 10 minutes. After this treatment the substrates were removed from the water and rinsed with isopropyl alcohol (IPA). A second ultrasonic cleaning was then carried out for 10 minutes in IPA. The final phase of the cleaning procedure was a 15 minute treatment in a vapor degreaser, which employed IPA as the solvent. Substrates were slowly removed from the vapor, which allowed the condensed vapor droplets to evaporate. To check for cleanliness substrates were examined by edge illumination against a black background. This permitted observation of any contaminants on the surface of the substrate in addition to any small flaws in the surface.

To deposit thin films, substrates were mounted on a substrate holder and positioned in the deposition system immediately after

cleaning. The deposition system was pumped down to a pressure of  $< 1.0 \times 10^{-6}$  torr before backfilling with the sputtering gas. The IC-6000 was usually programmed for a fast ramp up to the desired power level and then a rate controlled presputter was initiated before the shutter was opened. If a sputtering target was newly installed, a presputter burn-in of 30 minutes was carried out; otherwise the target was presputtered for 5 minutes before exposing the substrate to the plasma. The IC-6000 automatically controlled the deposition rate and thickness. Deposition rate was varied between 1 to 5 Å/sec and films for optical analysis were typically made 1  $\mu$ m thick, although the film thickness for other analysis was varied.

#### Substrate materials

Several different types of substrates were used to support thin films, depending on how the films were to be analyzed. Standard substrates for optical analysis were made of optical quality fused silica, typically one inch square and 1 mm thick. These substrates were found to have very few surface flaws and were essentially transparent over the optical region in which films were analyzed. The low index of refraction ( $n=1.46$ ) of these substrates was also necessary for measuring the refractive index of the film and for planar waveguide measurements. Some films were also deposited on silica for TEM analysis. Self-supporting TEM specimens were prepared by floating these films off the silica with a 1% HF solution.

Other films for optical analysis were deposited onto single crystal sapphire substrates. This was done to determine if the high

thermal conductivity of the sapphire would aid in reducing heating by the laser beam during low temperature spectroscopic measurements. These substrates were of very high quality with no detectable flaws and a very smooth surface finish. Some COSAD films were deposited onto sapphire substrates to aid in X-ray chemical analysis, since the sapphire had no X-ray lines which overlapped the lines in these films.

For other TEM analysis, films were deposited on slabs of single crystal NaCl and on TEM grids which held carbon support films. The TEM grid-carbon film combination was used for quick analysis of deposited films. Once the grid-carbon film assembly was prepared, thin films could be deposited directly onto the carbon film, and no other sample preparation was necessary. Films of thickness from 50 to 500 Å were typically deposited for TEM analysis. The carbon support film was made by thermally evaporating approximately 100 Å of amorphous carbon onto sheets of single crystal NaCl. After the carbon film was dried at the NaCl, 40 mesh TEM grids were carefully placed on the carbon film. The film and grids was then washed with water to remove the NaCl and dried at 100°C.

Single crystal NaCl was used as a substrate because it was found that after heat treatment it was resistant to high temperature deposition of thin films of various materials. It was found that substrates of NaCl were not suitable for deposition of thin films of various materials at low temperatures. The reason for this was that after heat treatment at low temperatures, the NaCl substrates were found to be very hygroscopic and would absorb water vapor from the atmosphere. This would cause the thin films to be deposited on the water vapor rather than on the NaCl substrate. The NaCl substrates were found to be very hygroscopic and would absorb water vapor from the atmosphere. This would cause the thin films to be deposited on the water vapor rather than on the NaCl substrate.

were also required for TEM analysis of COSAD films, since the HF solutions normally used to lift CdS off silica slides would strongly attack these films.

#### Substrate temperatures

Several different substrate temperatures were used to investigate the effect of deposition temperature on thin film grain size. With the  $\text{LN}_2$  feedthrough assembly that was described above, substrates could be cooled to  $\text{LN}_2$  temperatures in about 20 minutes. For some depositions a low temperature thermal contact paste was used to mount the substrate in the holder, although most frequently, standard hold down clips were used. An Iron-Constantan thermocouple was initially used to monitor the temperature of the substrate holder during a deposition. To use a digital meter to measure the output from this thermocouple during a plasma deposition, an RC circuit had to be used to decouple the RF signal that was imposed on the DC thermocouple signal. The RC circuit is essentially a low band pass filter. A schematic diagram of the circuit is shown in Figure 14. If this filter is not used, a very large RF signal can be induced in the lead wires, which will destroy most D-A converters used in digital meters.

For depositing films at room temperature, the  $\text{LN}_2$  feedthrough assembly (without  $\text{LN}_2$  in the reservoir) was used to hold substrates. These depositions were very close to room temperature, since it was found that even with the highest deposition rates, the holder would not heat up to  $150^\circ\text{C}$ . When substrate temperatures greater than this were required, the  $\text{LN}_2$  assembly was replaced with the resistively heated holder. Temperatures as high as  $300^\circ\text{C}$  could be obtained in

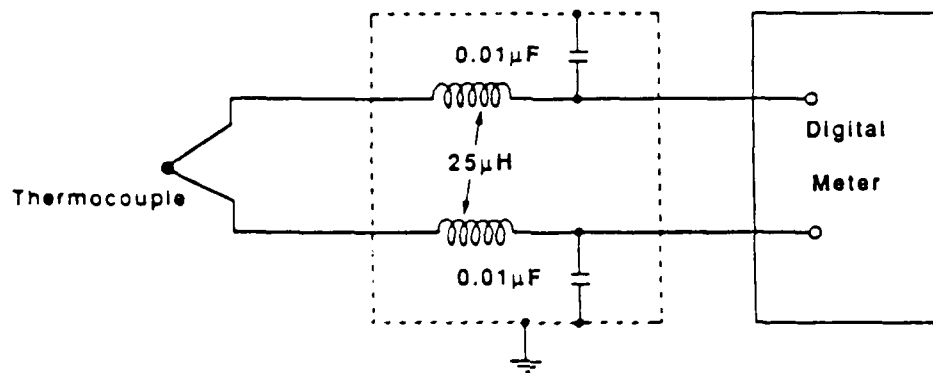
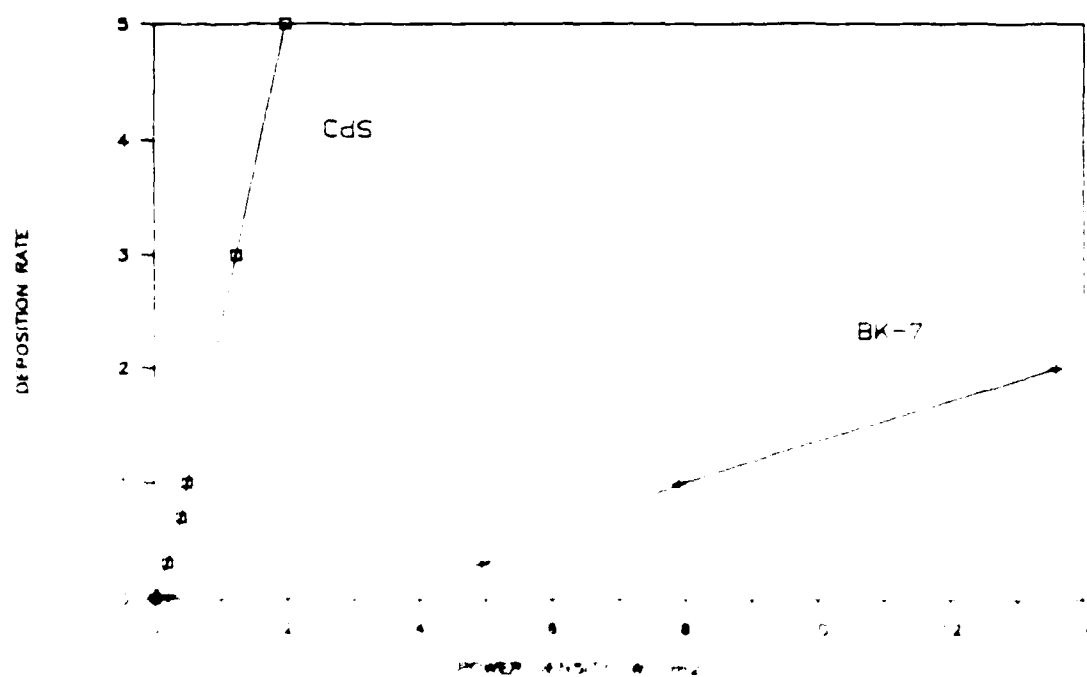


Figure 1. A  $25\mu\text{H}$  inductor and  $0.01\mu\text{F}$  capacitor decoupling circuit used protect thermocouple from RF transients.<sup>48</sup>



### Deposition rates

\_\_\_\_\_



were set up to sputter deposit at a static rate of 3 Å/sec. This is the maximum rate that could be used with the glass target without causing excessive heating. The circle over which the substrate was rotated was eight inches in diameter, so with the three inch diameter apertures used with the guns, the duty cycle was rather low, only 0.12 for each gun. With a rotation speed of 20 RPM, the resulting total dynamic deposition rate is less than 1 Å/sec. One possible way to increase this rate would have been to reduce the rotation speed. This, however, would also mean that the substrate would be spending more time over areas which were not depositing film and were actually depositing impurities.

The use of the computer controlled stepping motor to rotate the substrate holder alleviated the problem with the linear drive system. With this setup it was possible to increase the amount of time the substrate spent over a given source. At the same time, it reduced the amount of impurities deposited on the film because the stepping motor could be programmed to speed between the targets. In this way, the deposition rate could be increased by the computer program. This was done by programming the computer to rotate the substrate at a slower rate over the sources and at a faster rate between the sources.

annealing COSAD films high purity compressed air was used with the same furnace setup. Flow rates of 100 cc/m were typically used.

Temperature control was accomplished with a single setpoint temperature controller (Love Control Co.) which provided temperature control to  $\pm 1^\circ \text{C}$ .

Two thermocouples were used, one mounted outside the tube for control and one positioned inside the tube adjacent to the sample.

Heating rates of up to  $35^\circ \text{C/min}$  could be realized, and cooling rates of  $100^\circ \text{C/min}$  could be obtained by sliding the muffle tube out of the furnace hot zone. Temperatures for heat treating thin films ranged from  $200^\circ \text{C}$  to  $700^\circ \text{C}$ , with times ranging from 1 minute up to 5 hours.

To reduce the amount of grain growth that would occur as a result of high temperature heat treatments, some films were heated by a technique known as rapid thermal annealing. This process utilizes high power quartz lamps to rapidly heat the sample. Because of the low thermal mass that is achieved with this technique, heating rates in excess of  $500^\circ \text{C/sec}$  are possible. The sample is sandwiched between two thin sheets of graphite which act as black body absorbers and help to transfer the heat generated by the lamps to the sample. In this particular system lamps with a total power of 1000 watts were used. Heat treatment times of 1 to 10 seconds ranging from  $200^\circ \text{C}$  to  $700^\circ \text{C}$  were achieved under a flowing nitrogen atmosphere.

microstructure was made by electron microscopy. The various TEM specimens that were described in a previous section were examined in a JEOL 200 CX analytical microscope (Japanese Electron Optics Laboratory, Boston, MA.). This instrument was used in both transmission (TEM) and scanning transmission (STEM) modes to directly observe and measure the ultra-fine structure of thin films. Selected area diffraction (SAD) mode was used to conduct electron diffraction experiments for determination of crystal structure and orientation. In the SAD mode it was possible to obtain diffraction information from areas as small as 5  $\mu\text{m}$ . The line to line resolution observed in the TEM mode was 8  $\text{\AA}$ . Another technique used for determination of crystal orientation was dark field imaging. By tilting the primary beam in the microscope, the contrast that is observed in a dark field image is only due to those crystals or portions of crystals which are oriented for a specific Bragg reflection. Dark field imaging makes it possible to observe preferred orientation in a thin film or any portion of a crystal that contains defects (such as microtwins).<sup>49</sup> On the JEOL 200CX changing from bright field to dark field was accomplished with a single switch.

To study the topographical structure of thicker films a JEOL 35CF scanning electron microscope was used. Films which were made for optical analysis were frequently examined with this instrument. The advantage of this technique for TDS films was that no sample preparation was required except for sample mounting. The conductivity of these films was high enough not to warrant coating with a conductive film, although for SiAl<sub>x</sub> films a thin carbon film had to be deposited before these films could be examined. With this instrument the

presence of gross defects in the film such as pinholes or cracks could be observed, as well as the fine grain structure of certain films. The major disadvantage with this microscope, however, was a limiting resolution of about 300 Å which made it difficult to observe the grain size of as-deposited thin films.

X-ray diffraction was another technique used to measure the crystal structure and orientation of thin films. An APD 3720 computer-controlled diffractometer (Phillips Co.) was used to carry out diffraction experiments. Typically, diffraction was measured from two-theta values ranging from 15° to 90° with a angular step of 0.05°. Use of the computer to store X-ray diffraction spectra on disk greatly facilitated the determination of the change in crystal structure with heat treatments. Changes in peak positions and intensities could be readily determined, and by making high resolution scans (0.02°/step) over certain peaks it was possible to calculate the grain size and film strain using certain utility programs available in the computer system. Again, no sample preparation was necessary for this technique as diffraction from 1 µm films supported on silica substrates was readily observed.

#### Chemical Analysis

Initially, Energy Dispersive Spectroscopy (EDS) was used to measure the stoichiometry of thin films during both SEM and STEM observations; however, it was found to give results that were not quantitative. Particularly in the SEM, it was found that the results were very dependent on sample geometry with respect to the detector. A

technique known as X-ray secondary fluorescence was used instead to measure the stoichiometry of nearly every thin film that was made. The particular instrument used for these measurements utilized a silver X-ray tube to produce the primary X-ray beam. Tube voltages of 50 kV were used with a current of 30 mA. One of four different secondary targets could be selected to generate the X-rays that were used to analyze the sample. The advantage of this technique is that the background radiation from the X-ray tube (bremsstrahlung) is totally removed and only the very narrow X-ray line corresponding to the secondary target reaches the sample which results in a great reduction of the background counts. The particular geometry of this system limits the radiation to only one polarization which further reduces the background count.<sup>50</sup> Detection levels for most transition metals was  $\approx$  0.1 ppm. Beam size incident on the sample is 1 cm in diameter and penetration depth is only a few microns which makes this technique ideally suited for measuring thin films supported by substrates. The X-rays emitted from the sample are analyzed by EDS with this system; however, due to the above arrangements, a much more quantitative determination could be made when the results were compared to a standard reference.

The standard used, in this case, to determine the stoichiometry of thin films was a piece of target material. The stoichiometry of the target was verified by a wet chemical technique and electron probe microanalysis (EPMA) (JEOL 730 Superprobe). For solution analysis a portion of the target was dissolved in nitric acid and then this solution was diluted a given amount. The amount of Cd and S in

solution was determined by using an induction coupled plasma (ICP) spectrometer (Allied Analytical Systems, Waltham, MA). By comparing these amounts to those in standard solutions the stoichiometry was determined. For EPMA the stoichiometry of the target material was determined by use of standards and a ZAF or  $\phi\rho z$  program.<sup>51</sup> The ratio of the integrated peak intensities for Cd and S in the target was then determined by X-ray fluorescence. The ratio obtained from thin films was compared directly to this ratio to quantitatively determine the stoichiometry.

Film thickness could be readily determined with this technique by measuring the intensity of the silicon K-alpha peak that was emitted by the substrate through the film. The intensity of this line is exponentially attenuated by the thickness of material that it passes through and can be related by the following equation:

$$I = I_0 \exp^{-\alpha t} \quad (2.1)$$

where  $I_0$  is the intensity from a bare substrate and  $t$  is the film thickness. From equation 2.1 a linear relationship between a function of the intensity,  $F(I)$ , and  $t$  can be obtained by<sup>55</sup>

$$F(I) = -\log_{10} \frac{I}{I_0} \quad (2.2)$$

The intensity from three different films of known thickness (verified by profilometry) were measured and by plotting  $F(I)$  versus  $t$ , a master curve was generated. The thickness of an unknown film could then be found by solving the above equation for  $F(I)$  using the intensity from



the unknown. The x-coordinate on the curve for the unknown  $F(I)$  would give the thickness. Film thickness of up to 3  $\mu\text{m}$  could accurately be determined with this technique. Changes in density or loss of material as a result of heat treatment could also be monitored with this technique.

Several other analytical techniques were used to analyze the composition of thin films. In each case the results for thin films were compared to the results obtained from target material. The different techniques were used to both acquire information, which the specific technique is most suited for, and to cross-check the composition of thin films. Auger electron spectroscopy (AES Perkin-Elmer, Norwalk, CT) gave the least quantitative determination of the absolute composition, but the technique was very quantitative for determining differences between samples. X-ray photoelectron spectroscopy (XPS Kratos, UK) gave semi-quantitative results and also showed how the surface of thin films were altered by heat treatment, a result which was not detected with any other technique.

#### Optical Measurements

By far the most extensive measurements made on thin films were optical measurements. The availability of several spectrometers, monochromators, lasers, and optical hardware greatly facilitated these measurements. The UV-VIS spectrophotometer used for many measurements was a Perkin-Elmer Lambda 9 (Norwalk, CT). Photoluminescence was measured with both a Princeton Applied Research Optical Multichannel Analyzer (Princeton, NJ), and an Instruments SA Raman spectrometer

(Metuchen, NJ). A variety of lasers were used for different experiments, although most photoluminescence experiments were made with a Spectra-Physics model 2025 Argon Ion laser (Mountain View, CA). Many measurements were made at both room temperature and at temperatures down to 9° K. Low temperatures were obtained with an Air Products (Allentown, PA) closed-cycle helium cold finger and digital temperature controller. Experiments carried out with these instruments will be extensively detailed in the following sections.

#### Index of Refraction

A very unique technique for measuring the dispersion or index of refraction as a function of wavelength was used on thin films. Normally the index of refraction of a material is related to the percent of transmitted light by the well known equation:

$$T = \frac{(1 - R)^2 \exp(-at)}{1 - R^2 \exp(-2at)} \quad (4.1)$$

where the reflection,  $R$ , is given by  $(n - 1)^2/(n + 1)^2$ . The situation is much more complicated, however, for a thin film supported on a substrate with a different refractive index. The reflection that occurs at the film/substrate interface must be dealt with as well as the reflections that occur at the other interfaces. This leads to a more complicated expression:

$$T = \frac{(1 - R_1)(1 - R_2)(1 - R_3) \exp(-at)}{(1 - R_2 R_3) \{ 1 - [R_1 R_2 + R_1 R_3 (1 - R_2)^2] \exp(-2at) \}} \quad (4.2)$$

where  $R_1$ ,  $R_2$ , and  $R_3$  are the reflectivities of the air-film, film-substrate, and substrate-air interfaces, respectively.<sup>16</sup> The values of the  $R_1$ ,  $R_2$ , and  $R_3$  are given by the same equation stated above with the refractive indices of the three materials (air, film, and substrate) substituted for  $n$ , respectively. Even if the value of the absorption coefficient is known, the transmission must be measured to 0.5% to get a 1% accuracy in the refractive index,<sup>52</sup> which is experimentally very difficult to do unless a specially designed spectrometer is used.

When the refractive index of the film is significantly different from that of the substrate (as the case with CdS on silica) a very strong wavelength dependent interference effect occurs. The effect can be explained by examining Figure 16. When the incident light beam passes through the thin film and encounters the interface it will be reflected due to the differences in refractive indices. Depending on the thickness and the refractive index of the film (the product of these two values determines the optical path length) the reflected ray will either constructively or destructively combine with the incident beam. This is the same process that occurs in a Fabry-Perot interferometer described previously. However, instead of changing the physical distance of the cavity to change the optical path length, resonance is achieved by scanning the wavelength of incident light. In terms of the total transmission that is measured, a series of interference fringes is observed, which vary with wavelength. These fringes are known as fringes of equal chromatic order (FECO), and the wavelengths at which maxima and minima in transmission occur is given by the same equation used for resonance conditions in a Fabry-Perot

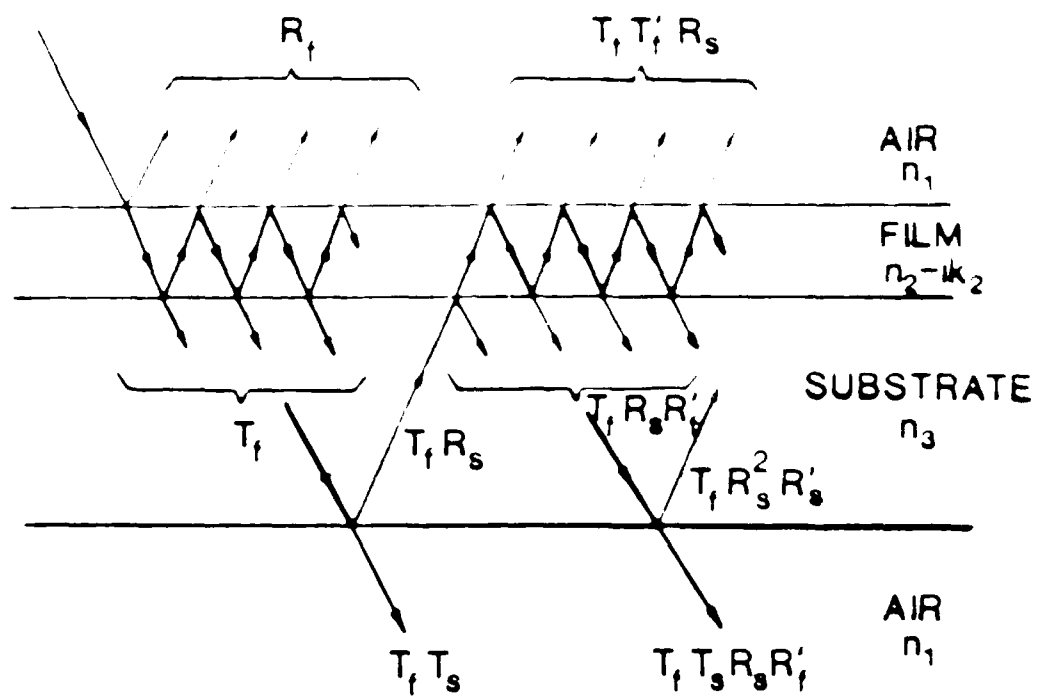


Figure 16 Interference effects at thin film, substrate, and air interfaces.

$$m\lambda = 2nt \quad (4.3)$$

where  $m$  is the order number of the fringe,  $t$  is the thickness, and  $n$  is the refractive index. In order to take advantage of this effect to determine the refractive index of a film, assumptions must be made. The first is that the order number is not a discrete number but that it can vary continuously. An analysis of this is important will be described shortly. The second assumption is that the dispersion of the refractive index can be described by the following equation:

$$n^2 = \frac{A}{\lambda^2} + B \quad (4.4)$$

where the square root of  $B$  gives the infinite wavelength refractive index and  $A$  and  $\lambda$  are constants.

To make use of this effect, a FECO spectrum is obtained at normal incidence. A typical spectra from a 2  $\mu\text{m}$  CdS film is shown in Figure 17a. Curves are drawn tangent to the maximum and minimum peaks and the values of the wavelength of the tangent points are determined. The sample is then rotated in the beam by 30°, resulting in an increase in the optical path length by a factor of  $1/(\cos 30^\circ)$ . The assumption that the order number is a continuous mathematical variable means that the normal incidence spectrum can be shifted to a shorter wavelength by increasing each order number by an amount  $\delta m$ .<sup>34</sup> This increase produces a shift in the FECO spectra shown in Figure 17b. Again, tangent curves are drawn and the tangent points to the interference spectrum are determined. The difference in the pairs of tangency points are then

INVESTIGATION OF NON-LINEAR OPTICAL BEHAVIOR OF  
SEMICONDUCTORS FOR OPTICA. (U) FLORIDA UNIV GAINESVILLE  
DEPT OF MATERIALS SCIENCE AND ENGINE. J H SIMMONS

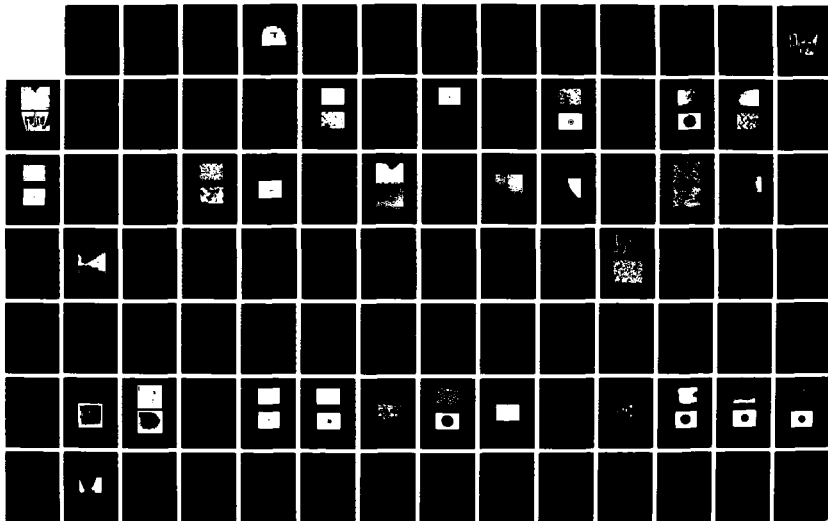
2/3

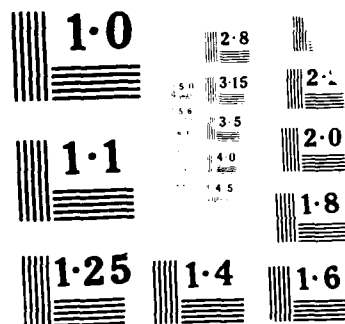
**UNCLASSIFIED**

30 SEP 87 AFOSR-TR-88-0133 AFOSR-84-0395

**F/8 20/6**

■





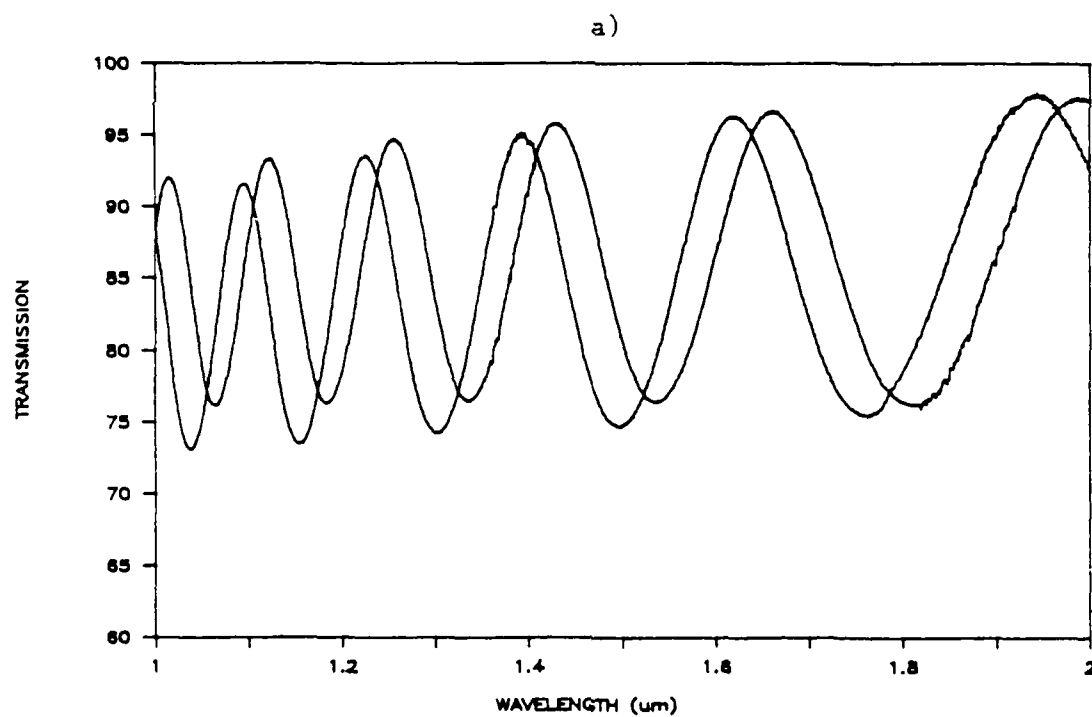
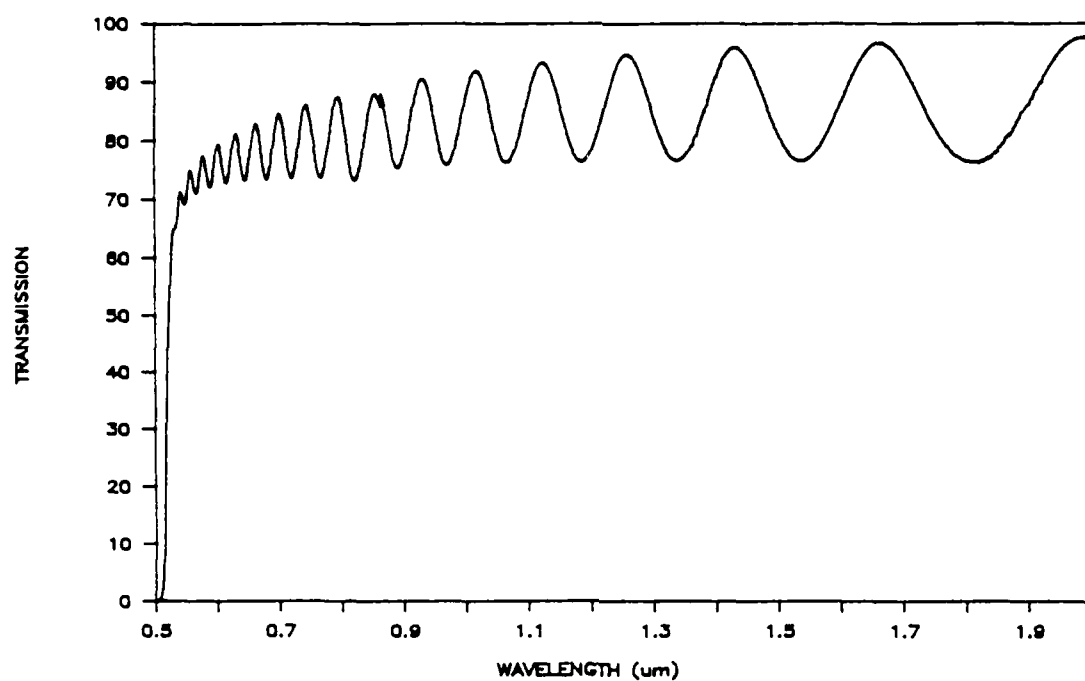


Figure 17 Fringes of equal chromatic order (FECO) spectrum for 2.0  $\mu\text{m}$  thick film of CdS on a silica substrate. a) Normal incidence spectrum showing many orders; b) Expanded abscissa scale showing shift in FECO spectrum for  $30^\circ$  incidence.



used in an iterative calculation to determine the values of A, B, x and n.

The problems associated with this technique involve precise placement of the sample at the focal point of the beam and accurate rotation of the sample about the axis which passes through the focal point. These problems were addressed by using a micrometer adjustable x-positioner and a micro-rotation stage, which are shown placed in the Lambda 9 spectrophotometer in Figure 18. Normal incidence to the film was determined by rotation of the stage a few degrees on either side of the initial zero and observing the shift in position of a given interference fringe. The true zero point was taken as the position which produced the midpoint between the two shifts. The focal point of the beam was then determined by observing the peak value of a given fringe as the sample holder was moved with the positioner.

The most difficult part of this technique (except for writing the iteration program for the analysis) was the manual determination of the value of the tangency points from the FECO spectra. The wavelength of the tangent point must be known to a precision of 0.1 nm to obtain an accuracy of three decimal places in the refractive index. Wavelengths can be measured with the spectrometer to this precision, but this precision could not be obtained by manual measurement of the tangent point from the printout of the spectra.

The problem was alleviated by interfacing the Lambda 9 to an IBM AT computer. Use of the computer greatly facilitated all aspects of using the spectrometer as spectra could be stored on disk and

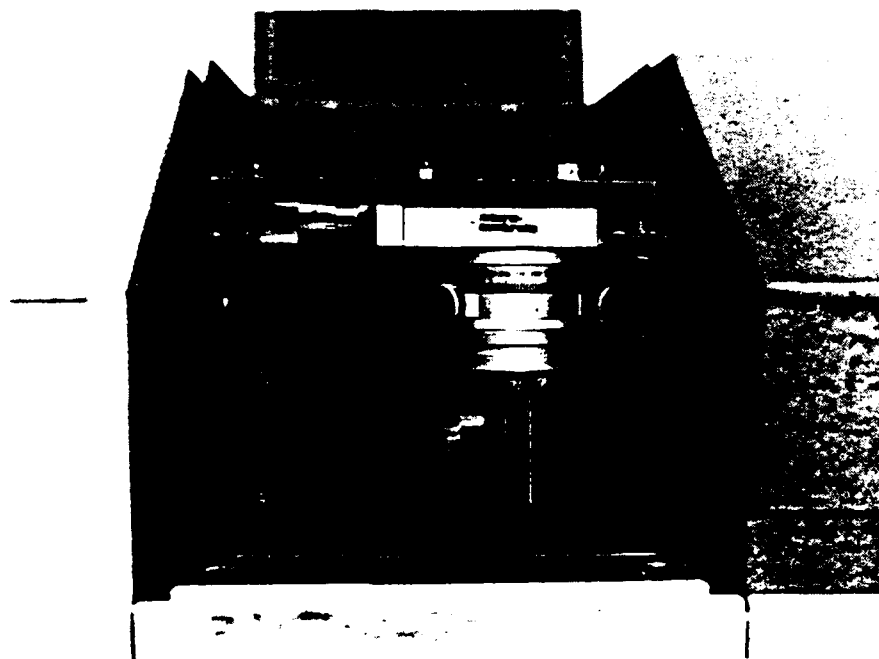


Figure 18    Photograph of micro-positioner stage used for acquiring  
FECO spectrum, shown mounted in Lambda 9 spectrophotometer.

manipulated later. The BASIC program used to remotely program, run, and accumulate data from the Lambda 9 is listed in Appendix A.

For the determination of the refractive index a particular software package available with the AT was found to be very useful. This software called is Asyst (McMillain Software Co.) and it is a very powerful mathematical analysis program. To determine the refractive index, the numbers representing the FECO spectra were imported into Asyst and stored in a two dimensional array. Using a very short program, the array was plotted, and the equations for the curves tangent to the maximum and minimum were fit. Next, arrays were generated to represent each of the tangent curves. Asyst could then be used to very easily determine the points where the three arrays intersected, with an accuracy of 0.1%. The intersection points were stored in a fourth array. This process was repeated for a 30° incidence spectra. The very long iterative BASIC program that was originally used to calculate the dispersion equation could be shortened considerably with utility functions available in Asyst. In fact, by manipulating the numbers as arrays, the calculation was much simpler and much faster.

Even though the above process produced an accurate result, a second technique, ellipsometry, was used to verify these results. Ellipsometry is based on the change in polarization of a light beam when it is reflected from a surface. Generally a plane polarized light beam is made incident on the surface of a material at an angle of 45°. The resulting reflected beam is elliptically polarized and from the

analysis of this polarization the optical constants of the material can be determined.

The problems associated with this technique mostly originated from the actual instrument. The computer-controlled Gaertner ellipsometer (Chicago, IL) is the industry standard; however, the unit available for use in this study was a manual model which greatly reduces the capacity for quantitative analysis. The problem does not so much have to do with manually setting the polarizer and analyzer, but rather in reading the analog scale to determine the node points. This was a special problem on this unit because the meter was nonlinear; the highest sensitivity was between a reading of 2 and 3 on a scale of 1 to 5. In addition, the gain for the photocell had to be manually adjusted as a node point was found. The gain was also nonlinear and there was a flat spot at one end of the range. These two problems contributed to difficulties in reproducing the results; however, the greatest problem with the analysis had to do with the computer program used to calculate the values of  $n$  and  $t$  from  $\psi$  and  $\delta$ . Supplied by Gaertner, this program did not actually calculate the values of  $\psi$  and  $\delta$ , but instead it looked up the values in a table, based on the values of the two pairs of angles that were inputted. From the table values of  $\psi$  and  $\delta$  the program then calculated the refractive index and thickness by an iterative technique. One difficulty with the program occurred if the particular combination of angles inputted were outside values in the table. The program would hang up and the only solution was to boot the program out. This actually happened a surprisingly large number of times, even when similar samples were analyzed. To

alleviate the problems with this program, a graphical method was developed to calculate the refractive index and thickness from the set of angles measured with the ellipsometer. A brief description of this method is given in Appendix B.

#### UV-VIS Absorption

Measurement of the fundamental optical absorption edge in semiconductors permits direct determination of the nature of the band gap. Optical absorption properties of thin films were measured over a variety of temperatures with the Lambda 9 spectrophotometer operating in one of several modes. In the transmission mode a linear, zero to 100% scale was used, which was useful measuring FECO spectra. A more useful mode for measuring the band edge, however, was to plot the transmitted light in terms of absorbance. Because the absorbance scale is the natural logarithm of reciprocal transmission, features of the band gap absorption above the band edge could be studied. In the transmission mode unless the scale was expanded these features would appear indistinct, because transmission above the band gap was typically less than 1% with the thickness of films usually studied. In the absorbance mode this 1% transmission would correspond to a value of 4.6 on a possible absorbance scale of 6.0. Another advantage of using the absorbance scale is that the spectra obtained qualitatively reflected the shape of the true absorption curve. As explained earlier in this chapter, the transmission spectrum that is measured of a thin film on a substrate is the result of a complicated combination of the reflections which occur at the various interfaces. The transmission,

however, is exponentially proportional to the absorption coefficient, which is why absorbance spectra approximate absorption spectra. The two terms will therefore be used interchangeably when describing spectra.

The band gap energy was taken as the point where the slope of the absorption curve was a maximum.<sup>54</sup> One unique feature of the Lambda 9 was that it allowed anywhere from the first to fourth derivative of a spectra to be taken. The maximum of the first derivative of the absorption edge was taken as the band gap energy. A calculation to verify these results will be described in Chapter V. Basically, it evolves solving equation 4.2 for  $\alpha$  using the absorbance spectra, and then plotting  $\alpha^2$  verses energy. A direct band gap material will give a straight line for this plot, and the extrapolation of the line to  $\alpha^2 = 0$  gives the optical band gap of the material.<sup>54</sup>

The temperature dependence of the band gap energy was measured by cooling the sample with the cold finger. The sample was mounted in a ring sample holder which would then be attached to the end of the cold finger. A radiation shield was then positioned around the cold finger and a vacuum insulation collar with fused quartz windows was then slid over the entire assembly. A vacuum of less than 1 micron pressure was then obtained in a few minutes by pumping the system with a Balzer's 70 l/sec turbomolecular pump. Once this vacuum was obtained in the collar, cooling of the sample to 9° K could be accomplished in less than 1 hour, although most measurements were made after 2 hours of cooling. Any intermediate temperature between 9° K and 250° K could be achieved with the digital temperature controller and heater assembly.

The cold finger assembly was mounted on a height-adjustable rack system so that once a sample was cooled to low temperatures the cold finger assembly could be moved so that measurements on different equipment such as the OMA and Raman spectrometers could be accomplished.

All aspects of the measurements with the Lambda 9 were greatly enhanced by interface to the AT computer. Spectra were stored as ASCII files which later could be imported into a LOTUS worksheet (Lotus Development Co., Cambridge, MA) for manipulation and plotting. The BASIC program listed in Appendix A would accumulate spectra in the form of a long column of numbers, each number representing the absorption or transmission at a given data point. The data interval was based on the slit width used for the analysis. The slit defines the bandpass that determines the resolution to which features can be resolved. Usually a data interval of one-third the slit width was used for the analysis. Slit widths from 4 nm down to 0.5 nm were used depending on the required resolution. As the slit width is decreased, the signal to noise ratio is also decreased. This means that the amount of time that is spent at a given data point must be increased. Computer control of the spectrophotometer was indispensable for making high resolution runs where very slow scan speeds were necessary.

#### Photoluminescence and Raman

Further investigations of the band structure of semiconductors can be made by measurement of the emission bands or peaks produced by photoluminescence and resonant Raman scattering. Measurement of these emissions for this study were made with the two spectrometers described

above. The majority of the measurements, however, were made with the optical multichannel analyzer (OMA) and a 0.33 meter Instruments SA monochromator. Most measurements were made at low temperatures, using the cold finger to cool the sample.

The detection system of the OMA spectrometer consisted of a linear silicon photodiode array which was 1024 elements wide with the diode centers spaced every 25  $\mu\text{m}$ . Approximately 700 of the center diodes were intensified to increase their light conversion efficiency. The diode array was connected to a multichannel analyzer and the array was scanned by the MCA to generate a spectra. Scan rates as fast as 16.6 msec/scan could be used, although to obtain a higher number of counts, scan rates of 500 msec were typically used. The computer system controlling the MCA was setup to accumulate a number of scans so that signal averaging could be used to reduce noise levels. Also, the dark current or background noise could be automatically subtracted from a spectrum. The diode array could be cooled to 5° C with a Peltier cooler to further reduce the background noise level. With the monochromator and grating combination the MCA window was about 20 nm. This is the width of the spectra which was displayed on the screen. The grating in the monochromator was rotated to change the wavelength window.

The third meter monochromator was used with a 2400 lines/mm grating. The f-stop or light gathering capability of the monochromator was calculated with



$$f\text{-stop} = \frac{\text{focal length}}{\text{grating size}} \quad (4.5)$$

where grating size is the linear dimension of the grating. With a 55 mm grating, the f-stop of the monochromator is f6. The reciprocal linear dispersion (RLD) of a monochromator is a measure of its ability to disperse light, and can be calculated by

$$\text{RLD} = \frac{1}{f} \times \frac{dL}{d\theta} \quad (4.6)$$

where  $d\theta/dL$  is the angular dispersion (in rad/mm) and is approximately equal to the number of grating lines per mm. The RLD for this monochromator was calculated to be 1.25 nm/mm. The bandpass or resolution of a monochromator is usually calculated by multiplying this number by the width of the slit used. With a linear diode array detection system, however, the resolution is determined by the spacial resolution of the array. Assuming that three diodes can resolve a peak, which correspond to 75  $\mu\text{m}$ , the resolution of this system was 75  $\mu\text{m}$  X 1.25 nm/mm or 0.9 nm.

A schematic of the experimental setup is shown in Figure 19 and photographs of the system are shown in Figure 20a and Figure 20b. An f2 lens was used to focus emitted light into the spectrometer and a 100 mm focal length lens was used to focus the laser beam on the sample. Typically a focused spot size of 50  $\mu\text{m}$  was used, so with an incident power of 1 mW, the focused power density corresponds to 400 W/cm<sup>2</sup>. As

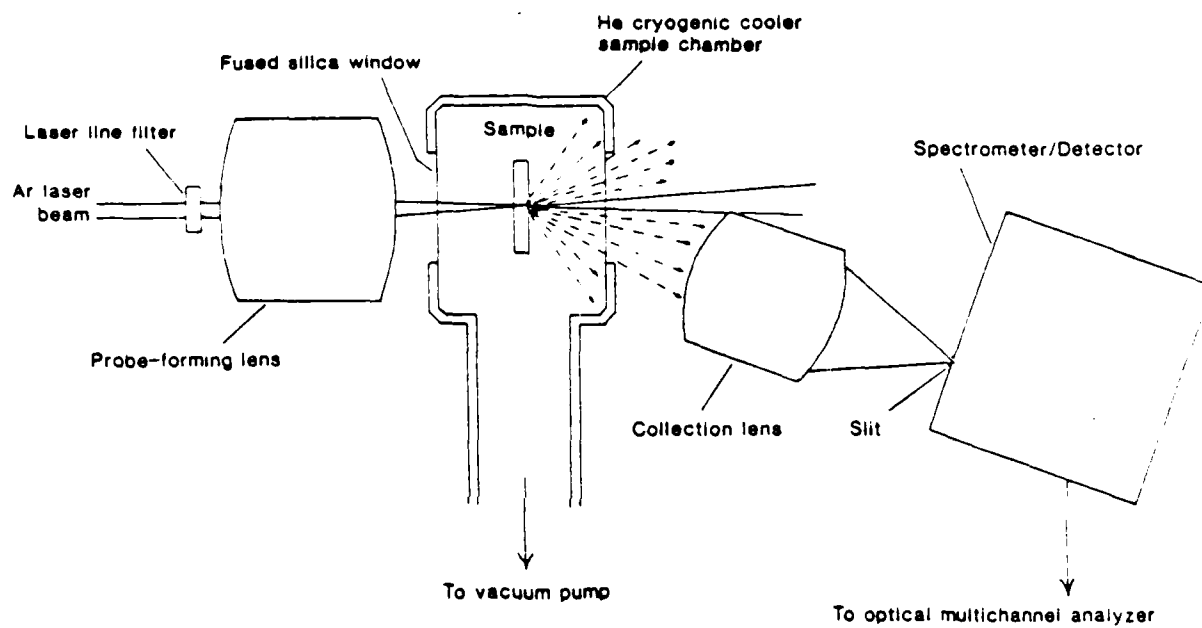


Figure 19 Schematic diagram of experimental setup used for measuring photoluminescence.

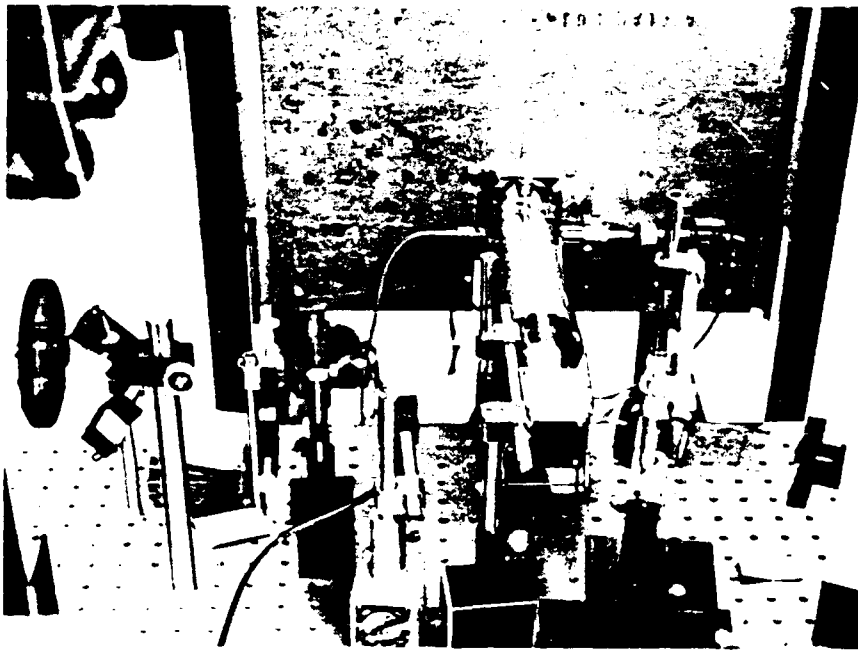
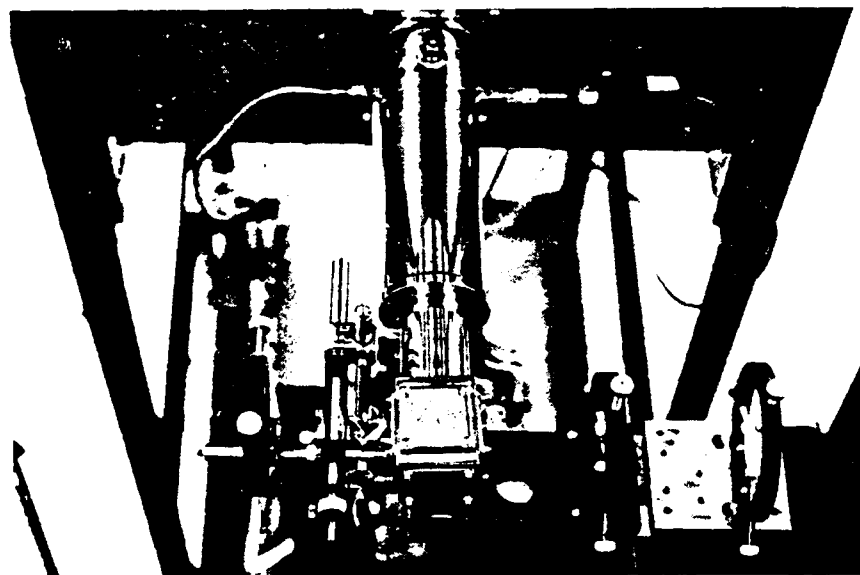


Figure 20 Photograph of OMA setup which was illustrated in Figure 19.



a)



b)

Figure 21 Photographs of setup for Raman spectroscopy. a) shown are the computer for acquiring data and the vacuum pumping system for the cold finger.; b) similar optics setup to OMA shown. Laser beam is brought in from the left, focussed on sample in cold finger, and the emitted light is focussed into the first slit of the spectrometer, at the far right.

indicated in the schematic, the laser beam was passed through a variable neutral density filter and a sharp cutoff spike filter. The variable density filter was used to adjust the power of the incident laser beam before being focused on the sample. The spike filter was an indispensable item which was used to remove plasma lines from the laser beam. Plasma lines originate from the argon plasma that is used to generate the laser beam. The lines are incoherent radiation, but they are very sharp transitions which can be mistaken as photoluminescent transitions as they occur over the entire visible wavelength range. A given spike filter passes only a very narrow wavelength range of light which corresponds to the laser line, therefore, a spike filter can only be used with its designated laser line. These filters are rather expensive so spike filters for only the 488 nm and 457 nm lines were available. The argon laser emits five other lines that occur at 514 nm, 496 nm, 476 nm, 465 nm, and 454 nm. Plasma lines were removed from the other laser lines by using a spatial filter. This filter consists simply of a grating and it works by diffracting the laser line at a different angle from the plasma lines. The spatial filter only works if a high number grating is used or if the laser beam can travel several feet before being focused.

To verify that the OMA was not missing any features of the photoluminescence, spectra were measured with the Instruments SA Raman spectrometer. This spectrometer utilized a double pass one meter monochromator with a photon counting photomultiplier tube and a digital discriminator. Photographs of the experimental setup are shown in Figures 21a and 21b. A simple lens system consisting of two plano-

convex lenses was used to focus the light emitted from the sample into the monochromator. Other than this difference, the setup was the same as the OMA. With 1800 lines/mm gratings the RLD of the monochromator was calculated to be 0.24 nm/mm. The width of the four slits used in this instrument determine the resolution, so with the smallest practical slit of 10  $\mu\text{m}$ , a resolution of 0.024 nm could be realized. The small linear dimension of the gratings (125 mm) with respect to the long local length however, reduced the light gathering capability to an f8. This turned out to be a very serious limitation for using the spectrometer to measure photoluminescence, as integration times of up to 5 sec per data point were required. A typical run was made using slit widths of 100  $\mu\text{m}$ , which gave nearly four times the resolution of the OMA, and data was collected every 0.05 nm for 2 sec. For a 20 nm window this meant that a single scan would take 15 minutes. At least three scans were required to reduce noise levels by signal averaging, which meant that for only one wavelength window, 45 minutes were required to acquire data. To make the accumulation of data easier, the Z-158 computer was interfaced to the spectrometer controller, and is shown in Figure 21b. The BASIC program to run the spectrometer was so long however, that it had to be compiled to reduce running time.

## CHAPTER V RESULTS AND DISCUSSION

### Thin Film Physical Properties

The primary focus of the experimental results presented in this section are on the variation of the microstructure, composition and electrical properties of thin films as a function of deposition parameters and post deposition treatments. First the properties of as-deposited thin films will be described and then the variation of properties with different heat treatments will be reported. Finally, the various physical properties of COSAD thin films will be described. The variations presented in this section will be correlated to optical properties presented in a subsequent section.

### Microstructure Characterization

#### Transmission electron microscopy

Room temperature depositions. A wide variety of microstructures were obtained by altering the substrate temperature during deposition. The great majority of thin films made for this study, however, were deposited onto substrates held at room temperature. Several advantages were realized by using this temperature: 1)the deposition process was greatly simplified, 2)very high quality thin films could be produced, and 3)optimum optical properties were obtained by heat treating films deposited at this temperature. These heat treatments, however,

inevitably increased the grain size of the thin films from values obtained with cooled or room temperature substrates.

The resulting microstructure of thin films deposited at room temperature is found to be independent of the substrate material. TEM micrographs of three representative thin films are shown in Figures 22, and 23. These micrographs show the structure of films 1000 Å in thickness that were deposited at 1 Å/sec onto a carbon support film (Figure 22), a silica slide (Figure 23a), and a NaCl substrate (Figure 23b). All three films display polygonal shaped grains with an average grain size of 250 Å. Many grains are highly faulted showing a defect structure of microtwins and stacking faults. Due to the extremely small size of these grains the microtwin orientation cannot be determined. Another predominant feature displayed by the microstructure of these thin films is the large number of Moiré fringes, indicated by the highly parallel lines with an average spacing of 10 to 15 Å. These patterns occur when two crystals overlap each other with a specific orientation. When a large number are observed in a polycrystalline film it is an indication that the grains of the film have a preferred orientation, although the orientation cannot be directly determined.

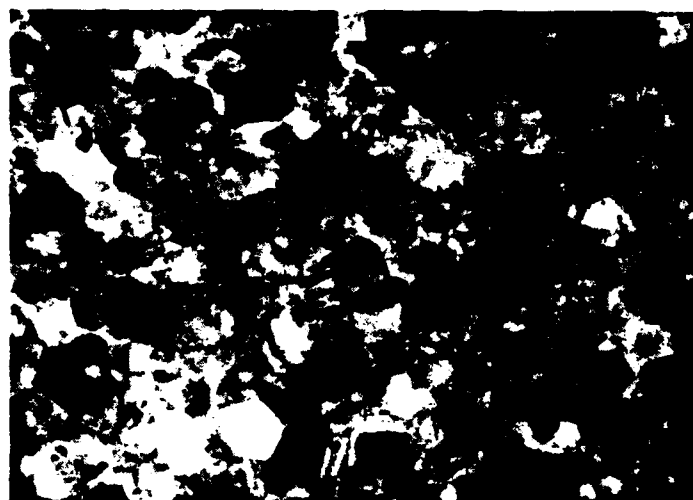
By performing diffraction experiments, the orientation could be determined. The grains were found to be oriented with the basal plane of the hexagonal lattice parallel to the substrate plane. This is indicated by the strong cubic reflections observed in the selected area diffraction pattern (SAD) shown in Figure 24a. In comparison to the indexed schematic pattern shown in Figure 24b, many of the hexagonal





67 nm

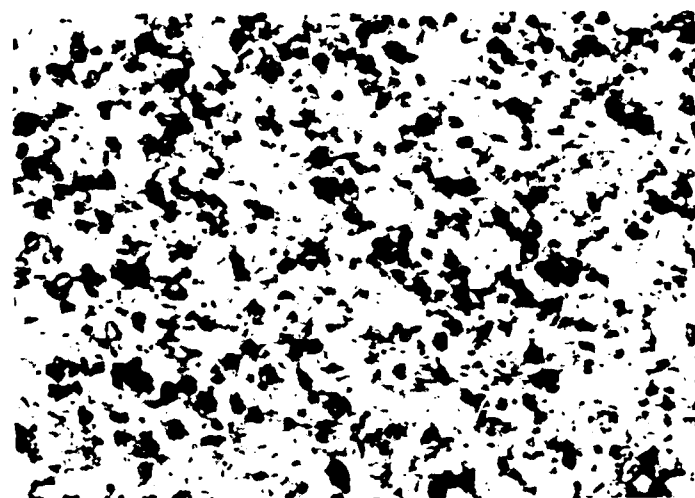
a)



30 nm

b)

Figure 22 TEM bright field micrographs of 1000 Å thick film deposited onto carbon support film. a) low magnification showing uniformity of grain size; b) high magnification showing microtwins and stacking faults.



a)

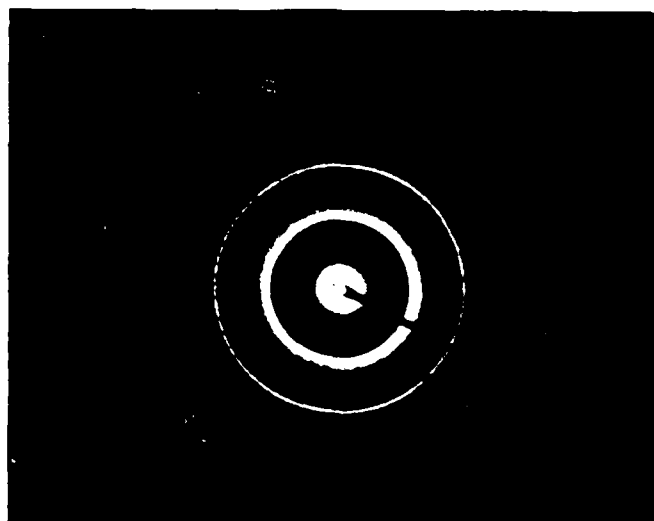
100 nm



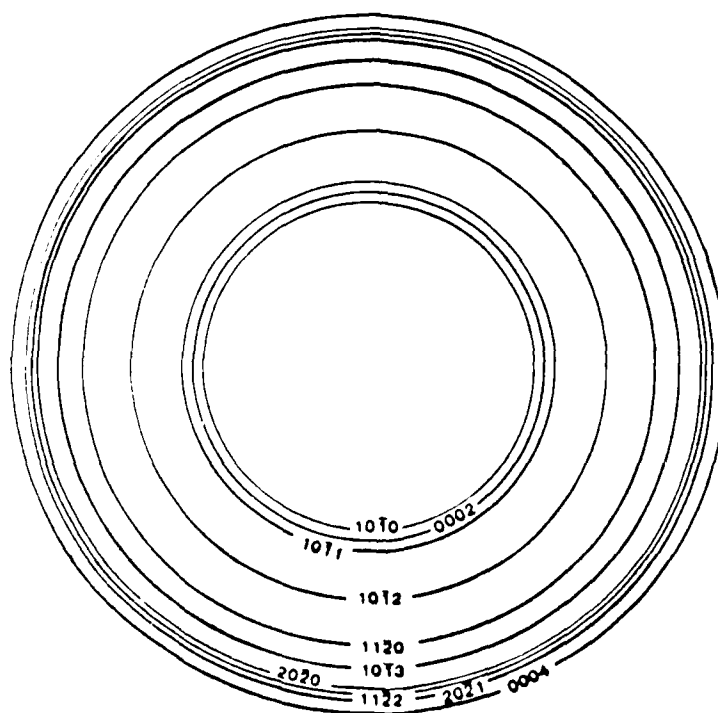
b)

200 nm

Figure 23 TEM micrographs of thin films deposited onto alternate substrates. a) silica glass slide; b) NaCl slab.



a)

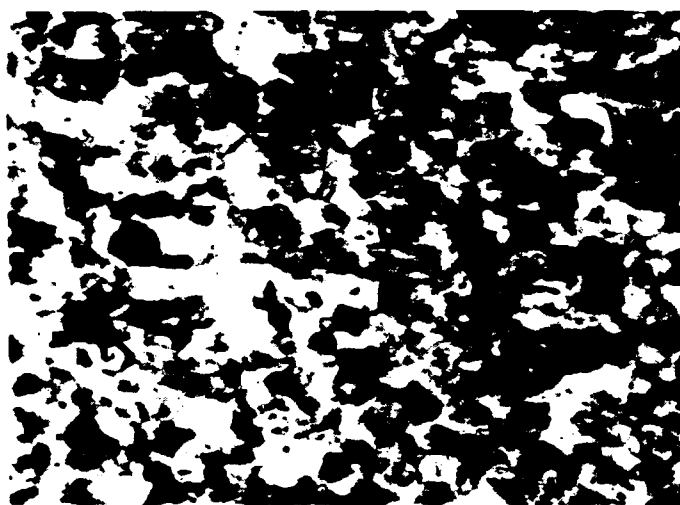


b)

Figure 24 Selected area diffraction pattern of thin film. a) actual pattern; b) indexed schematic pattern.

reflections appear to be missing; however, upon close examination all the spacings for hexagonal wurtzite can be found. The lines for these spacings are too faint to show up in the SAD pattern reproduced here. The orientation seen here is not dependent upon the substrate since similar films were made on both amorphous and crystalline substrates. These results are consistent with the early work on thermally evaporated CdS.<sup>56</sup> It is not clear why this specific orientation results because the close packed plane (i.e. (0002) hexagonal plane) is the slow growth plane. This means that the orientation is more closely related to the nucleation rate of the thin film rather than the growth rate, although this orientation was observed with all substrate materials, deposition rates, and at all substrate temperatures.

The grain size seen here is smaller than the 500 Å size reported by Martil et al.<sup>38-41</sup>. Grain size determinations by SEM of the films studied here do show a different size (see SEM section below) but, another reason for the difference can be attributed to differences in the sputtering technique used to produce the films studied here. As previously described, planar magnetron sputtering results in a lower film and substrate heating due to electron bombardment, therefore a smaller grain size should result. Higher deposition rates were found to increase the substrate temperature. However, even with a deposition rate of 5 Å/sec the substrate temperature was found to only increase to 15° C. Analysis of Figure 25 shows that no significant increase in grain size has resulted from the increased deposition rate; however, the micrograph does indicate that many more microstructural defects are present. The higher supersaturation of the vapor results in additions



50 nm

a)



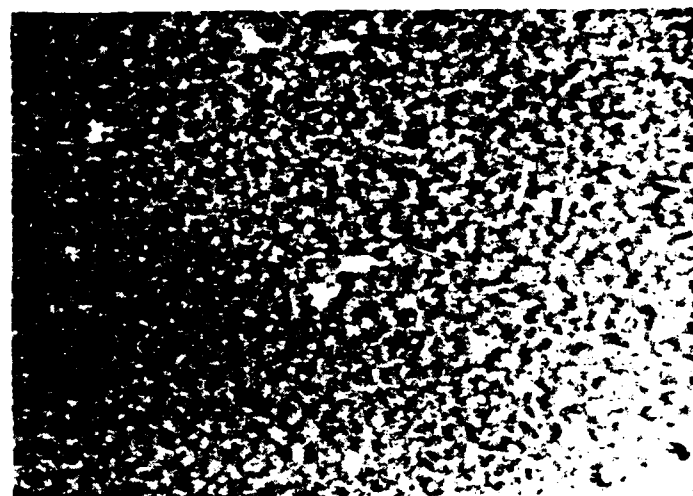
b)

Figure 25 Thin film deposited at high deposition rate. a) TEM micrograph showing large number of defects; b) corresponding SAD pattern.

of atoms onto non-favorable positions, which increase the number of defects during growth. Higher deposition rates should increase the amount of stress induced in the film. Strain determinations by X-ray line broadening measurements will be described in a following section.

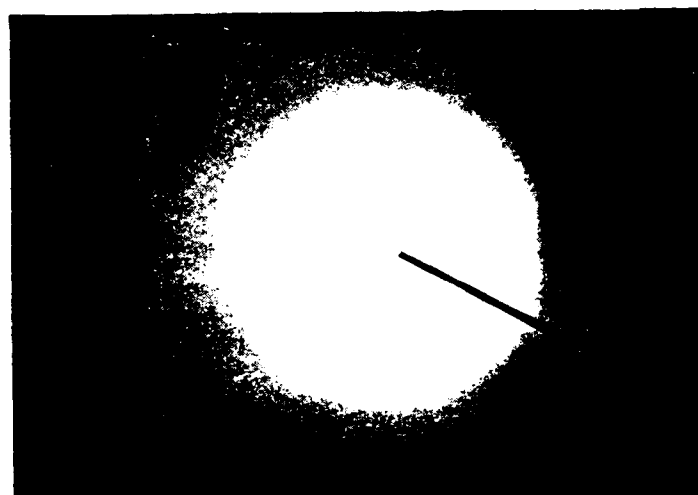
Low temperature depositions. Although high quality thin films could be produced at room temperature, some films were deposited onto substrates cooled to  $\text{LN}_2$  temperatures to determine if a grain size small enough for quantum confinement could be produced. Wolgemuth et al.<sup>29</sup> showed that evaporated material deposited at this temperature was found to be amorphous as determined by X-ray diffraction. In that work a high supersaturation was used to produce these films which may have also contributed to the amorphous structure. A much lower deposition rate was used in this study to help promote crystal growth, so that combined with the low temperature, a very small grain size would result. Figure 26a shows the micrograph of a film deposited at 3 Å/sec onto a carbon support film which was attached to a substrate cooled to 80° K. The "grain" structure that is observed is not due to individual grains but rather to a columnar structure with low density areas indicated by the low contrast between the columns. The SAD pattern shown in Figure 26b indicates that the film is somewhat crystalline, but highly faulted as evidenced by the width of the rings. The three rings corresponding to the cubic reflections are still present indicating that only the nearest neighbor spacing is present. No hexagonal lines can be found in SAD patterns of these films.

An indication of how a film grows on a cooled substrate is shown in Figure 27a. This section of a film increases in thickness from left



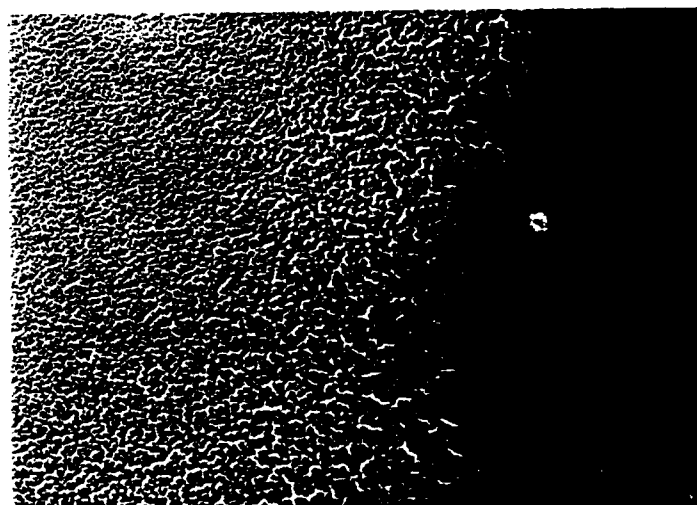
125 nm

a)



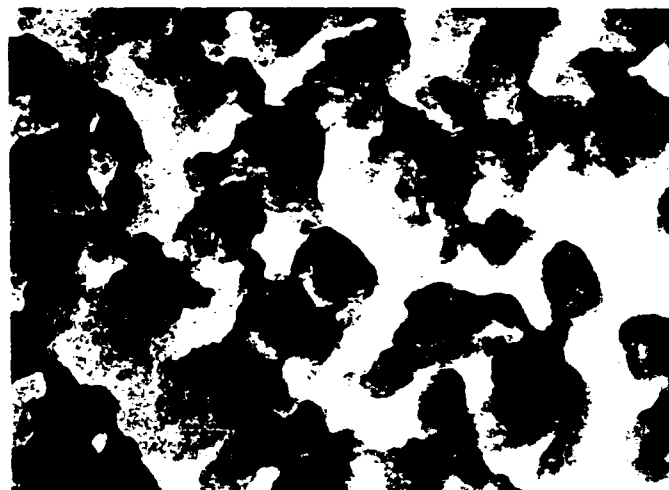
b)

Figure 26 Thin film deposited at  $\text{LN}_2$  temperatures. a) TEM micrograph showing low density columnar structure; b) corresponding SAD pattern indicating a semi-amorphous structure.



670 nm

a)



30 nm

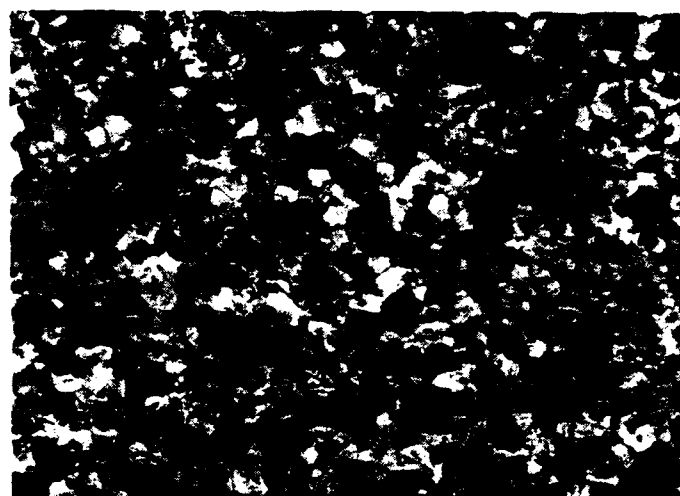
b)

Figure 27 Thin film deposited at  $\text{LN}_2$  temperatures. a) low magnification TEM micrograph showing section of film increasing in thickness from left to right; b) high magnification TEM micrograph showing island structure.



to right. The film is supported by a carbon film. At the far left an individual island structure is observed. The high magnification micrograph shown in Figure 27b indicates that the islands are mostly amorphous, with very small microcrystallites imbedded in the amorphous matrix. The microcrystallites are characterized by the darker contrast of approximately 80 Å in size within the globular structures. The very fine mottled structure is the background amorphous structure of the carbon support film. The SAD pattern included in the Figure shows that only the nearest neighbor spacing is present, and the crystal structure is highly distorted. Referring back to Figure 27a, as the film thickness increases to the right, the islands grow to form a columnar structure. The columns become fairly thick before they coalesce to form a low density continuous films, indicated at the far left in the Figure.

High temperature depositions. Other attempts to alter the microstructure of thin films were made by deposition onto heated substrates. Both room temperature and  $\text{LN}_2$  deposited films reported above display large numbers of crystallographic defects, which as described in a later section, degrade the optical properties. By depositing films onto substrates held at 200° C, microstructures with fewer defects could be produced. A higher deposition temperature should lead to fewer defects because the deposited atoms have more energy to diffuse to more favorable positions. Temperatures above 200° C, however, produced films which were very strongly bonded to the substrate and hence could not be removed for examination. A representative thin film deposited at 200° C which was "floated-off" a



100 nm

a)



b)

Figure 28 Thin film deposited at high temperature. a) TEM micrograph showing large defect free grains; b) corresponding SAD pattern.

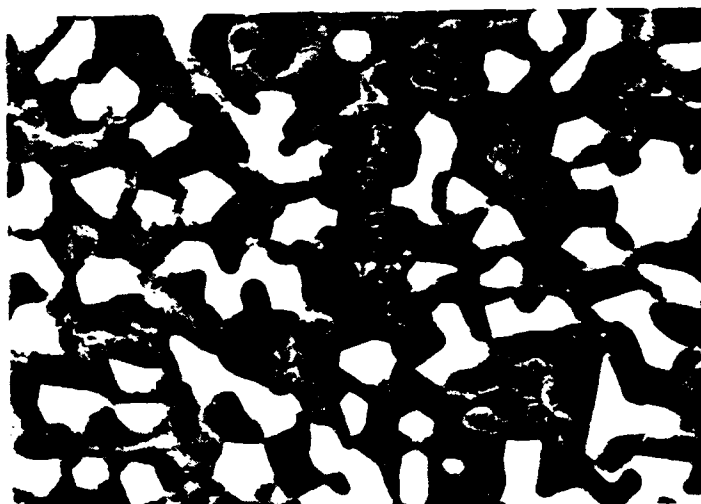
silica substrate and its corresponding SAD pattern are shown in Figures 28a and 28b. The absence of any contrast in many of the grains indicates a highly ordered crystal structure. The grains are again polygonal in shape with an average size of 800 Å. The SAD pattern shows that the preferred orientation is still maintained, but several of the other hexagonal reflections are now more predominant. Although fewer crystallographic defects are observed in these films, the "bulk" structure was found to be very nonuniform. Variation in color of the film across the substrate indicated a variation in composition and/or thickness, which made these films unsuitable for optical studies. Films deposited at temperatures greater than 200° C were found to be even more nonuniform. The nonuniformities result from nonuniform thermal contact because silica substrates are such poor conductors of heat. Thermal contact paste was not used due to concerns about contamination from the paste. The nonuniformities encountered at high deposition temperatures will be detailed more thoroughly in a following section on the scanning electron microscopy of thin films.

Heat treated thin films. Once the optical properties of as-deposited thin films were determined, it became apparent that to obtain optimum optical properties some type of thermal treatment had to be conducted on the films to remove the defect structure produced by the deposition process. However, due to difficulties with the increased bonding strength of thin films to substrates as a result of even mild heat treatments, very few TEM micrographs were obtained. The primary technique used for observing the microstructure of heat treated thin films was by SEM, and the results are presented in the following

section. The TEM micrographs that were obtained of a heat treated film are shown in Figures 29a and 29b, and the SAD pattern for this film is shown in Figure 30. A film with an original thickness of 1000 Å was deposited on a NaCl substrate and then heat treated to 650° C for 4 minutes. By dissolving the substrate the film was captured on a TEM carrier grid. The micrographs in Figure 29 show the film to be very porous with an interconnected grain network. This high porosity results when a large amount of grain growth occurs in a very thin film because there simply is not enough material to produce a continuous structure. The grains within the network display an average size of 2000 Å and many dislocations, stacking faults and bend contours are indicated by the variation in contrast observed within grains. These defects might be intrinsic or they may have occurred when the film was "floated-off" the substrate. It is interesting to note that very few if any microtwins can be observed in this structure. This result indicates further that these defects are growth related. The SAD pattern shown in Figure 30 displays a single crystal pattern with a basal plane zone axis, which means that the preferred orientation observed in as-deposited films is maintained after heat treatment, although this orientation may have been enhanced somewhat because the film was heated on a crystalline substrate.

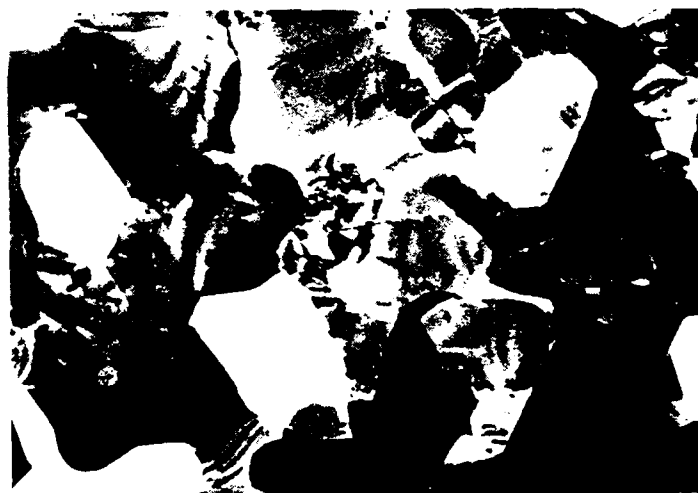
#### Scanning electron microscopy

As-deposited thin films. The microstructure of thin films was determined by SEM for several reasons. As explained above, most heat treated thin films could not be removed from their substrates for TEM



500 nm

a)



200 nm

b)

Figure 29 Thin film deposited on NaCl substrate and subsequently heat treated. a) TEM micrograph showing porous network; b) TEM micrograph showing dislocations and stacking faults.

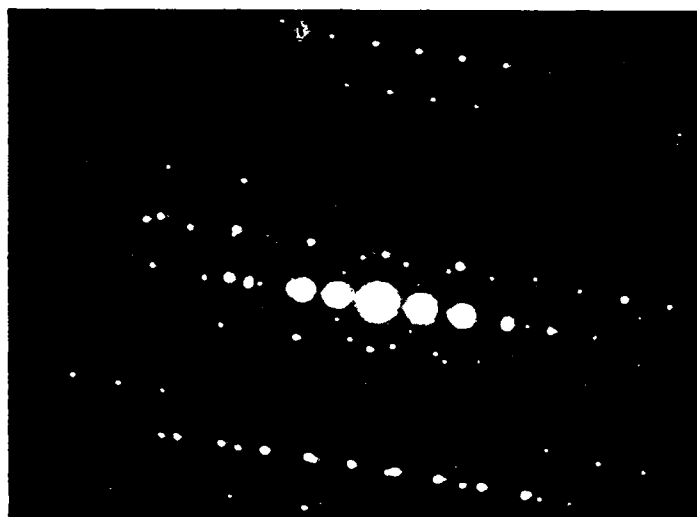
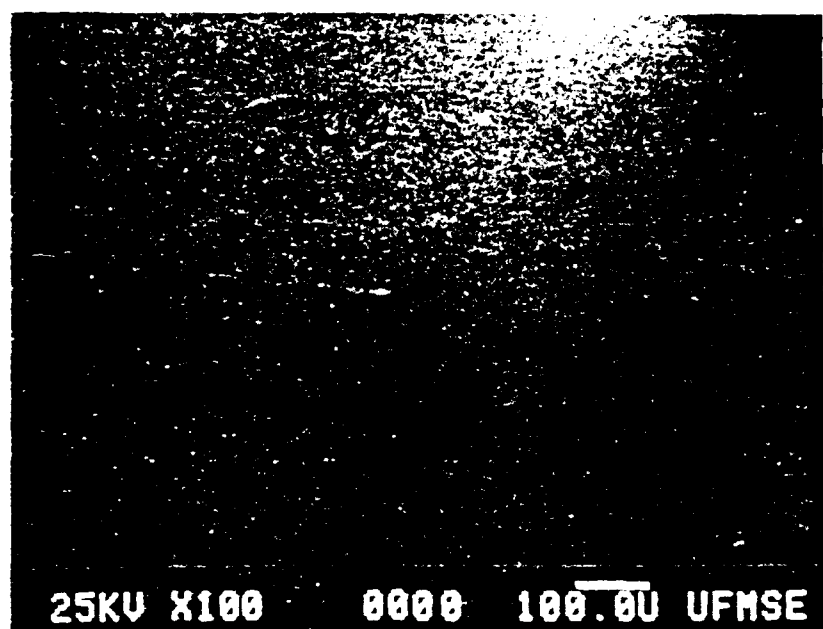


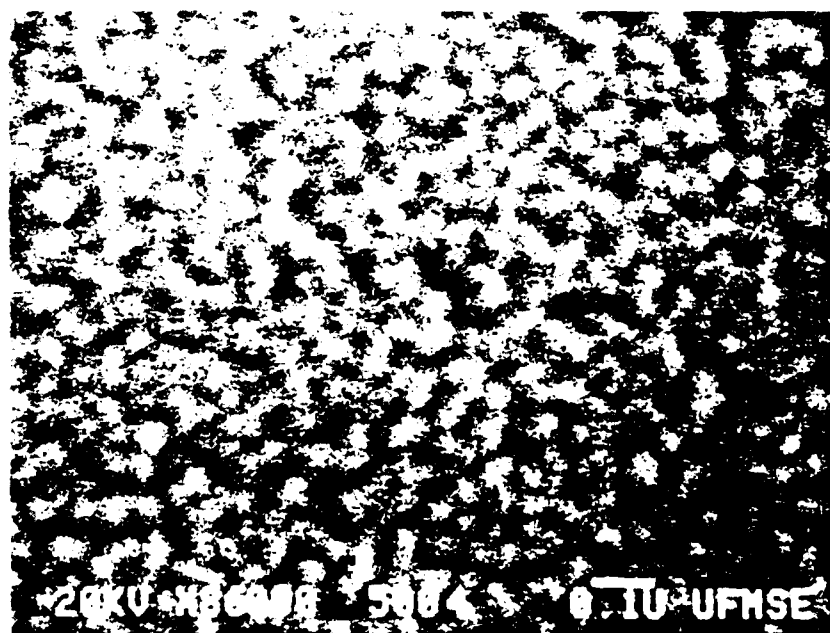
Figure 30 Selected area diffraction pattern of thin film shown in Figure 29.

examination. Also, films of useful thickness for optical studies were much too thick for TEM. Finally, no specimen preparation was required to examine the films, other than mounting the substrate with film on a specimen holder. This afforded the ability to examine any type of film regardless of thickness or treatment. The limited resolution of the SEM, initially, was a problem, especially for as-deposited thin films with very small grain size. However, optimization of the technique yielded high magnification SEM micrographs (86,000X with 400 Å resolution).

The typical low magnification structure seen in 1.0  $\mu\text{m}$  thick films deposited at room temperature is shown in Figure 31a. The micrograph shows these films to be of very high quality with very few large defects such as pin holes or cracks. A high magnification micrograph typical of these films are shown in Figure 31b. By making line intercept measurements on Figure 31b, and assuming that the change in contrast from point to point is due to a grain boundary, an average grain size of 480 Å is measured. Although this number is only approximate, this size is nearly twice that measured by TEM observations and is slightly less than the size observed by Martil et al. The difference in size between TEM and SEM observations of the films studied here is greater than the difference in magnification calibration between the two instruments, therefore the difference is most likely due to the fact that the grain size observed at the surface of a thin film is not the same as that observed in the interior. Also, because the SEM micrographs were obtained near the resolution limit of the microscope, there is considerable distortion of the image. The one



a)



b)

Figure 31 SEM micrographs of as-deposited thin film. a) low magnification; b) high magnification showing grain structure.



conclusion derived from SEM micrographs that cannot be readily determined by TEM relates to the lack of flatness on the surface of these films, on this size scale. This may be the result of columnar growth on a very fine scale.

The columnar structure observed by TEM in thin films deposited at  $\text{LN}_2$  temperatures is not readily seen by SEM, as shown in Figure 32. The size of the structure observed in this  $1.0\text{ }\mu\text{m}$  film is greater than the grain size observed by SEM of room temperature deposited films, albeit this is a much lower resolution micrograph so the size may be distorted. By referring back to Figure 26 one can see that the width of the columns is approximately  $500\text{ }\text{\AA}$ . The size measured here is approximately  $800\text{ }\text{\AA}$ , which is similar to the differences between the grain size measured by TEM and SEM on room temperature deposited films. From Figure 32 it is not possible to determine that a semi-amorphous columnar structure is present in this thicker film, which is one drawback of using SEM for microstructure determinations.

Other capabilities of the SEM, however, make the observation of other physical properties possible. The nonuniformities seen in films deposited at temperatures greater than  $200^\circ\text{C}$  are greatly enhanced by imaging backscattered electrons from the film. The energy of backscattered electrons is dependent upon composition, so the contrast observed in the micrograph of Figure 33 is related to the compositional nonuniformities of a film deposited at  $300^\circ\text{C}$ . These results correlate well with those reported by Cook and Christy,<sup>27</sup> who found that deposition above  $200^\circ\text{C}$  yielded poor quality thin films. The large

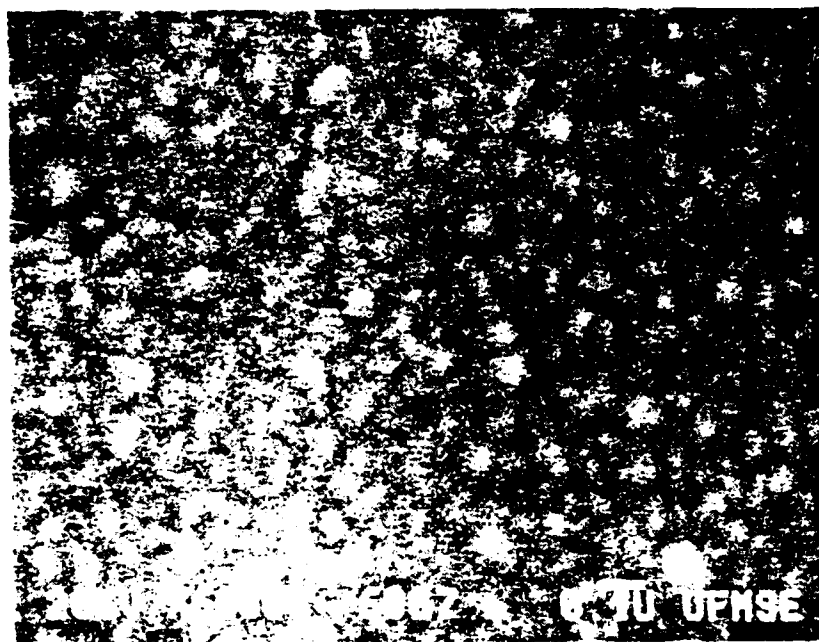


Figure 32 SEM micrograph of thin film deposited at  $\text{LN}_2$  temperatures.

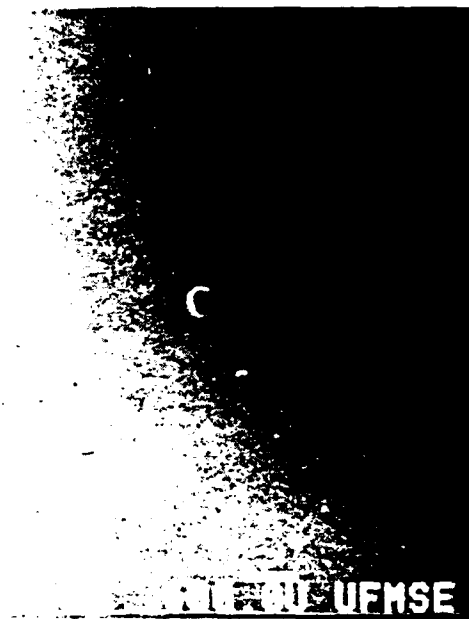
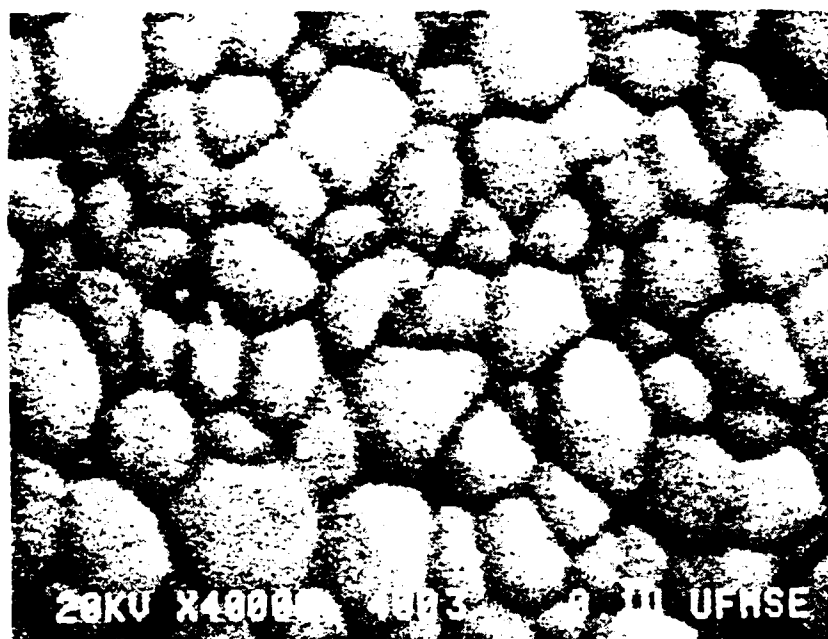


Figure 33 SEM micrograph of thin film deposited at 300° C, backscattered electron image.

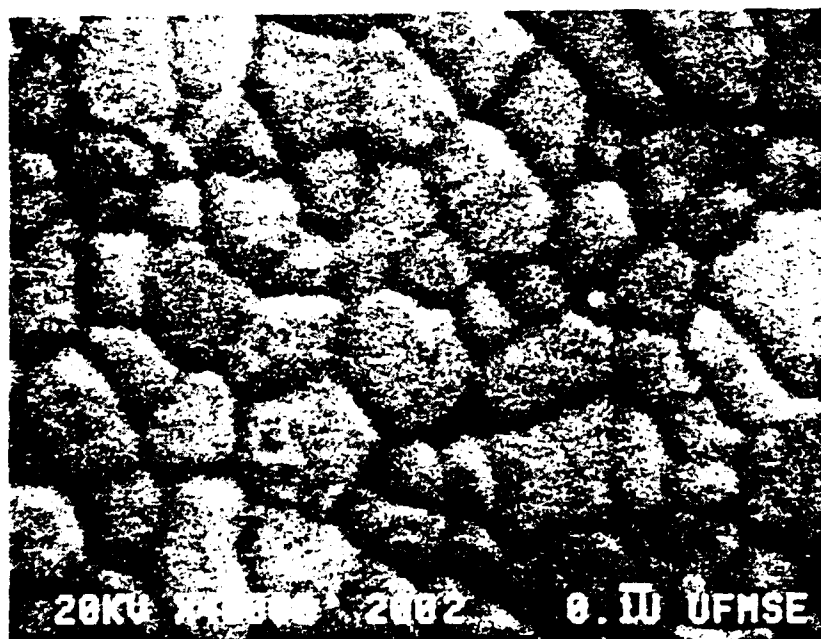
differences in sticking coefficients of cadmium and sulfur at high temperatures is responsible for this result.

Heat treated thin films. Furnace heat treatments similar to those carried out by Martil et al.<sup>41</sup> were used to study the grain growth of thin films, in addition to heat treatments by rapid thermal annealing. Optimum film properties were obtained by furnace heat treating to 500° C for 5 hours, or to 650° C for 4 minutes. Typical microstructures obtained of 8000 Å thick films subjected to these heat treatments are shown in Figures 34a and 34b. The grains appear isotropic with an average size (determined by a line intercept method) of 2850 Å for the 500° C treatment and 3000 Å for the 650° C treatment. These grain sizes are similar to the size observed in the porous network displayed in the TEM micrograph of a very thin film heated to these temperatures (Figure 28). Thermal shock, mismatch of the film and substrate expansion coefficients, or excessive grain growth could be responsible for the cracking of films which is sometimes observed when films are subjected to fast furnace heating rates. This cracking is shown in Figure 35.

From other heat treatments at 200 and 350° C for times of 5 hours, it was found that the grain size exhibited two regions of growth. This is shown in Figure 36, which is a plot of average grain size versus reciprocal temperature, for constant time. The two regions of growth exhibited in the plot are a classical indication that two different mechanisms are responsible for grain growth in these films. At low temperatures the grain growth is slow with a nearly constant rate. This is an indication that grain growth occurs only by grain boundary



a)



b)

Figure 34 SEM micrographs of heat treated thin films. a) heat treated 650° for 4 min; b) heat treated 500° C for five hours.

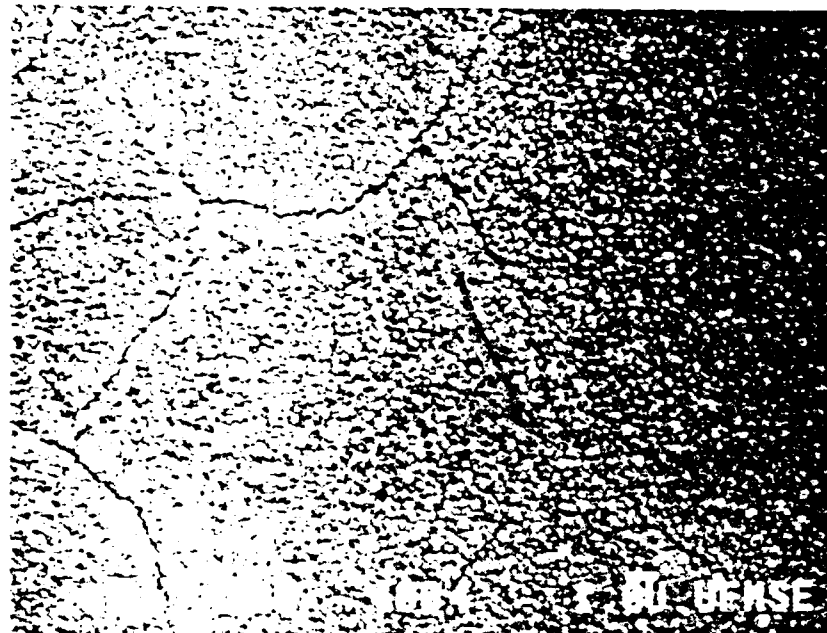


Figure 35 Low magnification SEM micrograph of thin film shown in Figure 34a.

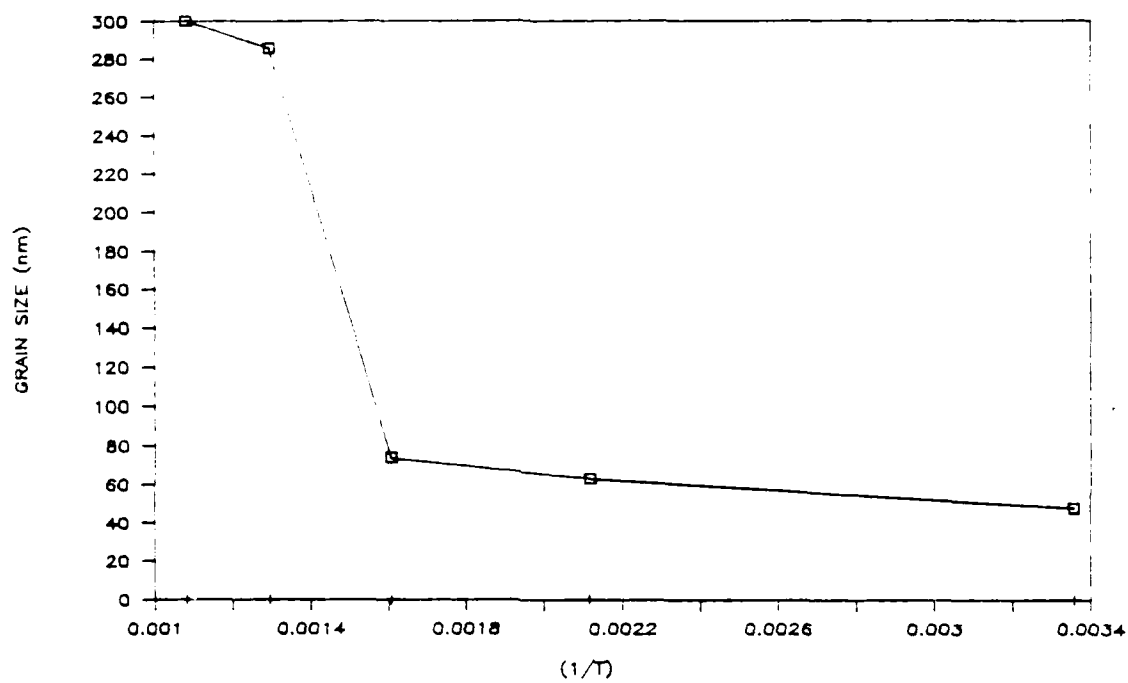


Figure 36 Plot of average grain size versus heat treatment temperature.

diffusion, which is a low energy process. At higher temperatures, enhanced diffusion of impurities at the grain boundaries results in a large increase in grain growth. Grain growth is therefore controlled by the activation energy for impurity diffusion. The curve appears to flatten out at the highest temperatures, which is possibly due to two effects. First, since the film is of a finite thickness, there must be a limit on the maximum size of the grains. Generally the largest grain size obtainable should correspond to the thickness of the film, but when a film is in contact with a substrate, this constraint will depend upon the interface energy between the film and substrate. The more likely effect, however, is due to a loss of material at higher temperatures. Thin films were found to totally evaporate at 800° C in a very short time, even though the sublimation temperature of bulk CdS is 925° C. At 650° C for long times a loss of material was also found to occur which would disrupt the grain growth process.

Although some of the optical properties were optimized by heat treatments to 650° C, the larger grains and cracking of these films increased the amount of light scattering. Rapid thermal annealing (RTA) permitted high temperature treatments for very short times, which resulted in very little grain growth and no cracking of the film. Figure 37 shows a high magnification micrograph of a film that received an RTA treatment at 650° C for 30 sec. The film displays an average grain size of only 900 Å, which is considerably smaller than the size obtained by furnace heat treatments to this temperature. Since this film was subjected to a very large thermal stress, it appears that the



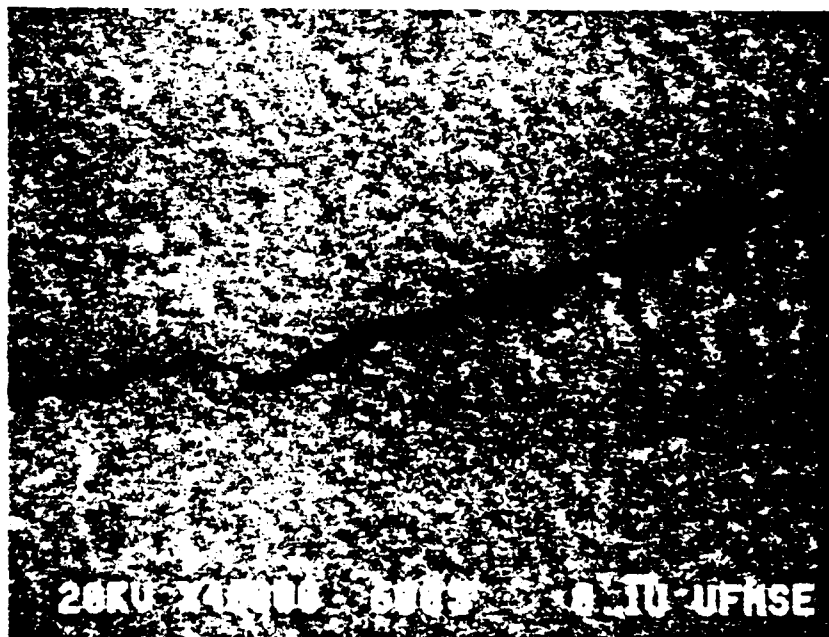


Figure 37 SEM micrograph of thin film subject to rapid thermal anneal (RTA) heat treatment.

cracking seen in the furnace heat treated films is a result of the large and rapid grain growth that occurs.

#### X-ray diffraction experiments

Diffraction spectra. Although SEM observations gave an indication of microstructure morphology of thicker films, the technique did not provide any crystal structure information. To determine the crystallography of thicker films X-ray diffraction (XRD) was used. The computer controlled diffractometer used for these measurements greatly facilitated the determination of microstructure changes with heat treatment, as well as permitting quantitative analysis of X-ray spectra. Programs for calculating diffraction peak line broadening due to strain and size effects and for calculating precision lattice constants were available with this system.

The diffraction spectra obtained from films 8000 Å thick, deposited at three different temperatures are displayed in Figure 38 and the diffraction spectra obtained after heat treating these films are shown in Figure 39. Many of the features observed in SAD patterns are evident in these X-ray diffraction patterns. The broad band peak centered at  $\approx 20^\circ$  in all patterns is due to amorphous scattering from the substrate.

In Figure 38a, of a film deposited at  $LN_2$  temperatures, the amorphous peak is much more intense and the intensity of the (0002) peak is considerably reduced. This supports the results obtained from TEM analysis that the structure of these films is highly disordered, but there is some indication of crystallinity. After heat treatment,

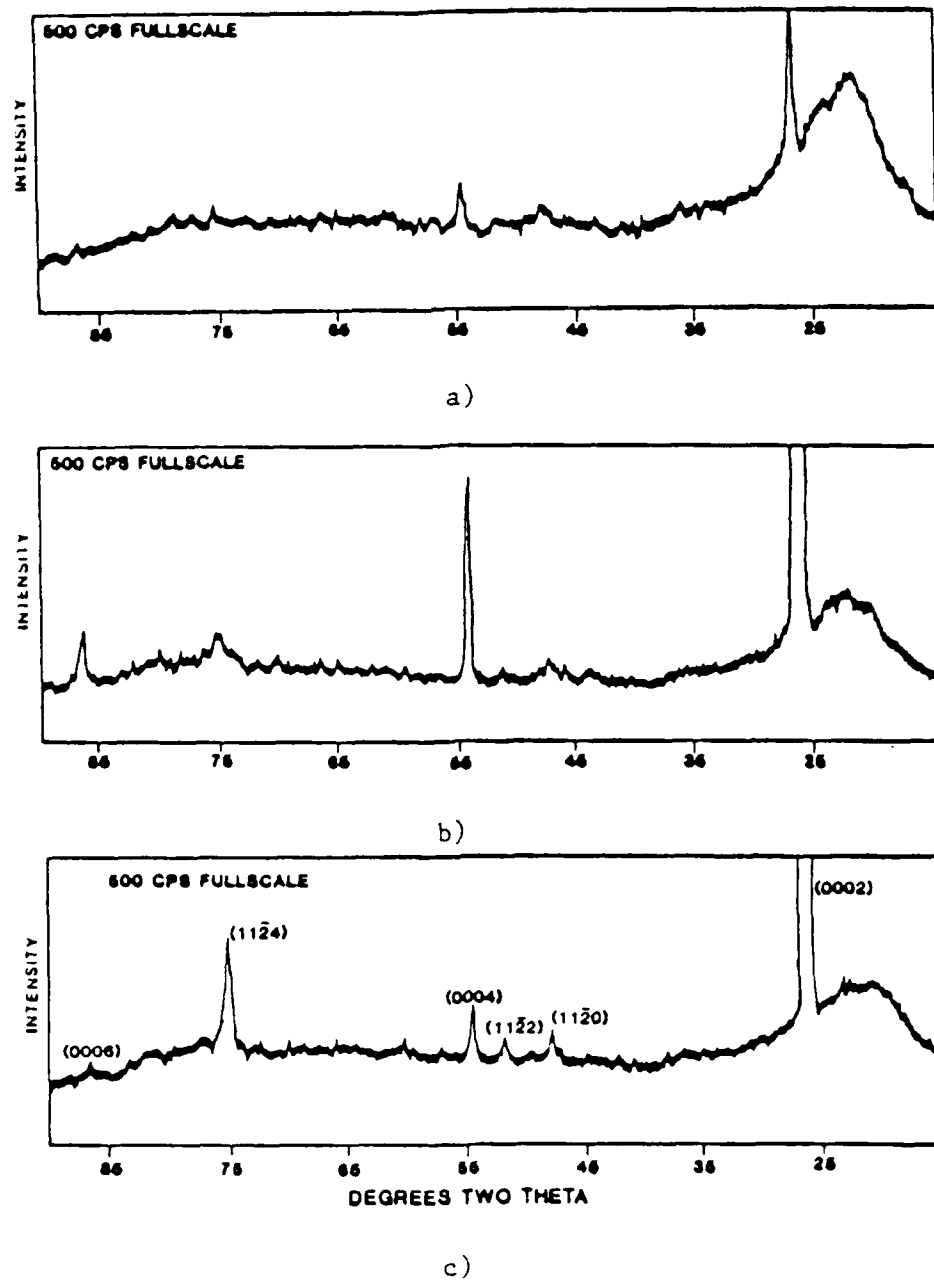
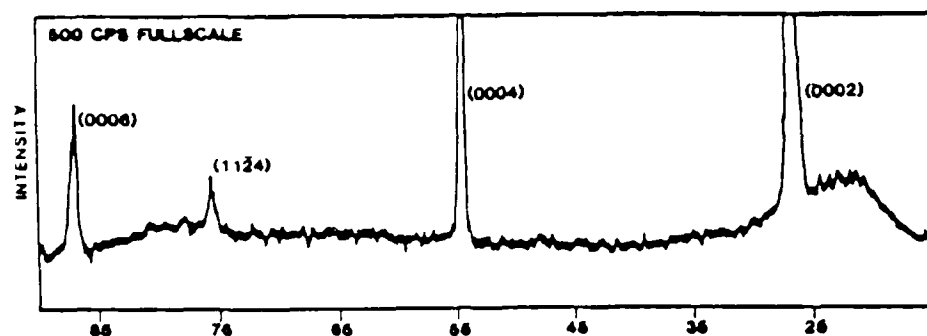


Figure 38 X-ray diffraction patterns of as-deposited thin films. a) deposited at LN<sub>2</sub> temperatures; b) deposited at room temperature; c) deposited at 300° C.

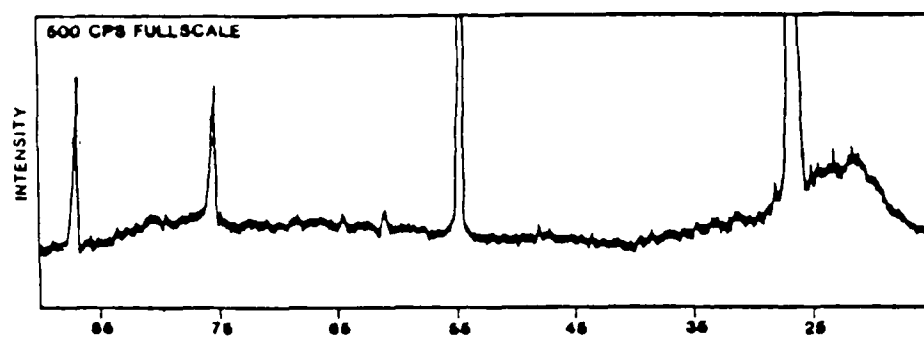
Figure 39a shows the amorphous peak to be greatly reduced and crystallization has taken place with the strong cubic preferred orientation.

Figure 38b shows that films deposited at room temperature exhibit a strong cubic preferred orientation which is shown by diffraction at (0001) where  $l=2,4,6$ . The other hexagonal lines seen in SAD patterns are not as readily observable in this pattern, particularly the other two lines which are closely spaced to the (0002) peak. Those two lines were clearly resolved in SAD patterns, but appear to be totally absent here. This shows how much more sensitive electron diffraction is to the local crystal structure. When this film is heat treated, the preferred orientation is maintained as shown in Figure 39b. All diffraction peaks become much narrower and more intense, as an indication of grain growth. Figure 39c indicates that when this film is heat treated to an even higher temperature, the orientation is maintained, but the intensity of other hexagonal diffraction lines is increased.

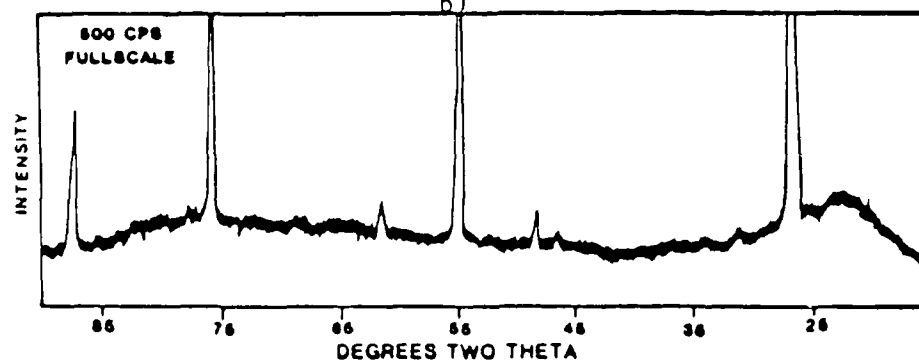
The most predominant hexagonal lines are seen in the XRD pattern obtained from a film deposited at 300° C, shown in Figure 38c. Again a preferred orientation is indicated, but other hexagonal lines are shown to occur in a different ratio to the cubic lines, which indicates there is another orientation present. This second orientation was not observed in the TEM analysis because the film examined was deposited at 200° C. It appears this orientation only occurs at higher temperatures.



a)



b)



c)

Figure 39 X-ray diffraction patterns of heat treated thin films from Figure 38; a) film of Figure 38a, heat treated 500° C, one hour; b) film of Figure 38b, same heat treatment; c) film of Figure 38b, heat treated 720° C, ten minutes.

Strain determinations. Residual strain in thin films can be manifested as both a shift and a broadening of X-ray diffraction lines. However, broadening of X-ray lines due to strain will only occur if a nonuniform microstrain is present (usually due to plastic deformation). Broadening usually is a result of a very small grain size. Digital manipulation of the diffraction data permitted determination of peak broadening due to nonuniform strain and grain size effects by use of an utility program available in the APD computer. The computer program, however, does not calculate the uniform strain which would produce a shift in peak positions. Residual uniform strain was determined by comparing the position of the (0006) diffraction line in thin films to the position observed in a powdered sample of CdS. By differentiating Bragg's law, the change in lattice parameter due to a uniform strain was calculated from the shift observed in the peak positions.<sup>62</sup> Figure 40a shows a comparison of the broadening and peak position seen in films deposited at two different rates and the line width and position which results when these films are fully annealed. The tick mark shows the position of the (0006) line of the powdered sample. The calculated uniform strain which would produce the observed line shifts and the effective mean nonuniform strain and effective mean grain size that would produce the broadening are listed in Table 2. Also shown are the values which would cause the broadening if only grain size effects were present.

Thin films were considered to be uniformly strained, therefore the results calculated by the APD program for nonuniform strain are not considered relevant. The grain size effects listed in the last column

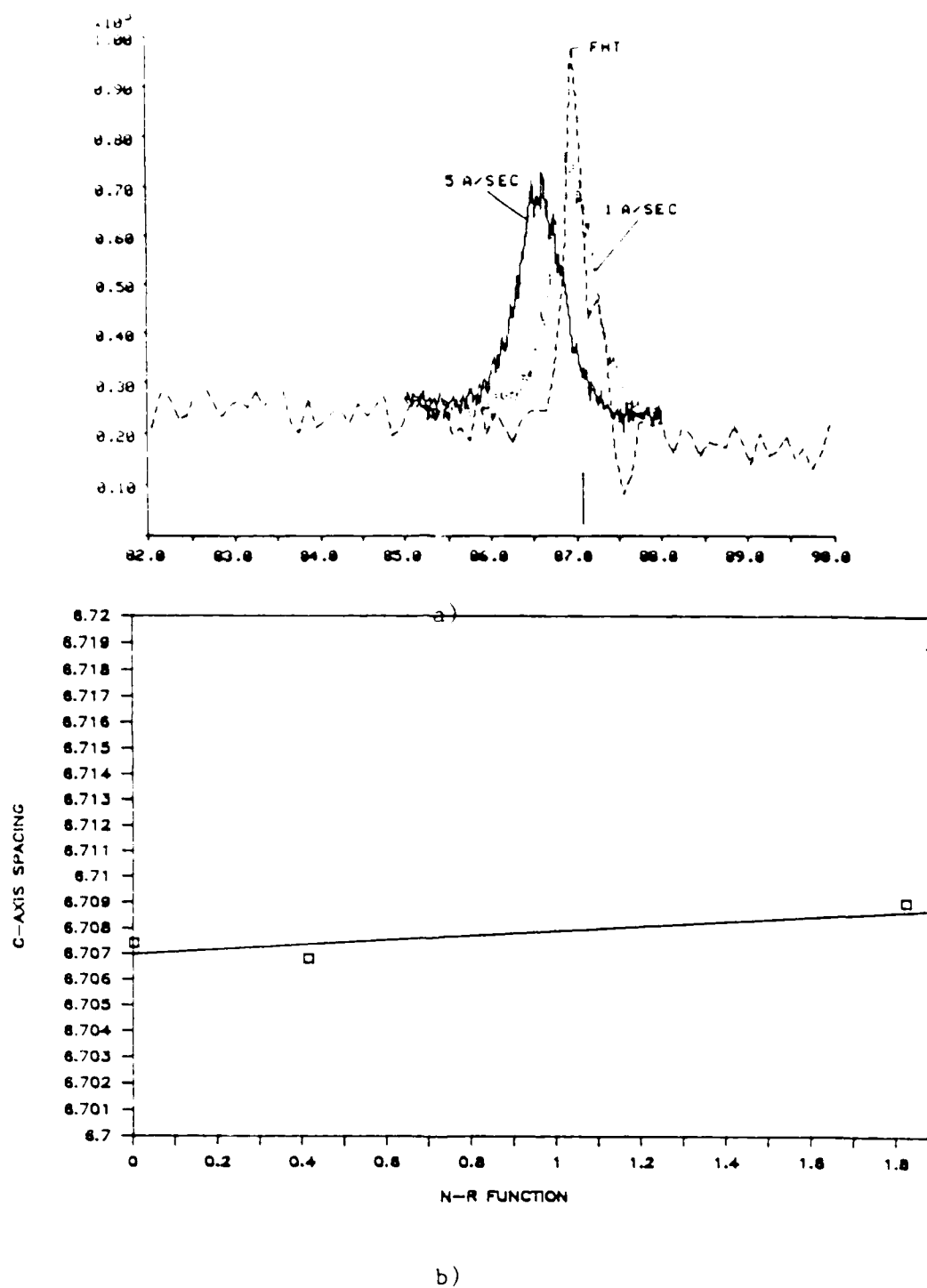


Figure 40 Analysis of X-ray diffraction spectra. a) (0006) X-ray diffraction peak of two as-deposited and one furnace heat treated thin films showing position shift and broadening due to strain and grain size effects; b) plot of c-axis lattice parameter versus Nelson-Riley function for precision lattice determination.

TABLE 2

Calculated strain and size effects which would produce the X-ray line shifts and broadening observed in diffraction patterns

| Sample       | Effective<br>Nonuniform<br>Mean Strain <sup>1</sup><br>% | Effective<br>Mean Size <sup>1</sup><br>Å | Calculated<br>Uniform<br>Strain <sup>2</sup><br>% | Size<br>Effects<br>Only <sup>3</sup><br>Å |
|--------------|--|--|---|---|
| ASDP 1 Å/sec | 0.189  | 1148.7                                   | 0.16  | 252.7                                     |
| ASDP 5 Å/sec | 0.179  | 1983.6                                   | 0.39  | 284.3                                     |
| FHT 650 C    | 0.041  | 2528.0                                   | 0.08  | 1005.2                                    |
| RTA 650 C    | 0.122  | 837.8                                    | 0.12  | 332.6                                     |

Key: ASDP - as-deposited; FHT - furnace heat treated;  
RTA - rapid thermal anneal. Heat treated films were deposited at  
1 Å/sec

<sup>1</sup>Calculated with utility program available in APD computer. Mean values are given which would combine to cause the observed broadening.

<sup>2</sup>Calculated from shift in X-ray line position.

<sup>3</sup>Calculated with utility program available in APD computer. Values of grain size which would produce the observed broadening.



of the Table do, however, correlate closely to grain size observed by TEM for as-deposited thin films. The shift of the higher rate film to a smaller two-theta value indicates the presence of a tensile stress. Higher stress levels in higher rate films may be due to growth related defects and the inclusion of impurities. The higher stress level in these films causes the film to exfoliate within several hours after exposure to the atmosphere. Figure 41a shows an optical micrograph of a film exhibiting the onset of this exfoliation, and Figure 41b displays the appearance of a film after several days of exposure. The appearance of the exfoliation shown in Figure 41a is characteristic of a tensile stress. Exposure to atmosphere leads to the absorption of water on the film surface, which apparently increases the stress to a value large enough to cause the film to break away from the substrate. Some type of stress related corrosion process may also contribute to this result. Lower deposition rate films were found to be stable with exposure to the atmosphere indefinitely, so X-ray line shift due to uniform strain was expected to be less.

Precision lattice constant. A calculation of the precision lattice constant of heat treated thin films was made from the positions of diffraction peaks measured from thin films. Due to the strong preferred orientation only the c-axis lattice constant could be determined and because small two-theta values had to be used, the calculated lattice parameter was plotted versus the Nels. -Riley function.<sup>63</sup> The plot shown in Figure 40b indicates an extrapolated lattice parameter of  $c_0 = 6.707 \text{ \AA}$ , which is 0.09% less than the JCPDS card file value of  $6.713 \text{ \AA}$ .<sup>63</sup>



a)



b)

Figure 41 Optical micrographs of exfoliated thin film, 100X magnification. a) after four hours exposure to atmosphere; b) after two days exposure.

### Compositional Analysis

#### Stoichiometry determination of target material

The first parameter needed to establish the composition stoichiometry of thin films was the composition of the target material from which films were made. Once this composition was determined, the target material could be used as a standard for all other analytical techniques. Both induction coupled plasma (ICP) and electron probe microanalysis (EPMA) were used to determine the stoichiometry of the target material. These two techniques are by far the most quantitative because the results are determined by comparison to known standards. Additional measurements were made by standardless techniques which rely on sensitivity factors for quantitative analysis, such as: X-ray photoelectron spectroscopy (XPS) and Auger electron spectroscopy (AES). The manufacturer of the target material claimed the composition to be slightly sulfur rich, but as can be seen Table 3, both ICP and EPMA data indicate the target material to be slightly cadmium rich, although the variation is within a few standard deviations of each other. In either case the results indicate the target material to be stoichiometric to 0.50 %, which for the other analytical techniques used to measure thin films, is an acceptable variation. XPS gives a result that is very close to the expected value; however, AES shows a very large difference from the other results which demonstrates that the technique is not useful for determining absolute concentrations, but as described below, the technique is very sensitive for determining differences between samples.

TABLE 3

Concentrations in atomic percent of cadmium and sulfur  
found in target material

| Analytical<br>Technique | Cd concentration | S concentration |
|-------------------------|------------------|-----------------|
| ICP                     | 50.96 +/- 0.09   | 49.04 +/- 0.12  |
| EPMA                    | 50.33 +/- 0.21   | 49.67 +/- 0.21  |
| XPS                     | 51               | 49              |
| AES                     | 60.7             | 39.3            |

The results for the four different analytical techniques used for determining the composition of thin films are listed in Table 4. The absolute values of the sulfur and cadmium concentrations are shown to vary greatly between different techniques; however, the difference between as-deposited and heat treated thin films is nearly the same in each case, except for the XPS results. Films that were heat treated to 650° C were used because of their use for optical properties studies. They were also found to show the greatest difference. The discrepancy in the XPS results for heat treated thin films and the implications of the results of the other techniques will be discussed below. The primary indication of these results, however, is that as-deposited thin films contain  $\approx 2\%$  excess sulfur and once they are heat treated, this excess increases to  $\approx 4\%$ . As indicated by the precision lattice parameter described above, the unit cell of heat treated thin films is very close to the ideal structure of CdS, so very little of this excess sulfur is interstitial, or very few cadmium vacancies are present. This means that the sulfur must be a second phase.

#### Analytical techniques

Use of electron probe microanalysis (EPMA) for determining the composition of thin films was first thought to be the best method and most quantitative, for the same reasons stated above. Not even qualitative results, however, could be obtained. The standard ZAF or  $\rho\rho z^{40}$  programs used to calculate composition consistently gave results of less than 100 weight percent for the composition of thin films. Even a thin film program which relies on some approximations, did not

TABLE 4

Comparison of results from different analytical techniques  
used to determine the composition of thin films

| Analytical<br>Technique | As Deposited<br>Atomic % |            | Heat Treated<br>Atomic % |            |
|-------------------------|--------------------------|------------|--------------------------|------------|
|                         | Cd                       | S          | Cd                       | S          |
| EDS                     | 47.7                     | 52.3       | 46.8                     | 53.2       |
| XRF                     | 44.6                     | 55.4       | 43.1                     | 56.9       |
| XPS                     | 50.6                     | 49.4       | 70.9                     | 29.1       |
| AES                     | 37.3(47.6)               | 62.7(52.4) | 35.7(46.0)               | 64.3(54.0) |

produce a reasonable result. It could not be determined if there was a problem with the software or the instrument. Even if EPMA results could have been obtained it would have been impractical to analyze every film produced and every heat treatment studied.

X-ray fluorescence was originally considered to be the best technique for the general analysis of thin film composition for several reasons: 1) the intensities of the X-ray fluorescence lines should be directly proportional to the amount of material present in the thin film, 2) high peak intensities gave a large signal to noise ratio, 3) no sample preparation was necessary and analysis was quick (typically 15 minutes), 4) film thickness could be readily determined and 5) the results were found to be very reproducible. Different films that were deposited under exactly in the same conditions and heat treated exactly the same way were found to give nearly the same peak intensities for the cadmium and sulfur lines. An example of this reproducibility is shown in Figure 42 which shows peak intensity and integrated peak intensity ratios for several identical samples. A problem with the technique occurs if a linear correlation factor is used to calibrate the XRF spectra obtained from thin films: the amount of sulfur appears to be too high, when compared to the other techniques. The correlation factor is based on the ratio of the intensities of the cadmium and sulfur lines obtained from the target material, assuming a stoichiometric composition for the target. One possible explanation for the high value is that a matrix effect that alters the ratio of the X-ray lines measured for the target material may not occur in a thin

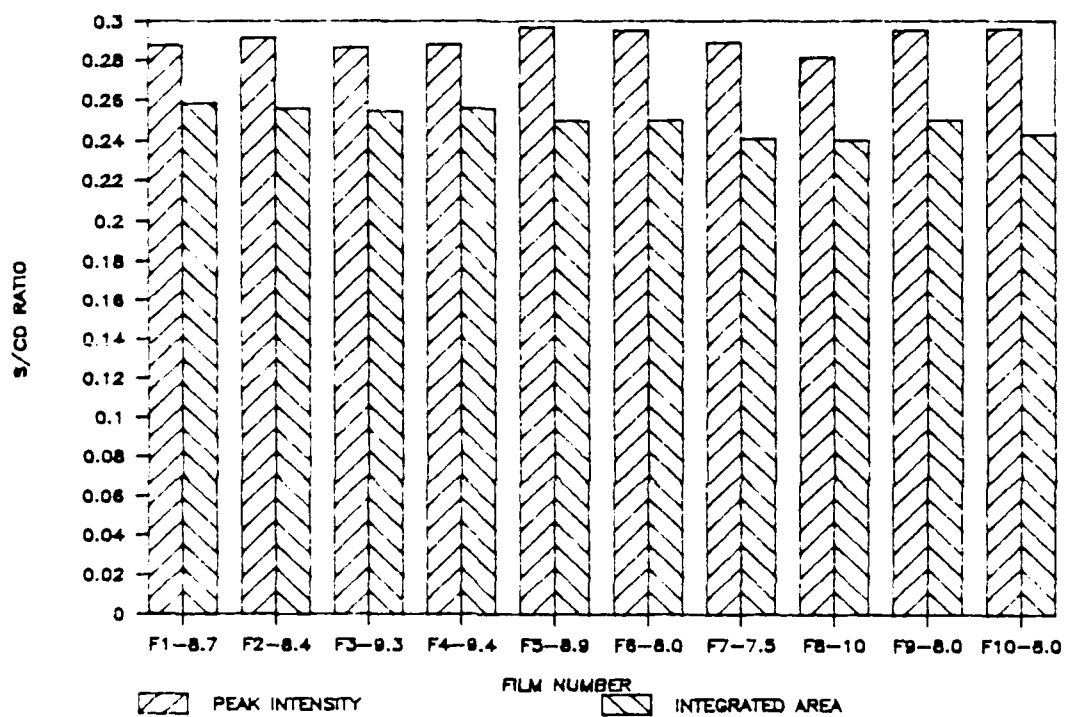


Figure 42 X-ray fluorescence sulfur to cadmium peak ratios for several identical thin films.



film, which would lead to an incorrect correlation factor and incorrect estimation of the composition of thin films.

The reproducibility obtained by XRF could not be accomplished by energy dispersive spectroscopy (EDS) obtained during SEM observations. This was primarily due to the inability to measure the specimen current of the electron beam used to generate secondary electrons for imaging and X-rays for composition analysis. Widely different intensity values were often obtained from the same sample when measured at different times. This problem was alleviated to some degree by mounting a piece of target material on each sample mount so that the intensities of the X-ray lines obtained from thin films could be normalized to a standard. A hole was drilled in the sample mounts so that the surface of the target material would be level with the substrates and geometric differences would be reduced. Again, a correlation factor was used to calculate the composition of thin films based on the intensities of the X-ray lines measured from the target material. The matrix effect that might occur in XRF would be less pronounced in EDS, because the electron penetration depth that generates X-rays is much less than the X-ray line that produces the secondary fluorescence in XRF.

The absolute values of the composition obtained by Auger electron spectroscopy (AES) are considered to be reasonable since the accuracy of the technique is limited to  $\pm 30\%$  when published values of the sensitivity factors are used.<sup>57</sup> However, since very similar values for the composition of the target material were obtained, a very simple correction factor can be applied to the sensitivity factors to give the correct results. The corrected concentrations are given in parenthesis

in Table 4, and they show comparable results to the other techniques. Typical AES spectra obtained from target material and heat treated thin films are shown in Figure 43a and 43b. The shape of the peaks are qualitatively the same, although the heat treated spectrum has been shifted to higher energy due to a charging effect. The difference between the ratios of the Cd peak-to-peak distance to the sulfur peak-to-peak distance gives a quantitative indication of the difference in the concentration of cadmium in the two samples. AES should be very quantitative for measuring the differences between similar samples, so the values obtained most likely represent the true difference, although this technique does not indicate how the sulfur exists in the structure.

To attempt to determine the chemical state of the sulfur, X-ray photoelectron spectroscopy (XPS) was used. This technique is very sensitive to changes in the binding energy of core electrons, which reflects changes in the local chemical environment.<sup>58</sup> The presence of significant concentrations of free sulfur, would either shift the sulfur lines, split, or broaden them. A high resolution scan of the sulfur 2p transition for an as-deposited (ASDP) and a furnace heat treated (FHT) thin film are shown in Figure 44. Both films were deposited at room temperature and at a rate of 1 Å/sec. Very little shift is observed and no significant broadening is seen. The position of the 2p transition for free sulfur would be at a binding energy of 165 eV. The only unique feature is the two shake-up peaks, labeled SU and both of these show very little shift in energy. The satellite peak labeled SAT is an artifact peak and has no meaning.

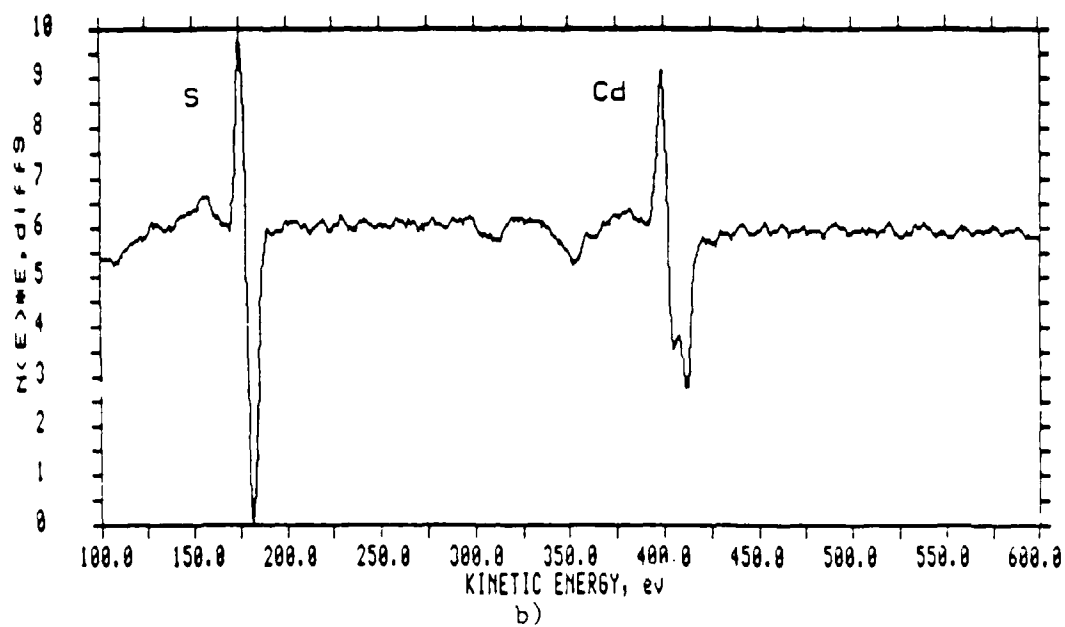
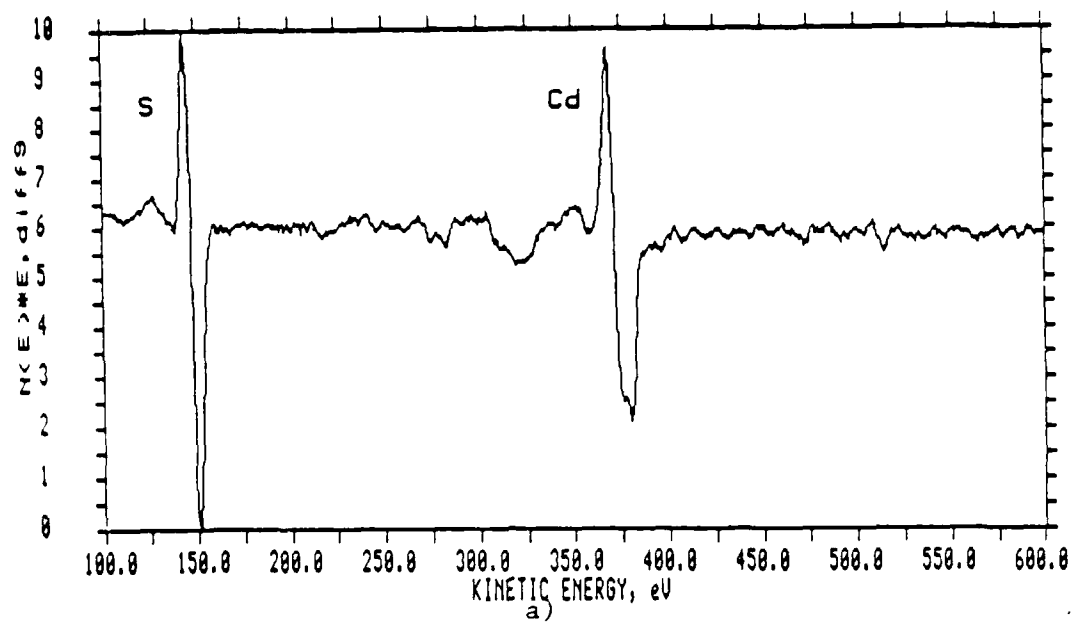


Figure 43 Auger electron spectroscopy survey scans. a) Target material; b) heat treated thin film.

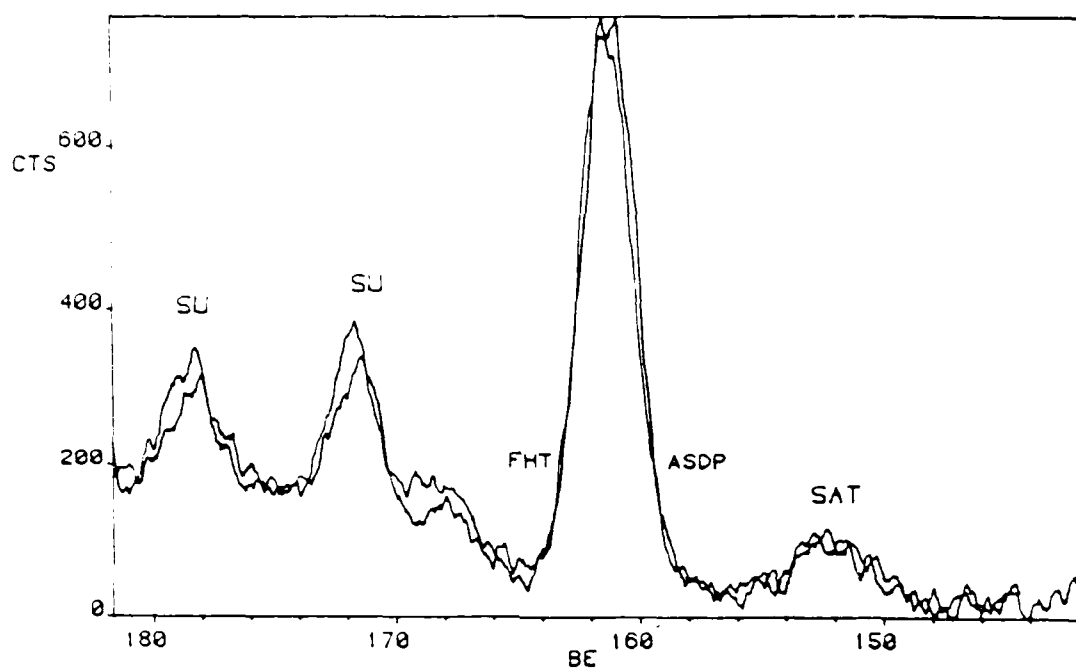


Figure 44 X-ray photoelectron spectroscopy (XPS) high resolution scan of sulfur 2p peak, exhibited by an as-deposited (ASDP) and a furnace heat treated (FHT) thin film. Heat treated thin film peak shifted slightly to higher binding energy. Shake-up peaks are indicated by SU and satellite peak is marked SAT.

As indicated in Table 4, there is significant differences between as-deposited and heat treated thin films. The concentration calculations in XPS are based on quantification factors and on integrated peak intensities. Since the factors are constants, the result presented in Table 4 indicate that the integrated area of the cadmium peak has nearly doubled in heat treated films as compared to as deposited. A high resolution scan of the cadmium 3p5 and 3p3 transitions is shown in Figure 45. Surprisingly there is a significant shift in the peak position in addition to a broadening. By comparison to published XPS spectra on cadmium compounds<sup>59</sup> this shift could possibly correspond to cadmium bonded to oxygen. The survey scans displayed in Figure 46 and Figure 47 exhibit oxygen 1s peaks in both films and the peak appears to be more intense in the heat treated film (compare the height of the O 1s peak to the Cd 3p3 peak). Figure 48a displays a high resolution scan of the oxygen peak and Figure 48b shows the same scan after a one minute sputter etch, which removes approximately 100 Å. The large reduction in the intensity of this peak after sputtering is an indication that a thin oxidized surface layer is present. Unfortunately, a high resolution scan of the Cd 3d peaks was not acquired after the sputter etch to determine if the shift in the peak position is due to the oxidized surface layer. Analysis was performed on a second XPS instrument (Perkin-Elmer) which was equipped with a sputter gun. The results for a heat treated film before and after a one minute sputter etch are shown in Figure 49. Several differences between this spectrum and the spectrum obtained with the Kratos XPS can be observed. First, the 3d peaks in Figure 49 are

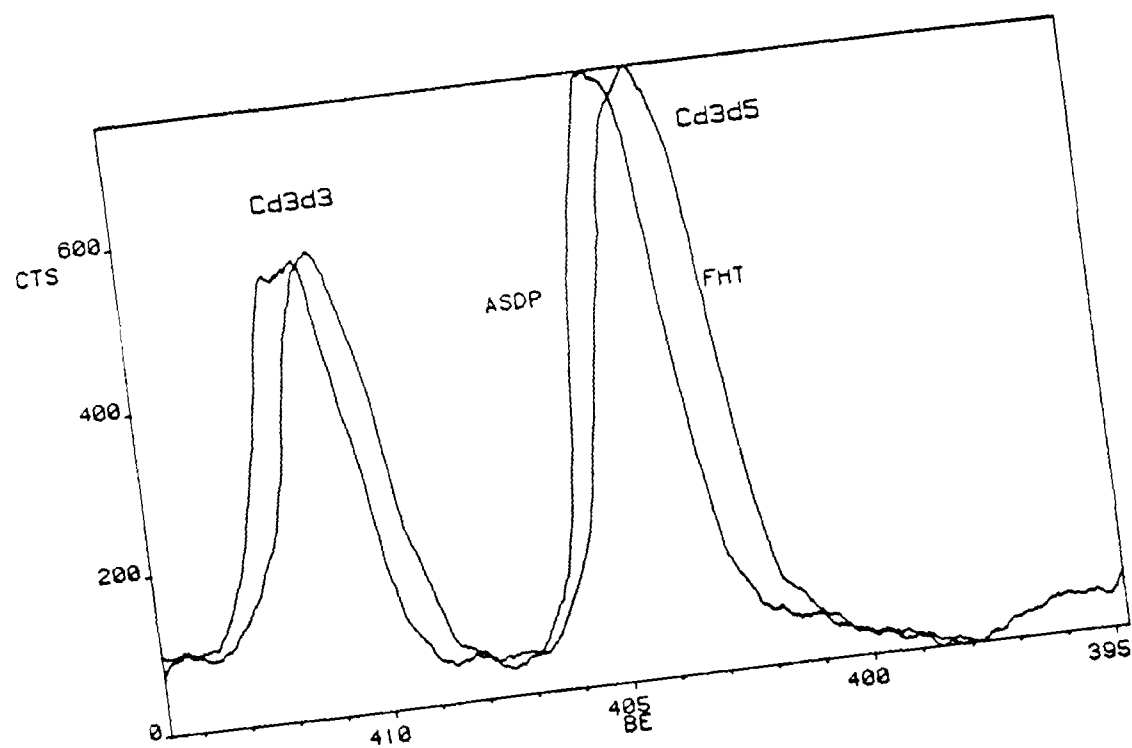


Figure 45 XPS high resolution scan of cadmium 3d3 and 3d5 peaks of an as-deposited (ASDP) and furnace heat treated (FHT) thin film.

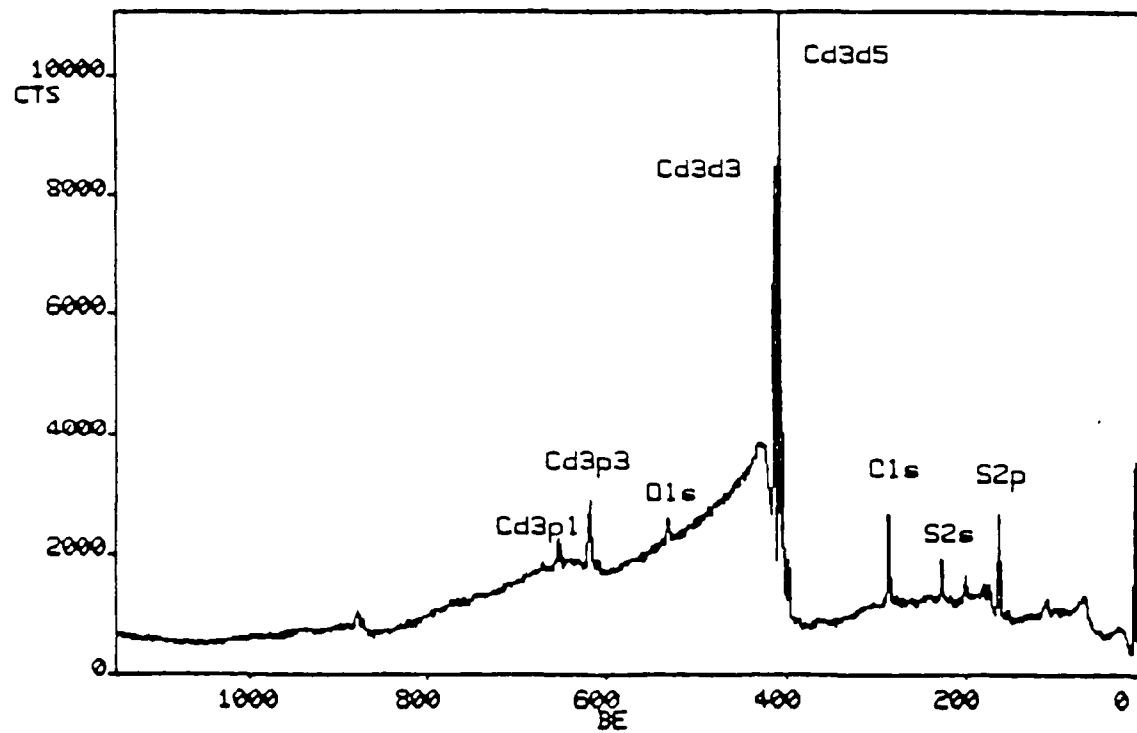


Figure 46 XPS survey scan of as-deposited thin film.

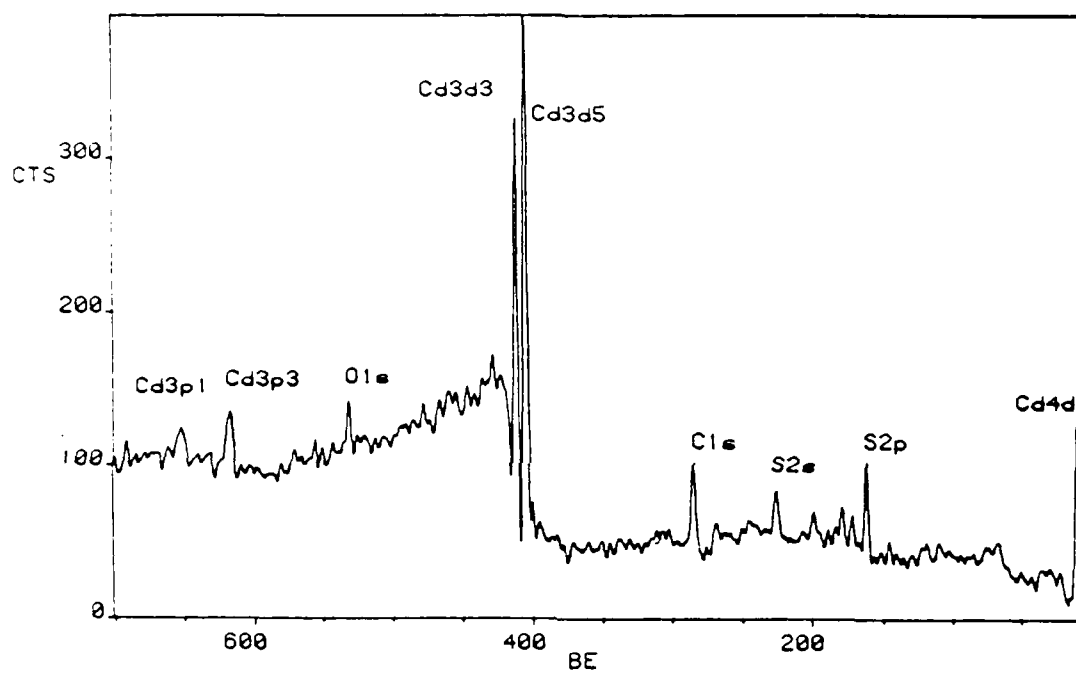
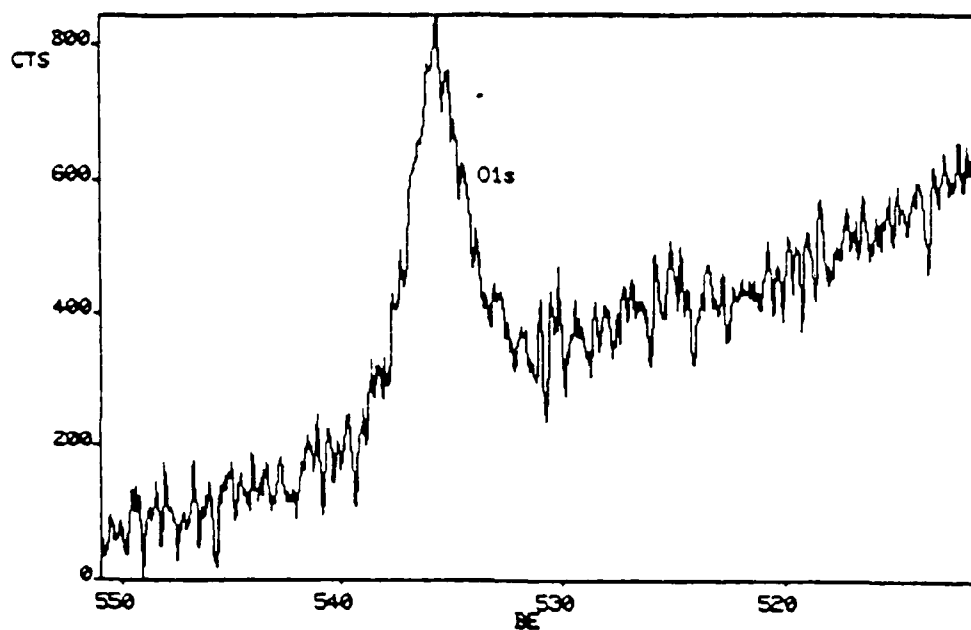
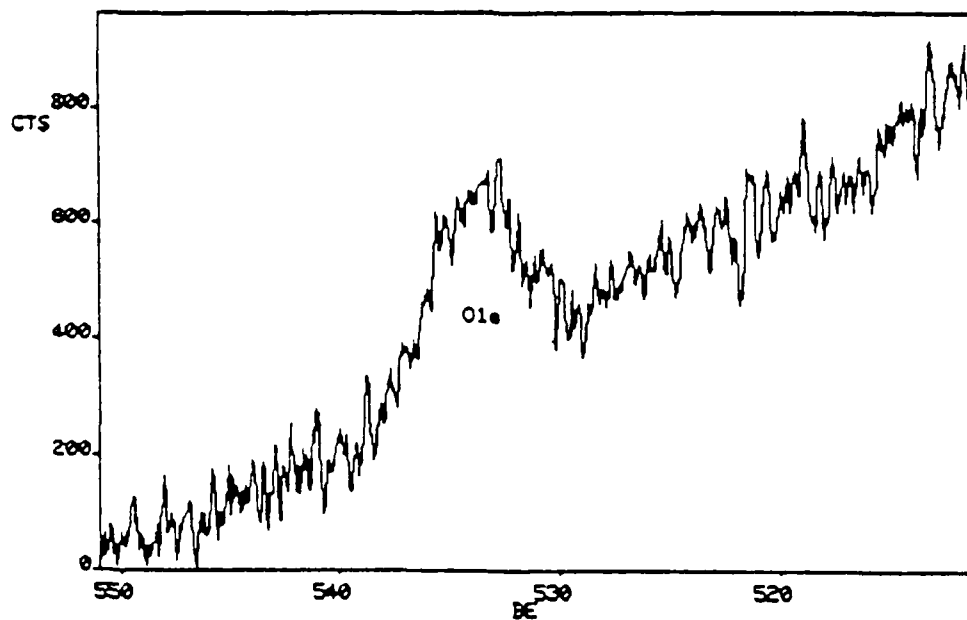


Figure 47 XPS survey scan of furnace heat treated thin film.





a)



b)

Figure 48 XPS high resolution scans of oxygen 1s peak. a) furnace heat treated thin film; b) after one minute sputter etch.

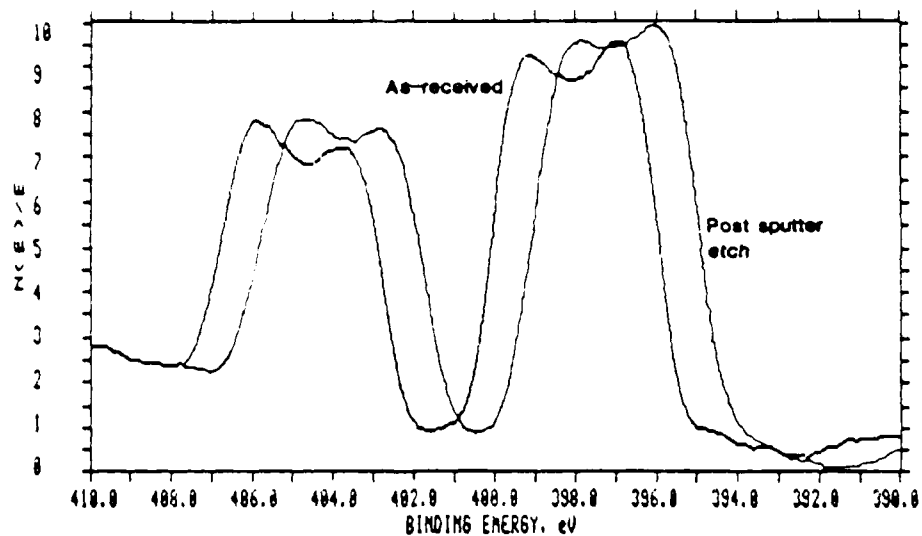


Figure 49 XPS high resolution scan of cadmium 3d3 and 3d5 peaks obtained from Perkin-Elmer instrument. Spectrum are of a heat treated thin film, as-received and after a one minute sputter etch.

nearly twice as wide as the peaks seen in Figure 45. Second, the peaks are shifted to lower binding energy and third, a very definite doublet peak is observed. The first two differences may be due to charging effects. Charging was not observed in the Kratos spectrum (Figure 45) because a low energy electron flood gun was used to compensate the build-up of static charge.<sup>58</sup> The clear resolution of a doublet that was not resolved in Figure 45 is, however, an anomalous result. Also, unexpectedly, the Cd peaks have shifted in the opposite direction after the sputter etch. This may be due to preferential sputtering of the sulfur, so that more metallic cadmium is present. It may also be due to a change in grounding potential, which would effect the static charge built-up on the sample.

Apparently XPS is not sensitive enough to determine if the small amount of excess sulfur present in thin films exists as a distributed second phase. The final technique that was used to determine this distribution is X-ray mapping. Although this type of X-ray analysis by EPMA would have been the most quantitative, the probe size used in the EPMA is not small enough to spatially resolve the grain boundaries of thin films, which is where the sulfur is most likely to exist. By using EDS X-ray mapping with the SEM, high spatial resolution could be obtained. Simultaneous maps of sulfur and cadmium were acquired at a magnification of 20,000X, which represented about 150 grains. A low energy electron beam of 10KV was used to reduce the volume of material sampled and a high density 256 x 256 image, with 8 bit resolution, and a 200 msec dwell time was used to generate the X-ray maps. Even at this high magnification, if the cadmium and sulfur were evenly

distributed, an image with very little contrast should result. The area sampled is displayed in Figure 50, which is a digitized SEM image. The contrast that is observed is due to the grain boundaries of the surface grains and can be compared to the contrast observed in a normal SEM micrograph, shown in Figure 39. Figure 51a shows that the cadmium map has a low even contrast, but the sulfur map shown in Figure 51b is highly mottled, indicating an uneven distribution of sulfur. This indicates that the sulfur is distributed as a second phase, at the grain boundaries.

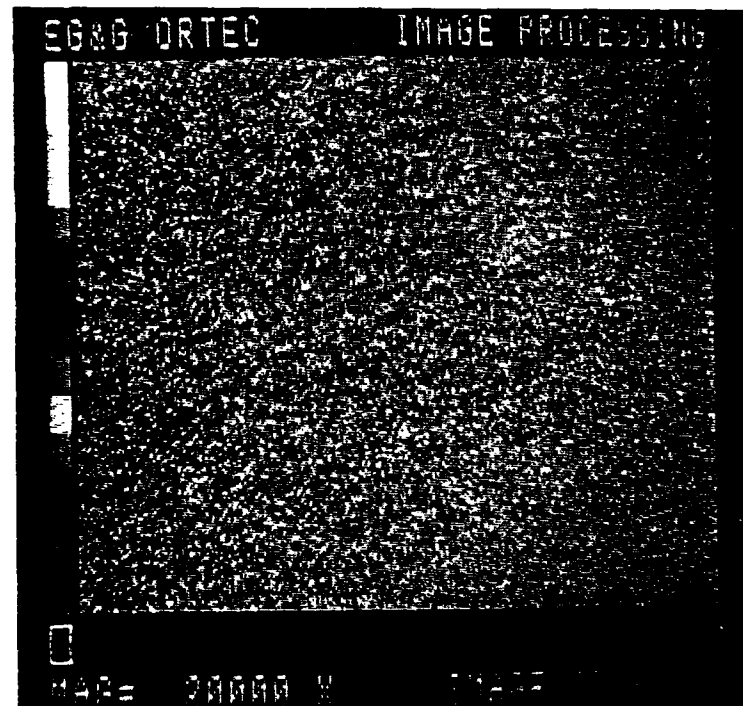
#### Co-Sputter Alternating Deposition

##### Microstructure

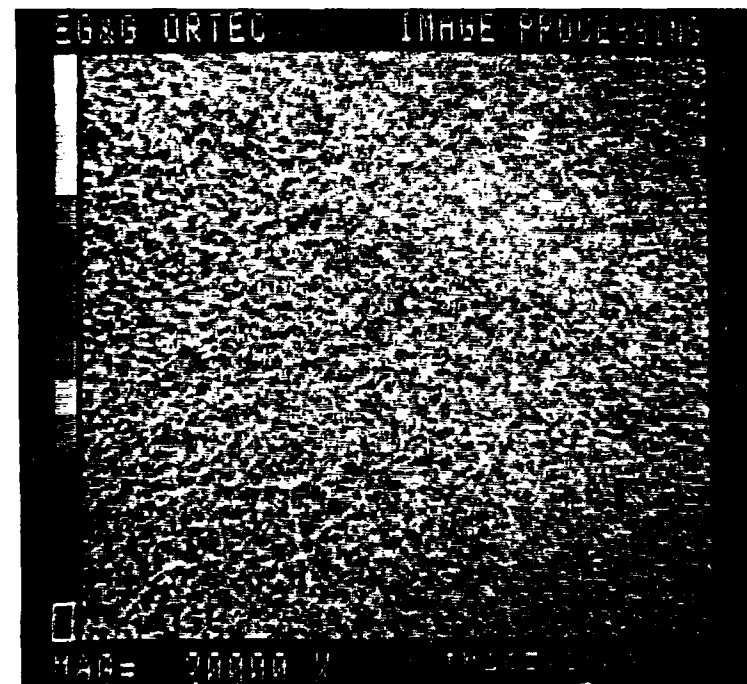
The purpose of making COSAD films was to produce a two phase structure, in which very small crystallites of CdS are embedded in a glass matrix. The intent of this phase of the research was to determine if a structure could be produced in a thin film with small semiconductor microcrystallites isolated in a dielectric matrix with the crystals small enough for quantum confinement. Thin films made by COSAD were therefore primarily analyzed by transmission electron microscopy, since the required size of the crystallites was less than 100 Å. By changing the ratio of deposited CdS to glass different structures could be produced. The most stable films were those made with a small ratio of CdS to glass, while films made with equal ratios were found to phase separate during examination in the TEM. An example of the two extremes of the variation that could be produced will be described here.



Figure 50 Digitized image from scanning electron microscope, secondary electron image.



a)



b)

Figure 51 Digitized element maps. a) high magnification cadmium X-ray map; b) high magnification sulfur X-ray map.

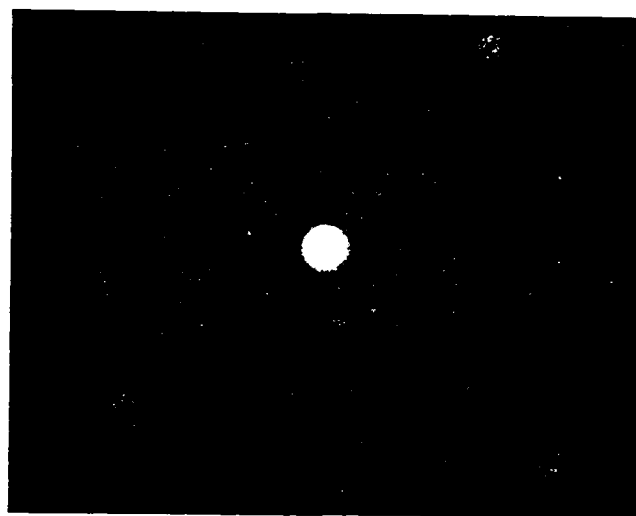
COSAD films with equal proportions of semiconductor and glass were the first to be produced. These films will be referred to as COSAD1. A representative film which was deposited onto a carbon support film is shown in Figure 52a. The structure appears very indistinct and appears to be amorphous, but the SAD pattern shown in Figure 52b indicates there is some crystallinity in the structure. If the electron beam is condensed on this type of film, the structure is found to phase separate very quickly, as displayed in Figure 53a. The SAD pattern in 53b shows that a significant amount of crystallization has occurred and the pattern indicates a hexagonal CdS non-oriented crystal structure.

If this type of film is furnace heat treated a significant change in microstructure also occurs. Heat treating to 500° C results in total phase separation and the growth of spherical shaped CdS crystallites, with an average size of 300 Å. This structure is shown in Figure 54. By heating this type of film to 650° C, these crystallites are found to grow and form a fairly evenly dispersed bimodal size distribution microstructure, which is shown in Figure 55a. The average size of the larger spherical crystals is 700 Å and the smaller crystallites have an average size of 200 Å. The SAD pattern for this structure is shown in Figure 55b. All the reflections for hexagonal CdS are present, in addition to some reflections for an unidentified phase. Because these reflections are so closely spaced in the pattern, it was not possible to determine their source by dark field imaging. A typical dark field image obtained from the inner most diffraction rings is shown in Figure 56. The bright crystals in the image are those which are properly oriented for diffraction and as can



50 nm

a)



b)

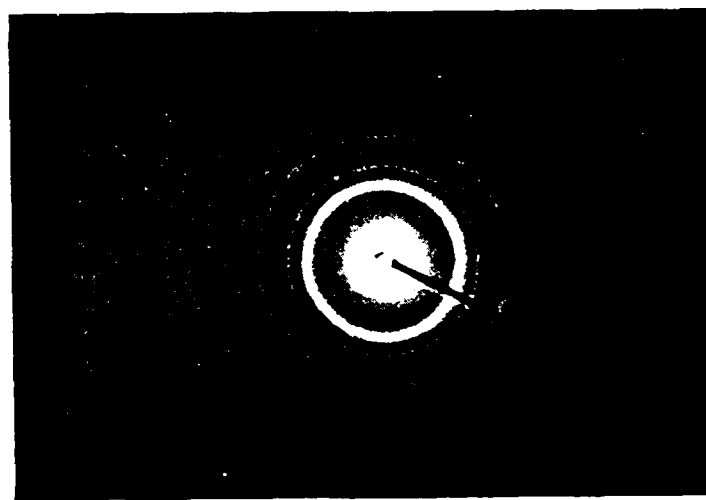
Figure 52 TEM micrograph of COSAD1 thin film. a) as-deposited on carbon support film; b) corresponding SAD pattern.





a)

50 nm



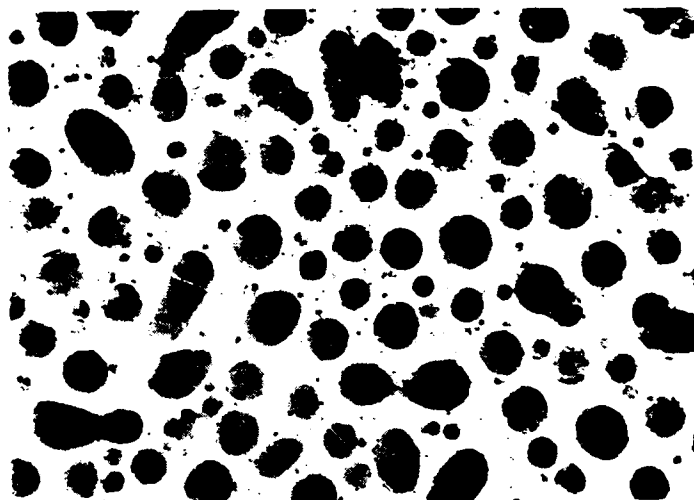
b)

Figure 53 TEM micrograph of COSAD1 thin film. a) after five minute exposure to condensed electron beam; b) SAD pattern.



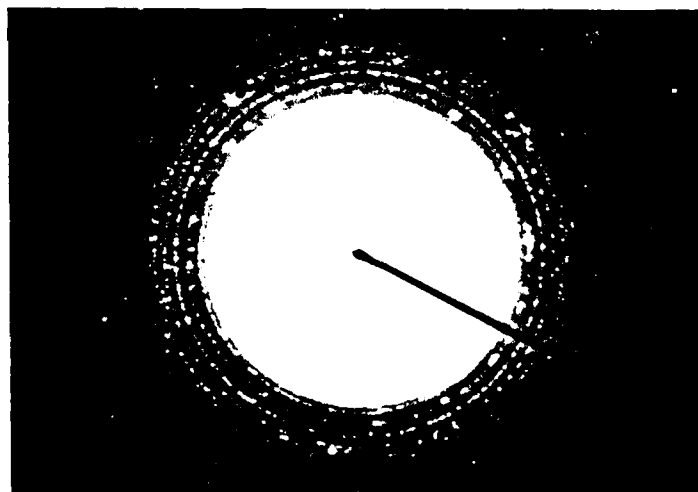
100 nm

Figure 54 TEM micrograph of COSAD1 thin film, after heat treatment to 500° C for one hour.



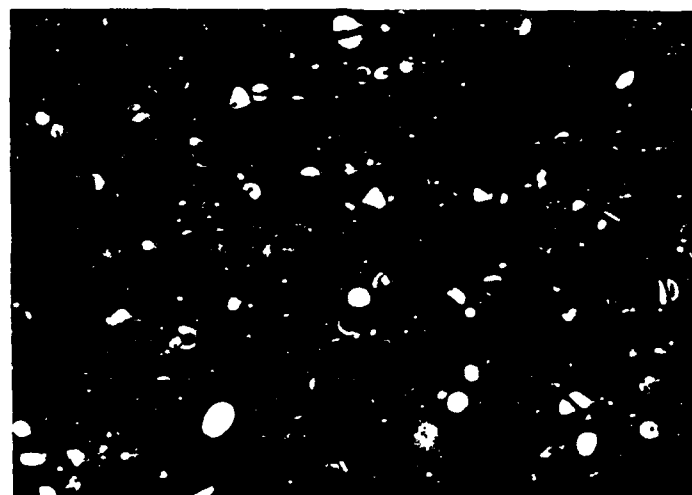
100 nm

a)



b)

Figure 55 TEM micrograph of COSAD1 thin film. a) after heat treatment to 650° C for 30 min.; b) SAD pattern.



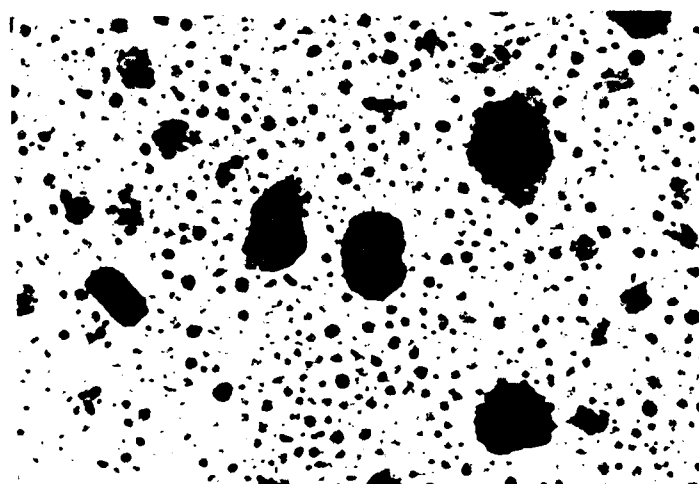
200 nm

Figure 56 Dark field TEM image of COSAD1 thin film shown in Figure 55a.

be seen, crystals of both size distribution are lit up. The dark field image also shows that several of the large crystals are twinned, indicated by the change in contrast within a crystal. Another abnormality exhibited by the higher temperature heat treated films was the additional appearance of large faceted shaped crystals, shown in Figure 57. The crystallographic identity of these crystals could not be determined; however, they were only found in certain areas of the film, and they may correspond to some type of contamination.

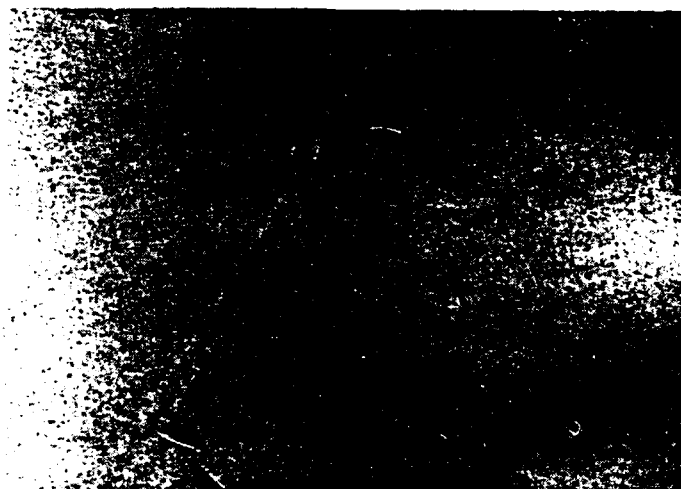
COSAD films which were made by controlling the alternating deposition process with a computer controlled stepping motor could be produced with very low ratios of CdS in the glass. Alternating layers of material could be produced by stopping the substrate over a source for a given amount of time. This permitted the deposition of several monolayers in each pass. Ratios which resulted in about 5% CdS dispersed in the glass (designated COSAD2) resulted in structures such as the one displayed in Figure 58a. The extremely fine dark structure in the micrograph is most likely due to CdS microcrystallites; however, the accompanying SAD pattern (Figure 58b) indicates the structure to be amorphous. When the electron beam is condensed on this type of film a phase separation is shown to occur, but as exhibited in Figure 59a it grows to a smaller size than shown in Figure 53a. The accompanying SAD pattern in Figure 59b also indicates that the structure is still amorphous.

When this type of film is heat treated to 650° C, two different structures result. First, large semi-faceted shaped crystals are exhibited as shown in Figure 60a. Although a single crystal



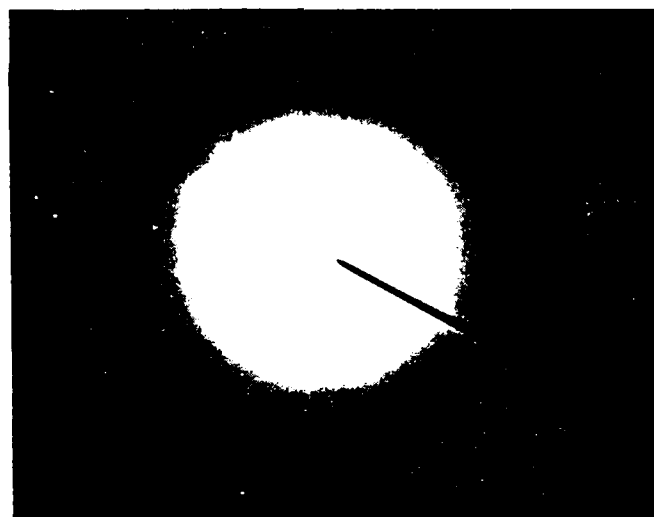
200 nm

Figure 57 TEM micrograph of heat treated COSAD1 thin film, showing large unidentified crystals.



100 nm

a)



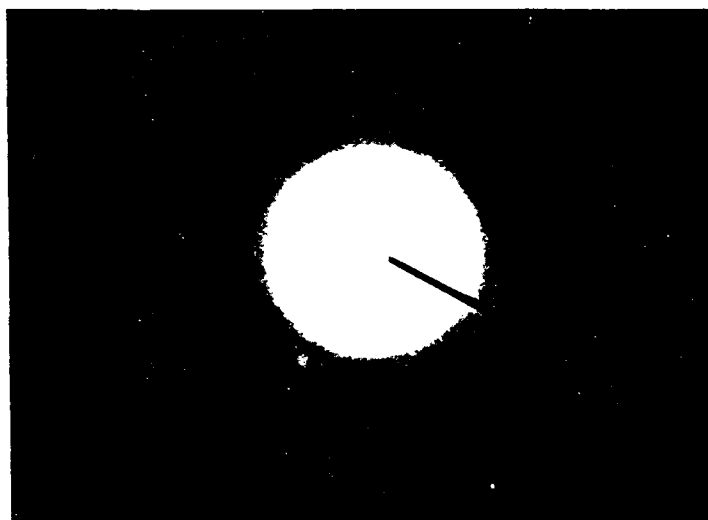
b)

Figure 58 TEM micrograph of COSAD2 thin film. a) as-deposited; b) SAD pattern indicating amorphous structure.



50 nm

a)



b)

Figure 59 TEM micrograph of CO<sub>2</sub>/D<sub>2</sub> thin film. a) after ten minute exposure to condensed electron beam; b) SAD pattern.



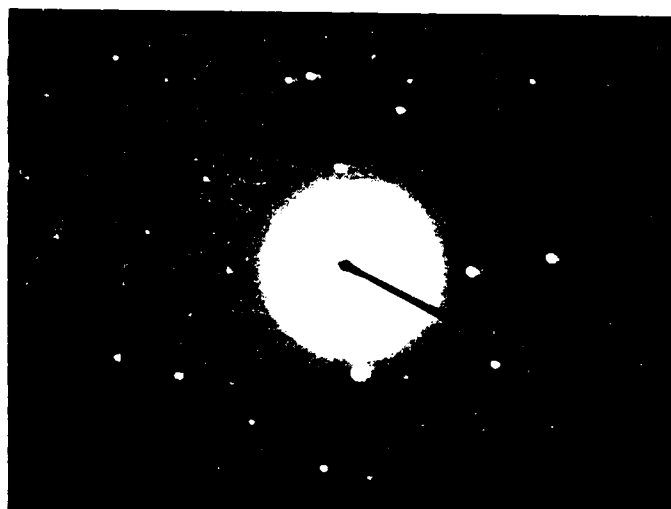
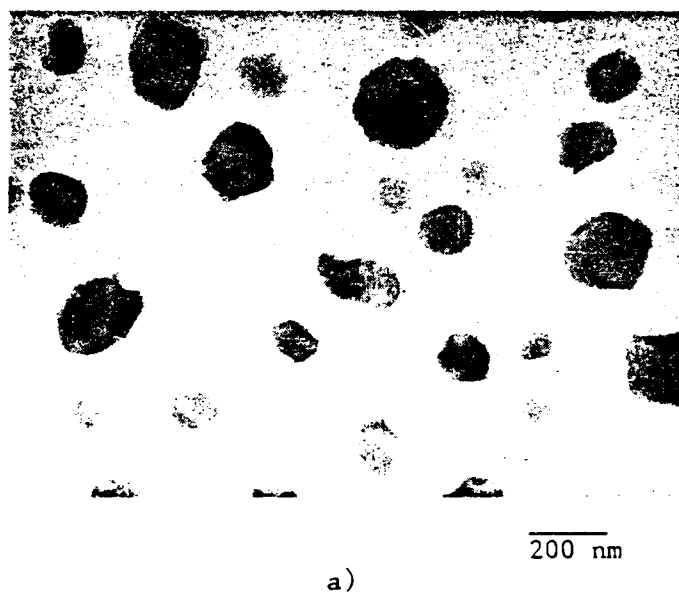
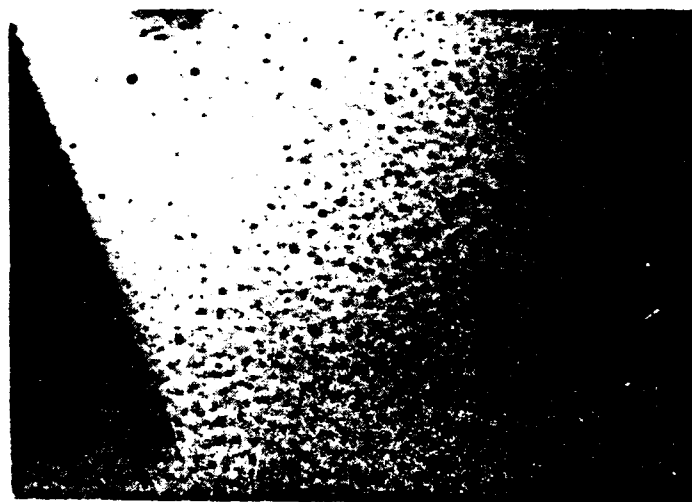


Figure 60 TEM micrograph of COSAD2 thin film. a) after heat treatment to 650° C for 30 min, showing large unidentified crystals; b) SAD pattern showing both single crystal pattern from large crystals and diffuse pattern from thin film.

diffraction pattern could be obtained from these crystals (shown in Figure 60b), they could not be identified. Again these large crystals were found to be unevenly distributed on the film and therefore considered to be due to contamination. At very high magnification, the second structure of these films can be observed. Very small spherical microcrystallites, of 50 Å approximate size are shown in Figure 61. Only a very diffuse diffraction pattern shown in Figure 60b could be obtained, so it is difficult to identify the microcrystallites as CdS, although the pattern does resemble the pattern of the semi-amorphous LN2 film described above. A large number of these microcrystallites is seen, so a stronger pattern should result. This particular film, however, is relatively thick ( $\approx 3000$  Å), so it only appears there are many microcrystallites. The pattern is diffuse because the glass matrix has a much larger volume fraction compared to the microcrystallites.

#### Composition

Very little compositional analysis was carried out on COSAD films, primarily because most of the films made were for TEM analysis, and therefore were too thin for quantitative analysis. The composition of a few of the phase separated particles discussed above however, were determined by EDS while imaging the film in the STEM mode of the JEOL 100 CX electron microscope. The particles were found to contain aluminum and sulfur, but the intensity levels for these two peaks were not high enough to get an accurate determination of the stoichiometry. This is particularly true of the particles displayed in Figure 61. A



50 nm

Figure 61 High magnification TEM micrograph of heat treated COSAD2 thin film showing fine dispersion of microcrystallites.

typical EDS X-ray spectrum obtained while operating the JEOL 200 CX in the STEM mode is shown in Figure 62. This spectrum was acquired from the film displayed in Figure 61 and it shows that the particles are CdS. Except for silicon, the other constituents of the glass matrix (e.g. Ca and K) could not be determined with this technique because of their low concentration and the thickness of the film. The copper peak originates from the TEM support grid.

The compositions of thicker films made for optical analysis were determined by XRF. One difficulty encountered in using this technique was that the potassium  $K\alpha$  line overlapped the cadmium  $L\beta$  line, so the amount of potassium could only be roughly determined. For COSAD films deposited on silica substrates the total amount of silicon also could not be determined, due to fluorescence of the substrate. The relative amounts of cadmium and sulfur, however, could be determined and it was found that peak intensity ratios very close to those of as deposited pure CdS films were obtained with COSAD films with both high and low amounts of CdS. A few COSAD films were deposited on single crystal sapphire to determine the composition separately from that of the substrate.

#### Thin Film Optical Properties

Now that the physical properties of thin films have been fully described, the results that are central to this dissertation will be presented in this section. These results describe how the changes in microstructure produced by various treatments affect the optical properties. UV-visible absorption, photoluminescence, and resonant

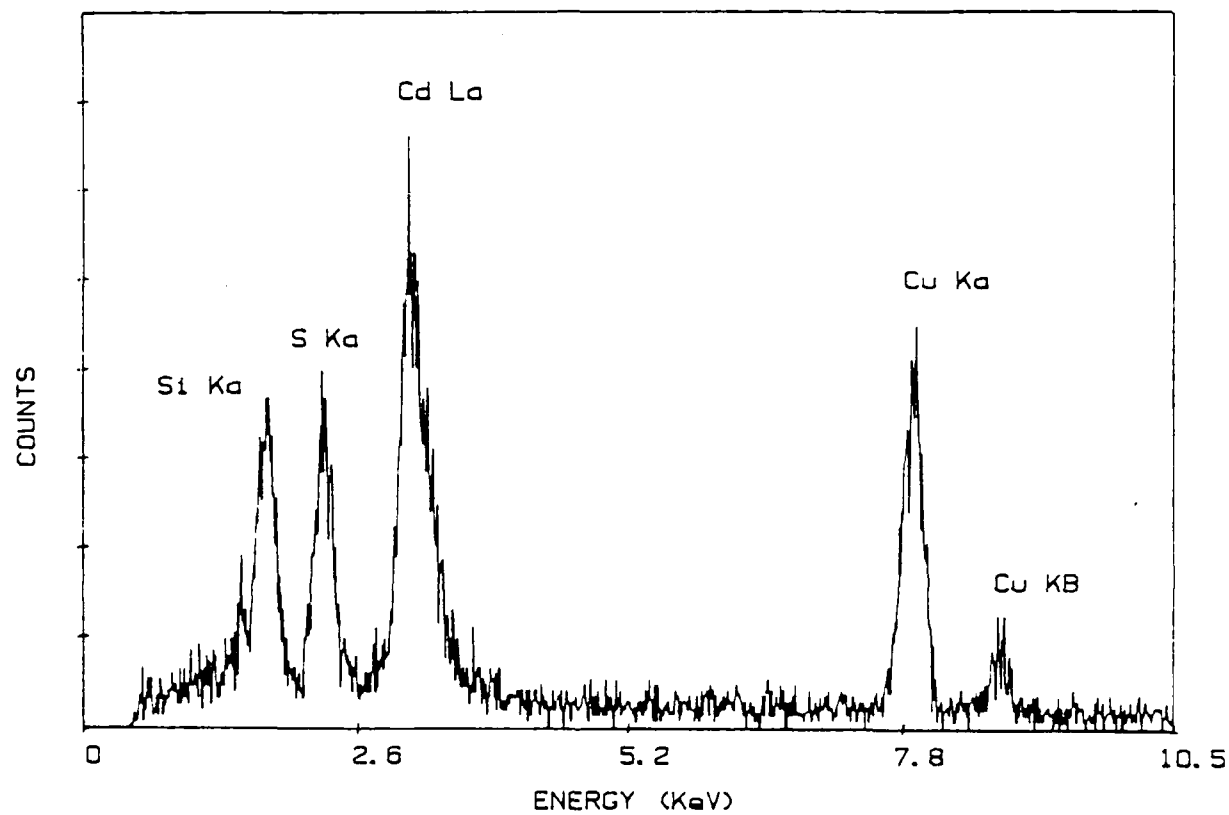


Figure 62 EDS X-ray spectrum of COSAD1 film.

Raman scattering were utilized at both room temperature and low temperatures to fully characterize the optical properties of thin films.

### Absorption Spectra

UV-VIS absorption was used in this study to establish the relationship between thin film processing conditions and their effect on the band structure of the material. The main emphasis of this study as stated before, was to produce a thin film with the same optical properties as those of bulk single crystal material. From the measurement of absorption spectra, it was possible to determine the presence of band defects such as band tailing, to determine the temperature dependence of the band gap energy and at low temperatures, to observe exciton transitions.

By examining the shape of the absorption edge, a qualitative measure of the band gap structure could be determined. At energies below the absorption edge, the sharpness of the transition from low absorption to the edge gives an indication of the amount of band tailing. Only transitions which conserve momentum are allowed, therefore, for a direct band gap semiconductor, only  $k$  equals zero excitations occur without phonon scattering. When a great many crystallographic defects are present in a material, then the band structure will not be well defined. The presence of defects permits transitions at other values of  $k$  to be quantum mechanically possible, which in the absorption spectra is manifested as a tailing of the absorption edge at low energies.

Room temperature UV-VIS absorption

The position of the room temperature band gap absorption edge that was measured for as-deposited thin films was found to vary slightly with film thickness and deposition rate, but mostly with substrate deposition temperature. Films ranged in color from straw yellow to dark orange to nearly black, as the deposition temperature was varied from 300° C to LN<sub>2</sub>. Typical spectra of films deposited at 300° C, room temperature, and LN<sub>2</sub> using an absorbance scale are shown in Figure 63. The variation in absorbance spectra with film thickness is shown in Figure 64. As previously described, absorbance spectra show features above the band gap with more detail than transmission spectra. By taking the maximum slope of the absorbance, an approximate value of the band gap absorption edge is given and as can be seen in Figure 63, this position for the three curves varies considerably. A listing of the absorption edges determined by this technique for different deposition conditions is given in Table 5. From the Table, the maximum slope position for films deposited under the same conditions, but with different thicknesses varies only slightly and as shown in Figure 64 the shape of the absorbance curves is similar. In contrast, the shape and position of the three spectrum in Figure 63 of similar thickness films deposited at different temperatures is altered considerably. The film deposited at 300° C shows very flat absorption above the band edge indicating a well developed band gap, but the position of the edge is considerably shifted to longer wavelengths which is characteristic of a composition change. Also, because of the inhomogeneity of these films there is a reduction in transmission at long wavelengths due to

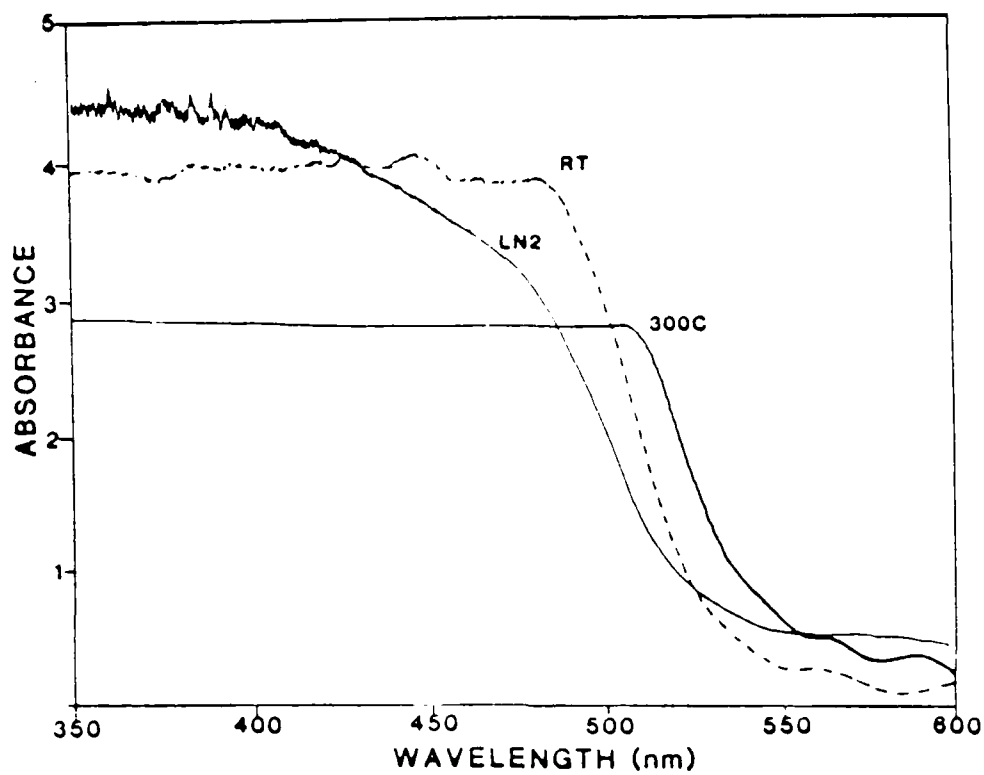


Figure 63 Room temperature UV-visible absorbance spectrum of films deposited at LN<sub>2</sub> temperature (LN<sub>2</sub>), room temperature (RT), and 300° C (300°C).



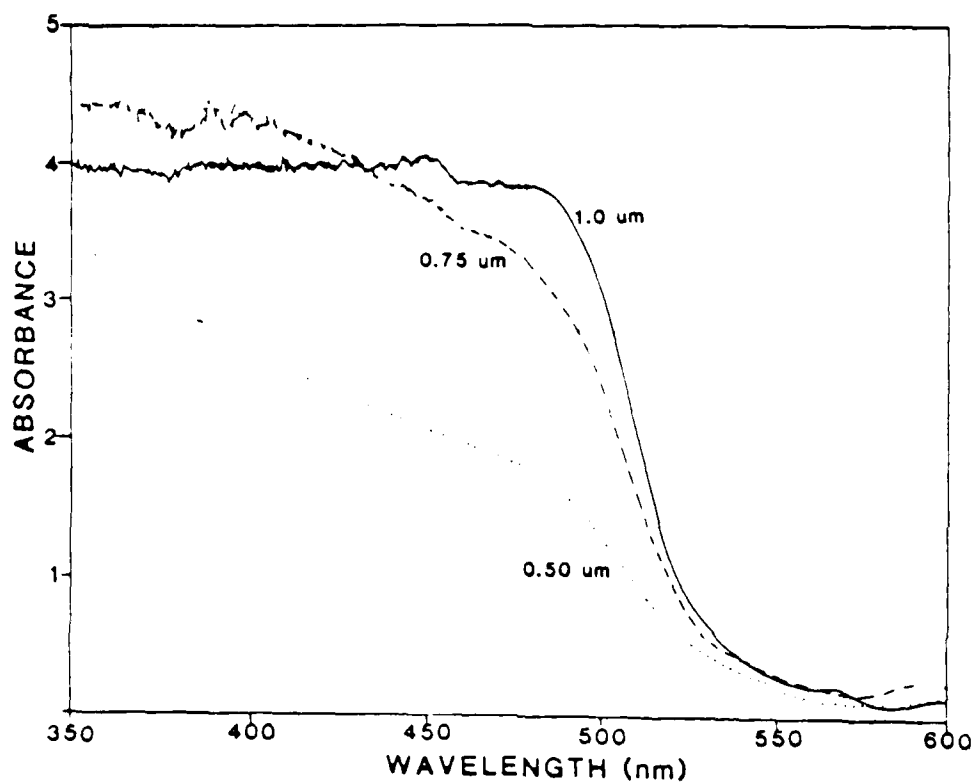


Figure 64 Room temperature absorbance spectra of different thickness films, deposited at 1  $\text{\AA}/\text{sec}$  onto room temperature substrates.

TABLE 5  
Band Edge Position for Several Different Films  
Determined by Maximum Slope Method

| Sample               | Maximum Slope Position<br>(nm) | Energy<br>(ev)                                   |
|----------------------|--------------------------------|--|
| ASDP 1 Å/sec         |                                |  |
| t = 0.5 μm           | 507.8                          | 2.442  |
| t = 0.75 μm          | 508.9                          | 2.437  |
| t = 1.0 μm           | 509.8                          | 2.432 (2.44) <sup>1</sup><br>(2.37) <sup>2</sup> |
| ASDP 3 Å/sec         | 508.5                          | 2.439  |
| ASDP 5 Å/sec         | 501.7                          | 2.472  |
| ASDP LN <sub>2</sub> | 496.5                          | 2.497  |
| ASDP 300° C          | 523.1                          | 2.370  |
| FHT 500° C<br>5 hr.  | 505.1                          | 2.455 (2.46) <sup>1</sup><br>(2.45) <sup>2</sup> |

<sup>1</sup>Determined by maximum slope of absorption curve (Figure 79a)

<sup>2</sup>Determined by intercept method (Figure 79b)

Note: All films measured were approximately 1.0 μm thick unless  
other wise stated.

scattering losses. For the  $\text{LN}_2$  deposited film, a large amount of band tailing is indicated by the higher absorbance below the band edge and higher absorbance above the band edge indicates the presence of uncompensated defects. The overall transmission of this film is reduced because of the presence of excess cadmium, which is the reason for the dark color of these films. Excess cadmium is also most likely responsible for the high absorbance above the band gap. A close relationship between the number of defects observed by TEM and the amount of band tailing is observed in these films. Band tailing is an indication of the structure of the band gap and the presence of band gap defects, which appear to be directly dependent on the number of crystallographic defects.

The band tailing-crystal defect relationship is further indicated when the absorbance of films heat treated to different temperatures is measured. The lower heat treatment temperatures at  $200^\circ$  and  $350^\circ$  C shown in Figure 65 do not indicate much of a change in the amount of band tailing; however, the heat treatment to  $500^\circ$  C has reduced nearly all band tailing, which reveals a distinct absorption band below the band edge. This is an interesting result, because this is the temperature at which grain growth was shown to drastically increase. Examination of Figure 65 also shows that the higher temperature heat treatment results in a slight shift of the absorption edge to higher energy. This might be related to the slight change in composition that occurs at the higher heat treatment temperature.

Because there is such a strong relationship between band tailing and crystal structure, examining the onset of absorption in thin films

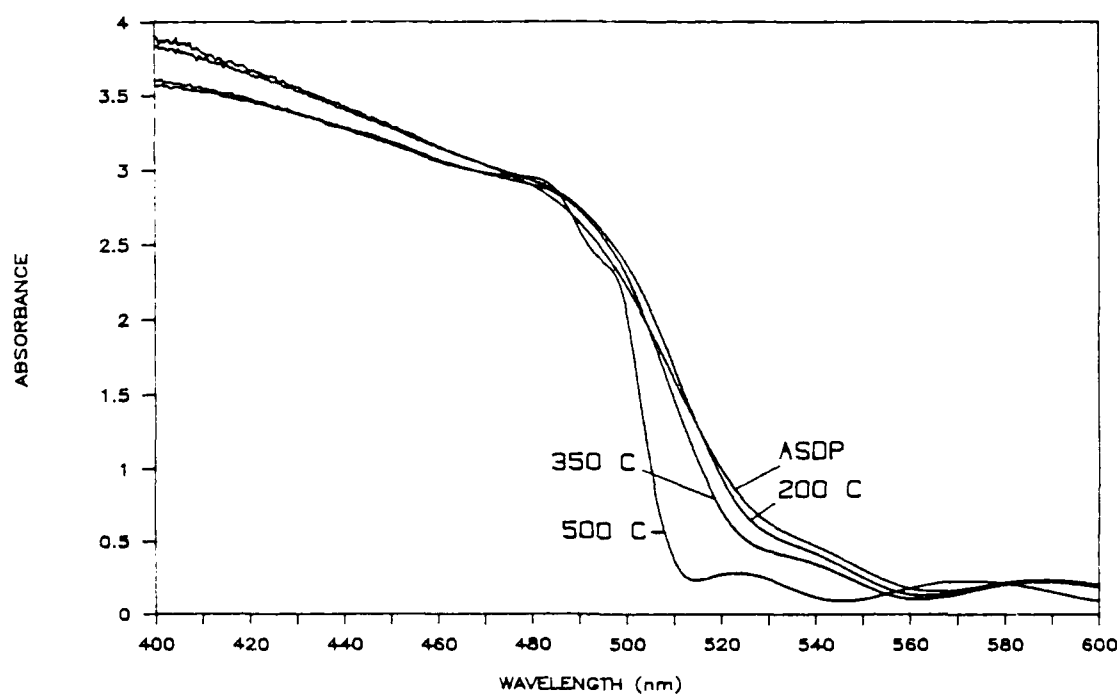


Figure 65 Room temperature absorbance spectra comparing as-deposited (ASDP) and heat treated thins. Temperature of heat treatment shown; all treatments for five hours.

is a useful technique for evaluating the results of different heat treatments. Figure 66 shows the total absorbance curve and Figure 67 shows an expanded abscissa scale for heat treatments of 650° C 30 sec, 650° C 4 min, and 500° C 5 hours. Figure 66 shows a structural change between RTA and the 500° C 5 hour heat treatment in the band tail and all three curves show two sub-edge features, both as shoulders above the sharp rise in absorption. Figure 67 indicates that furnace heat treating to 650° C for 4 minutes results in nearly the same low energy band structure as the heat treatment at 500° C for 5 hours. A rapid thermal anneal (RTA) film displays the same curve shape at high values of absorbance, but as indicated in Figure 67, there still is some band tailing present.

#### Low temperature UV-VIS absorption

At sufficiently low temperatures, many features of the absorption spectrum appear more clearly and can be related to the band structure in these films. Spectra were obtained at temperatures down to 9° K by cooling a sample with the closed loop helium refrigerator. With a decrease in temperature several changes in the absorbance curve are observed. First the band edge shifts to higher energy, both due to a change in the lattice parameter and to the temperature dependence of the band energy. A plot of the band gap energy as a function of temperature is displayed in Figure 71b.

Second, the amount of band tailing is shown to significantly decrease in heat treated films; however, the decrease is not as predominant in as-deposited thin films. The indirect transitions which

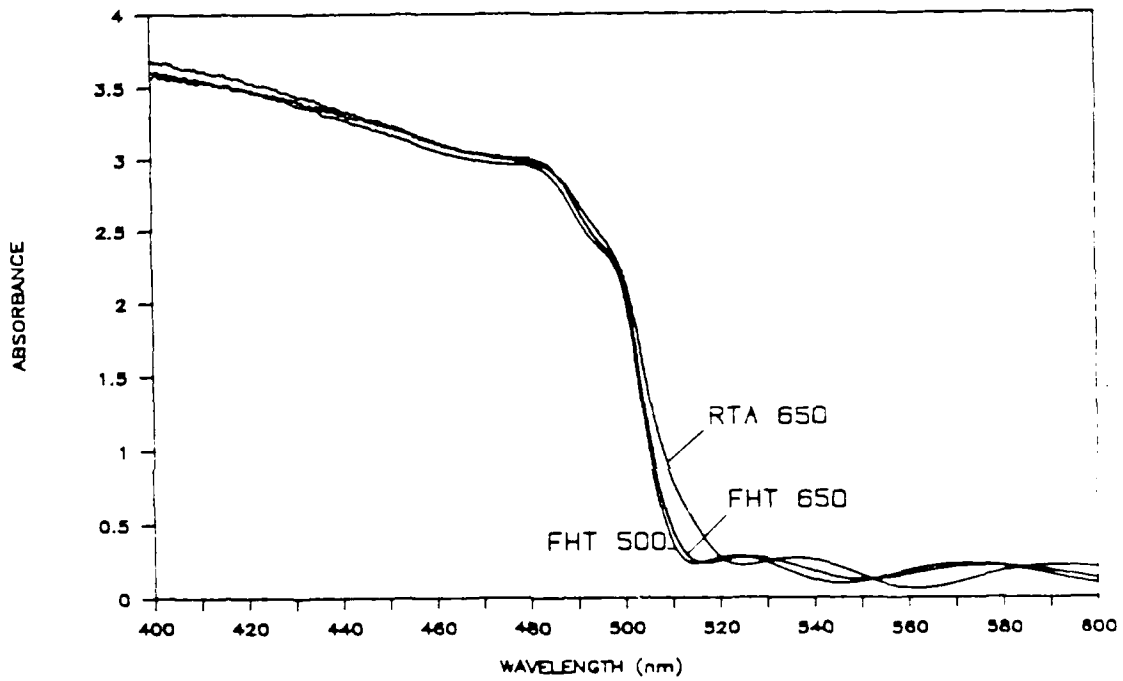


Figure 66 Absorbance spectra of different heat treatments. Furnace heat treatment: 500° C, five hours (FHT 500); furnace heat treatment 650° C, four minutes (FHT 650); rapid thermal anneal heat treatment, 650° C, 30 seconds (RTA 650). All films deposited at 1 Å/sec.

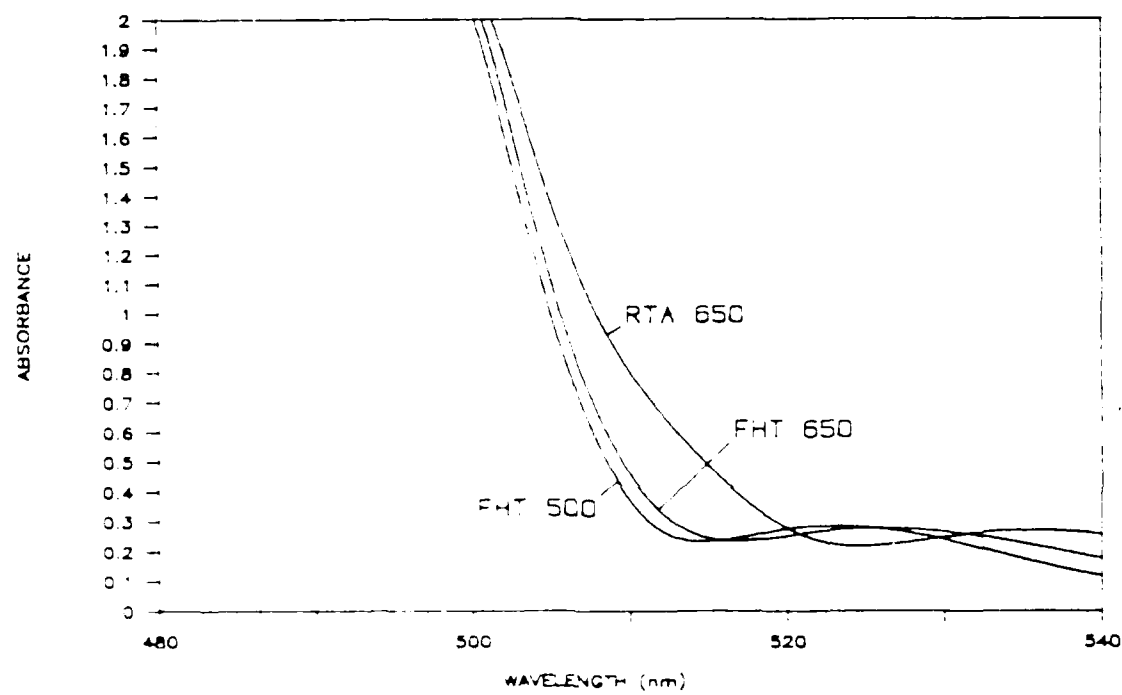


Figure 57 Same designations as Figure 66, with expanded abscissa scale.

NO-0191 297

INVESTIGATION OF NON-LINEAR OPTICAL BEHAVIOR OF  
SEMICONDUCTORS FOR OPTICA. (U) FLORIDA UNIV GAINESVILLE  
DEPT OF MATERIALS SCIENCE AND ENGINE. J H SIMMONS

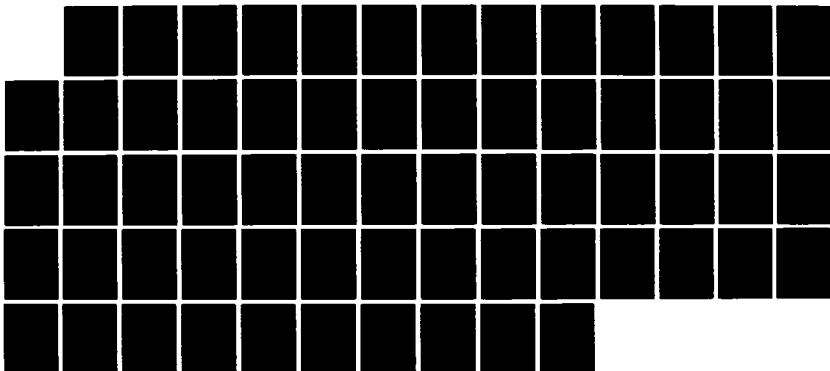
2/3

UNCLASSIFIED

30 SEP 87 AFOSR-TR-88-0133 AFOSR-84-0395

F/B 28/6

NL







1.0



1.1



1.25



2.8



3.15



3.5



4.0



4.5



5.0



5.6



6.3



7.1



8.0



9.0



10.0

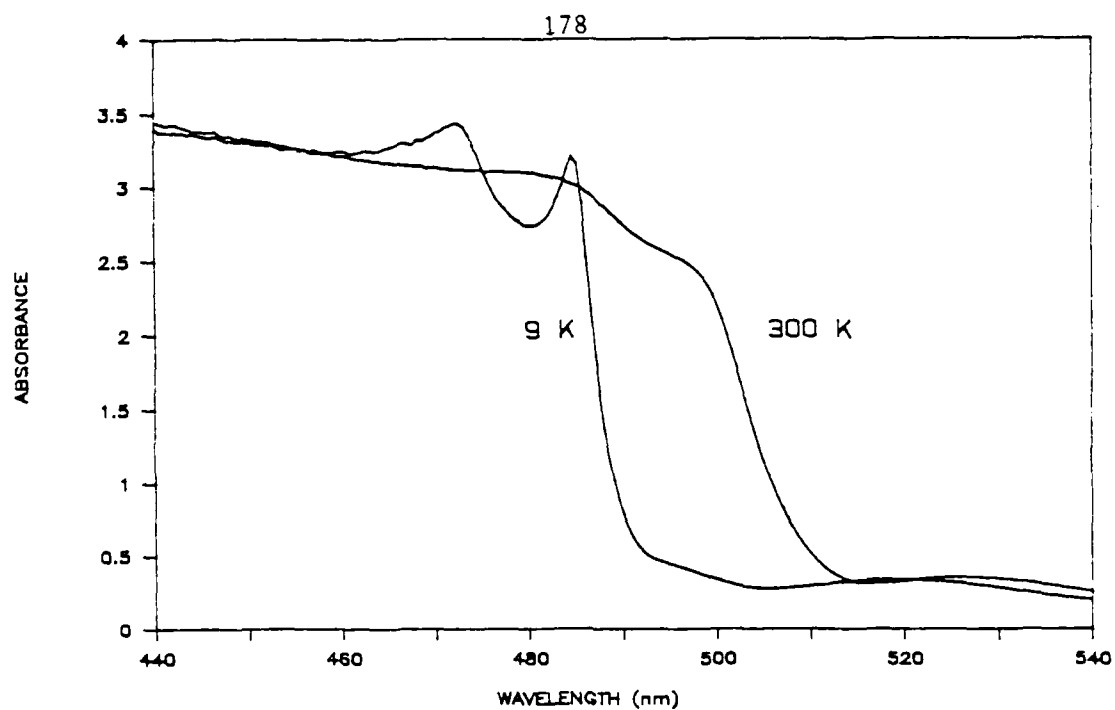


11.2

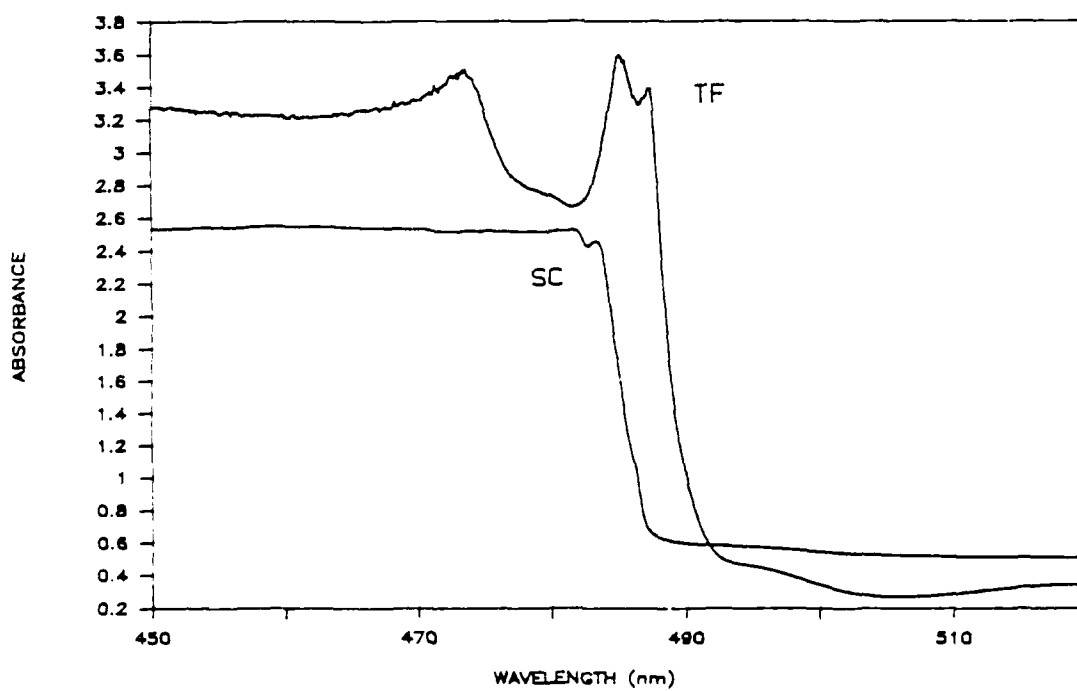
are responsible for most of the band tailing are phonon assisted transitions and with the lowering of the temperature, these transitions are no longer possible. Band tailing is not completely reduced in the as-deposited thin films because there are other defect states present in the band gap (created by the crystallographic defects) which do not require phonon scattering for transitions.

The most significant change in the absorbance spectra at low temperature is shown to occur in films heat treated at high temperatures. The appearance of several sharp absorption bands which correspond to exciton transitions are observed. Figure 68a displays these bands and other changes in the absorbance spectra of a  $1.0\text{ }\mu\text{m}$  thick film, deposited at  $1\text{ }\text{\AA}/\text{sec}$ , that was heat treated to  $650^\circ\text{C}$  for 4 minutes. Shown in Figure 68b is the absorbance spectrum from a  $10\text{ }\mu\text{m}$  thick single crystal platelet of CdS, measured under the same conditions as the thin film. The platelet was oriented with the c-axis perpendicular to the incident beam. Above the band edge, the two sharp peaks observed in the thin film spectrum appear similar to the platelet spectrum, but the features are more pronounced in the thin film spectrum. Also, the entire curve for the thin film is shifted to lower energy. The similarities of these band edge features, however, do indicate the presence of exciton states in the polycrystalline thin films.

Further proof is afforded by plotting the absorption peaks on an energy scale, as shown in Figure 69a. The spectrum obtained in this study can be directly compared to reflection spectrum of a bulk single crystal CdS shown in Figure 69b. A comparison of the peak energies is

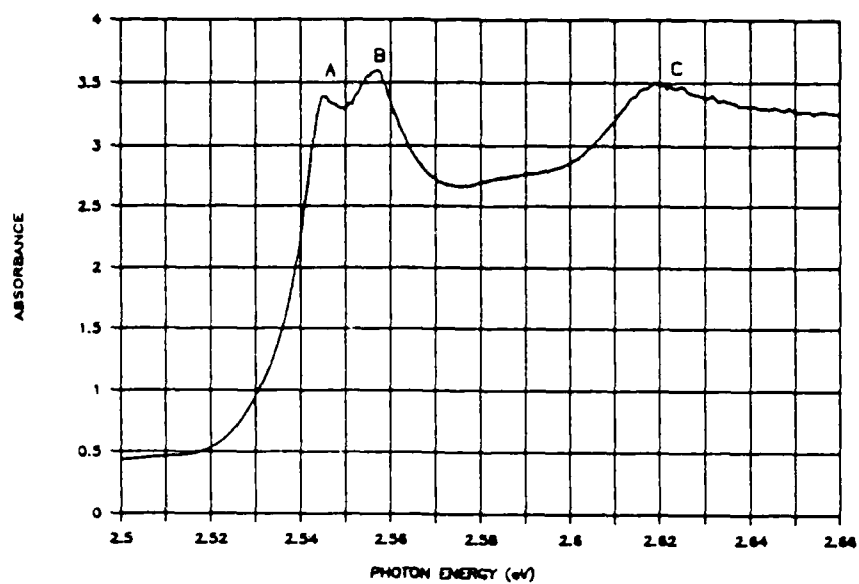


a)

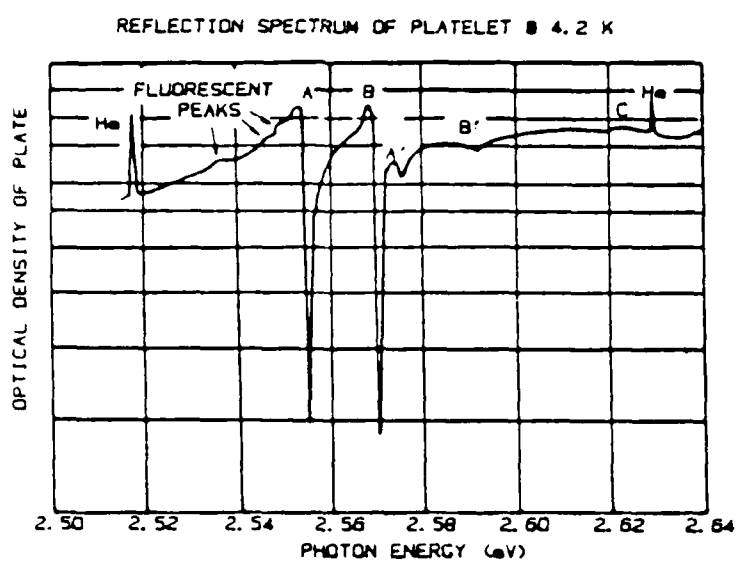


b)

Figure 68 Variation of absorbance spectra with temperature. a) spectrum observed at room temperature and 9° K; b) low temperature spectrum of thin film (TF) and single crystal platelet (SC).



a)



b)

Figure 69 Comparison of low temperature spectra. a) absorbance spectrum of thin film, with energy abscissa scale; b) reflection spectrum of single crystal, 4.2° K.<sup>14</sup>

listed in Table 6. The absolute values of the peak energies are slightly different, but the energy difference between the A, B and C levels is nearly the same in both spectra. The difference in absolute values may be attributed to the same source which produces the difference in the absorption band edge, displayed in Figure 68b. The peaks are much sharper in the reflection spectra because the technique is very sensitive to changes in reflectivity and also because the reflection spectrum was taken at 4.2° K. The broader peaks observed here may be due to temperature broadening, as well as orientational broadening in the polycrystalline films.

The observation of exciton absorption peaks was made in all films heat treated to above 500° C. With the large grain growth that occurs with high temperature furnace heat treatments, it is not surprising that exciton levels should occur in a polycrystalline thin film, because even with a grain size of 3000 Å, the band gap should be well established. An interesting result however, is indicated by Figure 70 which shows exciton levels to be present in a RTA film in which the grain size is only 900 Å. The absorption peaks are less intense and slightly shifted, but they are definitely present. This indicates that large grain growth is not required to produce polycrystalline thin films which display exciton levels. What is needed is only the annealing of certain defects.

Another interesting observation is the variation of the exciton peaks with temperature. Figure 71a shows that only a slight shift and decrease in intensity occurs when the temperature is increased to 40° K, but at 100° K the A exciton peak has become a shoulder, the B and C

TABLE 6  
Comparison of Exciton Reflection and Absorption  
Peak positions

| Exciton | Peak Position<br>CdS Platelet | Energy<br>Delta | Peak Position<br>CdS Thin Film | Energy<br>Delta |
|---------|-------------------------------|-----------------|--------------------------------|-----------------|
| A       | 2.555                         | 0.015           | 2.545                          | 0.013           |
| B       | 2.570                         | 0.080           | 2.558                          | 0.072           |
| C       | 2.630                         |                 | 2.620                          |                 |

Note: All energy values given in electron volts, eV.

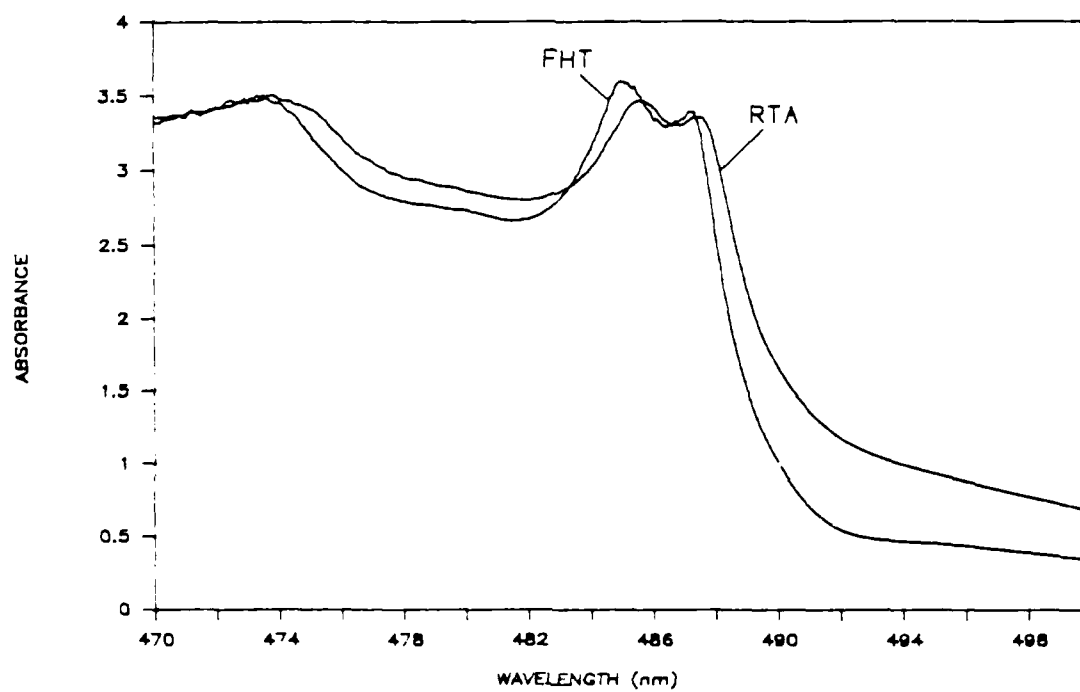


Figure 70 Low temperature absorbance spectra of furnace heat treated (FHT) and rapid thermal anneal (RTA) thin film.

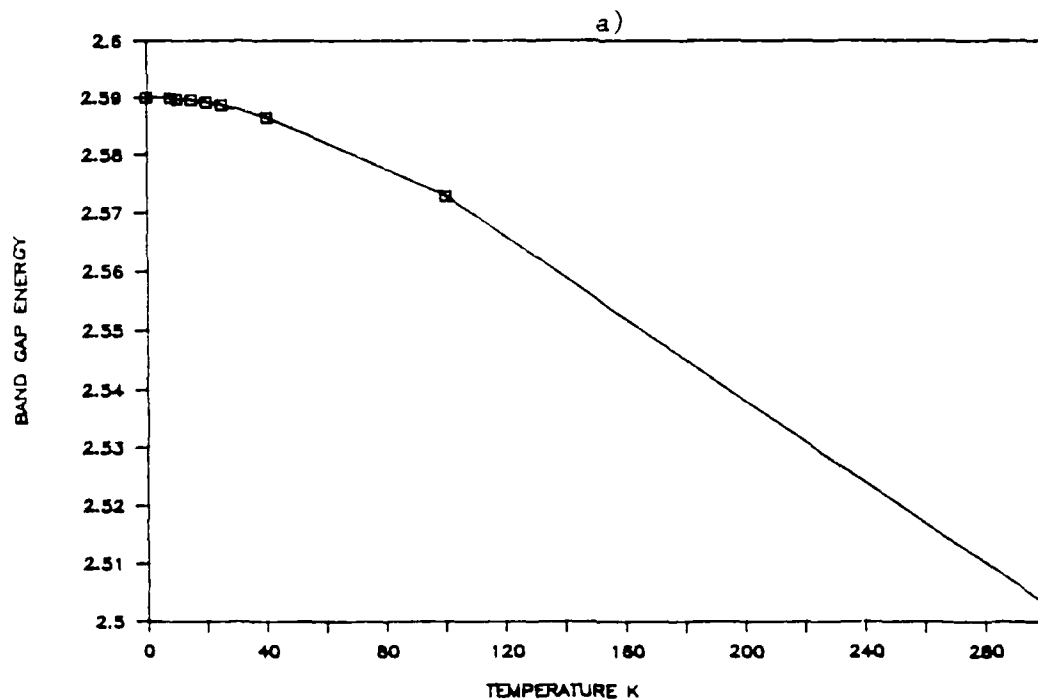
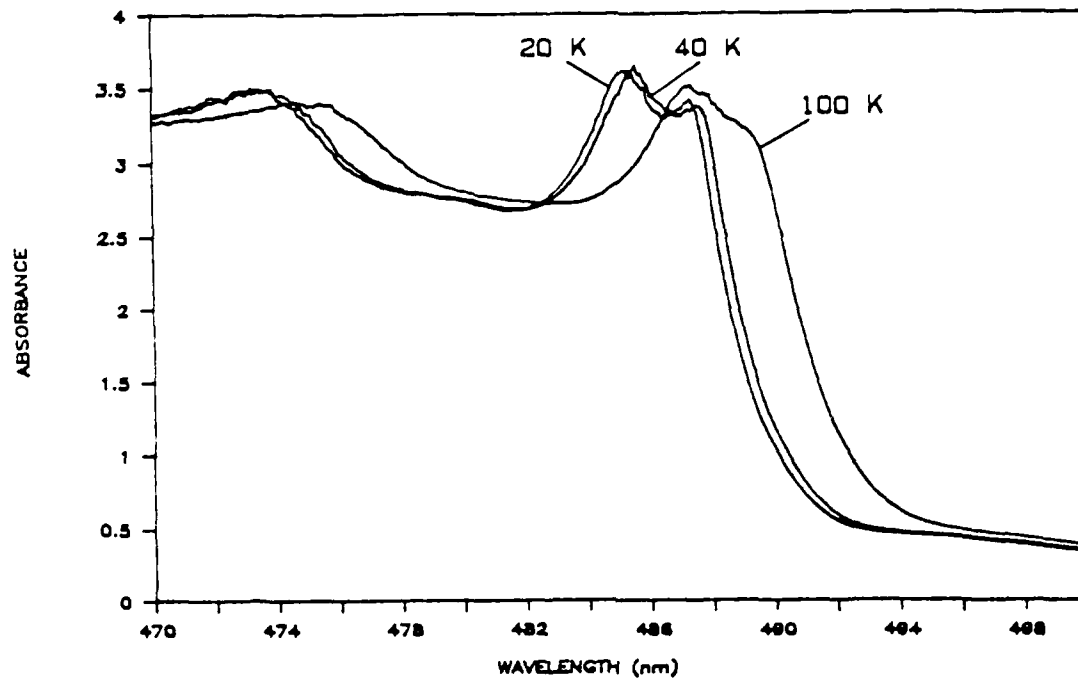


Figure 71 Variation of band gap energy with temperature. a) position of absorbance spectrum with temperature; b) plot of band gap energy versus temperature.



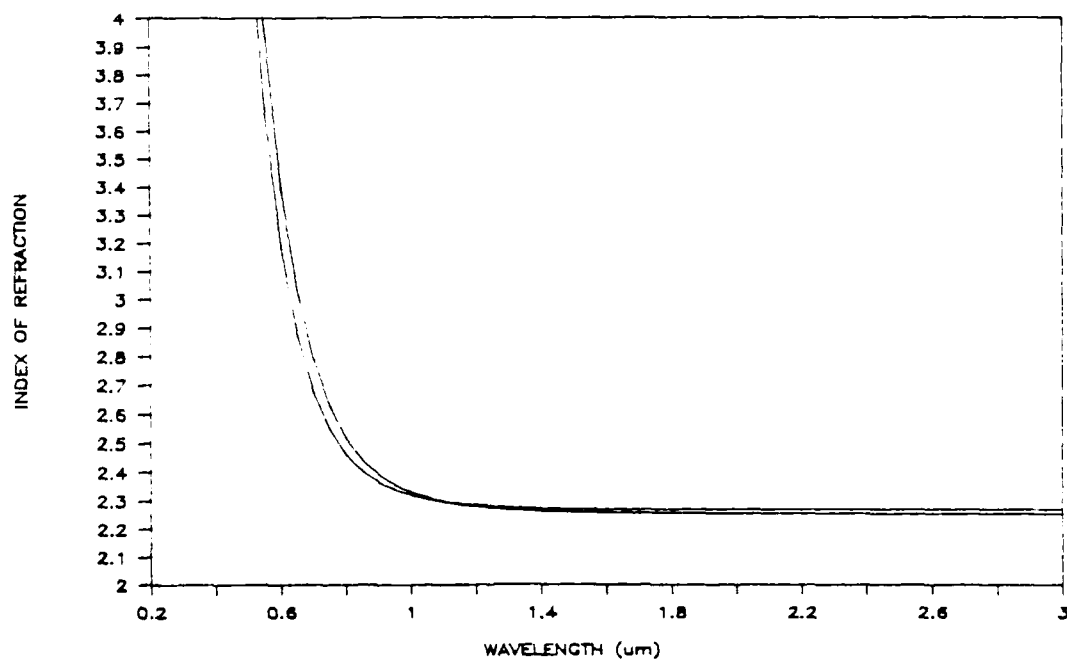
excitons peaks have broadened considerably. The disappearance of the A exciton peak at 100° K is consistent with the calculated binding energies of excitons, as the A exciton has a binding energy of 8 meV,<sup>19</sup> which corresponds to 92° K. Above this temperature a sharp transition should not be possible and we see that the peak broadens into a shoulder. It is interesting to note, however, that even at 300° K, as shown in Figure 68, an exciton-like shoulder is still present. Figure 71a also shows the temperature dependence of the band edge, and a plot of this variation as a function of temperature is shown in Figure 71b.

In the Bibliographic Review chapter (Chapter III), the description of the exciton states in CdS characterized the states in terms of crystallographic orientation and therefore their observation is dependent on crystal orientation with respect to the polarization of the probe beam. The fact that the grains in the films studied here have a strong preferred orientation is one reason why all three excitons are observed. In CdS single crystal platelets, all three excitons are observed when the E-field is perpendicular to the c-axis, but only the B and C excitons are observed with the E-field parallel to the c-axis. Although a circularly polarized beam is used in the Lambda 9, the beam is correctly oriented at any one point on the film because the orientation of the grains can be considered to be circular about the c-axis pole. TEM and X-ray diffraction results indicate that many grains are oriented with the basal plane of the unit cell parallel to the film and substrate plane, so one direction vector of the unit cell is perpendicular to the film plane. The other two direction vectors which fully describe the unit cell and crystal orientation are randomly

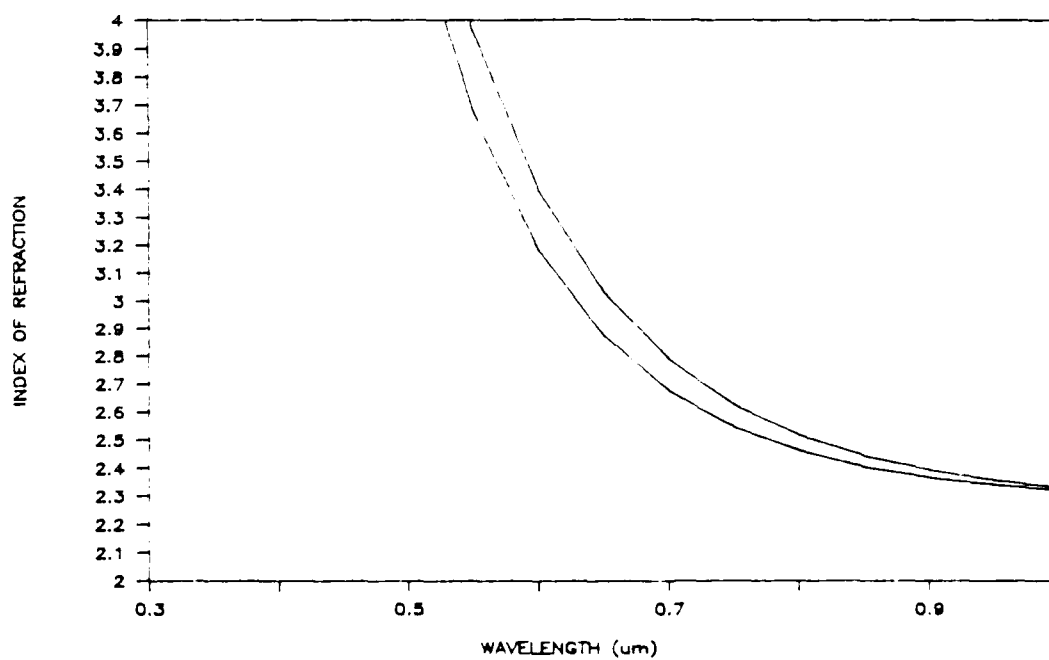
oriented, but should be rotated about the c-axis direction vector. It is therefore highly probable that a grain will have the proper orientation to the circularly polarized beam and all three exciton transitions should be measured.

#### Index of refraction

Fringes of equal chromatic order. Measurement of fringes of equal chromatic order (FECO) was a very useful technique for determining the dispersion of the refractive index at wavelengths longer than the absorption edge. Unfortunately, equation 4.4 which was used to model the dispersion could not be used to calculate the refractive index at the absorption edge or at shorter wavelengths. This is because the equation over-estimates the large change in absorption coefficient that takes place near the band edge. As shown in Figure 9 (Chapter III) the refractive index for bulk CdS is found to peak at the absorption edge and then decrease at shorter wavelengths. The problem with equation 4.4 is that it indicates that the refractive index converges to infinity at short wavelengths. This is shown graphically in Figure 72a and 72b, which are plots of equation 4.4, using the coefficients obtained from the FECO spectra of two different films. Figure 72b shows the calculated dispersion near the absorption edge. The Figures show that the curves converge at long wavelengths and give nearly the same value for the long wavelength limit of the refractive index. However, even at a wavelength 100 nm longer than the absorption edge, the refractive index is overestimated. Table 7 is a listing of the refractive index calculated at different wavelengths using equation 4.4



a)



b)

Figure 72 Index of refraction calculated from FECO spectrum. a) showing long wavelength conversion; b) variation near the band gap.

TABLE 7

Comparison of Refractive Index Determined by  
FECO method and Ellipsometry

| Sample              | FECO<br>Refractive Index | Ellipsometry<br>Refractive Index |
|---------------------|--------------------------|----------------------------------|
| ASDP 1 Å/s          | 3.036                    | 2.667                            |
| FHT 200° C<br>5 hr. | 3.120                    | 2.827                            |
| FHT 350° C<br>5 hr. | 3.098                    | 2.805                            |
| FHT 500° C<br>5 hr. | 2.874                    | 2.448                            |

Note: All heat treated films deposited at 1 Å/sec.

and the coefficients obtained from FECO spectra of several films. The refractive index was calculated at a wavelength of 632 nm for comparison to the value of refractive index obtained by ellipsometry, listed in the last column of the Table. Table 7 shows that the FECO method for determining refractive is only valid at long wavelengths.

Ellipsometry measurements. By using the graphical method described in Appendix B to determine the refractive index from the polarization angles measured with the ellipsometer, very accurate results could be obtained. These results are useful for quantitative comparison of different films, unfortunately this comparison could only be made at one wavelength; i.e. 632 nm, the wavelength of the HeNe laser used with the ellipsometer. Table 7 shows there is a significant change in refractive index when a thin film is heat treated. This should be expected because the density of the film changes considerably, particularly from high temperature heat treatments. The results show that ellipsometry is sensitive to the slight differences in microstructure of thin films deposited at different rates. In addition to these advantages, the technique is also very useful for refractive index and thickness determinations on very thin films, which cannot be measured with the FECO technique.

Absorption coefficient. A very close approximation to the wavelength dependence of the absorption coefficient can be made by taking the absorbance spectra and applying a few simple relationships. First, the extended equation for the transmission of light through a thin film supported on a substrate (equation 4.2, Chapter III) which

takes into account the reflections that take place within the film and the resulting interference can be written as

$$T = \frac{A e^{-\alpha t}}{1 - B e^{-2 \alpha t}} \quad (5.1)$$

where

$$A = (1 - R_1) (1 - R_2) (1 - R_3) (1 - R_2 R_3)^{-1}$$

and

$$B = (R_1 R_2 + R_1 R_3) (1 - R_2)^2.$$

Equation 5.1 can be simplified and written as

$$T = \frac{A}{e^{\alpha t} - B e^{-\alpha t}} \quad (5.2)$$

and the inverse is given by

$$\frac{1}{T} = \frac{1}{A} e^{\alpha t} - \frac{B}{A} e^{-\alpha t} \quad (5.3)$$

If the absorption coefficient  $\alpha$  is assumed to be very large ( $c \approx 10^4$ ) then the second term in equation 5.3 is essentially zero. Since the absorbance is defined as the natural logarithm of inverse transmission, then the absorption coefficient can be calculated from the absorbance spectra by applying

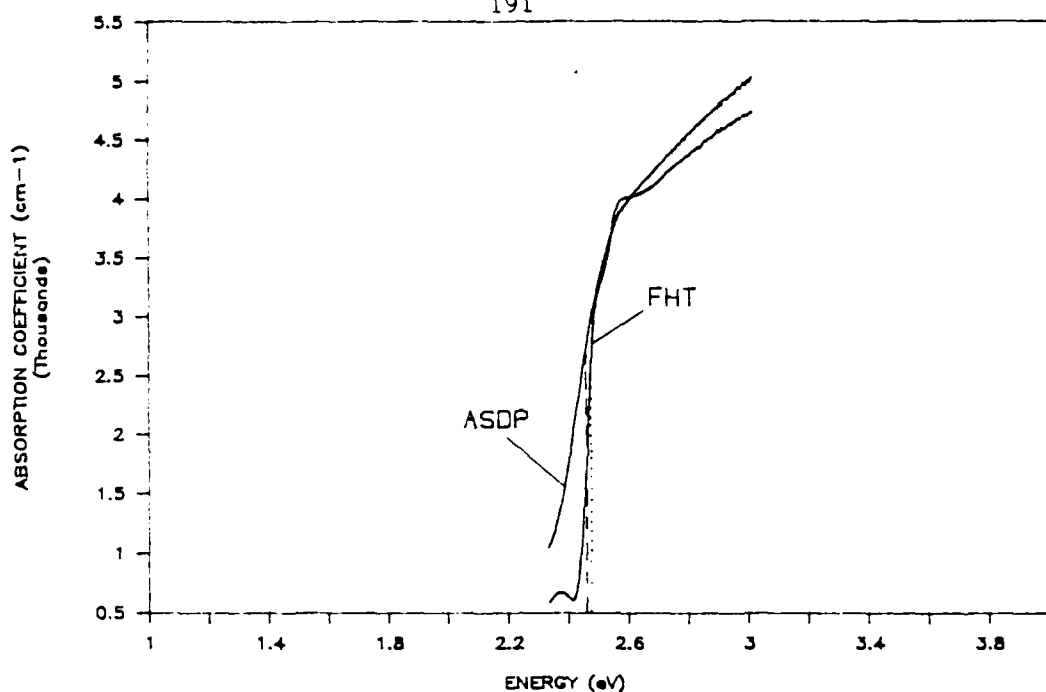
$$\alpha = \frac{\text{ABSORBANCE} + \ln A}{t} \quad (5.4)$$

The term  $\ln A$  represents the losses due to reflection interference and the value can be determined from the absorbance spectra of different thickness films, such as Figure 64, or a close approximation can be made by using the value of absorbance below the band edge, such as the value at 580 nm in Figure 64. The absorption coefficient spectra as a function of energy obtained by this calculation is shown in Figure 73a for both an as-deposited film and a heat treated film. The value of the optical band gap is given by either the maximum in slope of this curve, or by plotting the square of  $\alpha$  and extrapolating the linear portion of the curve to the intersection of the x-axis. The value of the x-axis intercept is the band gap energy. This plot is shown in Figure 73b for the same two films and a listing of other films and a comparison of the different techniques for calculating the band gap is presented in Table 5.

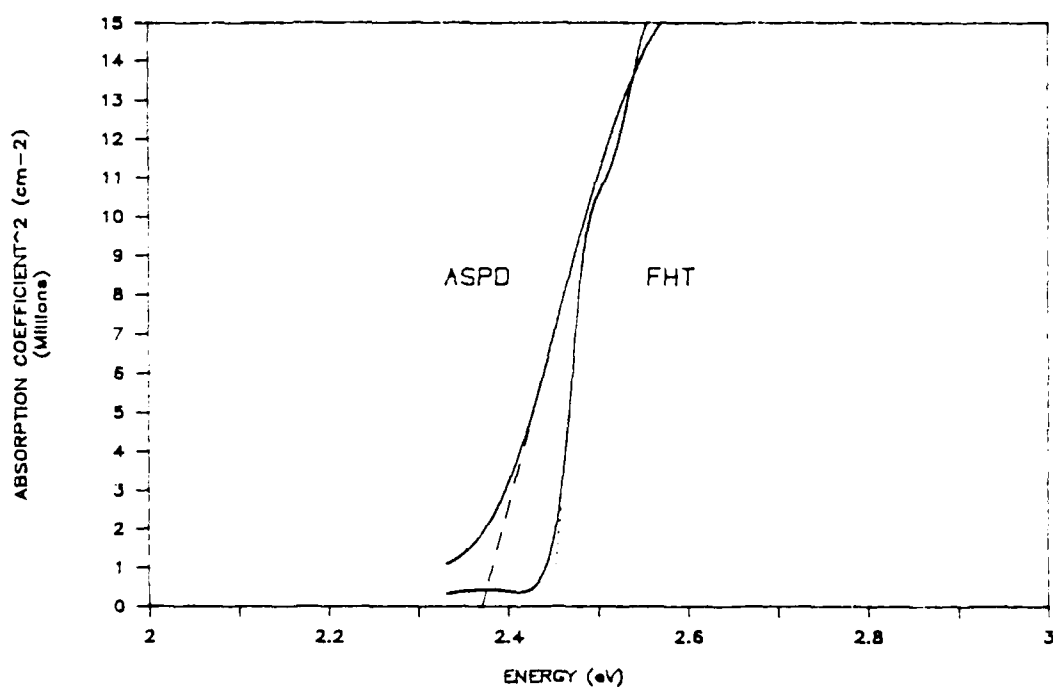
The above Figures and Table when compared to the data presented in the Bibliographical Review chapter show that the thin films produced in this study exhibit similar results to single crystal properties. This is another indication of the high quality of films which can be produced by the deposition process and subsequent heat treatments that were used in this study.

#### Photoluminescence and Raman Spectroscopy

Photoluminescence offers a complementary analysis to absorption measurements. While the optical transitions involve similar states,



a)



b)

Figure 73 Alternate methods for determining the value of the optical band edge. a) plot of absorption coefficient calculated from Equation 5.4 versus photon energy, point of maximum slope gives the band energy; b) plot of  $\alpha^2$  versus photon energy, extrapolation to  $\alpha^2 = 0$  gives band gap energy.



they are not subject to the same selection rules. For direct band gap semiconductors, radiative recombinations generally occur near  $k=0$ . Just as all the different defect states in the band gap lead to discrete lines, or bands, or tailing in absorption spectra, they can also lead to photoluminescence spectra which are indicative of these defects. As described earlier, the defect states that are of the greatest interest to this study are the exciton states and photoluminescence is an excellent technique for studying their occurrence and behavior.

Use of the optical multichannel analyzer (OMA) and the Raman spectrometers permitted a wide variation in the resolution and spectral window over which the photoluminescence and Raman scattering of thin films could be measured. For analysis of certain thin films which displayed very low intensity, wide band photoluminescence, the OMA could be used with a very low dispersion grating (152 lines/mm). While giving very poor spectral resolution this arrangement still permitted detection of very low light levels. To measure high intensity, narrow bandwidth peaks, the low dispersion grating was replaced with a very high dispersion 2400 lines/mm grating. As explained in the Experimental Method chapter (Chapter IV) this grating permitted a bandpass resolution of 0.9 nm, but a spectral window of only 20 nm. To assure calibration and permit an even higher bandpass resolution, the Raman spectrometer was used. By controlling the slit widths of the monochromator, resolutions down to 0.05 nm could be obtained.

Photoluminescence spectra

As-deposited thin films. Thin films which were deposited at room temperature were found to only give very low intensity, broad band photoluminescence. The defect structure of the band gap that led to the band tailing observed in the absorbance spectra of these films is also responsible for the low intensity observed in these measurements. These defects states provide non-radiative processes for the relaxation of excited states, so that the photoluminescence spectra have very low intensities. Because there are many different states with slightly different positions in the band gap, a broadening of the luminescence also occurs. A typical spectrum of films deposited at low rates, obtained at room temperature with the OMA and the low resolution grating is shown in Figure 74. This is an expanded intensity scale so the signal to noise ratio is low. The sharp peak at 457 nm is the laser line used to excite the sample. Usually, the three different broad bands observed in this spectrum would occur in all films deposited at room temperature, but the intensity of the different bands would vary. For example, the higher intensity band centered at 535 nm was found to be of much lower intensity in films deposited at higher rates and it was totally absent in films deposited at 5 Å/sec. The energy of the 535 nm band corresponds to direct transitions in the band gap and is the "green-edge" emission that was discussed in the Bibliographical Review chapter (Chapter III). The radiative transitions from conduction to valance band or from shallow donor to shallow acceptor impurity levels are characterized by this emission. The two low intensity broad bands centered at 670 nm and 750 nm are

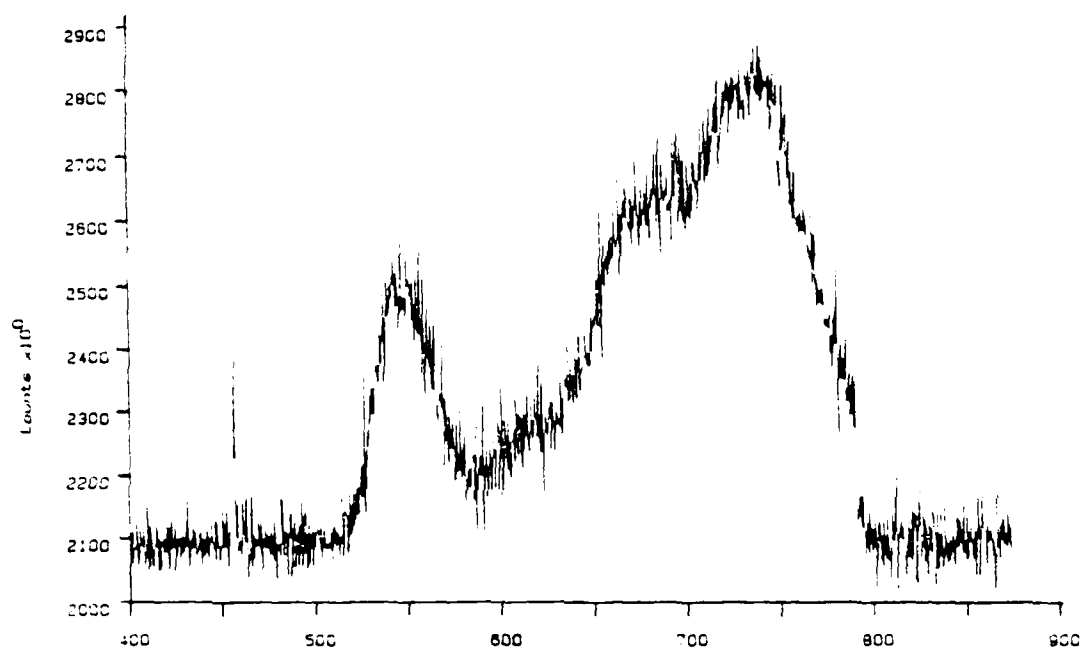


Figure 74 Low resolution photoluminescence spectrum acquired with optical multichannel analyzer (OMA).

associated with deep impurity level luminescence. The relative intensities of these two bands could be altered with slight changes in the geometry of the detection system. The width of these bands made it difficult to center the grating so that the diode array was evenly illuminated. This is one example of problems associated with a linear diode array detection system. If the array is not evenly illuminated the relative intensities displayed in the emission spectra will not be proportional.

Films deposited at  $\text{LN}_2$  temperatures only displayed the longer wavelength bands and at an even lower intensity level. The green edge emission is not observed in these films because the band structure is not well defined, due to the large number of crystallographic defects. The long wavelength bands are observed because deep level traps do not need a well established band gap to cause radiative transitions. They can be likened to impurity color centers, which are associated with a single impurity atom, or in this case with a vacancy or interstitial atom associated with an impurity. The identity of this impurity is unknown, but some authors have reasoned that it could be a halogen atom such as chlorine.<sup>33,34</sup>

Heat treated thin films. A very significant change in the photoluminescence of thin films occurs in films which are heat treated at high temperatures, even for relatively short times. The intensity of the green edge emission increases over 5x for the same excitation intensity and the peak position shifts to a higher energy. The relative intensity of an as-deposited thin film and a film heat treated to 500° C for 30 minutes are shown in Figure 75 and the relative peak

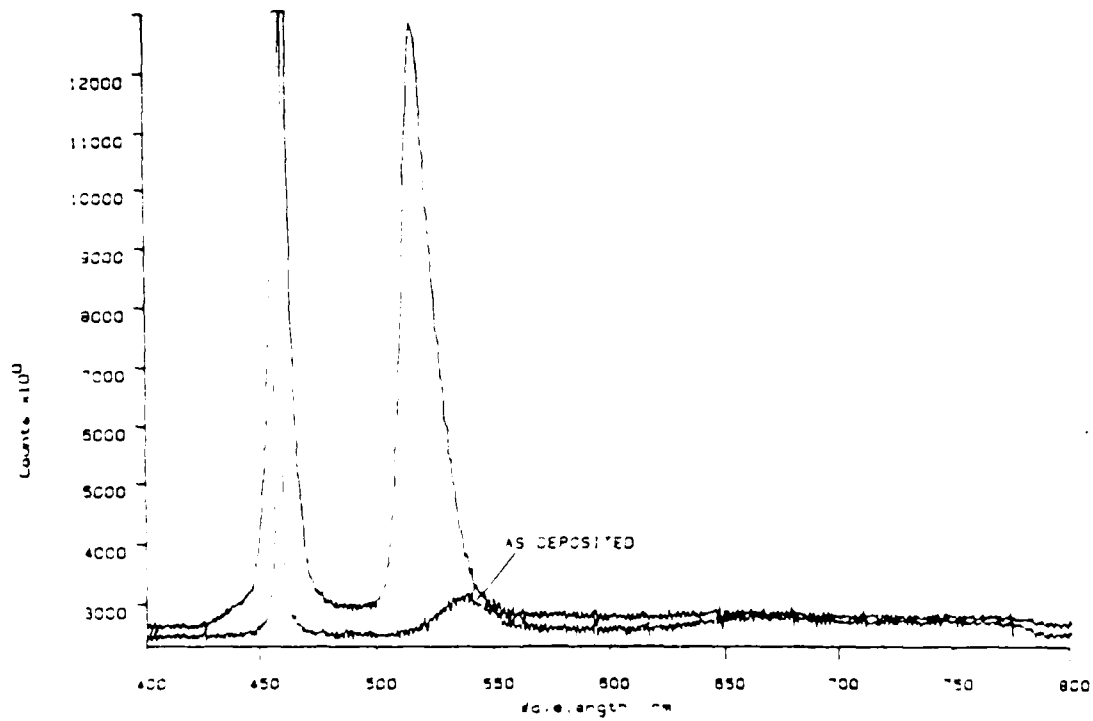


Figure 75 Low resolution photoluminescence spectra of heat treated and as-deposited thin films, showing relative intensities.

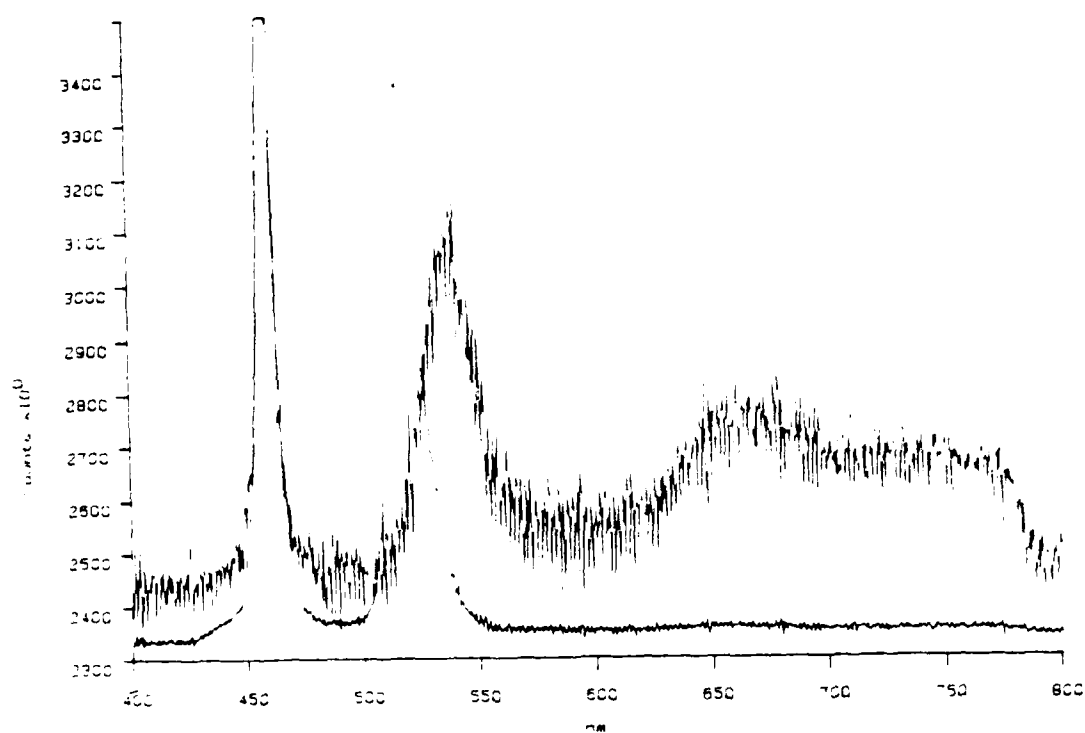


Figure 76 Same spectra as Figure 75, relative peak positions.

positions are shown in Figure 76. Both of these changes occur because the band gap is better defined after the annealing heat treatment. With this change in band structure, the band edges are sharper, which shifts the energy and increases the probability of a radiative transition. Figure 75 also shows that the intensity of the laser line has increased significantly, which is most likely due to an increase in scattering of the laser line.

All films which were heat treated to high temperatures displayed a high intensity edge emission peak and the peak position was found to be nearly the same. One difficulty with determining peak position, however, was that absorption of the laser line would cause enough heating of the film to shift the position of the peak to lower energy. A graph of the shift in peak position with incident laser power is displayed in Figure 77. At very low powers only a small shift occurs, but at higher incident powers the shift is significant. At even higher incident powers the focussed laser beam would cause vaporization of the thin film. Very low incident laser powers were therefore used to study the room temperature photoluminescence of thin films, although low power excitation reduced the intensity of the emission.

The problem with power dependent peak shift was reduced considerably by cooling the thin film with the cold finger and acquiring photoluminescence spectra at low temperature. As with UV-visib' spectroscopy, several significant changes in thin film photoluminescence are observed when the film is cooled to 9° K. First, the green edge emission band increases in intensity and shifts to a higher energy corresponding to the increase in band gap energy with

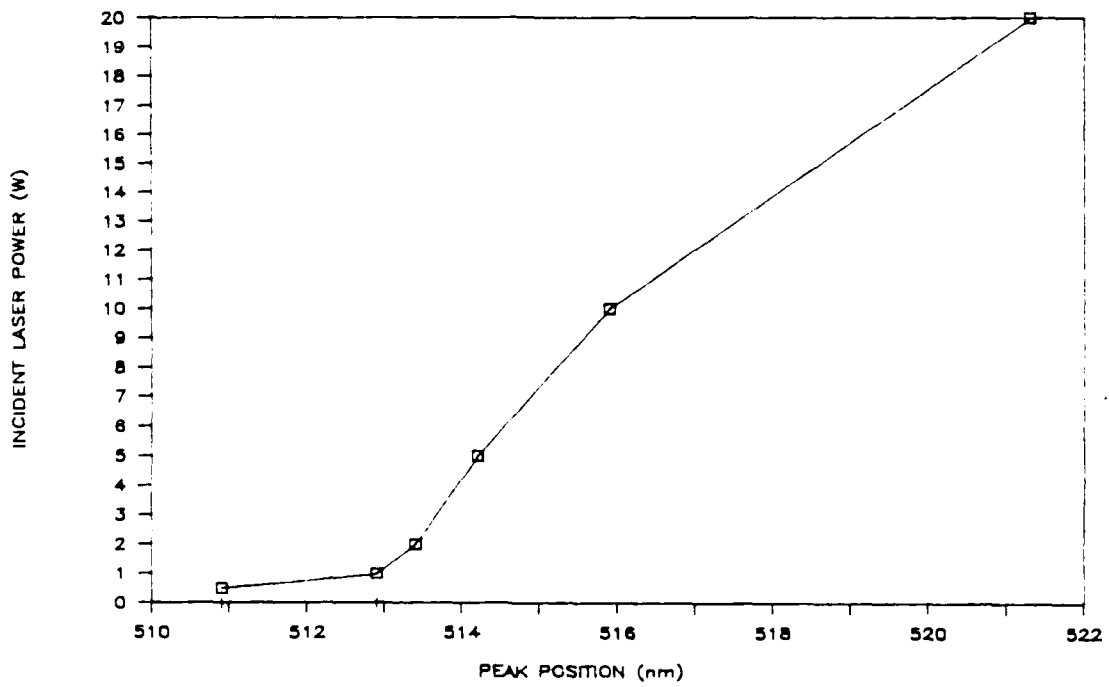


Figure 77 Graph of band edge luminescence peak position versus incident power.



decrease in temperature. Second, the peak position becomes less sensitive to incident power levels, i.e. no shift occurs unless very high powers are used. Finally, the most significant change which corresponds to the exciton absorption peaks seen in the UV-visible spectra, is the appearance of the "blue-edge" emission peak. Because of the narrow bandwidth of this peak the high resolution grating had to be used in the OMA monochromator. A typical photoluminescence spectrum of the blue edge emission exhibited by a thin film which also displayed the measurable absorption peaks is shown in Figure 78 and a composite spectra showing the relative intensities of the two emission bands is shown in Figure 79. The sharp peak at 492.3 nm in Figure 78 corresponds to one of the exciton transitions, although it is not clear which one. The first two absorption peaks in the absorbance spectrum separated  $\approx 3$  nm should exhibit two photoluminescence peaks, but only one can be seen here. The photoluminescence spectrum obtained from the same single crystal platelet used in the absorption measurements (Figure 68b) is shown in Figure 80, compared with the blue edge emission measured in the film described above. The platelet displays both the  $I_1$  and  $I_2$  bound exciton peaks and as can be seen, the transitions are much sharper and shifted to energies higher than the photoluminescence exhibited by the thin film. The shift in position is identical to that seen in the absorption edge displayed in Figure 67b. The shape of the thin film photoluminescence is similar to the platelet; the high energy side is steeper. The peak width of the thin film emission is nearly five times wider. In other work on both on bulk single crystal CdS and CdS epitaxial thin films, exciton

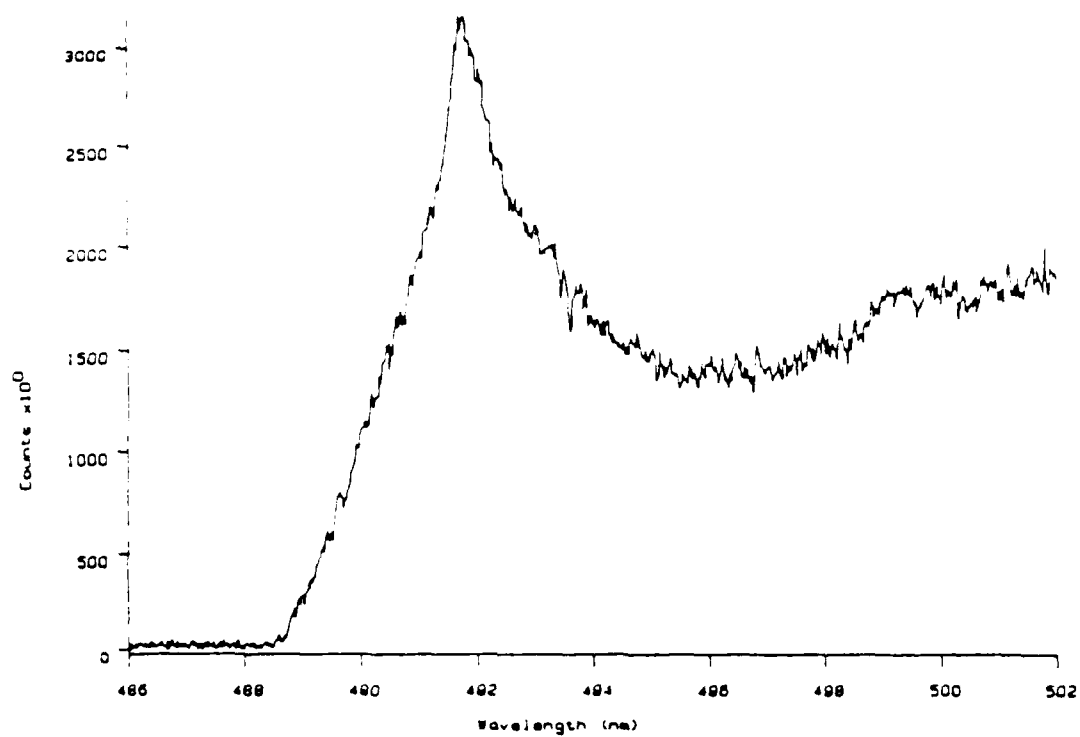


Figure 78 High resolution OMA spectrum of heat treated thin film at 9°K, showing exciton photoluminescence.

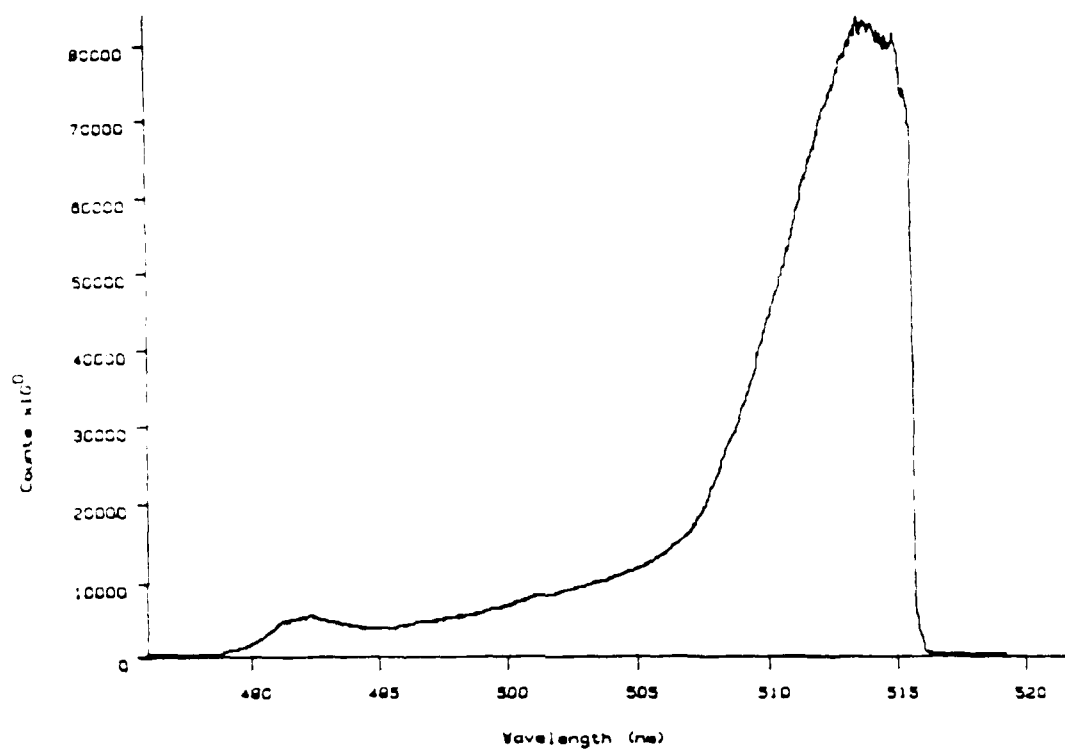


Figure 79 Composite low temperature OMA spectrum showing relative intensities of band edge and exciton emissions.

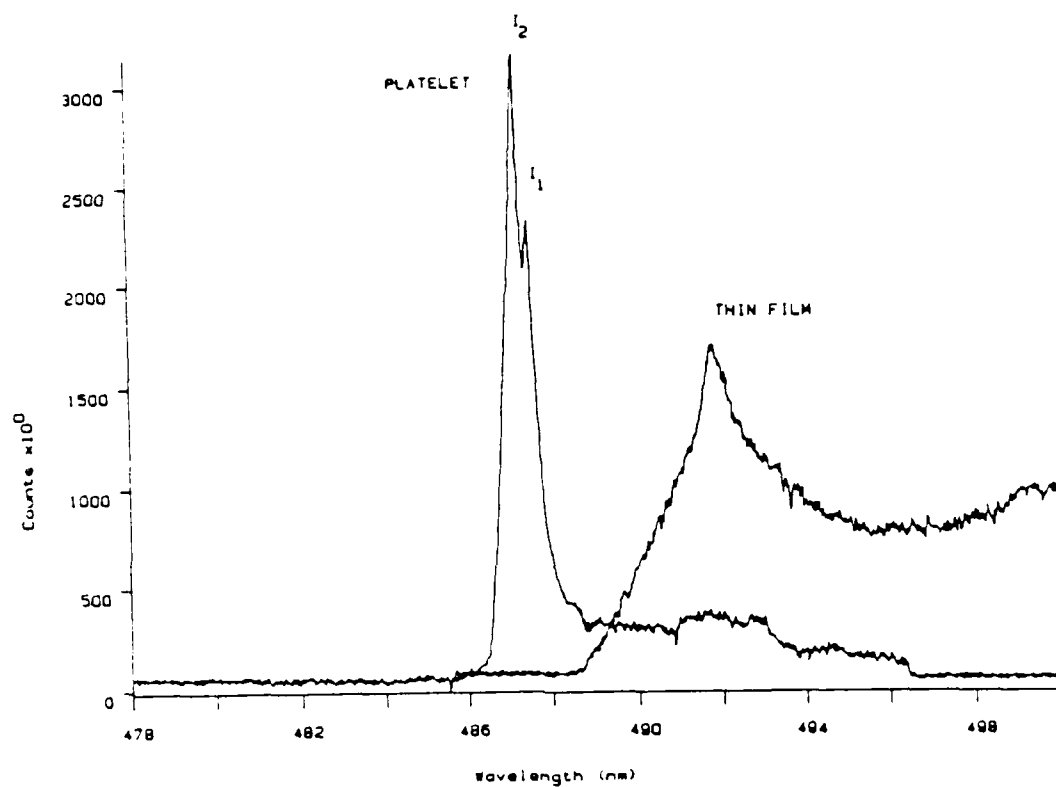


Figure 80 Low temperature OMA spectra of thin film and single crystal platelet, showing relative peak positions. The bound  $I_1$  and  $I_2$  excitons are labeled on the platelet photoluminescence.

transitions were exhibited by very sharp emission bands, although these measurements were made at lower temperatures. The measurements of single crystal platelets made here show that the exciton emissions are just as sharp at 9° K. This rules out the possibility that the emissions measured from thin films are temperature broadened. One possible reason for the observed broadening may be orientational broadening or the presence of grain boundaries. All materials which have displayed sharp exciton photoluminescence have been essentially single crystals. The impurity centers near grain boundaries which excitons are bound to may vary in energy slightly from those impurity centers within the interior of grains. This might produce the broadening of the exciton photoluminescence observed in polycrystalline thin films.

The photoluminescence spectra displayed here exhibits another difference from the absorbance spectra. The three absorbance bands were characterized as free exciton transitions, based on their position and shape. The blue edge emission exhibited by thin films, however, is more characteristic of bound exciton transitions. As previously explained, these are excitons which are bound to impurity sites. Usually the impurity is a neutral acceptor or neutral donor, which give rise to an  $I_1$  or an  $I_2$  bound exciton, respectively. It is certainly reasonable to expect that these types of impurity centers exist in the thin films studied here. Sulfur interstitial atoms or cadmium vacancy atoms could act as donor impurity sites, which correlates well with the single peak exhibited in the blue-edge emission of thin films. However, compared to the single crystal platelet photoluminescence, the

blue-edge emission is certainly broad enough for both bound excitons to be present. The bound exciton is a much stronger transition, so it should be easier to detect in photoluminescence measurements. The free exciton emission may be too low in intensity to detect. For absorption measurements the cross section of the free exciton is much larger than the bound exciton, because it does not have the same momentum constraints as the bound exciton. Therefore, the absorption spectra of free excitons should be broad and the bound exciton should exhibit a sharp absorption band. Estimations show that the UV-VIS spectrophotometer may not have a high enough resolution to observe the bound exciton absorption peaks. Photoluminescence on the other hand does not have the same momentum constraints, therefore the emissions will have different characteristics. Since the bound exciton has both a higher oscillator strength and more efficient radiative conversion, bound excitons should be more predominant in photoluminescence spectra.

The blue edge emission displays a temperature dependence similar to optical absorption. This is shown in Figure 81. As the temperature is increased, the photoluminescence peak shifts to longer wavelengths (lower energy) and decreases in intensity. As with the UV-visible spectra, the peak is still present at 40° K, but at 100° K it becomes indistinct. The Figure also shows that with an increase in temperature the intensity of the green edge emission peak decreases. The decrease occurs because as the temperature is increased, more phonons become available to cause non-radiative transitions.

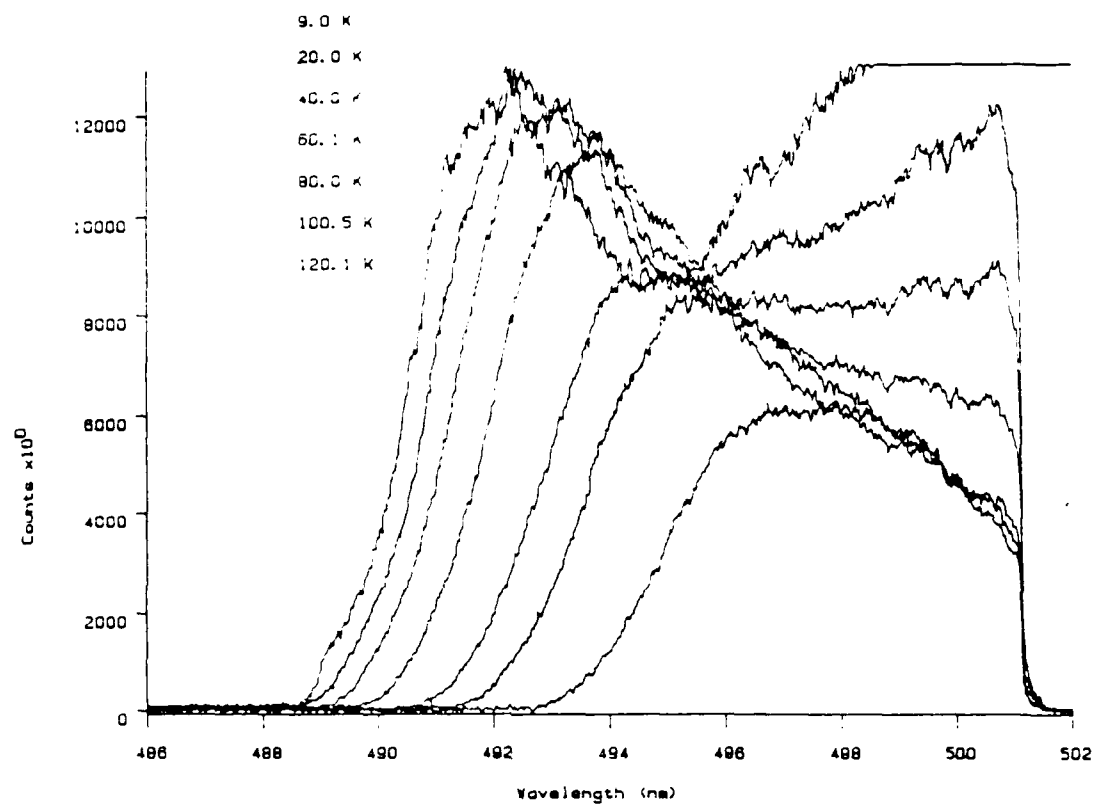


Figure 81 Temperature dependence of blue edge photoluminescence.

Raman spectroscopy

The photoluminescence measurements described above were conducted by exciting the films with a laser beam of energy much greater than the band gap. Excited states which are generated must first drop to a lower energy corresponding to either an impurity level, or an exciton level by way of a non-radiative transition before a radiative transition can occur. When an excitation energy is used that is very close in energy to the excited state, the energy can be absorbed and then scattered by a phonon state. The scattering by the phonon results in the re-emission of the light at a different frequency. Because the excitation energy is very close to the excited state level, a resonance effect takes place and an enhancement of the scattering results. This process is called resonant Raman scattering and in thin films it was found to be a very pronounced effect when a laser energy near the energy of the exciton level was used to excite the film. Resonant Raman scattering by the longitudinal optical (LO) phonon of the 488 nm laser line would result in a series of equally spaced peaks that were shifted  $\approx 300 \text{ cm}^{-1}$  from the laser line. These peaks were very intense and could be measured with either the OMA or Raman spectrometers. A typical spectrum of the first two LO phonon peaks which was acquired with the OMA and plotted in terms of Raman shift from the laser line is shown in Figure 82. This spectra was acquired with similar scan parameters and laser intensity as photoluminescence spectra, but the intensity of the 1LO phonon is much greater than any photoluminescence peak. The temperature dependence of this emission is shown in Figure 83. A similar low temperature spectrum obtained with the Raman



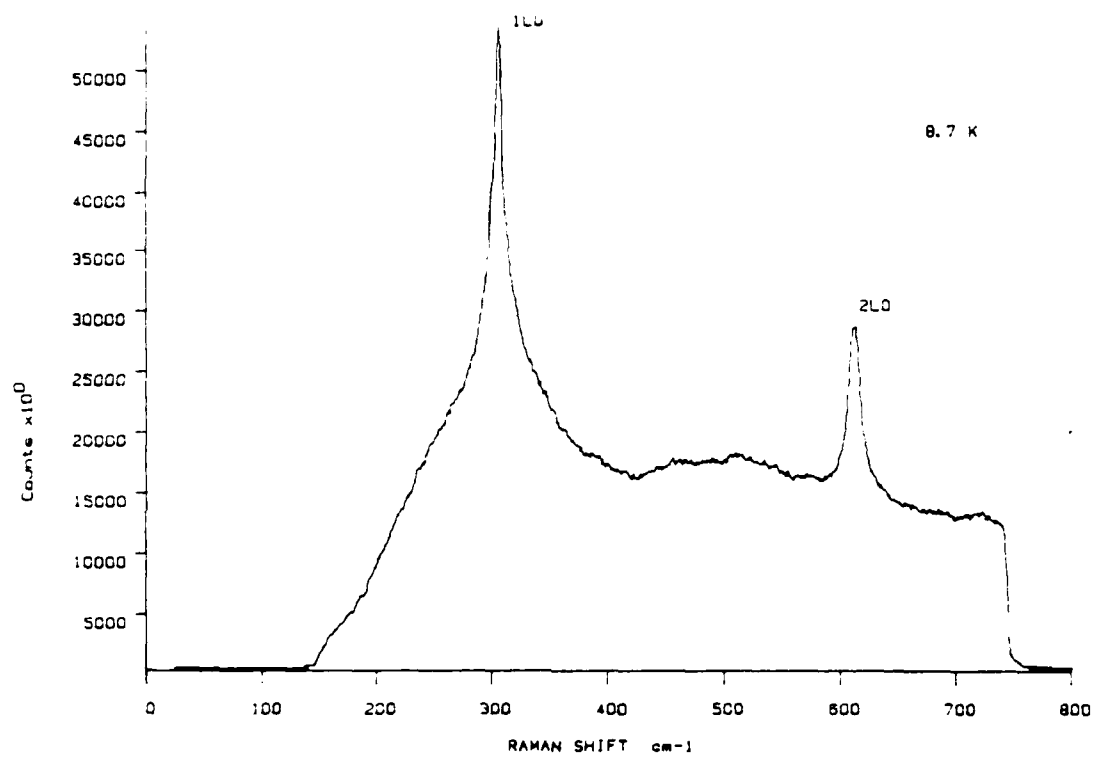


Figure 82 Longitudinal optical (LO) resonant Raman peaks measured with OMA.

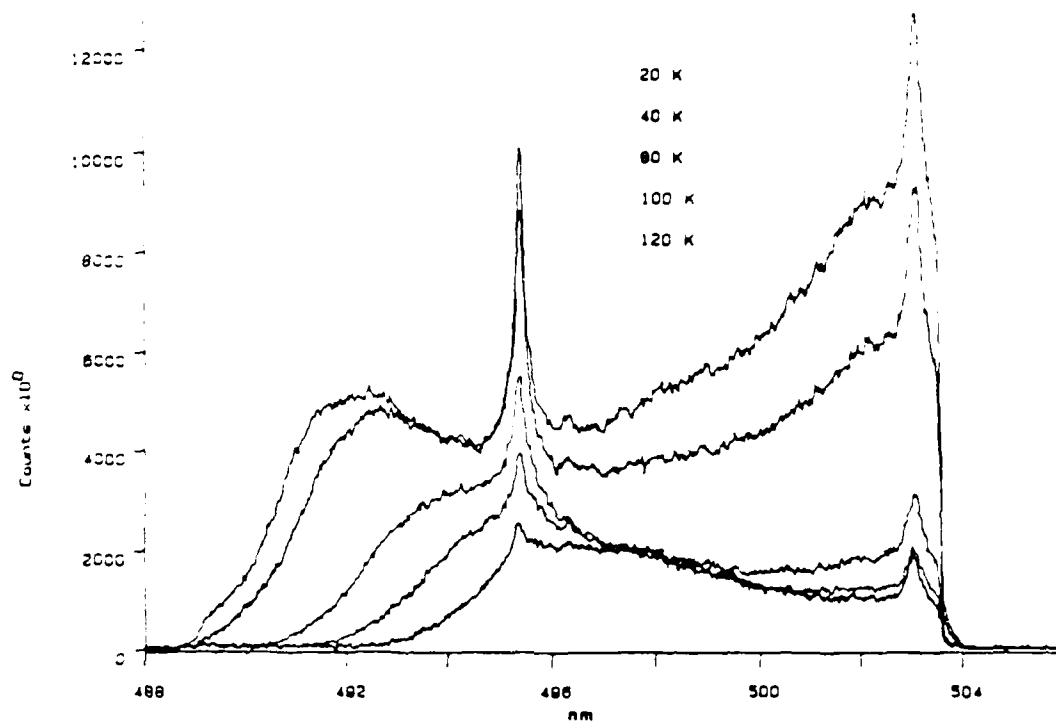


Figure 83 Temperature dependence of resonant Raman peaks.

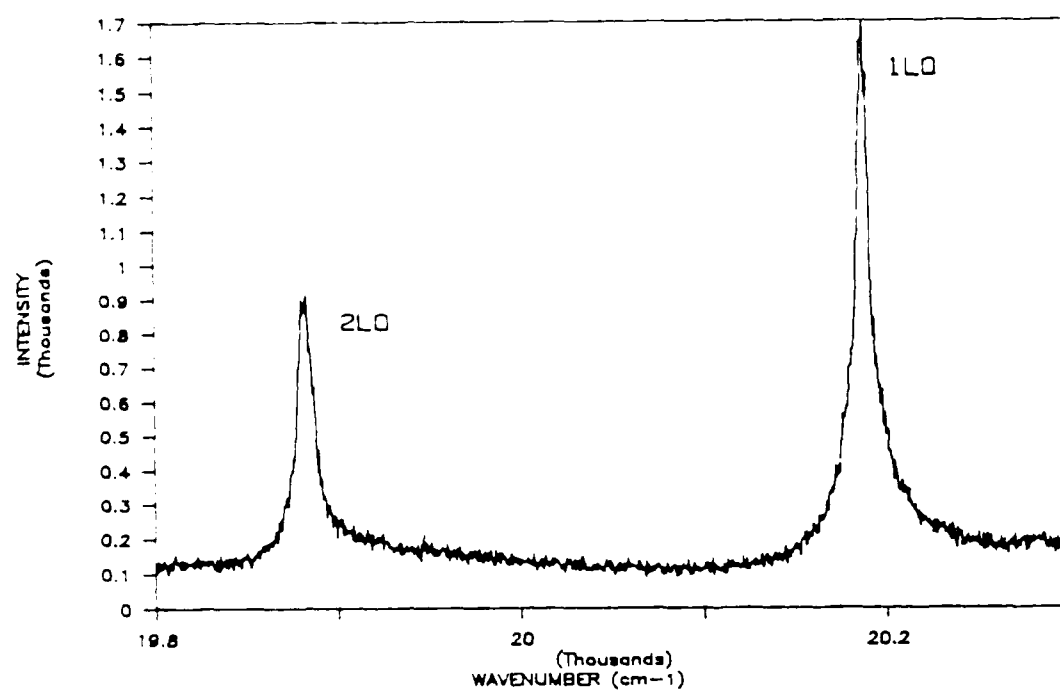


Figure 84 Same LO peaks displayed in Figure 82, shown here measured with the Raman spectrometer.

spectrometer and plotted in wavenumbers is displayed in Figure 84. The same laser power was used to excite the sample, but as can be seen a much lower intensity is measured. This indicates how much lower the light gathering ability of the Raman is compared to the OMA. The spectra however, also show that the resonant Raman effect is strong. Laser powers for normal Raman spectroscopy typical are in the range of a few watts. Even with this high power the Raman scattered peaks are very low in intensity. The laser power used to excite the samples measured in this study was only one milliwatt! The high intensity of the 1LO peak is due to a strong interaction with the exciton state. This is further proof of the existence of exciton levels in the polycrystalline thin films.

#### COSAD Optical Properties

The microstructure analysis described in the physical properties section has indicated that it is possible to produce structures with finely dispersed CdS crystallites in a glass matrix thin film. The important question about these structures is whether quantum confinement occurs, which would be indicated by a shift in the optical absorption edge to higher energies. Unfortunately, a shift could also be produced by a change in composition. Since COSAD1 films were made with a high CdS content, which once heat treated, leads to structures too large for quantum confinement, it would be expected that any shift in the band edge would be due to compositional effects. On the other hand COSAD2 films should exhibit a shift due to quantum confinement, because of the small particle size displayed in these films.

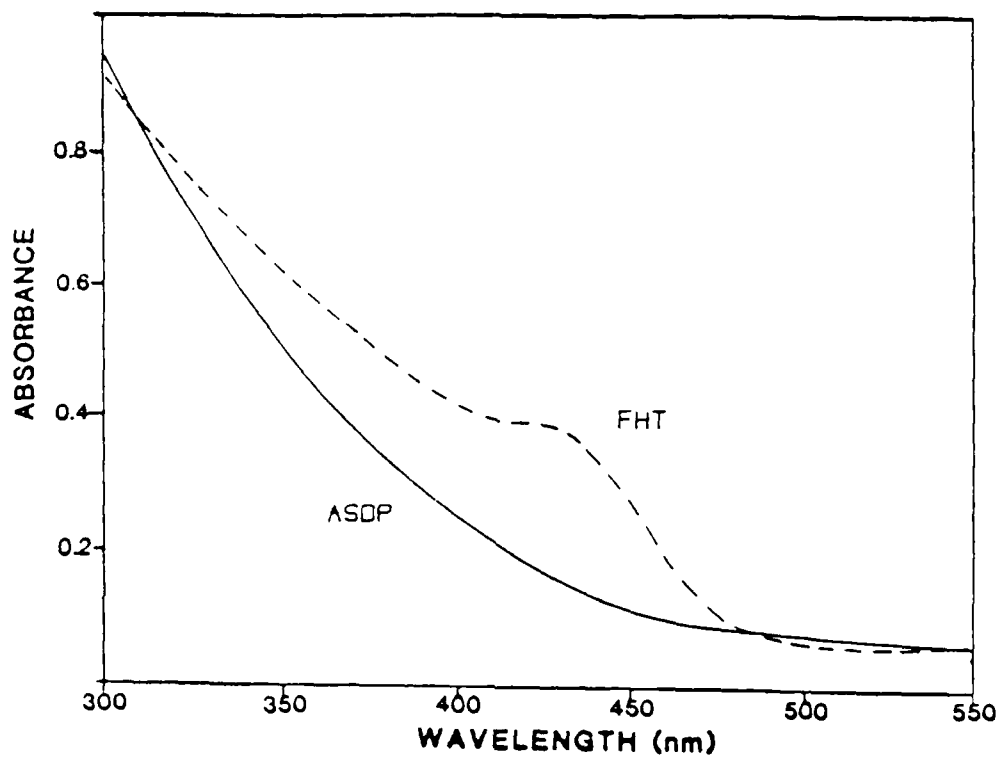


Figure 85 Room temperature absorbance spectrum of COSAD1 thin film. As-deposited (ASDP) and after heat treatment to 650° C, 60 minutes (FHT).

A typical absorbance spectrum of an as-deposited COSAD1 film is shown in Figure 85. The high absorption tail at short wavelengths is due to the glass matrix. This type of absorption is an indication of a nonstoichiometric oxygen content and has been shown to occur in other glasses which were sputter deposited with an argon plasma.<sup>60</sup> The spectrum of the as-deposited COSAD film shown in the Figure exhibits no appearance of a band edge, which is inconsistent with the microstructural analysis that indicated a semi-crystalline structure. Also shown in Figure 85 is the absorbance spectrum of a COSAD1 type film heat treated to 650° C in an air atmosphere. This spectrum, at first, certainly appears to be the result of quantum confinement; the band edge has shifted to 460 nm (2.70 eV) and the exciton shoulder is more pronounced. Microstructure analysis on this type of film however, indicated a crystallite size much too large for quantum confinement, which means that this shift in band edge energy is most likely a crystal composition effect. Further proof that this is a chemical shift is shown in Figure 86 which displays the spectrum of a COSAD1 type film heat treated in an argon atmosphere. The band edge shift is less and the exciton shoulder is less pronounced.

It is probably not correct to call the feature on the absorption edge an exciton shoulder, as the shape of this feature does not change considerably as the temperature is decreased. In pure films of CdS the room temperature shoulder resolved into two sharp absorption bands at low temperatures. As shown in Figure 87 the shoulder does not appreciably change shape at 9° K and there is only a small shift in the band edge.

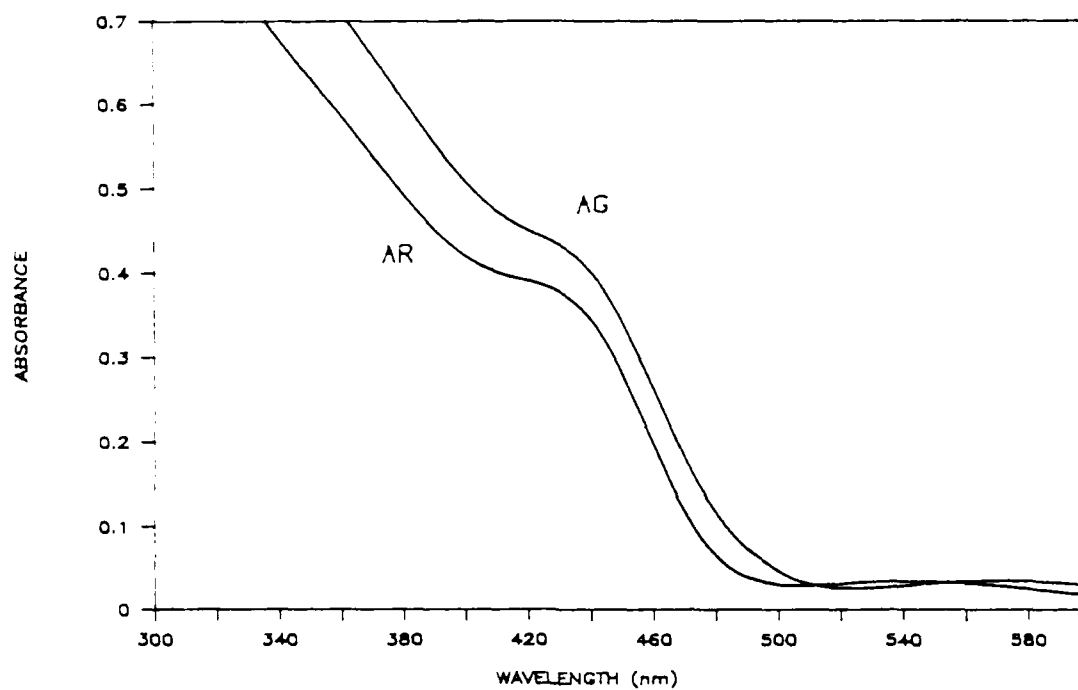


Figure 86 Room temperature absorbance spectrum of COSAD1 thin film heat treated in air (AR) and argon (AG), at 600° C, for 30 minutes.

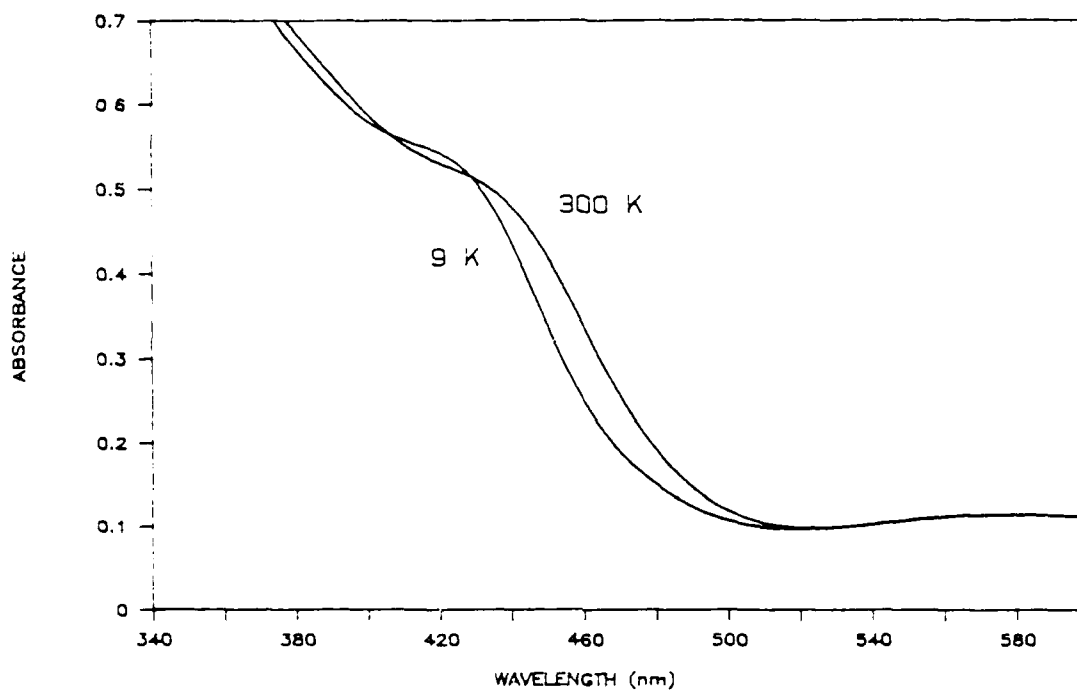


Figure 87 Low temperature absorbance spectrum of COSAD1 thin film.



A much different absorbance spectrum is displayed by the COSAD2 type films. Shown in Figure 88 are the spectra of both an as-deposited and a heat treated thin film. Unlike COSAD1 films this type of film shows the appearance of a band edge which is shifted to a very high energy, even in the non-heat treated state. This is an interesting result, because although the microstructure of this type of film is very small, it appeared to be amorphous. Heat treatment to 600° C in an argon atmosphere produced only a small change in the edge position, but it was still shifted to a higher energy than COSAD1 films. The large shift in band energy must be related to a confinement process. Another interesting result is indicated by the absorbance scale, which is an order of magnitude less than the scale used to measure COSAD1 films. This is an indication that there is considerably less CdS in the structure of COSAD2 films.

Unfortunately no photoluminescence spectra could be obtained from either type of COSAD film. This may be due to a dilution effect, due to both a low CdS concentration in these films and a small thickness. Also, because the band edge was shifted to such a high energy in the COSAD2 films it was not possible to excite the sample, even when using the highest energy argon laser line.

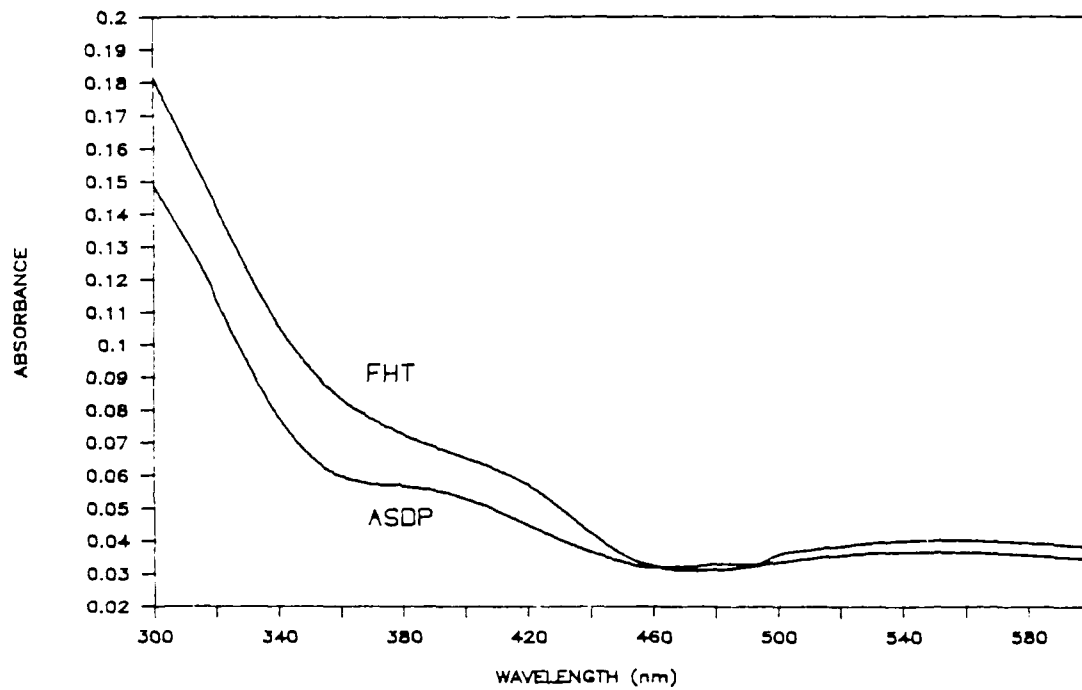


Figure 88 Room temperature absorbance spectrum of COSAD2 thin film. As-deposited (ASDP) and after furnace heat treatment at 650° C for ten minutes (FHT).

## CHAPTER VI CONCLUSIONS

1. RF magnetron sputtering of cadmium sulfide has proven to be a valuable deposition technique for producing high optical quality thin films. The as-deposited thin film structure can be controlled by a variation of the deposition rate and substrate temperature. Unique structures can be produced by deposition onto substrates held at  $\text{LN}_2$  temperatures. A low density columnar structure is produced in which small microcrystallites are embedded in a semi-amorphous matrix. Electron diffraction experiments indicate that the microcrystallites are highly faulted, which leads to a degradation of the optical properties. The crystallographic defects provide defect states in the band gap which are indicated by the large amount of band tailing observed in optical absorption spectra. Optical properties are further degraded by the presence of excess cadmium. The large number defects responsible for band tailing provide non-radiative transitions so that band edge photoluminescence is not observed in these films.
2. High density fine grained polycrystalline films result when sputtered material is deposited onto substrates held at room temperatures. Many of the grains appear to be faulted, with the presence of stacking faults and microtwins. The number of faults increases with the deposition rate, therefore the faults are related to the growth rate of the thin film. Electron and X-ray diffraction

experiments indicate the film has a very strong preferred orientation, with the basal plane parallel to the substrate plane. It is not clear if this orientation is nucleation or growth controlled. The close-packed plane is the slow growth direction, which would indicate the preferred orientation is controlled by nucleation. This same orientation, however, was observed over a substrate temperature range of nearly 500° K and with various substrate materials. It is unusual that a nucleation controlled process would extend over such a large temperature range, although with this material the nucleation range may be very wide. A combined effect may actually control the process if the crystallites can be modeled as thin disks. Once the initial orientation is nucleated, only a small step in the z-direction could cause a large increase in growth in the lateral direction. X-ray line shifts indicate films deposited at high rates contain large residual tensile stresses, which leads to their exfoliation when exposed to the atmosphere. Optical absorption spectra indicate some band tailing to be present in room temperature deposited films, which is related to the crystallographic defects that are present. The band structure in these films is defined well enough so that band edge photoluminescence is exhibited; however, the large number of defects present in the band gap leads to a decrease in the photoluminescence yield.

3. When CdS is deposited onto substrates held at high temperatures a reduction in the number of crystallographic defects is observed. With higher substrate temperatures, adsorbed atoms have more energy to move around and find favorable positions with which to bond. The preferred orientation is still maintained, however, other hexagonal orientations

can be observed because other growth planes may become active at higher temperatures. With the decrease in the number of crystallographic defects, band tailing is reduced indicating a better defined band gap; however, a shift in the absorption edge is observed. The shift is due to a change in composition, as these films are found to be nonstoichiometric. A higher sulfur content in these films occurs because the sticking coefficient of cadmium is reduced at higher substrate temperatures. Due to large nonuniformities in the composition across the film area a degradation in the optical properties at wavelengths longer than the band edge occurs.

4. To produce the highest quality thin films for optical applications a post deposition heat treatment must be instituted to remove defects created by the deposition and growth processes. Heat treatments of less than 500° C cause a small change in grain size which appears to be linear with the increase in heat treatment temperature. Low temperature treatments also lead to a small change in the optical properties. Band tailing is still present and photoluminescence yield is still low. With heat treatments to 500° C and above, a dramatic increase in grain size occurs. Higher temperatures may provide the activation energy required for impurity assisted diffusion at the grain boundaries. Associated with this grain growth is a reduction in the amount of band tailing and a large increase in the photoluminescence yield. These results are due to a removal of crystallographic defects with grain growth, which are related to defects in the band gap.

5. For the first time absorption bands and photoluminescence associated with exciton states have been observed in polycrystalline

thin films. Associated with the changes in microstructure that occur upon heat treatment to high temperatures is the appearance of exciton levels. These levels appear as sharp absorption bands or as low intensity blue edge photoluminescence. There is, however, considerable broadening of the blue edge photoluminescence associated with the exciton levels. The shape of the emission peak is similar to that observed in single crystal platelets; however, it is  $\approx 5$  times wider. This broadening may be due to orientation effects or the presence of grain boundaries which provide different environments for the annihilation of excitons to produce the photoluminescence.

6. Heat treating films by rapid thermal anneal (RTA) produces films which also exhibit exciton levels. The grain size of these films is three times smaller than furnace annealed thin films, which indicates that for excitons to be present in sputter deposited thin films, only the annealing of certain defects is required, not large grain growth. The actual defects which must be removed are not known, but they must be those associated with band tailing, as the appearance of exciton levels is coincident with the removal of band tailing. From TEM micrographs of unheat treated films, these defects most likely are the stacking faults associated with microtwins.

7. Thin films were found to be nonstoichiometric, particularly after high temperature heat treatments where the sulfur content was found to increase to approximately 4%. The increase in sulfur is obviously due to a loss of cadmium, which has a much higher vapor pressure than sulfur at the heat treatment temperature. Only a small portion of the excess sulfur may exist interstitially, as the indication from other

chalcogenide compounds is that this type of defect would be limited to less than 1%. Calculations show that if all the excess sulfur were present at the grain boundaries as a thin layer, then this amount of sulfur would be six to seven monolayers, which corresponds to a grain boundary layer  $\approx 14 \text{ \AA}$  thick. For an average grain size of  $3000 \text{ \AA}$ , this is not an unreasonable thickness for grain boundaries. The uneven contrast observed in X-ray maps of sulfur in heat treated films indicates that there is an uneven distribution of sulfur and therefore it may exist as small pockets, instead of a thin evenly distributed second phase. The presents of this second phase does not effect the optical properties significantly, but it may be responsible for the large resistivity observed in high temperature heat treated thin films.

8. The limited study on COSAD films indicates that it is possible to produce a structure where very fine particles of a semiconductor are embedded in a glass matrix. By variation of the amount of CdS that is co-deposited a wide variation in the structure of the film can be accomplished. High amounts of CdS produce a film which readily phase separates during examination in the TEM. When this type of film is heat treated to high temperatures a very distinct two phase structure results where the CdS is dispersed as a bimodal distribution of spherical particles. The larger particles have an average size of  $500 \text{ \AA}$ , and the smaller particles are sized at  $200 \text{ \AA}$ . When very low concentrations of CdS are co-deposited, then a structure which does not phase separate results. After heat treatment, very small particles of less than  $70 \text{ \AA}$  result.

9. Shift of the absorption edge in COSAD films appears to be mostly a chemical shift and not due to quantum confinement. Heat treatments to the same temperatures and times, but in different atmospheres result in different shifts of the band edge. Heat treatments in an oxidizing atmosphere produced a larger shift in the band edge than heat treatments in an inert atmosphere. This could be due to the formation of cadmium oxide, which has a larger band gap energy than cadmium sulfide. The large shift of the band edge, however, cannot be entirely due to the formation of an oxide, as the edge observed in films treated in inert atmospheres is still considerably shifted from the energy of pure CdS. There may be other unknown chemical effects or some confinement process occurring. Another possible reason for the shift could be due to surface states, which would be enhanced by the large difference in dielectric constant at the interface and by the large stress created by the high curvature of the spherical particles.
10. The broad shoulder on the top of the absorption edge, which appears similar to the room temperature exciton shoulder observed in pure films of CdS is of unknown origin in COSAD films. The shoulder does not change shape with decreases in temperature, although there still could be considerable orientational broadening even at low temperatures. Unfortunately no photoluminescence was observed in COSAD films primarily due to a dilution effect, arising from the thickness of the films and the relatively small amount of CdS. Photoluminescence would have indicated the presence of excitons.



## CHAPTER VI FUTURE WORK

There are several aspects of cadmium sulfide and COSAD thin films which require further study and investigation.

Obviously, the first study is to make a nonlinear optical measurement to determine if the exciton states in the pure films of CdS can be saturated to produce an effect that is comparable to the large nonlinear refractive index observed in single crystal platelets. Since the films are of high enough optical quality to act as thin film Fabry-Perot interferometers, a very simple intensity saturation experiment could be conducted.<sup>10</sup> The only difficulty in this experiment is the need for a high resolution tunable dye laser which can be operated in the wavelength region of 488 nm, the wavelength required for exciton saturation.<sup>4</sup> A shorter wavelength, high speed pulsed laser could also be used to measure the nonlinear absorption, (due to a free carrier plasma) by measuring the temporal waveform of a transmitted pulse.<sup>26</sup> If this pulsed laser could be used with the dye laser, the change in the waveform as the laser is tuned near the exciton level would provide valuable information. Finally, if a nonlinear intensity saturation was observed, then a pump-probe experiment could be carried out to determine the switching speed of the thin film Fabry-Perot.<sup>11</sup>

Further work on the stoichiometry as a function of heat treatment atmosphere should be carried out to determine the influence of sulfur

concentration on the band structure. Heat treatments in equilibrium sulfur or cadmium atmospheres may produce stoichiometric thin films. It would be interesting to know if the electrical conductivity and photoluminescence change when the excess sulfur is removed. Other post deposition treatments which should be further investigated are heat treatments by RTA, to determine if very small, defect free crystals could be produced in a thin film.

A large research effort should be directed towards further investigations of COSAD thin films, since these films appear quite promising for quantum confinement devices. Studies of the deposition conditions and heat treatment schedules on the microstructure development in these films could provide both a parallel confirmation of the effects observed in bulk filter glasses and permit a further understanding of the confinement processes that take place in these materials. Photoluminescence studies of thicker films would positively identify a confinement process, by correlation of the blue shift with particle size. If well characterize COSAD thin films could be produced, nonlinear optical measurements are easily made because these films on the proper substrate should act as low loss planar waveguides. When prisms are used to couple light into and out of thin film waveguide, the angle at which the light couples is dependent upon the refractive index of the film. The nonlinearity of these films could be determined by measuring a power dependent coupling angle. If these experiments proved successful, then the next step would be either to attempt logic gate experiments by utilizing small scale integration, or

examine a different semiconductor to determine if a confinement process could be induced.

APPENDIX A  
BASIC PROGRAM USED FOR EXTERNAL CONTROL OF LAMBDA 9

```
1000 REM LAMBDA 9 COMMUNICATIONS PROGRAM
1010 REM VER. UVVIS6.BAS
1015 REM WRITE COMMAND USED TO OUTPUT DATA TO FILE NAME *.PRN
1020 REM FOR ASYST PROGRAM INPUT AND LOTUS WORKSHEET
1030 CLEAR:CLOSE:KEY OFF:CLS
1040 DIM X(3000)
1045 REM ARRAY MUST BE LARGE ENOUGH TO ACCOMMODATE ENTIRE SCAN
1050 INPUT "TRANSMISSION OR ABSORBANCE SCAN T/A ";ANS$
1060 IF ANS$="T" THEN 1070 ELSE 1080
1070 SB=0:PRINT "TRANSMISSION SCAN":GOTO 1090
1080 SB=5:PRINT "ABSORBANCE SCAN"
1090 INPUT "SELECT ABSCISSA MAX ";AH
1100 INPUT "SELECT ABSCISSA MIN ";AL
1110 INPUT "SELECT SCAN SPEED ";SS
1120 INPUT "SELECT DATA INTERVAL ";DI
1130 INPUT "SELECT RESPONSE ";FR
1140 INPUT "SELECT SLIT WIDTH ";SL
1150 SL=SL*100:REM CONVERT SLIT SETTING
1160 REM CALCULATE NUMBER OF DATA POINTS
1170 XPTS=(AH-AL)/DI
1180 INPUT "SELECT NORMAL (1) OR EXTENDED RANGE (2) ";RA
1190 INPUT "SELECT CHART REGISTRATION: OFF(0),SERIAL DASH (1),
OVERLAY DASH (2)";CR
1200 IF CR=0 THEN 1260
1210 INPUT "SELECT PRINTER FUNCTION: OFF (0),GRID + SCALE (1) ";PR
1220 INPUT "SELECT PEN LINE MODE (1-4) ";PE
1230 INPUT "SELECT RECORDER FORMAT (nm/cm) ";RS
1240 INPUT "SELECT ORDINATE MAXIMUM ";MX
1250 INPUT "SELECT ORDINATE MINIMUM ";MI
1260 IF CHG$="Y" THEN 1350
1270 REM OPEN COMMUNICATIONS PORT
1280 OPEN "COM1:4800,E,7,1" AS#1
1290 PRINT #1,"$RE 0"
1300 PRINT #1,CHR$(17)
1310 INPUT #1,D$
1320 PRINT #1,"$PA 2"
1330 INPUT #1,D$
1340 PRINT D$
1350 REM SET UP INSTRUMENT
1360 PRINT #1,"$SB" + STR$(SB)
1370 INPUT #1,D$
1380 PRINT #1,"$AH" + STR$(AH)
1390 INPUT #1,D$
1400 PRINT #1,"$AL" + STR$(AL)
```

```

1410 INPUT #1,D$
1420 PRINT #1,"$SS" + STR$(SS)
1430 INPUT #1,D$
1440 PRINT #1,"$DI" + STR$(DI)
1450 INPUT #1,D$
1460 PRINT #1,"$FR" + STR$(FR)
1470 INPUT #1,D$
1480 PRINT #1,"$SL" + STR$(SL)
1490 INPUT #1,D$
1500 IF CR=0 THEN 1590
1510 PRINT #1,"$CR" + STR$(CR)
1520 INPUT #1,D$
1530 PRINT #1,"$RS" + STR$(RS)
1540 INPUT #1,D$
1550 PRINT #1,"$PE" + STR$(PE):INPUT #1,D$
1560 PRINT #1,"$PR" + STR$(PR):INPUT #1,D$
1570 PRINT #1,"$MX" + STR$(MX):INPUT #1,D$
1580 PRINT #1,"$MI" + STR$(MI):INPUT #1,D$:GOTO 1600
1590 PRINT #1,"$CR 0":INPUT #1,D$
1600 PRINT #1,"$RA" + STR$(RA):INPUT #1,D$
1610 PRINT CHR$(10);"CONFIRM SELECTED VALUES ON LAMBDA 9 SCREEN"
1620 INPUT "CHANGE ANY VALUES Y/N ";CHG$
1630 IF CHG$="Y" THEN 1640 ELSE 1650
1640 CLS:GOTO 1050
1650 PRINT #1,"$SC"
1660 INPUT #1,D$
1670 PRINT D$
1680 REM PRINT DATA
1690 FOR I=1 TO XPTS+12
1700 INPUT #1,X$
1710 S$=LEFT$(X$,1)
1720 S=VAL(S$)
1730 IF S=0 THEN S=LEN(X$) ELSE 1750
1740 X1$=RIGHT$(X$,S-1):X$=X1$
1750 X(I)=VAL(X$)
1760 NEXT I
1770 INPUT "STORE DATA ON DISK Y/N ";ANS$
1775 IF ANS$="Y" THEN 1780 ELSE 1910
1780 INPUT "INSERT DATA DISK IN DRIVE A AND TYPE R ";R$
1790 IF R$="R" THEN 1800 ELSE 1780
1800 INPUT "NAME OF FILE (MAXIMUM OF 8 CHARACTERS)";FILN$
1810 IF LEN(FILN$)>8 THEN 1800
1820 IF LEN(FILN$)=0 THEN 1800
1830 OPEN "O",#2,"A:"+FILN$+".PRN"
1840 N=XPTS+11
1850 PRINT #2,AH:PRINT #2,AL:PRINT #2,DI
1860 FOR I=1 TO 11:WRITE #2,X(I):NEXT I
1870 IF SB=0 THEN SCALE=200 ELSE 1890
1880 FOR J=11 TO N:WRITE #2,X(J)/SCALE:NEXT J:GOTO 1910
1890 SCALE=10000

```

```
1900 FOR J=11 TO N:WRITE #2,X(J)/SCALE:NEXT J
1910 PRINT #1,"$MA":INPUT #1,D$:PRINT D$:CLOSE #2
1920 INPUT "MAKE ANOTHER RUN OR STOP R/S ",ANS$
1930 IF ANS$="R" THEN 1940 ELSE 1960
1940 INPUT "ENTER NEW VALUES OR USE CURRENT SETUP N/C";ANS$
1950 IF ANS$="N" THEN 1030 ELSE 1290
1960 STOP:END
```

## APPENDIX B ELLIPSOMETRY

When an elliptically polarized beam of light is reflected from a surface, its polarization direction is changed by the refractive index and absorption coefficient of the reflecting surface. If the surface is a thin film, then the film thickness also enters into the reflection equations (Drude Equations).

Ellipsometer instruments can be purchased with prepackaged computer programs to calculate the film thickness, refractive index and extinction coefficient from the ellipsometry data.

We recently acquired a Gaertner Ellipsometer and conducted tests with the following results.

a) While the ellipsometer uses a laser source, and 0.01 degree of resolution, for the polarizer and analyzer settings, the data was not accurate enough to measure a standard.

b) The program supplied was adequate for substrates with vastly different indices from the deposited films, but was totally useless for systems where the indices were even relatively far apart, such as CdS films on silica substrates.

Therefore, an intensive analysis of the sources of error in both the experimental apparatus and in the calculation program was conducted. The results showed that with some modifications in the instrument and with a new program, the ellipsometer can be used very

accurately to measure the film refractive index and, if the thickness is approximately known, to measure the film thickness.

### Instrument Modifications

Sources of error in an ellipsometer are numerous but only a few have a large effect on the results.

1. Polarizer, Analyzer. Their accuracy is very adequate ( $0.01^\circ$ ), even for fine work. Their relative alignment can be checked by placing the arms of the ellipsometer in line with each other. After removing the compensator the positions of maximum transmission and extinction can be checked. Angular tracking can then be checked by rotating the polarizer.

2. Quarter wave plate compensator. Our ellipsometer has a fixed compensator at  $+90^\circ$ . By inserting it into the beam, its position can also be checked. If the compensator, is defective, it can still be used with a slight modification of the equations.

3. Incidence Angle. This is the most critical adjustment in the instrument. A variation in the angle between source and detector of less than  $1^\circ$  can change the refractive index in the first place. We found that despite a well collimated laser source, our instrument was designed to accommodate changes in the angle of incidence of more than several degrees. This was done by using a wide angle collection system with a 2cm x 2cm photocell. This very sloppy alignment was used in order to collect light from samples which were not plane parallel.



Here a modification was necessary. We placed a small aperture at the entrance to the collection optics. Then we placed the detection photocell at the end of a 30cm long tube, behind a second small aperture. The two apertures, separated by 30cm reduced the acceptance angle of the detector system to: 0.2 degrees. With the arm of the detection, this was further lowered to 0.05 degrees.

In order to accept non planar or parallel samples, the stage was adjusted to tilt until the reflected light was aligned with the detection system.

4. Multiple reflections. Imperfect substrates and thin substrates can produce multiple reflection beams, arising from substrate striae or the bottom surface. These should be masked and only the top surface reflection should be received at the detector.

Using the above alignment procedures, two standards were run every day and the angle was adjusted when necessary. Care was taken not to change the alignment until the standards were again measured. An accuracy of the 4th place in index could be obtained.

#### Data Analysis

Ellipsometry equations for the calculation of index and thickness, require a measurement of the quantities  $\chi$  and  $\Delta$ , as shown below. However, the instrument yields polarizer  $P_i$  and analyzer  $A_i$  readings. These readings can be used to calculate the values of  $\chi$  and  $\Delta$ , however, this operation is not straight forward.

The various polarizer and analyzer readings fall into four sets of readings called zones, two zones with the fast axis of the compensator set at  $+45^\circ$  and two zones at  $-45^\circ$ . There is one independent set of readings for each zone, giving four independent sets. However, both the polarizer and analyzer may be rotated by  $180^\circ$  without affecting the results, thus yielding 16 sets of readings, which can grow to 32 sets if the compensator is rotated by  $180^\circ$ .

Depending upon which set of readings one is making, the calculation of  $\chi$  and  $\Delta$  may be different. Furthermore, Brewster's angle ( $\tan \phi_B = n_1/n_0$ ) is about  $56.3^\circ$  at a glass-air interface and  $\Delta$  changes phase by  $180^\circ$  at this point. When working at ellipsometer angles of  $50^\circ$  and  $70^\circ$ , certain film substrate configurations can develop which cross Brewster's angle. This leads to the necessity to change the  $\chi$ ,  $\Delta$  definitions.

#### Calculations

The equations are well known Drude Equations which will not be reproduced here. The reader is referred to Azzam and Bashara, Ellipsometry and Polarized Light, North Holland 1977 and reference number 64. A two-step approach which was developed to solve the Drude equations to determine the refractive index and thickness will however, be outlined here. In the first step,  $n_1$  is calculated using a Lotus routine for plotting, as follows:

- a) The data is used to calculate  $\chi$  and  $\Delta$ .

b) A wide range of  $n_1$  values and  $d$  values is selected and the Drude Equations are solved for  $\chi_c$  and  $\Delta_c$ .

c) A graphical comparison of the measured  $\chi$ ,  $\Delta$  is made with  $\chi_c$  and  $\Delta_c$  for each set of  $n$  values over the range of  $d$  values. Since  $d$  varies cyclically, it is not important which  $d$  values are used as long as they span the cycle ( $\lambda$ ).

d) This allows a rapid calculation of  $n$  since the approach of the calculation to the data can be seen in the plots.

e)  $n$  can be calculated with desired accuracy.

f) Once  $n$  is known,  $d$  can be calculated from the Drude Equations using the well known quadratic formula, with possible solutions at  $\theta$ ,  $-\theta$ ,  $2m\pi-\theta$ ,  $2m\pi+\theta$  where  $m$  is the integer order number. Thus the thickness calculation cannot yield a unique value. However, if one knows the approximate thickness, so that  $m$  may be defined, then an accurate value can be obtained.

## BIBLIOGRAPHY

1. T. Y. Chang, "Fast Self-Induced Refractive Index Changes in Optical Media: A Survey," *Opt. Eng.*, 20, 220 (1981).
2. M. Warren, Y.H. Lee, G.R. Olbright, B.P. McGinnis, H.M. Gibbs, N. Peyghambarian, T. Venkatesan, B. Wilkens, J. Smith, and A. Yariv, "Fabrication and Characterization of Arrays of GaAs All-Optical Logic Gates," *Optical Bistability III*, ed. by H.M. Gibbs, N. Peyghambarian, and H.S. Smith, (Springer-Verlag, Berlin, 1985), p. 39.
3. M. Dagenais and W.F. Sharfin, "Fast All-Optical Switching at Extremely Low Switching Energy in CdS Platelet," *Optical Bistability III*, ed. by H.M. Gibbs, N. Peyghambarian, and H.S. Smith, (Springer-Verlag, Berlin, 1985), p.122.
4. M. Dagenais, "Low Power Optical Saturation of Bound Excitons With Giant Oscillator Strength," *Appl. Phys. Lett.*, 43, 742 (1983).
5. B.S. Wherret and N.A. Higgins, "Theory of Nonlinear Refraction Near the Band Edge of a Semiconductor," *Proc. R. Soc. Lond. A*, 379, 67 (1982).
6. D.A.B. Miller, S.D. Smith, and B.S. Wherrett, "The Microscopic Mechanism of Third-Order Optical Nonlinearity in InSb," *Opt. Comm.*, 35, 221 (1980).
7. R.K. Jain and M.B. Klein, "Degenerate Four-Wave Mixing Near the Band Gap of Semiconductors," *Appl. Phys. Lett.*, 35, 454 (1979).
8. A. Yariv, *Quantum Electronics*, (John Wiley and Sons, New York, 1975), chap. 8.
9. E. Abraham, C.T. Collins, and D. Smith, "The Optical Computer," *Sci. Amer.*, 248, 85 (1983).
10. D.A.B. Miller, "Refractive Fabry-Perot Bistability with Linear Absorption: Theory of Operation and Caviety Design," *IEEE J. Quant. Elect.*, QE-17, 306 (1981).
11. M. Dagenais, W.F. Sharfin, "Picojoule, Subnanosecond, All-Optical Switching Using Bound Excitons in CdS," *Appl. Phys. Lett.*, 46, 230 (1985).
12. G. Dieter, *Mechanical Metallurgy sec.ed.*, (McGraw-Hill, New York, 1961), p.139.

13. W. Albers, "Physical Chemsitry of Defects," Physics and Chemistry of II-VI Compounds, ed. M. Aven and J.S. Prener, (North-Holland Publishing Co. Amsterdam, 1967), p.137.
14. B. Segall and D.T.F. Marple, "Intrinsic Exciton Absorption," Physics and Chemistry of II-VI Compounds, ed. M. Aven and J.S. Prener, (North-Holland Publishing Co. Amsterdam, 1967), p.319.
15. B. Segall, "Band Structure," Physics and Chemistry of II-VI Compounds, ed. M. Aven and J.S. Prener, (North-Holland Publishing Co. Amsterdam, 1967), p.3.
16. F.A. Kroger, "Luminescence and Absorption of Solid Solutions in the Ternary System ZnS-CdS-MnS," Physica, 7, 92 (1940).
17. R.E. Halsted, "Radiative Recombination in the Band Edge Region," Physics and Chemistry of II-VI Compounds, ed. M. Aven and J.S. Prener, (North-Holland Publishing Co. Amsterdam, 1967), p.385.
18. R.J. Collins, "Mechanism and Defects Responsible for Edge Emmision in CdS," J. Appl. Phys., 30, 1135 (1959).
19. D.G. Thomas and J.J. Hopfield, "Optical Properties of Bound Complexes in Cadium Sulfide," Phys. Rev., 128, 2135 (1962).
20. C.H. Henry, R.A. Faulkner, and K. Nassau, "Donor-Acceptor Pair Lines in Cadmium Sulfide," Phys. Rev., 183, 798 (1969).
21. C.H. Henry, K. Nassau, and J.W. Shiever, "Optical Studies of Shallow Acceptors in CdS and CdSe," Phys. Rev. B, 4, 2453 (1971).
22. C.H. Henry and K. Nassau, "Lifetimes of Bound Excitons," Phys. Rev., 1, 1628 (1970).
23. D.G. Thomas and J.J. Hopfield, "Spin-Flip Raman Scattering in Cadmium Sulfide," Phys. Rev., 175, 1021 (1968).
24. R.C. Leite, J.F. Scott, and T.C. Damen, "Multiple-Phonon Resonant Raman Scattering in CdS," Phys. Rev. Lett., 22, 780 (1969).
25. R.C. Leite, J.F. Scott, and T.C. Damen, "Resonant Raman Effect in Semiconductors," Phys. Rev., 188, 1285 (1969).
26. K. Bohnert, H. Kalt, and C. Klingshirn, "Intrinsic Absorptive Optical Bistability in CdS," Appl. Phys. Lett., 43, 1088 (1983).
27. R.K. Cook and R.W. Christy, "Optical Properties of Polycrystalline CdS Films," J. Appl. Phys., 51, 668 (1980).
28. L.I. Maissel and R. Gland, Handbook of Thin Film Technology, (McGraw-Hill, New York, 1970), chap. 1.

29. J.H. Wohlgemuth, D.E. Brodie, and P.C. Eastman, "A Comparison of the Optical Properties of Crystalline and Amorphous CdS," Can. J. Phys., D8, 581 (1975).
30. M. Cardona and G. Harbeke, "Optical Properties and Band Structure of Wurtzite-Type Crystals and Rutile," Phys. Rev., 137, A1467 (1965).
31. E. Khawaja and S.G. Tomlin, "The Optical Constants Of Thin Evaporated Films of Cadmium and Zinc Sulphides," J. Phys. D, 8, 581 (1975).
32. M.H. Christmann, K.A. Jones, and K.H. Olsen, "Formation of Hexagonal Flat Tops on the Surface of Heteroepitaxial (0001) CdS Films," J. Appl. Phys., 45, 4295 (1974).
33. J. Humenberger, G. Linnert, and K. Lischka, "Hot-Wall Epitaxy of CdS Thin Films and Their Photoluminescence," Thin Solid Films, 121, 75 (1984).
34. M. Gracia-Jimenez, G. Martinez, J.L. Martinez, E. Gomez, and A. Zehe, "Photoluminescence of Chemical Deposited CdS Films," J. Electrochem. Soc., 131, 2974 (1984).
35. B.J. Feldman and J.A. Duisman, "Room-Temperature Photoluminescence In Sprayed-Pyrolyzed CdS," Appl. Phys. Lett., 37, 1092 (1980).
36. I. Lagnado and M. Lichtensteiger, "RF-Sputtered Cadmium Sulfide Thin Crystals," J. Vac. Sci. Technol., 7, 318 (1970).
37. J.A. Thornton, D.G. Cornog, W.W. Anderson, and J.E. Philips, Proc. of the 16th IEEE Photovoltaic Specialists Conf., 737 (1982).
38. I. Matril, G. Gonzalez-Diaz, F. Sanchez-Quesada, and M. Rodiguez-Vidal, "Deposition Dependence of RF Sputtered CdS Films," Thin Solid Films, 90, 253 (1982).
39. I. Matril, G. Gonzalez-Diaz, and F. Sanchez-Quesada, "Temperature and Bias Effects on the Electrical Properties of CdS Thin Films Prepared by RF Sputtering," Thin Solid Films, 114, 327 (1984).
40. I. Matril, G. Gonzalez-Diaz, F. Sanchez-Quesada, and M. Rodiguez-Vidal, "Structural and Optical Properties of RF Sputtered CdS Thin Films," Thin Solid Films, 121, 85 (1984).
41. I. Matril, G. Gonzalez-Diaz, and F. Sanchez-Quesada, "Heat Treatments of RF Sputtered Films for Solar Cell Applications," Sol. Eng. Mat., 12, 345 (1985).
42. F.B. Michwletti and P. Mark, "Ambient-Sensitive Photoelectronic Behavior of CdS Sintered Layers," J. Appl. Phys., 39, 5274 (1968).

43. J. Warnock and D.D. Awschalom, "Quantum Size Effects in Simple Colored Glasses," *Phys. Rev. B*, 32, 5529 (1985).
44. J. Warnock and D.D. Awschalom, "Picosecond Studies of Electron Confinement in Simple Colored Glasses," *Appl. Phys. Lett.*, 48, 425 (1986).
45. N.F. Borrelli, D.W. Hall, H.J. Holland, and D.W. Smith, "Quantum Confinement Effects in Semiconductor Microcrystallites in Glass," to be published in *J. Appl. Phys.*
46. US Guns, Cambell, CA.
47. J.A. Thornton and A.S. Penfold, "Cylindrical Magnetron Sputtering," Thin Film Processes, ed. J.L. Vossen and W. Kern, (Academic Press, New York, 1978).
48. J.L. Vossen and J.J. Cuomo, "Physical Methods of Film Deposition," Thin film Processes, ed. J.L. Vossen and W. Kern, (Academic Press, New York, 1978). p.38
49. E.M. Clausen Jr., "The Gamma to Alpha Transformation in Thin Film. Alumina," Master's Thesis, University of Florida, (1985).
50. P.C. Baker, "Trace Element Analysis of Limestone by Secondary Fluorescence X-ray Spectroscopy," Master's Thesis, University of Florida, (1981).
51. J.I. Goldstein, ed. Scanning Electron Microscopy and X-ray Microanalysis, (Plemun Press, New York, 1981).
52. R. Swaneopeol, "Determining Refractive Index and Thickness of Thin Films From Wavelength Measurements Only," *J. Opt. Soc. Amer. A*, 2, 1339 (1985).
53. E. Hecht and A. Zajac, Optics, (Addison-Wesley Publishing. Co. Reading, MA, 1979), p. 306.
54. T.S. Moss, Optical Properties of Semiconductors, (Butterworths Scientific Publishing. London, 1959), p. 34.
55. J.E. Cline and S. Schwartz, "Determination of the Thickness of Aluminum on Silicon by X-ray Fluorescence," *J. Electrochem. Soc.*, 144, 605 (1967).
56. L.I. Maissel and R. Gland, Handbook of Thin Film Technology, (McGraw-Hill, New York, 1970), chap. 15.
57. A. Joshi, "Auger Electron Spectroscopy," Metals Handbook Volume 10: Materials Characterization, 9th ed, (American Society for Metals, Cleveland, 1986), p. 549.

58. D. Briggs and M.P. Seah, Practical Surface Analysis by Auger and X-ray Photoelectron Spectroscopy, (John Wiley and Sons, New York, 1983), p.119.
59. S.W. Gaarenstroom and N. Winograd, "Initial and Final State Effects in the ESCA Spectra of Cadmium and Silver Oxides," J. Chem. Phys., 67, 3500 (1977).
60. K. Urbanek, "Magnetron Sputtering of SiO<sub>2</sub>; An Alternative to Chemical Vapor Deposition," Solid State Technol., April, 87 (1977).
61. V.E. Mashchenko, "Interaction of Excitons and LO Phonons in CdS Under High Excitation and At High Temperature," Opt. Spectrosc., 42, 116 (1977).
62. B.D. Cullity, Elements of X-ray Diffraction, (Addison-Wesley Publishing Co., Reading, MA, 1978), p. 458.
63. B.D. Cullity, Elements of X-ray Diffraction, (Addison-Wesley Pub. Co., Inc., Reading, MA, 1978), chap. 11.
64. E. Elizalde and F. Rueda, "On the Determination of the Optical Constants  $n(\lambda)$  and  $\alpha(\lambda)$  of Thin Supported Films," Elect. Opt., 122, 45 (1984).
65. K.A. Simmons and J.H. Simmons "Graphical Method for Solution of Ellipsometry Data" to be published in J. Appl. Phys.



END

DATE

FILMED

5-88

DTIC